Lacunarity and Chaos in Nature

Leonard Allen Smith

Thesis

Submitted in partial fulfillment of the requirements for the
Degree of Doctor of Philosophy in the
Graduate School of Arts and Sciences

Columbia University

1987

ABSTRACT

Lacunarity and Chaos in Nature

Leonard Allen Smith

The general solution of self-similar scaling equations is seen to contain an oscillatory component. The lacunarity of a self-similar set is reflected in this oscillatory component of the set's scaling statistics. Strange attractors found in nonlinear dynamical systems often possess self-similar structure. After introducing some new results regarding a strange attractor of astrophysical interest and considering the effects of using digital computers to study chaos, we demonstrate that the standard method of characterizing the global structure of these sets is vulnerable to errors arising from a misinterpretation of the oscillatory component. A new method of describing strange attractors by a spectrum of local scaling exponents computed about unstable periodic orbits is proposed. In addition to being computationally tractable, this approach utilizes the lacunarity oscillation to compute an accurate estimate of the residual error.

The lacunarity oscillation exists both for self-similar physical distributions and strange attractors. The role of this oscillation in the structure functions of fully developed fluid turbulence is exhibited through the β model. The physical structure of the observable matter distribution in the universe is also considered.

A new example of Hamiltonian chaos which is of geophysical interest is introduced. Specifically, a model is developed to simulate the motion of slowly settling tracers in a time-dependent flow. Here the time development of the length of a material line of

tracer particles is shown to be quite complicated even when the background flow field is laminar. A class of two-dimensional maps that simulate this type of flow is developed. Finally, the concept of a strange accumulator is introduced to describe the strong inhomogeneities observed to form in the probability distribution of a single chaotic trajectory.

Acknowledgments

First it is a pleasure to thank Ed Spiegel for his guidance throughout this project and for infecting me with an idea of what it means to be serious. Although the New York Convective Collective has dissipated, the ideas still being thrown about in the attic of Pupin have been a major source of inspiration for me. I am particularly indebted to P. Cvitonovic, J.-D. Fournier, I. Proccacia, K. Prendergast, C. Sparrow, M. Tabor and A. Wolf.

I am happy to acknowledge the financial support provided by Jim Hansen and the Goddard Institute for Space Sciences via NASA Cooperative agreement #NCC 5-29. In addition to financial aid, the Institute provided generous computer resources without which the studies reported here would not have been possible. I would like to thank Nadim Habra and the systems group at GISS for their patience and understanding that chaos and virtual machines sometimes interact in a violent manner. I owe a great debt to Rene Galarza for letting one more plot through, several times.

For allowing and encouraging me to roam this far from home I thank my parents; for various absurd notions and cards I thank my sister, Wendy Faheysmith. I am grateful to Bryan and Terrie Katz for a chance to really play with Squiggles. For their ever present friendship I thank Pat and Tip LaPorte, with a special thanks to Tip for reminding me that things are not always what they seem.

For the personal support I have received in New York I owe thanks to far too many people to name here. For sanity and focus I wish to

thank Kazumi Tabata and Stuart Chassen. My first years in New York were made livable through the craziness and caring of Dan Johnson, Walter Robinson and Audrey Wolf.

My successful completion of this project was possible only with the love, friendship and support of Bonnie Scarborough, Dave DeBeer and Richard Seager. This debt I hope to partially repay over the next two years, or so.

Preface and Overview

The study of nonlinear dynamical systems has provided a deterministic framework for the analysis of physical systems which behave in an irregular, seemingly stochastic manner. A major goal of this research is to discover, from an observational record, a system of equations governing the process, or failing this, a model of sufficient sophistication to be of use in understanding the character of the system and its behavior. The initial steps in this direction require a method of characterizing the complexity of a system's dynamics in its phase space. The recent development of a procedure for reconstructing this trajectory from an observed signal has inspired a great deal of interest interpreting the nature of these orbits. For ergodic systems, a trajectory may explore all energetically accessible regions of phase space, while in many interesting physical systems the trajectory appears to be restricted to a small subset of this region. The complexity of a system's dynamics are reflected in the properties of this trajectory which is taken to approximate the set of all accessible states. The focus of this thesis is on methods of characterizing the resulting set. This is done, for the most part, through the calculation of scaling exponents (generalized dimensions). These exponents provide estimates of the number of excited degrees of freedom in the system and thus a lower bound on the complexity of a model.

This thesis is divided into five chapters. Chapter 1 is titled "Concepts of Dimension and their relevance to Mechanics" and introduces the concepts of self similarity through a new analysis of

an old strange attractor (Moore and Spiegel, 1966). The notion of the scaling exponents of a distribution is discussed and the existence of an oscillatory component of the scaling functions of self-similar sets is established. It is the existence of this oscillatory function which provides, for the first time, a method of reliably evaluating the accuracy of numerically determined scaling exponents. In Chapter 2 the question of determining scaling exponents from data is considered. Two common methods are reviewed and their shortcomings are demonstrated. Specifically, we consider the methods of Broomhead and King (1986) and Grassberger and Procaccia (1983). It is shown by example that the former method fails to converge in test cases where the full structure of the system generating the data is known. Using the second method, the oscillatory component of the correlation integral in some simple fractal sets is examined. When the magnitude of this component is large, the method may converge (locally) yet provide a poor estimate of the correlation exponent. A fundamental issue for all methods of this type (which consider the large scale structure of a set) involves the quantity of data required for a reliable result. In the fourth section of Chapter 2 an absolute lower bound on the amount of optimally distributed data required as a function of the dimension of the set is established. Further restrictions implied by the use of a single time series are also discussed.

The local scaling of fractal sets is investigated in Chapter 3. Using the periodicity of the oscillatory component of scaling functions, a new method of characterizing this scaling is developed

which provides an estimate of the accuracy of the results obtained.

The oscillation in the scaling of physical systems is considered in Chapter 4. In fluid turbulence, where recent experiments suggest the presence of an oscillatory term, a self similar model of the turbulent cascade is generalized to demonstrate the observable manifestations of this phenomena. The presence of an oscillatory component is inherent to the geometry of self-similar distributions, whether the distribution arises from the dynamics of a system in its phase space or a physical distribution in real space. One of the oldest systems to be considered self-similar is the distribution of matter in the Universe; this distribution is considered in the second part of Chapter 4. No oscillatory component is evident in the data set examined.

In the final chapter, Chapter 5, a model for the motion of a particle in a two dimensional time dependent flow is developed. The chaos described there is of a different sort than that observed in dissipative systems. The development of self-similar structures in the flow indicates that flow visualization techniques should be interpreted cautiously when non-ideal tracers are used. Considering the model as a dynamical system, it is shown that the self-similar structure of the probability distribution of (finite length) trajectories can also bias measurement of the scaling exponents.

Overall, the research reported here is a study of an oscillatory component in what has often been considered a line. This phenomenon holds deep implications for existing methods of measurement of

scaling sets, and also suggests new approaches which circumvent the shortcomings of existing methods.

TABLE OF CONTENTS

CHAPTER I Concepts of Dimension and Their Relevance to Dynamics

Introduction

The laws which govern many physical processes may be expressed through systems of nonlinear equations. In first attempts to solve such systems, the nonlinearity is often assumed to be small and is suppressed or ignored entirely. Study of the resulting linear equations has established many time-honored methods of analysis, the failure of which was once taken to imply pathological behavior such as random noise disturbing the system. This is no longer the case. Beginning with Lorenz's numerical experiments in 1963, it has been recognised that signals which appear noisy and intermittent may be generated by completely deterministic nonlinear processes. Instead of requiring an external stochastic source term, the nonlinearities of these systems rapidly (exponentially) amplify small differences in the initial conditions. Deterministic systems with sustained dynamics that show **sensitive dependence on initial condition**[1] are called chaotic; their trajectories in phase space are said to display deterministic chaos in contrast to truly random or stochastic processes. Identifying a complicated physical system as chaotic provides insight into the processes that govern the system. Attempts to quantify these ideas have lead to a variety of scaling exponents (dimension(s), generalized dimensions, Lyaponov exponents, and so on), which are introduced in §§2 and 4 of this chapter. First we

---

[1] This phrase, coined by Ruelle (1980), describes the main feature of generic chaos.

give an idea of the range of physical phenomena to which these ideas are relevant.

The lack of linearity normally implies the loss of superposition; nonlinearity couples modes which would act independently in the corresponding linear system and it promotes interaction between disturbances of all scales. As noted by Lorenz (1986), atmospheric motions (weather) and climate models provide examples of this coupling where small-scale effects play a crucial role in large-scale dynamics. Often a self-organization is imposed via this coupling, and the properties which characterize the system are invariant under certain magnifications (changes in scale). This scaling behavior is observed in physical distributions. Typical examples include diffusion limited aggregates (Witten and Sander, 1981, 1983) and the distribution of visible matter in the Universe (de Vaucouleurs, 1971, Mandelbrot, 1972), coastlines (Richardson,1961) and the fracture surfaces of metals (Mandelbrot et al, 1984). Mathematical structures which display scaling behavior include strange attractors (e.g. Hénon , 1976; Ruelle, 1980; Spiegel, 1986), strange accumulators (e.g. Smith and Spiegel, 1987), the boundaries of the basins of attraction (Grebogi et al. 1984) and fat fractals (Umberger and Farmer,1985, Grebogi et al., 1985). As a result of the reconstruction theorem due to Takens (1981), the phase space structure of a host of physical systems has been elucidated in terms of "simple" nonlinear systems. These systems include particular behaviors of Josephson junctions (Iansiti, et al., 1985), lasers (Albano, et al. 1985) and Rayleigh-Bernard convection in a variety of fluids: mercury (Libchaber et al.,

1982), liquid Helium (Libchaber et al., 1982) and water (Giglio et al., 1984). Even some of the behavior of a "leaky" faucet is found to be in quantitative agreement with a simple mapping (Martien et al., 1985).

Since the particular subject of inquiry may be drawn from diverse catagories, the entity (set, surface, boundary, trajectory, ...) to be investigated will be referred to simply as an object or set. This is natural since, in all computational realizations, the entity will be represented as a denumerable collection of distinct points specified with finite accuracy. Similar techniques may be used to analyze objects from each class, although the class of the object often provides information useful in analyzing its structure. For example, a static physical boundary may be embedded in three dimensional space. Similarly, the solution of a set of ordinary differential equations must lie in a space of dimension less than or equal to the degree of the system.

Why should sets and their scaling parameters be of interest to the physicist? A precise knowledge of the geometric and probablistic structure of dynamical systems provides detailed limits on the predictability and dynamics of the system. Even a rough knowledge of the simplest geometrical quantities can provide insight into the nature of a system. Consider the power spectrum shown in Figure 1.1 (page 35). Traditionally, such "broadband noise" is interpreted as an indication that the system possesses many active degrees of freedom; if so, a complete description of the system would necessarily be complex. The power spectrum alone cannot

differentiate non-deterministic noise from highly structured chaos, but scaling exponents distinguish between the two and quantify the latter. In many cases, the state of the system may be completely described by only a few independent coordinates (in the case of Figure 1.1, three; see §1.3). Equivalently, the system's dynamics are restricted to a subspace of all possible states and this subspace may be embedded in a Euclidian space of small dimension. This means that after transients, the dynamics may be described by a model with only a few degrees of freedom (relative to the dimension of the full phase space of the system). A standard example from chemistry is the Belousov-Zhabotinsky experiment which involves chemical reactions between 30 chemical species under a variety of interaction parameters (Zaiken and Zhabotinsky, 1970). Parameter regimes exist where, for a variety of initial conditions, this system exhibits deterministic chaos; the asymptotic motion in phase space lies in a low dimensional subspace and may be completely described by many fewer variables than the number required to specify an arbitrary initial condition in the original 30+ dimensional phase space. Two examples from fluid dynamics, where the phase space is infinite dimensional, are Rayleigh-Bernard convection and Taylor-Couette flow (Branstater et al., 1983). Again there exists a parameter range where the system trajectory is restricted through self-organization to motion within a subspace of small dimension. Swinney and coworkers have described the transition of Taylor-Couette flow from a (zero dimensional) fixed point behavior up through chaotic behavior. In these cases, a knowledge of the geometry of the system provides a quantitative

measure related to the fundamental complexity of the problem.

The development of a formalism with which to describe nonlinear systems has a colorful, multiply connected history and is still incomplete. A survey might start with Poincaré's work on the three body problem at the turn of the century. For the most part, these ideas were developed by mathematicians during the first half of this century. They were advanced further in the work of probability theorists, meteorologists, astrophysicists, psychologists and computer scientists interested in pattern recognition during the sixties and early seventies, to be re-embraced by physicists, employed by a diverse cross-section of scientists including chemists, ecologists, population biologists and neurologists, and applied to a still increasing variety of systems today.

With no attempt to disentangle this development, the current formalism will be introduced in parallel with several ideas from the theory of dynamical systems which provide physical motivation. The discussion is presented with the bias found in the work of Farmer and Procaccia. It begins with a discussion of the meaning of dimension in §1.1 where two fundamental notions of dimension are developed and related to several of the "dimensions" commonly referenced in the literature. After the relevance of these ideas to physical models is presented in §1.3, the generalized dimensions of a probability distribution are defined.

SECTION 1.1 Two Concepts of Dimension

There are many different conceptions of dimension. For the sets discussed by Euclid, the different definitions based on each of these concepts often coincide in the same, integer value; while for many physical boundaries and most of the objects of nonlinear systems, this is not true. Two ideas form the basis for the majority of definitions of dimension to be dealt with here. The first, formulated by Poincaré, is related to the notion of the number of "distinct directions" on the set; the second, credited to Hausdorff, is derived by examining how the "volume" of an object changes as it is measured with increasing precision.

First, consider what is now called the topological dimension, based in the ideas of Poincaré and later supplied with a firm mathematical foundation by Brouwer, Menger and Urysuhn. Our discussion draws heavily from the complete development presented in Hurewicz and Wallman (1941). Poincaré suggested that the intuitive notion of the dimension of a given set or space is formed from consideration of the properties (dimension) of the simplest space capable of isolating a region in the original space. If a point has zero dimension, the dimension of higher continua may be established inductively:

> I shall base the determination of the number of dimensions on the notion of <u>cuts</u>. Let us consider first of all a closed curve, that is, a continuum of <u>one</u> dimension. If on this curve we take any two points through which we shall not permit ourselves to pass, the curve will be cut into two parts, and it will become impossible to go from one to the other, still remaining on the curve, but not passing through the excluded

> points. Let us consider, on the other hand, a closed surface which forms a continuum of <u>two</u> dimensions. It will be possible to take on this surface one, two, or any number of excluded points whatever. The surface will not be divided into two parts because of this; it will be possible to go from one point to another on this surface without encountering any obstacle because it will always be possible to <u>go around</u> the excluded points...
>
> We now know what a continuum of <u>n</u> dimensions is. A continuum has <u>n</u> dimensions when it is possible to divide it into many regions by means of one or more cuts which are themselves continua of <u>n-1</u> dimensions. The continuum of <u>n</u> dimensions is thus defined by the continuum of <u>n-1</u> dimensions. This is a definition by recurrence.[2]

In the formulation of Menger, this idea is capsulized in the definition of the <u>topological dimension</u>, D_T. Specifically, the topological dimension of the empty set is -1; for any nonempty set, D_T is equal to the least integer n such that every member of the set has arbitrarily small neighborhoods, the boundaries of which have dimension less than n.

It follows that if every point in the set has arbitrarily small neighborhoods with empty boundaries, the set has $D_T = 0$. This is clearly the case for any finite set of points and it is straightforward to show that D_T is equal to zero for any countable set as well as the set of all rational (or irrational) numbers on the unit interval. Furthermore it may be proven (Hurewicz and Wallman, Chapter 4) that the Euclidian N space, E^N, has $D_T = N$.

The utility of the topological dimension is limited by the difficulty of its determination from experimental data (Farmer, 1982). For the majority of systems found in texts on classical

---

[2] From Poincaré (1963) [originally 1913] page 29; a similar discussion may be found in Poincaré (1982) [originally 1913] page 256.

mechanics, however, this concept is sufficient and may be directly related to the number of degrees of freedom of the system. This is shown in the following section. Before doing so, we consider a second notion of dimension, the capacity.

The general trend is to establish by analogy a definition which admits real values equal to the topological dimension for Euclidean objects but is sensitive to the scaling behavior of more general sets. The mathematical framework here is found in the arguments of Hausdorff (1919) and Besicovitch (1953; and references therein).

Consider a geometrical object embedded in E^N, such as a rectangular solid in a 3-dimensional space. Put M(r) equal to the minimum number of N-dimensional spheres (N-spheres) of radius r required to cover the entire set. When r is decreased by a factor of two, M(r) increases by a factor of 2^N (e.g. 8 for the rectangular solid). The capacity dimension d_c is then defined as:

$$d_c = \lim_{r \to 0} \frac{\log M(r)}{\log r} \quad . \tag{1.1}$$

Here d_c is not restricted to integer values. There is, of course, no restriction to noninteger values; a set that has no topological resemblance to a line may have d_c equal to one, an example is the Fournier Universe discussed in Chapter 4.

To demonstrate that the capacity and the topological dimension do not always coincide, consider the "middle thirds" Cantor set. This set is perhaps the simplest and is certainly the most common example for which these two notions of dimensions differ; its construction is shown schematically in Figure 1.2. Starting with the interval

$0 \leq x \leq 1$, delete the middle third, $^1/_3 < x < {}^2/_3$. Now repeat the process on each of the two remaining subintervals. And so on. This simple destruction algorithm may be used to generate members of a special class of Cantor sets (see §2.3). For the middle thirds Cantor set, a point is uniquely labeled by the record of which of the retained subinterval it was located in at each generation. At each iteration of the process the point in question will lie either on the right section (R) or the left section (L) of the subinterval. Recording these symbols in order identifies the point with a symbolic sequence; for example the point marked by the arrow in Figure 1.2 b is represented by the sequence LRRLLLLLL... This symbolic representation will prove useful when we consider the correlation integral in Chapter 2. Through the correspondence R → 1, L → 0, a member of the set may be identified with each binary fraction between zero and one inclusive, therefore the set contains an uncountable infinity of points.

In order to determine the topological dimension of this set, note that the location of any member of the set can be expressed as

$$x = \sum_{n=1}^{\infty} \frac{a_n}{3^n} \qquad a_n = 0 \text{ or } 2 \ .$$

Thus there exist arbitrarily small neighborhoods about each point with empty boundaries and the set has $D_T = 0$. As shown below, it has a nonzero capacity dimension.

Every Cantor set may be decomposed into an integer number, ρ, of identical subsets A_i each of which reproduces the structure of the entire set when magnified by a factor $1/\sigma$. Any set with this

property is called strictly self-similar with similarity ratio σ and structure ratio ρ. If only general properties of a distribution are reproduced, it is called statistically self-similar or simply, self-similar. The middle thirds Cantor set is strictly self-similar with $\rho = 2$ and $\sigma = 1/3$.

The capacity dimension of a strictly self-similar set is nonzero. If m spheres of radius ℓ are required to cover the set, $m\rho^N$ spheres of radius $\ell\sigma^{-N}$ will be required. This is true for any integer N. Thus

$$M(\ell/\sigma) = \rho\, M(\ell) \tag{1.2}$$

with

$$M(\ell) \sim \ell^{d_c} \tag{1.3}$$

implies

$$d_c = - \frac{\log \rho}{\log \sigma} \tag{1.4}$$

For the Cantor set above with $\rho = 2$ and $\sigma = 1/3$

$$d_c = \frac{\log(2)}{\log(3)} = 0.63093\ldots .$$

Many of the statistics of self-similar sets obey an equation of the form

$$C(\ell/\sigma) = \rho\, C(\ell) \tag{1.5}$$

the general solution of which is (Smith et al, 1986)

$$C(\ell) = \chi(\ell)\, \ell^{d} \tag{1.6}$$

with

$$d = - \frac{\log \rho}{\log \sigma} \tag{1.7}$$

where $\chi(\ell)$ is a log-periodic function[3] of ℓ. The importance of this oscillatory component of scaling is discussed in Chapters 2, 3, and 4. The power law component is often expressed as

$$C(\ell) \sim \ell^{d} \tag{1.8}$$

where the symbol "~" is read "scales as". Any quantity d that satisfies an equation of the form 1.8 is called a scaling exponent. The capacity dimension is the first of several scaling exponents which will be discussed in this thesis.

The fractal dimension, d_f, is a slight variation on the capacity. Instead of the minimal number of hyperspheres to cover the set, consider the coarse grained image of the set produced by a fixed, space-filling square mesh of grid size ϵ. Denote the number of hyper-boxes containing at least one member of the set as $M(\epsilon)$. The fractal dimension is then defined (Mandelbrot,1972) as

$$d_f = \lim_{\epsilon \to 0} \frac{\log M(\epsilon)}{\log \epsilon} . \tag{1.9}$$

For most physical examples, the fractal dimension and capacity dimension are thought to coincide. Questions regarding the effect of covering a set with boxes as opposed to spheres have been addressed by Cawley et al. (1985 preprint). The formal basis for both of these concepts is the Hausdorff-Besicovitch dimension, d_{HB}; the definition of which requires the introduction of several additional concepts in order to establish a more rigorous notion of covering a set.

Let **X** be a set in an N dimensional Euclidean space with metric d. Define $\delta(X)$, the diameter of **X**, as the maximum separation of any two

---

[3]Alternatively, if χ is considered a function of $\log(\ell)$, χ is periodic.

members of the set.

$$\delta(\mathbf{X}) = \sup\, d(x,y) \tag{1.10}$$

where the supremum is taken over all pairs of the elements of **X**. Decompose the set **X** into a countable number of subsets $\mathbf{A}_i$ each of which has diameter less than ϵ. For any real number p such that $0 \leq p \leq \infty$, define

$$m_p{}^{\epsilon} = \inf \sum_{i=1}^{\infty} [\delta(\mathbf{A}_i)]^p \ . \tag{1.11}$$

Here the infimum (minimum) is taken over all possible decompositions. This defines the minimal covering.

The p-dimensional measure of **X**, denoted $m_p(\mathbf{X})$ is given by

$$m_p(\mathbf{X}) = \sup_{\epsilon>0} \ m_p{}^{\epsilon}(\mathbf{X}) \ . \tag{1.12}$$

The Hausdorff-Besicovitch dimension of **X** is then defined as the supremum of all real numbers p such that $m_p > 0$.

While special cases may be constructed where the capacity dimension, fractal dimension and Hausdorff-Besicovitch dimension differ, it is not clear whether this will occur in any system of physical interest. Once self-similar behavior is assumed, many techniques are available to quantify it. Since each method yields a somewhat different quantity, a large number of "dimensions" have been defined. In most cases they are related to the three above.

The term <u>fractal</u> was originally introduced to describe sets whose Hausdorff dimensions exceed their topological dimensions (Mandelbrot, 1972). In this thesis the term is used for any set which scales in a self-similar manner. Fractals are then classified into groups: the

middle-thirds Cantor set is called a homogeneous fractal. The meaning of this qualification is made clear in §1.4. We find this preferable to the suggestion of Taylor (1987) to call only homogenous fractals "fractal."

In this section the two most common notions of dimension have been described. Before generalizing these geometric quantities to include probability distributions, we will demonstrate the physical relevance of these notions of dimension.

Section 1.2 Deterministic Dynamical Systems

A dynamical system may be defined as a collection of rules which prescribes the manner in which any initial point in phase space evolves as a function of time. Here the phase space of a system is an Euclidean N-space, E^N, where N corresponds to the number of independent real numbers required to completely specify an arbitrary initial condition (state) of the system. The phase space dimension of the system is equal to N and to every possible state of the system there corresponds an N-vector **x** in this space:

$$\mathbf{x} = (x_1, x_2, \ldots, x_N) .$$

As the system evolves in time, a trajectory is defined by the sequence of states through which it passes. The focus here will be on deterministic systems; a system is deterministic only if a complete knowledge of the future (and past) state of a given realization is encoded in its current state; given the rules governing the system, a single space-time point defines the entire

trajectory uniquely. This excludes any random or stochastic elements from the system. A chaotic system is completely deterministic in this sense.

Note that almost all "random number generators" available on digital computers are deterministic dynamical systems. Whether the distinction between random and deterministic generators is important depends on the application; numbers from deterministic generators will be called pseudo-random or p-random. An early p-random number generator suggested by Ulam and von Neumann (1947) is a special case of what is now one of the most studied chaotic systems - the logistic map (see §3.3). Its utility as a p-random number generator is still a subject of interest (Arneodo and Sornette, 1984).

The rules governing dynamical systems of physical interest are often described by difference or differential equations, the choice determined by whether it is more natural/convenient to treat time as a continuous or discrete variable (cellular automata (Wolfram, 1985) may be considered as an additional example). There has been some striking progress in the modeling and interpretation of physical systems through the use of nonlinear dynamical systems in this way. Qualitative behavior such as period doubling and quantitative predictions such as the values of "universal" numbers have been made in systems ranging from dripping faucets (Crutchfield et al., 1986) to the behavior of convection in liquid helium (Libchaber and Maurer, 1982). In addition to fixed points, limit cycles and chaos, seemingly chaotic behavior which slowly dies away has been observed in the work of some authors (e.g. Spiegel, 1986); this transitory

chaos has been called pandemonium.

Hamiltonian systems form an important special case of dynamical systems. Introductions to the exploration of chaos in Hamiltonian systems are given by Hénon (1983) and Berry (1978) and in the textbook of Lichtenberg and Lieberman (1983). This brief introduction demonstrates the fundamental role played by dimension in Hamiltonian dynamics and serves to preface the discussion of a system of this type given in chapter 5.

Consider a deterministic dynamical system with an N dimensional phase space. The system is Hamiltonian if it is possible to write the N variables x_i as n pairs of conjugate variables

$$q_i,\ p_i \quad i=1,2,\ldots,n; \quad n \quad n \quad = \begin{cases} N/2 & \text{for N even} \\ (N+1)/2 & \text{for N odd} \end{cases}$$

in such a way that the dynamics of the system are described by a single function $H(q_i, p_i)$ through the relations

$$H(p_i, q_i) = 0 \qquad \dot{p} = -\frac{\partial H}{\partial q} \qquad \dot{q} = \frac{\partial H}{\partial p} \quad . \tag{1.13}$$

In two-dimensional fluid dynamics, a stream flow is one for which there exists a function $\Psi(x,y,t)$ such that the velocity field determined by

$$\dot{x} = \frac{\partial \Psi(x,y,t)}{\partial y} \qquad y = -\frac{\partial \Psi(x,y,t)}{\partial x} \quad . \tag{1.14}$$

All such systems have Hamiltonian structure. The motion of tracers in this type of flow has been considered by Smith and Spiegel (1985;

also Smith, 1984 and Chapter 5). An experimental realization of Lagrangian turbulence has been analyzed and modeled by Chaiken et al. (1986, 1987).

A similar Hamiltonian structure exists for dynamical systems composed of interacting point vortices in two-dimensional flows. Vortex dynamics may be observed in superfluid helium (see Roberts and Donnelly, 1974). The appearance of chaotic motion in these systems has been studied by Aref (1983).

The Hamiltonian structure of a system imposes constraints on the types of motion it may exhibit. Such systems are deterministic (one to one), and the Liouville theorem (eg. Lichtenberg and Lieberman, 1983) guarantees that the N-volume of an ensemble of initial conditions will be preserved under the flow. By requiring the conservation of N-volume, Liouville's theorem excludes the existence of any attracting sets in the full phase space of a Hamiltonian system.

A system is <u>integrable</u> if there exists a canonical transformation to new variables P_i, Q_i such that

$$H_0(P_i) = 0, \quad \dot{P}_i = -\frac{dH_0}{dQ_i} = 0, \quad \dot{Q}_i = \frac{dH_0}{dP_i} \equiv \omega_i(P_1,\ldots,P_n) \quad . \quad (1.15)$$

Hence,

$$P_i(t) = P_i(t=0) \ , \qquad Q_i(t) = \int_{t_0}^{t} \omega_i(P_1,\ldots,P_n)\, dt \qquad (1.16)$$

and the system has been reduced to quadratures.

In the majority of pedagogical examples, a trajectory does not wander throughout phase space but is confined to a lower dimensional

surface by constants (integrals) of the motion, such as the total energy, the angular momentum and so on. If a sufficient number (N/2) of these integrals exist, the motion may be placed in the form of Equations 1.15. In this case, the motion of each (P_i, Q_i) pair is independent; each pair represents one degree of freedom of the system. If the solution is bound to a restricted region of phase space, the Q_i must appear as arguments of cyclic functions and the system evolves on an n-dimensional torus (an n-torus). Both the topological dimension and the Hausdorff-Besicovitch dimension of an n-torus are equal to n (as are d_c, d_f, and so on). For a typical integrable system, the topological dimension of the complete trajectory is equal to the number of degrees of freedom (over-integrable systems are an exception; see Henon, 1983). It is in this way that the topological dimension of an orbit is related to the properties of the system. While Liouville's theorem requires every ensemble to maintain an N-dimensional volume, the individual trajectories of an integrable system are each confined to a manifold whose topological dimension is less than (in general one half) the phase space dimension of the system.

This idea is demonstrated by two uncoupled pendula. The phase space of this system is four dimensional (angular position and velocity of each pendulum); trajectories are restricted by the total energy to a three dimensional surface. As long as they remain uncoupled, the energy is each pendulum is conserved individually and the motion is on a two-torus.

Due to the difficulty of visualizing objects which sit in spaces

of dimension greater than or equal to three, phase space trajectories are usually viewed by taking a surface of section. The method, credited to Poincaré, entails following a trajectory in N dimensions and recording the locations at which it passes through a given N-1 dimensional surface (in a given direction). For a system constrained to a three dimensional surface, this would correspond to recording the points at which the trajectory pierces a chosen plane. Many of the properties of the full flow may be determined from such a surface of section, for example the capacity and topological dimension of the section of an orbit should be one unit less than the corresponding value of the flow. For example, a Poincaré section of a 2-torus is a circle. Integrable Hamiltonian systems may be perturbed in two distinct ways. Consider first a perturbation, H', which does not destroy the Hamiltonian structure of the original integrable system, H_0. That is one which may be written

$$H = H_0 + \epsilon H' \qquad \dot{q} = \frac{dH}{dp} \qquad \dot{p} = -\frac{dH}{dq} \quad . \qquad (1.17)$$

At present, there is no method to determine a priori whether or not a given system is integrable. The current search for a general method to answer this question is discussed in its historical context by Tabor (1984). A complementary approach to the analytic search for integrals of the motion is provided by numerical examination of individual trajectories. The system is assumed to be integrable over any range of initial conditions where the computed trajectories appear to lie on tori. Trajectories which appear not to lie on any torus and seem to display sensitive dependence on initial condition are called chaotic. Computer surveys by Hénon and Heiles (1964) and

Walker and Ford (1969) revealed a complex, self-similar interweaving of chaotic and integrable trajectories. While the intricacy of this structure was envisioned by Poincaré; the question as to which type of motion prevailed in the limit of small but finite perturbation was not resolved until the 1960's (See Moser, 1973). A simple perturbed Hamiltonian system is discussed in Chapter 5.

Other physically motivated modifications of system 1.15 add terms which destroy the Hamiltonian structure. These systems are often referred to as dissipative regardless of whether or not they were derived from a Hamiltonian formulation. For such systems there is no Louiville theorem; the volume of an ensemble of initial conditions may contract as the ensemble evolves under the flow and the asymptotic motion of the system is generally governed by an attractor. Consider the system of two uncoupled pendula when both pendula are damped. For almost all initial conditions, the asymptotic state of the system is motionless with both pendula at the orientation of the downward plumb line. By almost all we mean that the set of all initial conditions which behave otherwise has Lebesgue measure zero (zero N-volume in a phase space of dimension N). Equivalently, this set has dimension less than the set of all initial conditions which approach the attractor, and a randomly selected initial condition will belong to the basin of the attractor with probability one. In this particular case, the attractor is a set of zero dimension (a point) and the basin of attraction consists of the entire four-dimensional phase space with the exception of the three-dimensional manifolds on which the kinetic energy of either (or both)

pendulum is such that the pendulum comes to rest at the unstable equilibrium point. Similarly, in the case of a simple limit cycle (damping of only one of the pendula) the attractor would be one-dimensional. Again, knowledge of the dimension of the attractor yields insight into the dynamics of the system.

In addition to limit cycles, attractors often are observed where the large time motion is neither periodic or quasiperiodic (motion on an n-torus), but which is irregular. A severe truncation of the equations describing convection, originally proposed by Lorenz (1963) to demonstrate that the difficulty of weather prediction might be intrinsic to the system, has produced the paradigm of strange attractors[5]. The Lorenz equations have been subjected to intense study which is surveyed and extended by Sparrow (1970). Similar "irregular behavior" was observed by Moore and Spiegel (1966) in a study of stellar pulsations. Here we review the tools of nonlinear dynamics through an examination of the attractors of this system. We note in passing that the phase space trajectories of both of these systems are particular cases of the motion of a particle in a time-dependent potential, where the potential is described by polynomial of the position (see Marzec and Spiegel, 1980).

The original Moore-Spiegel model is a simple thermo-mechanical oscillator; a fluid parcel oscillating vertically in a temperature-stratified background atmosphere. Physically, the restoring force for the oscillations may be, say, differential rotation; while the

---

[5]This term was first coined by Ruelle and Takens; we maintain the original definition as applying to any attractor the time dependence on which is not periodic or quasiperiodic.

thermal interaction of the parcel with the surrounding fluid leads to the asymmetries in the energy flow which may amplify the oscillations. All displacements are assumed to be small when compared to a scale height of the background atmosphere, implying a Boussinesq equation of state (the density variation of both the parcel and the ambient fluid is linearly proportional to the temperature deviation from some standard temperature). With the additional assumption that the thermal interaction is described by the Newton law of cooling (valid in the case of an optically thin parcel, see Spiegel, 1957), the system may be described by three time scales: the gravitational free fall time as modified by buoyancy, the cooling time due to thermal/radiative interactions, and the time constant of the restoring force.

For a parcel in a linear temperature field, small oscillations either grow or decay depending whether or not the stratification is stable. A nonlinearity is introduced through the consideration of a locally unstable temperature profile which varies quadratically with the vertical displacement, z. Such a profile mimics an unstable layer sandwiched between two stable layers. Measuring the time in units of the cooling time and distance in units of the half height of the unstable layer leads to the equation of motion of the parcel (Moore and Spiegel, 1966)

$$\frac{d^3z}{dt^3} + \frac{d^2z}{dt^2} + (T - R + Rz^2)\frac{dz}{dt} + Tz = 0, \qquad (1.18)$$

where T and R are positive real numbers. Physically, T represents the square of the quotient of the thermal relaxation time divided by

the free period of the oscillation while R is the square of the ratio of the relaxation time to the free fall time. For $R \gg T$ or $R \ll T$, numerical simulations of system 1.18 display, after a transient, periodic behavior; alternatively, in a band of R, T values near $R = T$, aperiodic motion is observed in a restricted region of phase space. A limit cycle behavior of the system is revealed in Figure 1.3a, where z(t) is plotted for the parameter values $R = 100$ and $T = 10$ (hereafter Case I); the motion lies on a periodic attractor and small perturbations relax back to this attractor. Two examples of aperiodic motion are found for $T = 26$ and $R = 100$ (Case II), and for $T = 36$ and $R = 100$ (Case III). Figures 1.3 b,c are time series of z in these cases. Case II is the source of the power spectrum of Figure 1.1. More detailed spectra of Cases I and II are provided in Figure 1.4. Periodic orbits exist for all three sets of parameter values (Baker, Moore and Spiegel, 1966, 1971). In Cases II and III there are several periodic orbits, all of which are unstable. In the Case II time series, the system trajectory is observed to wander between the neighborhoods of different periodic orbits in what appears to be an erratic manner. Understanding these unstable periodic orbits is central to describing the structure of strange attractors.

A stereogram of the phase space trajectory of Case I is shown in Figure 1.5. The complications of the chaotic trajectories reduces the quality of their stereograms; perspective projections of these trajectories from several viewpoints are shown in Figures 1.6 and 1.7.

A Poincaré section of a trajectory of Case I reveals a collection of points scattered about several specific locations (the number depends on the section taken) which are visited in a well defined order. The scatter is consistent with the numerical accuracy of the calculation. In contrast, a section from Case III reveals no simple geometry or ordered motion. Figure 1.8 is a section showing the velocity and acceleration at successive downward passes through the z=0 plane, while a blow up of this section is given in Figure 1.9. The section shown in Figure 1.8 and 1.9 corresponds to structure in the lower left branch of the attractor as viewed in Figure 1.7 a. Evidently, there is no simple description of the system in this parameter regime.

Long integrations of the Lorenz or Moore-Spiegel equations, and observations of the systems they are designed to represent, indicate that this complex motion is not transitory. Numerically, these systems display sensitive dependence on initial condition and they exhibit period doubling bifurcations as the parameters are varied (see Cvitanović 1984, introduction). The evolution of nonlinear ODE's which make up these systems requires a time consuming integration of the system. In an effort to make the structure of the attractors of such systems more accessible, Hénon (1976, see also Hénon and Pomeau, 1977) developed a two-dimensional iterative mapping to simulate the Poincaré sections directly. Designed to represent dissipative systems in general and the Lorenz system in particular,[6]

---

[6] A map designed to simulate Moore-Spiegel type systems has been developed by Arneodo et al. (1985).

Hénon determined the most general quadratic map with constant Jacobian to be:

$$\begin{aligned} x_{i+1} &= 1 - ax_i^2 + y \\ y_{i+1} &= bx_i \quad . \end{aligned} \tag{1.19}$$

This map has been discussed extensively in the literature. A review is given by Hénon (1980). When the absolute value of the Jacobian of a map (here equal to $|b|$) is less than one, the map is area contracting. In this case, the area of an ensemble of initial conditions will be reduced by a factor of $|b|$ after each iteration of the mapping. By demonstrating a region of the plane which is mapped into its interior, Hénon proved this mapping possessed a trapping region; such a region must contain an attractor. As the value of parameter a is increased, this mapping also follows a period doubling cascade to chaos (Derrida et al., 1978). For the canonical parameters ($a = 1.4$, $b = 0.3$) the mapping appears to have sensitive dependence on initial condition.

Figure 1.10 shows 2^{20} iterations of the map starting from a 64 bit approximation of the fixed point. It appears that this attractor is not periodic, an assumption given empirical support by the self-similar structure observed when the circled region is magnified. It is generally believed (although not proven) that the asymptotic motion described by this system has this type of structure at all scales. This set is the Henon attractor. Numerical evidence indicates that for this set (Russel et al., 1980)

$$d_c = 1.261 \pm 0.003 \quad .$$

In addition to the lack of strict self-similarity, two additional

quantitative features distinguish this set and those of Figures 1.5 and 1.6 from the middle thirds Cantor set. The first is a richer mathematical structure due to the nonuniform distribution of points on any coarse grained representation of the attractors. The second is a physical limitation of scaling properties due to the nature of the underlying physical (or computational) system. Physical constraints and the relevant probability theory are discussed in the next section where a few more scaling exponents are introduced. Further discussion of these features is presented in §3.1 where the oscillatory component of the scaling is utilized to quantify these properties with precision.

As an important aside we note that the orbit displayed in Figure 1.10 must evolve onto a periodic orbit. All the calculations were done on a digital computer capable of representing only a finite number of distinct values. Thus every deterministic trajectory must eventually close upon itself. Furthermore, there cannot be true sensitive dependence on initial conditions; if the initial condition is specified to an accuracy beyond the resolution of the numerical grid the future trajectories are identical. The theorems of dynamical systems were developed for continuous systems which are not accurately represented by discrete computational grids. The effects of treating finite separations as infinitesimal in the determination of Lyaponov exponents from experimental data has been studied by Alan Wolf (personal communication). The ultimate periodicity of orbits and apparent chaos in digital computers are explored in Appendix 1.

SECTION 1.3 Probability Distributions on Fractals

The mathematical definitions of dimension in the previous section were given in the limit of small scales. In physical realizations of scaling there exists an inner cutoff below which the scaling relations do not hold. The early 19th century wood print, **The Great Wave off Kanagawa** by Hokusai (see Mayor, 1985), often cited as representative of self-similar cascades in nature, also captures the fundamental limits to any realization of this self-similarity. The great wave is composed of lesser waves, each of which in turn has a finer structure similar in form to the first: hence, self-similarity. After several generations the cascade stops, there is a well-defined smallest wave size, as there is a largest; no wave exceeds Fuji. The concepts of an inner and outer cutoff of the scaling region are fundamental in all physical realizations of self-similarity. The terms self-similar and scaling are nonetheless used to describe physical and numerical distributions where the inner cut off prohibits complete reproduction under magnification. Implicit in doing so is the assumption that there exists a "large" range of scales over which scaling holds approximately. The question of quantifying these properties in empirical data is taken up in Chapter 2.

Even in the case of noise-free data, the inner cutoff may not be observable for at least two reasons. The limited accuracy of any measuring process imposes a partition upon the (assumed continuous) variables which are recorded. If this threshold is above the inner cutoff, the latter will not be observed. Even when the threshold is

sufficiently low as to make the cutoff observable in principle, the quantity of data required to detect it may exceed the capacity of the analysis. Since the amount of data required to determine a surface grows exponentially with the dimension of the set, the effect may pose a real, if technology dependent, constraint.

Consider an experiment in which the finest partition available fails to resolve the inner cutoff. From a histogram of the data, often computed as the experiment proceeds, the relative probability of the i^{th} partition, p_i, may be computed. The Hausdorff dimension (equivalently d_c and d_f) is not sensitive to the magnitudes of the p_i, but only to the number that are nonzero. Assuming this probability distribution converges (i.e. there exists an invariant measure underlying the system) one may compute d_I, the information dimension (Farmer 1982)

$$d_I = \lim_{\epsilon \to 0} \frac{I'(\epsilon)}{|\log \epsilon|} \tag{1.20}$$

where

$$I'(\epsilon) = \sum p_i \log p_i \tag{1.21}$$

where the sum is over all boxes with nonzero probability. $I'(\epsilon)$ represents the amount of information gained, on average, by an isolated measurement of the system using instruments of resolution ϵ.

The information dimension is just one of an infinite number of generalized dimensions originally defined in the context of information theory by Balatoni and Renyi (1956). General introductions to information theory are Shanon and Weaver (1964) and Renyi (1970, Appendix A); discussions in the context of dynamical

systems are available in Shaw (1981) and Farmer (1982, 1983, 1984). The mathematical foundations of the material presented in this section were laid by Renyi based on the ideas of Boltzmann, Kolmogorov and Shannon. Loosely speaking the amount of information in a signal (measurement) is related to the minimum number of bits required to identify that measurement from the set of all possible measurements. Following Renyi (1970), consider a random variable ξ which assumes denumerably many values x_k each with probability p_k. That is

$$p_k \equiv \text{Prob}(\xi = x_k) \qquad k = 1,2,3,... \tag{1.22}$$

and define the information of order α in the value of ξ, $I_\alpha(\xi)$, as

$$\begin{aligned} I_\alpha(\xi) &= \frac{1}{(1-\alpha)} \log\left(\sum_{k=1}^{\infty} p_k^\alpha\right) \qquad \alpha \neq 1 \\ I_1(\xi) &= \sum_{k=1}^{\infty} p_k \log \frac{1}{p_k} \quad . \end{aligned} \tag{1.23}$$

The ξ dependence of I_α is implicit in the determination of the p_k. If the distribution of ξ were continuous, a single irrational value of ξ would contain an infinite amount of information. With the physically motivated argument that ξ is known only with finite precision and on the assumption that the observed values converge to the continuous values as the precision is increased, Renyi introduces the partitioned variable

$$\xi_N = \frac{[\xi N]}{N} \tag{1.24}$$

where [x] denotes the greatest integer less than or equal to x. For a continuously distributed ξ, the information tends to infinity as N $\to \infty$ but the quantity

$$d_\alpha(\xi) = \lim_{N\to\infty} \frac{I_\alpha(\xi_N)}{\log N} \tag{1.25}$$

exists in many cases and is called the dimension of order α of the ξ. Renyi extends the definition to m-dimensional random vectors (m = 1,2,3,...), proving that for an absolutely continuous distribution the d_α are equal and correspond to the geometric notion of dimension (that is $d_\alpha = m$) and suggesting the application of the ideas of Hausdorff.

In the case $\alpha = 0$

$$I_0 = \log \sum_{k=1}^{\infty} (p_k)^0 = \log M(\epsilon)$$

where $M(\epsilon)$ is the number of hypercubes of side $\epsilon = 1/N$ which have nonzero probability. Thus

$$d_0 = \lim_{N\to\infty} \frac{\log I_0(\xi)}{\log N} = \lim_{\epsilon\to 0} \frac{\log M(\epsilon)}{|\log \epsilon|}$$

and d_0 is equivalent to the fractal dimension. Similarly d_1 is the information dimension

$$d_1 = \lim_{N\to\infty} \frac{\sum p_k \log p_k}{\log N} \equiv d_I \ .$$

This case has been studied extensively by Farmer in the context of dynamical systems.

Since

$$\begin{aligned} p_i^{\alpha'} &< p_i^{\alpha} && \text{for } \alpha < \alpha', \\ I_{\alpha'}(\xi_N) &\geq I_{\alpha}(\xi_N) && \text{for } \alpha < \alpha' \end{aligned} \tag{1.26}$$

which implies

$$d_{\alpha'} \geq d_{\alpha} \qquad \text{for all } \alpha < \alpha'. \tag{1.27}$$

Any set for which $d_0 > D_T$ and $d_\alpha = d_0$ for all α will be referred to as a homogeneous fractal. The middle thirds Cantor set is of this type. Note that d_α may depend on the geometry of the set, the metric, and the probability distribution. As pointed out by Renyi and emphasized by Ott et al. (1984), the d_α are not invariant to smooth changes in coordinate.

A similar formalism was described by Hentschel and Procaccia (1983) and applied to several problems of nonlinear dynamical systems theory. At this point we adopt their notation letting $\alpha \rightarrow q$ and $N \rightarrow 1/\epsilon$. Here q is considered a continuous real variable ($-\infty < q < \infty$) (see also Grassberger and Proccacia, 1984).

Recently, Halsey et al. (1986) and Kadanoff (1987) have introduced a new formalism which relates the d_q to a smooth function, $f(\alpha)$, by a Lengendre transformation. This function characterizes the strengths of the singularities of the set. Halsey et al. state the following relations (their equations 1.10 and 1.11)

$$d_q = \frac{1}{q - 1} \left[q\alpha(q) - f(\alpha(q))\right] \tag{1.28}$$

$$\alpha(q) = \frac{d}{dq} \left[(q-1)\, d_q\right] \quad . \tag{1.29}$$

$f(\alpha)$ is related to the dimension of the set upon which singularities of strength α lie. Having calculated the d_q with equation (1.25), one may compute $\alpha(q)$ with (1.29)[7] and then $f(\alpha)$ via (1.28). In cases where it can be determined, $f(\alpha)$ yields a new way to visualize the information in d_q. A comparison with experiment is provided in Libchaber (1986). Note that for homogeneous fractals all the d_q are equal and so

$$\alpha\,(q) = d_q = d_0 \quad . \tag{1.30}$$

Furthermore,

$$f(\alpha) = \alpha(q) = \text{constant}.$$

We shall consider the effects of sectioning and projecting on $f(\alpha)$ in Chapters 3 and 4, respectively. Calculation of d_q for large negative q from experimental data is difficult because these scaling exponents emphasize the structure of the lowest probability singularities of the set. A method which provides a useful lower bound on $d_{-\infty}$ is developed in Chapter 3. A dimension function has also been introduced by Badii and Politi (1985) who have directly extended the work of Renyi. A somewhat more complicated function representing the scaling structure of a set has been introduced by Feigenbaum (1978, 1979).

---

[7]Note that in general this requires differentiating a numerically derived quantity.

Conclusions

As evidenced by the dimension functions above, the structure of sets that scale is rich and a useful description requires the consideration of more than a single scaling exponent. The general solution to the scaling equations can be used to obtain additional information regarding a set beyond its dimension (Smith et al, 1986). When determining scaling exponents, we often write the general solution

$$C(\ell) = \chi(\ell)\ \ell^{d} \tag{1.6}$$

in the form

$$\log C(\ell) = d \log \ell + \log \chi(\ell)$$

and let

$$\psi(\ell) = \log \chi(\ell)$$

Since $f(\alpha)$ characterizes the singularities of a set, the $\psi(\ell)$ functions describe additional structure to which $f(\alpha)$ is insensitive. Once we have presented a method for calculating the correlation integral, we will examine the structure of this $\psi(\ell)$ function for several fractals.

The function $\chi(\ell)$ (or $\psi(\ell)$) characterizes a textural quality of the underlying distribution. Its precise interpretation depends on the statistical quantity in question, for the minimal cover (and also, though less strikingly, for the correlation integral) $\chi(\ell)$ describes the property of the set called lacunarity (Mandelbrot, 1973). The qualitative character implied by this term is difficult

to capture in a single parameter. The examination of several functionals of $\chi(\ell)$ indicates that it is preferable to retain the information intact in one period of χ itself. Lacunarity describes the lulls in a distribution. The periodicity of the oscillation reveals information as to how different scales are coupled, and as such provides valuable insight into such problems as the spacial intermittency of fluid turbulence. This is the topic of Chapter 4. First, we will discuss the problem of determining the scaling exponents of a distribution. We will see that the ψ functions plays a role here also.

Figure Captions

Figure	Caption
1.1	Power spectrum of a chaotic time series. This figure shows the case of the Moore-Spiegel system (introduced in Section 2) with parameters T = 26.0 R = 100.0 .
1.2	The first four steps in the construction of the middle thirds Cantor set by repeated application of the destruction algorithm. The arrow denotes the point LRRLLLL... .
1.3	Time series of z from the Moore-Spiegel system for parameter values R = 100 with a) T = 10 (Case I); b) T = 26 (Case II); and c) T = 36 (Case III). Data were generated using a 6^{th} order Runge-Kutta routine. The series is sampled with a time-step $\Delta t=0.05$, individual data points are noted by '+' on the interval $0 \leq t \leq 64$.
1.4	Details in the low frequency power spectra computed from the time series of z(t) for a) Case I and b) Case II.
1.5	Stereograph of the attractor for Case I.
1.6	A perspective view of the attractor for Case II from the point z = 27.0, $\dot{z}$ = 22.0, $\ddot{z}$ = 0.0
1.7	Two perspective views of the attractor for Case III T = 36.0 from the point (a) (z = 30.0, $\dot{z}$ = 5.0, $\ddot{z}$ = 0.0). (b) (z = 27.0, $\dot{z}$ = 22.0, $\ddot{z}$ = 0.0).
1.8	Poincaré section of the Moore-Spiegel attractor at z = 0 for T = 36 R = 100. This section corresponds to the lower left region of Figure 1.7a.
1.9	A close-up revealing the many leveled structure of the section shown in Figure 8
1.10	2^{20} iterations of the Hénon mapping (Equations 1.19). The region shown is -1.5<x<1.5, -1.5<y<1.5 .

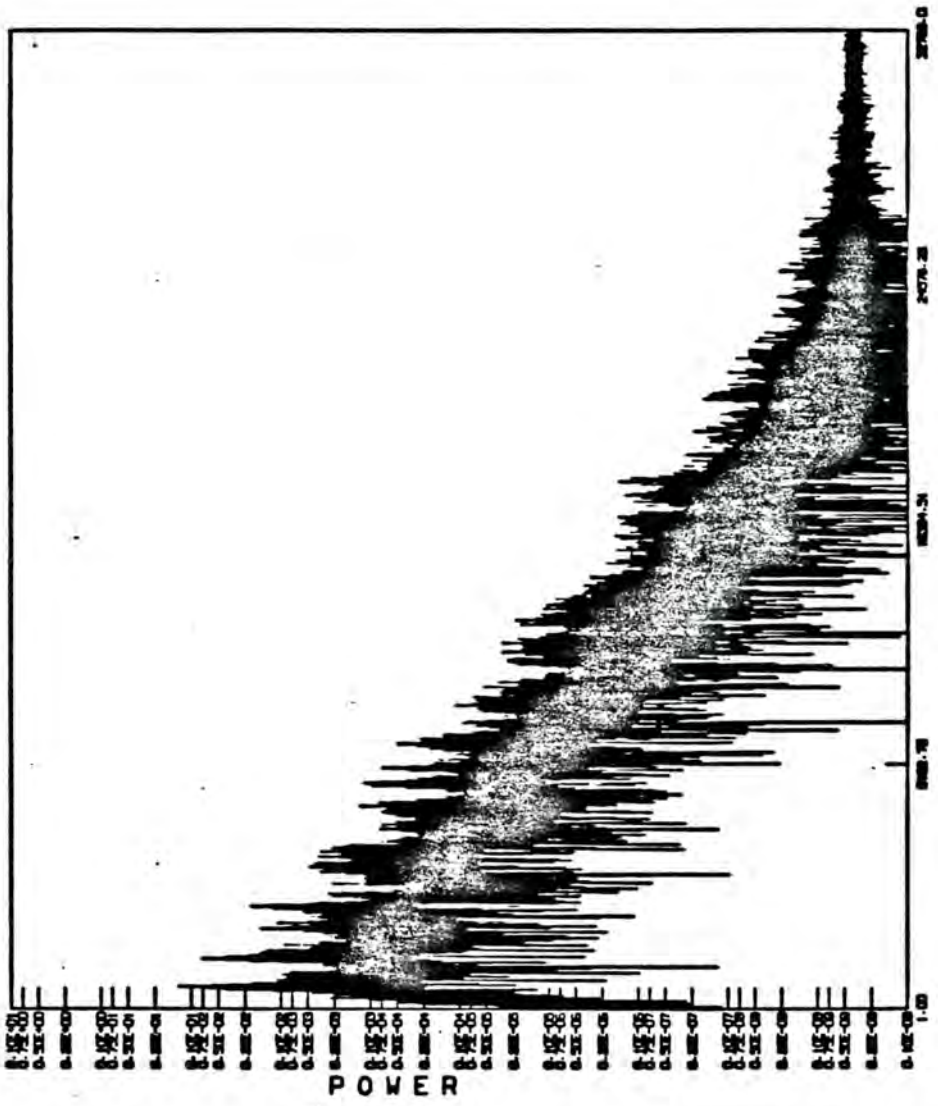

Figure 1

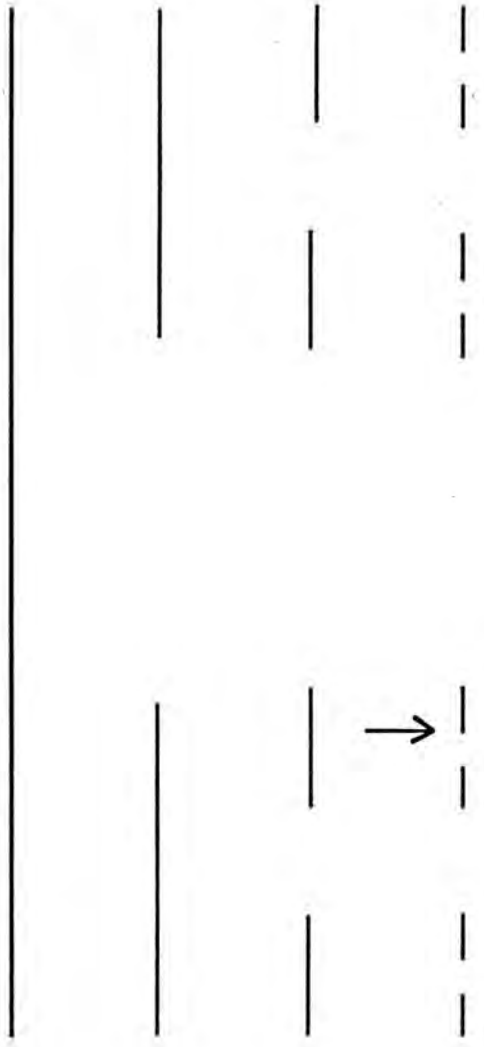

Figure 2

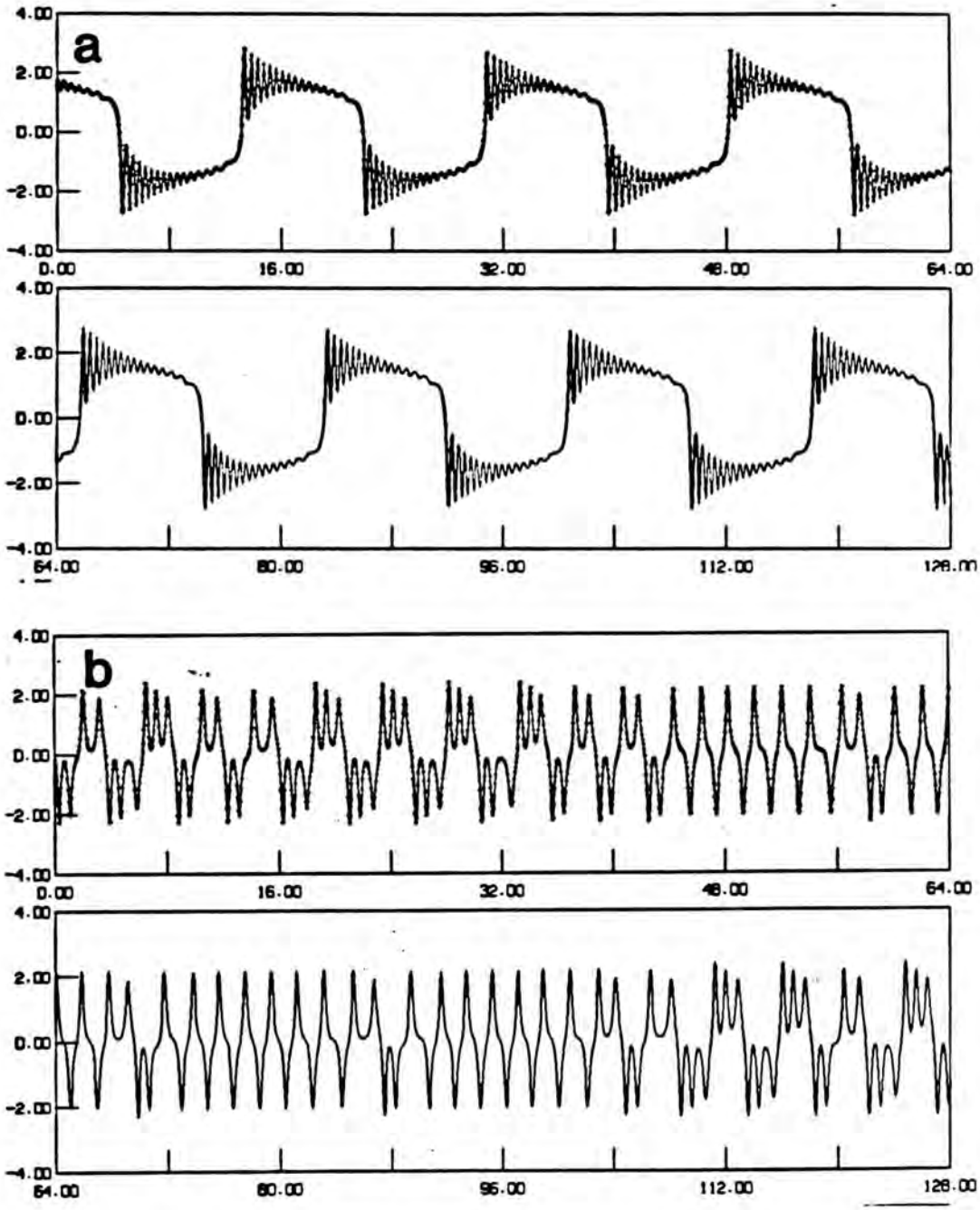
a
4.00
2.00
0.00
-2.00
-4.00
0.00
16.00
32.00
48.00
64.00
64.00
80.00
96.00
112.00
128.00
b
4.00
2.00
0.00
-2.00
-4.00
0.00
16.00
32.00
48.00
64.00
64.00
80.00
96.00
112.00
128.00

Figure 3

Figure 3

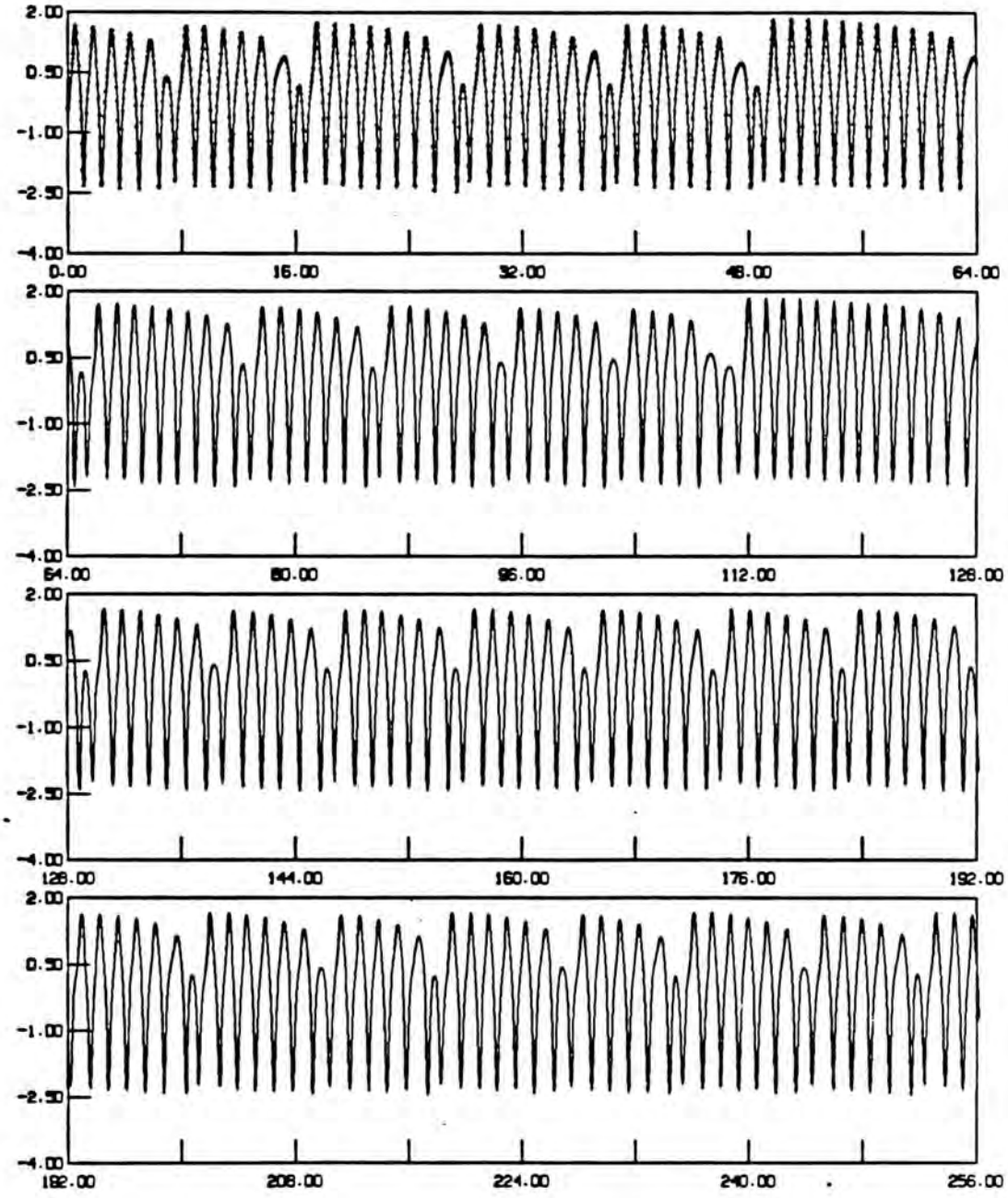
2.00
0.50
-1.00
-2.50
-4.00
0.00
16.00
32.00
48.00
64.00
64.00
80.00
96.00
112.00
128.00
128.00
144.00
160.00
176.00
192.00
192.00
208.00
224.00
240.00
256.00

C

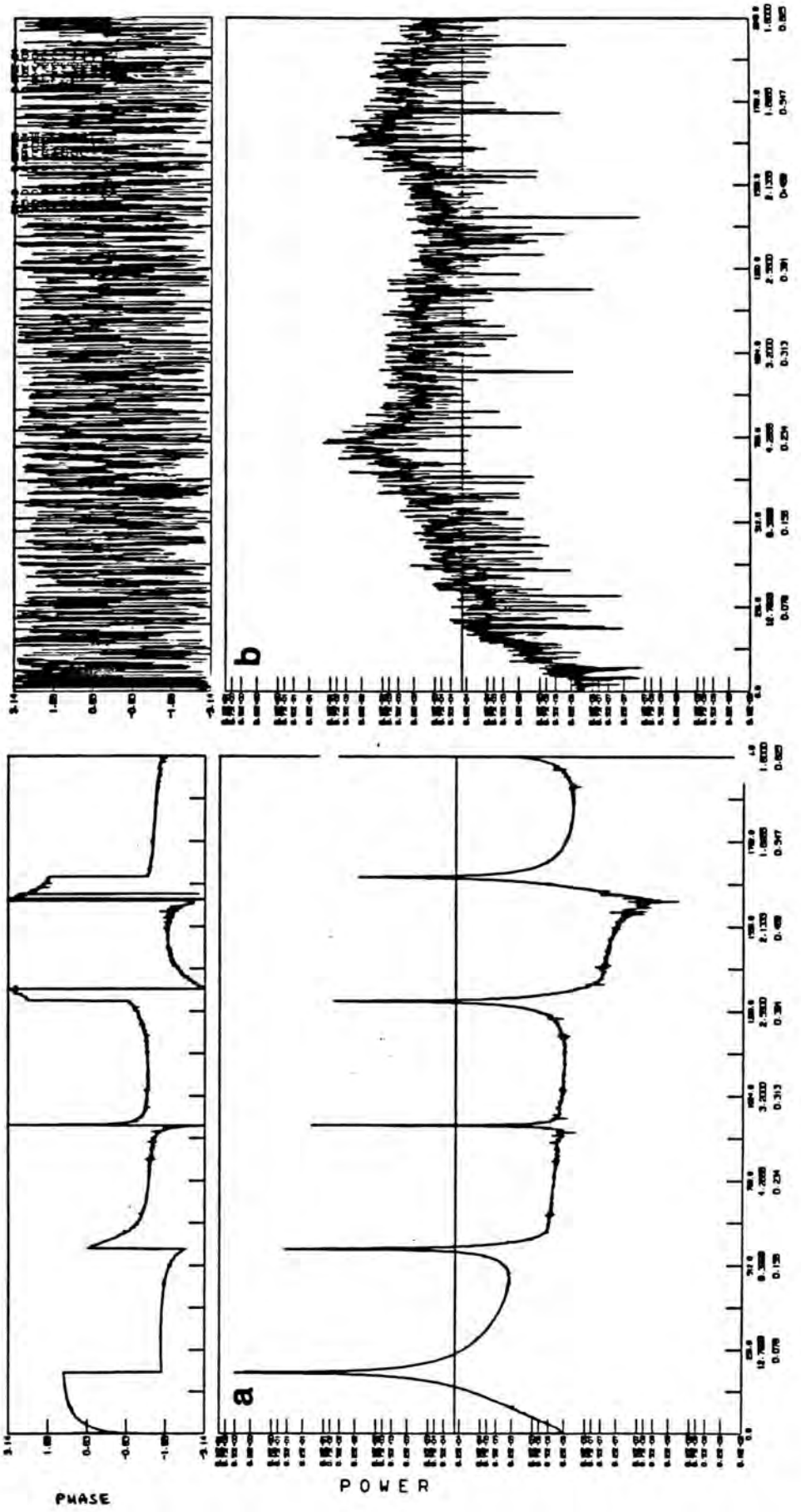

Figure 4

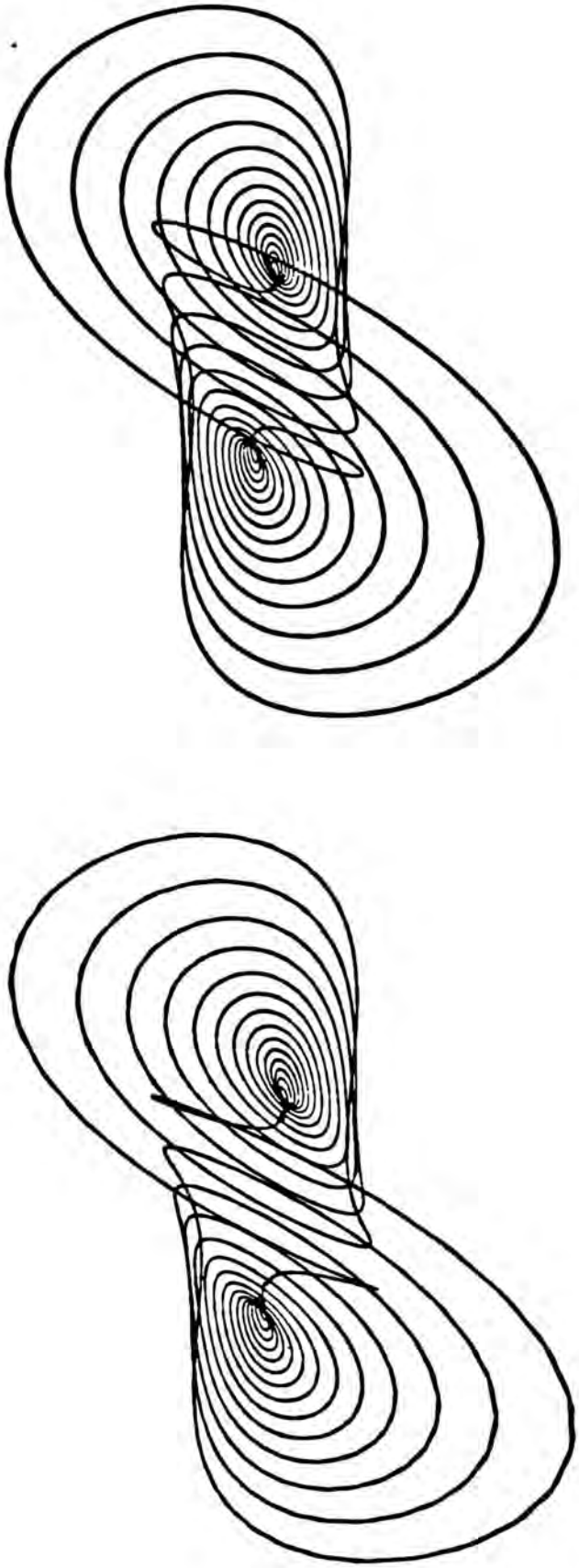

Figure 5

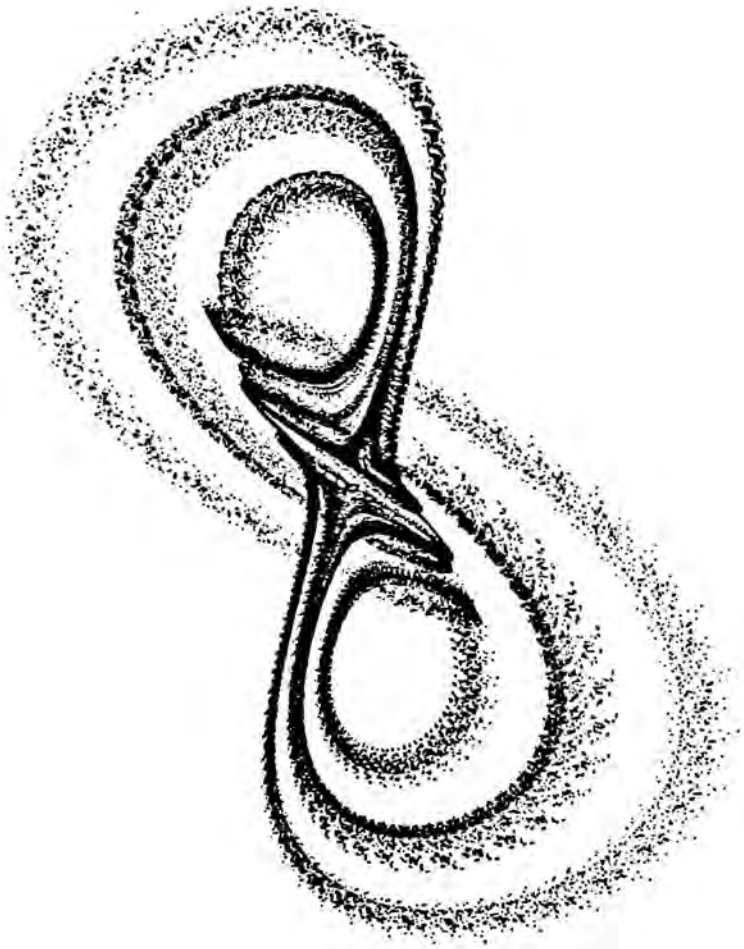

Figure 6

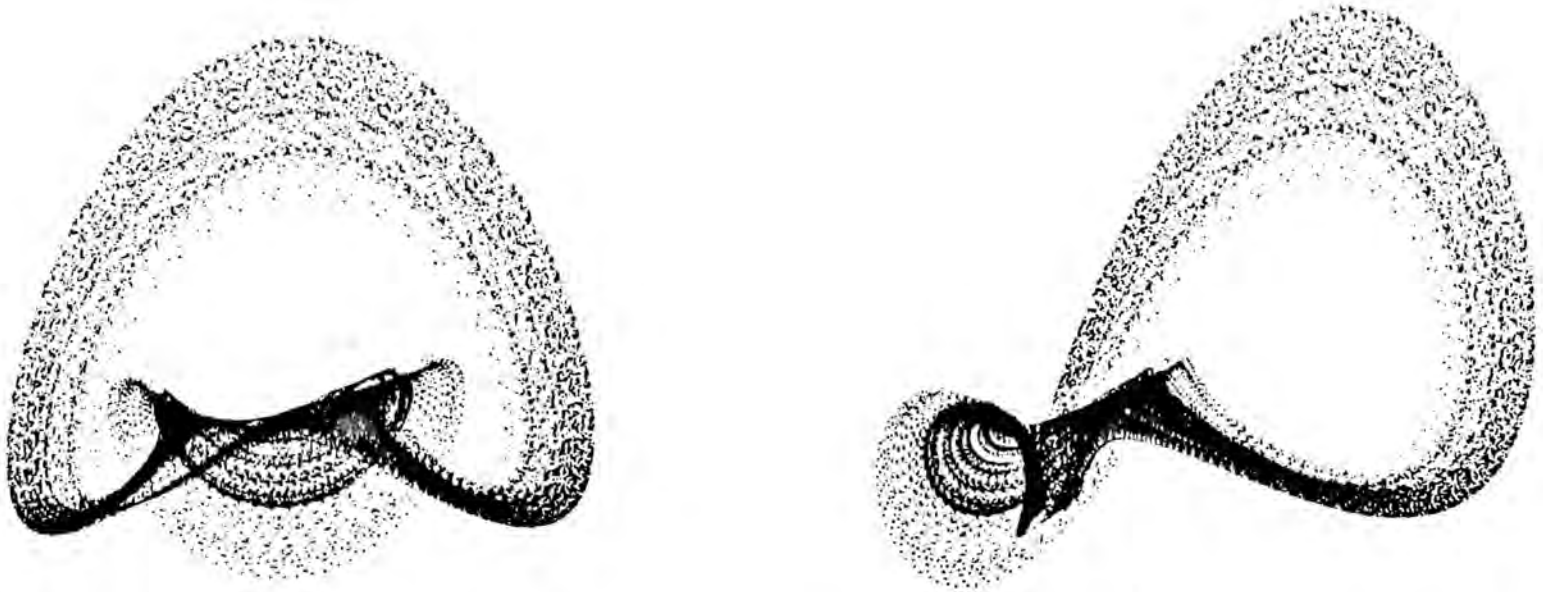

Figure 7

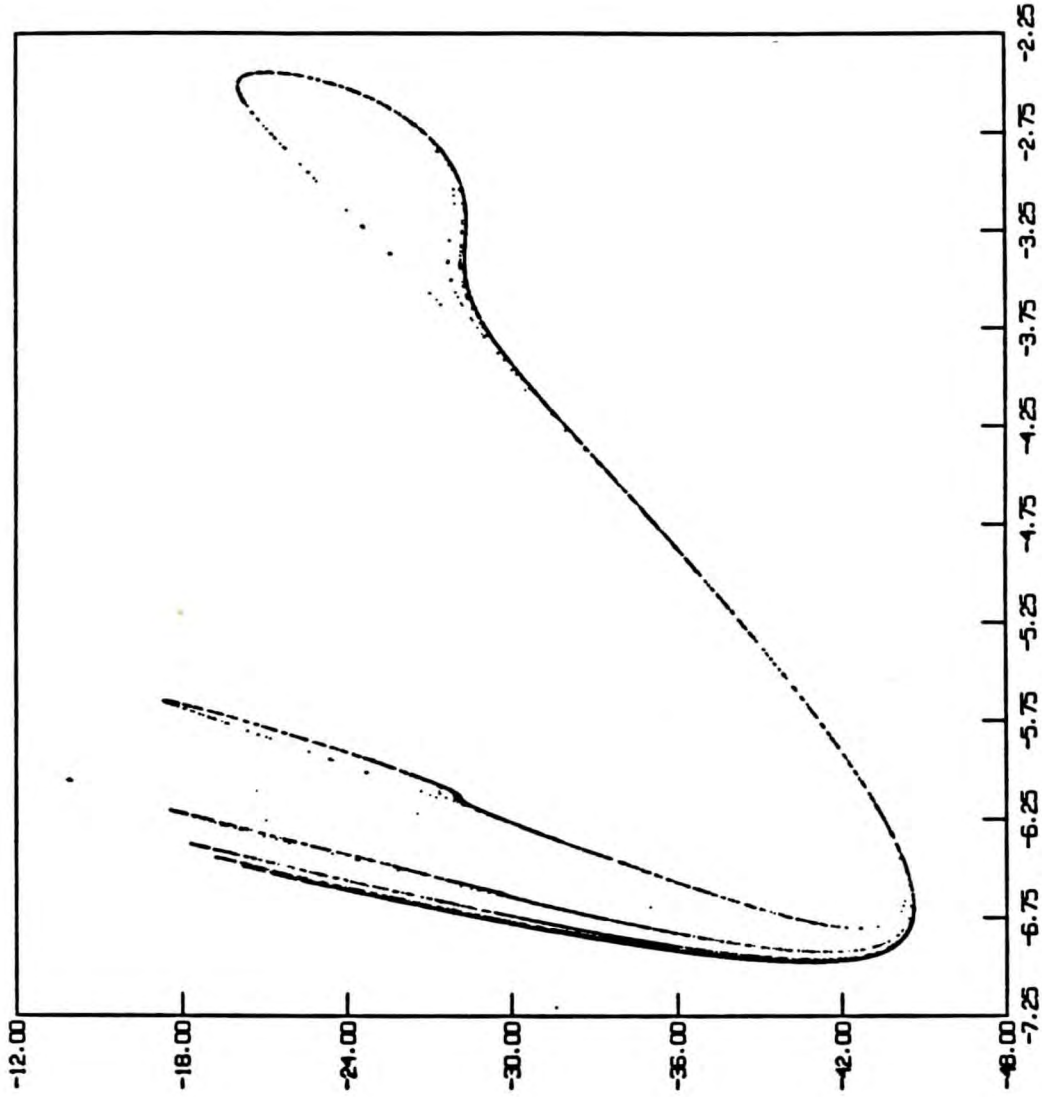
-12.00
-18.00
-24.00
-30.00
-36.00
-42.00
-48.00
-2.25
-2.75
-3.25
-3.75
-4.25
-4.75
-5.25
-5.75
-6.25
-6.75
-7.25

Figure 8

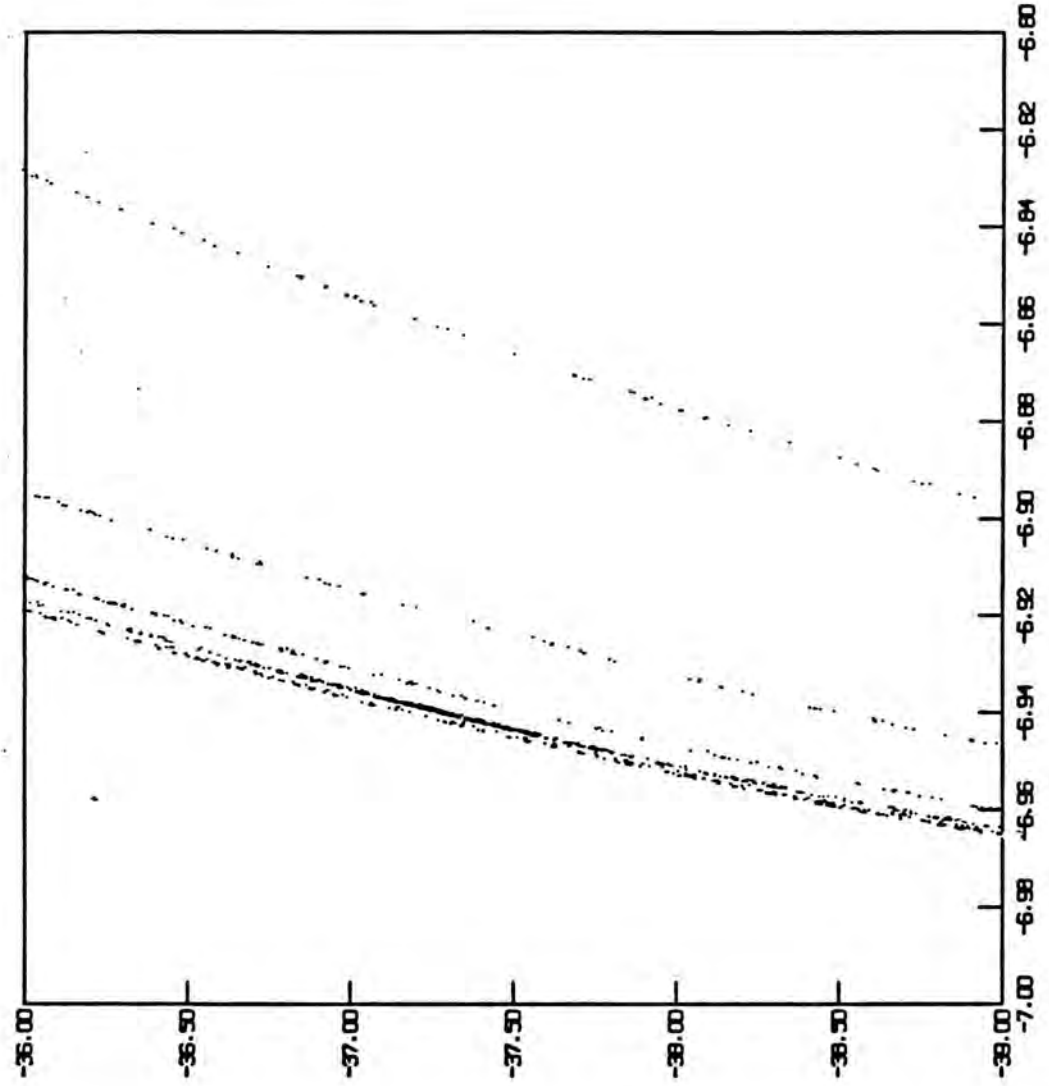
-35.00
-36.50
-37.00
-37.50
-38.00
-38.50
-39.00
-7.00
-6.98
-6.96
-6.94
-6.92
-6.90
-6.88
-6.86
-6.84
-6.82
-6.80

Figure 9

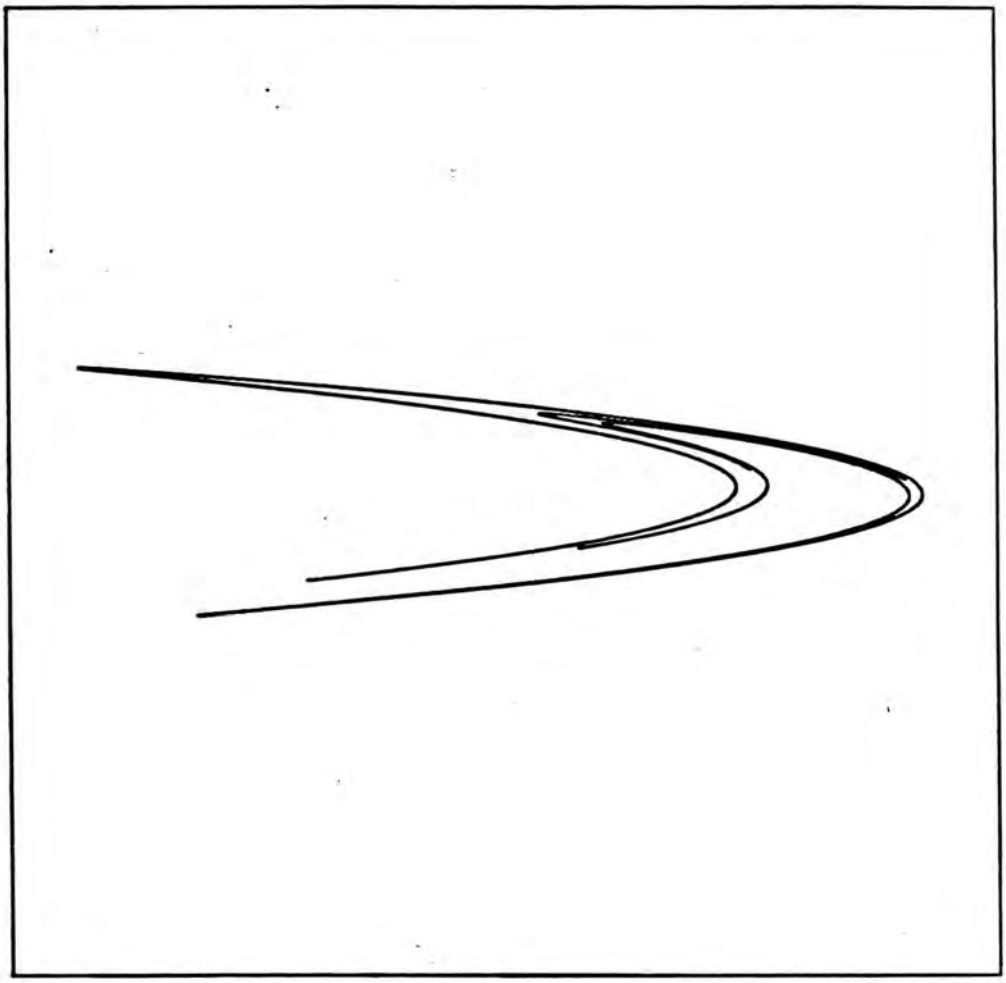

Figure 10

APPENDIX 1 Apparent Chaos in Digital Computers

In this appendix the effect of digitization on chaos is explored[1]. It is often remarked that recent advances in the study of nonlinear systems in general and chaotic dynamics in particular are due in large part to the use of modern digital computers. Paradoxically, these machines cannot display truly chaotic trajectories; real numbers are represented by a finite number of bits which implies that the dynamics occur on a finite grid. All bounded motion is eventually periodic. In this sense, the best one can hope for is pandemonium; truly chaotic trajectories are not realizable on a digital computer just as identical initial conditions are not available on an analog computer.

The numerical grid imposes an inner cutoff to both geometrical scaling and sensitivity to initial conditions; by determining the number of distinct states, the grid imposes an upper bound on the cycle time of any deterministic dynamical system. This cycle time may, of course, be very large: the Goddard General Circulation Model (see Hansen, 1983) has something like $(2^{32})^{2^{15}}$ potential states (though the vast majority of these are of no physical relevance). In studies of strange (fractal) attractors, where the quantities of interest are defined in the limit of small scales, the effects of digitization are more pronounced. As an example, consider a simulation of the Hénon map (Equations 1.19) carried out in 32-bit precision (REAL*4 with an IBM 360 architecture; for details, see

[1]This problem was suggested to me by Colin Sparrow.

Struble, 1975). A maximum of 2^{32} distinct values restricts the two-dimensional mapping to an orbit of at most 2^{64} iterations before the orbit repeats (or diverges). When the mapping is dissipative, the observed cycle time is significantly less than this.

There are several questions we can ask. How will this periodicity affect the representation of attractors? As the mesh becomes finer, will there by many periodic orbits or only a few? Perhaps even just one? If there are several, how do their structures compare? How are their basins of attraction divided? Does the relative probability of observing one attractor dominate? How machine-dependent are the answers to these questions? One approach to these questions is to examine the dynamics on grids that are sufficiently coarse that a complete catalog of behaviors can be computed, and then to observe how these behaviors change as the grid becomes finer. Consider a uniform grid with mesh ϵ where

$$\epsilon = \frac{1.0}{N}$$

and N is integer. To every real number X we associate an integer IX by

$$IX = [\, N \cdot X] = \left[\frac{X}{\epsilon} \right]$$

where [y] is equal to the greatest integer less than or equal to y. Here the origin is a grid point. On this grid, the Hénon map[2] becomes

---

[2] a discussion of the Hénon map is given in §3.3. For more details, see Hénon (1976).

$$IX' = [N + IY - ([(IA \cdot IX)/N_A] \cdot IX)/N]$$

$$IY' = [(IB \cdot IX)/N_B] \qquad \text{(A1.1)}$$

and the usual parameter choice (a=1.4, b=0.3) corresponds to

$$IA = 14 \qquad N_A = 10$$

$$IB = 3 \qquad N_B = 10 \quad .$$

Written in this way, the mapping may be iterated using only integer arithmetic.

Once N is specified, all periodic orbits may be identified, in principle, by tracing the path of every initial condition within a region which completely contains its image. While every orbit will eventually close upon itself, the many-to-one nature of the system will produce transient points to which a given trajectory will never return.

Consider the case N = 100. At this resolution it is practical to consider the entire self-mapping region and identify all the attracting orbits of the system. There are two: one of period 25, which attracts 99.56% of the initial conditions within the basin; the other a period 1 orbit corresponding to an unstable fixed point of the exact map (the orbits and their basins of attraction are shown in Figure A1.1). This result is not characteristic; for most values of N examined there exist about 6 orbits, two of which usually attract the majority of the initial conditions. An example of the manner in which the basins are interwoven is shown in Figure A1.2 using the

case N = 110. As N increases, the number of initial conditions in the bound region becomes too great for a complete search with our current resources. The difficulty is compounded by an increase in the length of transient with increasing N. The results given in Table A1.1 were computed by evaluating small regions of contiguous initial conditions. For the larger values of N, several such areas were evaluated. In general, different regions produces similar statistics for the high probability orbits, although some low-probability orbits were absent from some sample regions.

The use of the 32-bit integers in system [A1.1] places an upper limit on N near 10,000 (due to overflow in evaluating the quadratic term). It is interesting to note that, even at this value, the number of orbits is holding at around 6 or 7, with one or two of the orbits usually attracting 90% of the initial conditions. Throughout the range of grid spacings examined, the number of digitally periodic orbits remains small (say, of order 10), with the majority of points being drawn to one or two of these. The length of the most probable orbits generally increases with N; however, the longest orbit is often not the most probable. Finally, we note that the self-similar structures of Figure 3.8 are already apparent with N=10,000.

The Hénon attractor shown in Figure 1.10 was calculated using 64-bit real numbers. The structure of the periodic orbits of these evolutions is more complicated, partly due to the nonuniformity of the REAL grid; since real numbers are represented in exponent-mantissa form, the mesh varies over the plane, being finer near the coordinates on axes. To get an idea of the effect of this variable

grid and test the machine dependence of the results, a search for periodic orbits using REAL*4 variables was performed. As the number of initial conditions precluded a complete search, p-random initial conditions in the neighborhood of the unstable fixed point were determined. The results for several machines are shown in Table A2.

It is notable that still only a few orbits are found, with one of intermediate length dominating. Note also that the comparison across machines yields similar results.

One source of these orbits is clear -- unstable periodic orbits (stabilized by the grid) coincide with some of the observed low period, low probability orbits. Examining the basins of attraction of the remaining orbits suggests that the orbits fall into two categories: those orbits which move along a stable manifold until the grid pinches it off, and those which fall onto the image of the attractor. It is the digitally periodic orbits of the last class onto which the majority of initial conditions evolve.

To test this conjecture we examined a region that was relatively free of portions of the stable manifold of the interior fixed point. From the figure on page 764 of Franceschini and Russi (1981) [this figure is mislabeled as Figure 3], it seems that the region $x = -0.4 \pm 0.001$, $y = -0.8 \pm 0.001$ would be a good choice. For $N = 10{,}000$, all but 14 of the initial conditions were drawn to orbit A or orbit B (see Table A1.1). The initial conditions that did evolve to orbit D were all clustered near the edge of the test region. The results are shown in Figure A1.4. (In the REAL*4 calculations on the Amdahl, the probability of observing the Amdahl

orbit A increased by 10% when the initial conditions were drawn from the region given above.) These observations are consistent with the idea that the long, low probability orbits capture initial conditions on a stable manifold; the trajectories from these initial conditions, moving along the stable manifold, are eventually mapped into a gridbox that has been visited previously. The majority of initial conditions appear to evolve onto one or two orbits which resemble the Hénon attractor.

Given the required periodicity of digital orbits, why do such simulations appear chaotic? There are several reasons, not the least of which is the length of the cycle time. For two just-distinguishable initial conditions, both of which approach the same numerical attractor, the rate of separation is still, on the average, exponential; two such orbits may reach the attractor with uncorrelated phases after transients of very different lengths.

In summary, the digitally periodic orbits of the Hénon mapping have been determined for several numerical grids. The length and number of these orbits is surprisingly small considering the relatively high resolution of the grids. The use of this approach to characterize strange attractors at the smallest available scales may provide the ultimate box counting method for probing their structure.

FIGURE CAPTIONS

Figure	Caption
A1.1	The basins of attraction for the two digitally periodic orbits of the Hénon mapping with a = 1.4 and b = .30 when evolved on a grid with N = 100. The statistics of each orbit are tabulated in Table 1 . The basins shown correspond to (a) Orbit A and (b) Orbit B.
A1.2	Basins of attraction as described in Figure A1.1 for the case N = 110, (a) Orbit A (b) Orbit B.
A1.3	The digitally periodic orbits of the N = 10,000 grid. Statistics of the orbits are provided in Table 1 where (a) Orbit A, (b) Orbit B, (c) Orbit C, (d) Orbit D, (e) Orbit F. Orbit E, an unstable fixed point, is not shown.
A1.4	The basins corresponding to the orbits shown in Figure A1.3. In each case the initial conditions which evolve to an orbit in figure 3 are shown in the corresponding panel here. Initial conditions are from the region $-0.81 < x < -0.79$, $-0.81 < y < -.79$.
A1.5	The basins of (a) Orbit A, (b) Orbit B, and (c) Orbit D on the N = 10,000 grid. The region was chosen to avoid the stable manifold as described in the text. No initial conditions observed in this region evolved onto the other orbits.
Table A1.1	Statistics for the orbits observed on uniform numerical grids for a variety of grid resolutions.
Table A1.2	Statistics of the digitally periodic orbits observed on REAL*4 grids for a variety of computer architectures.

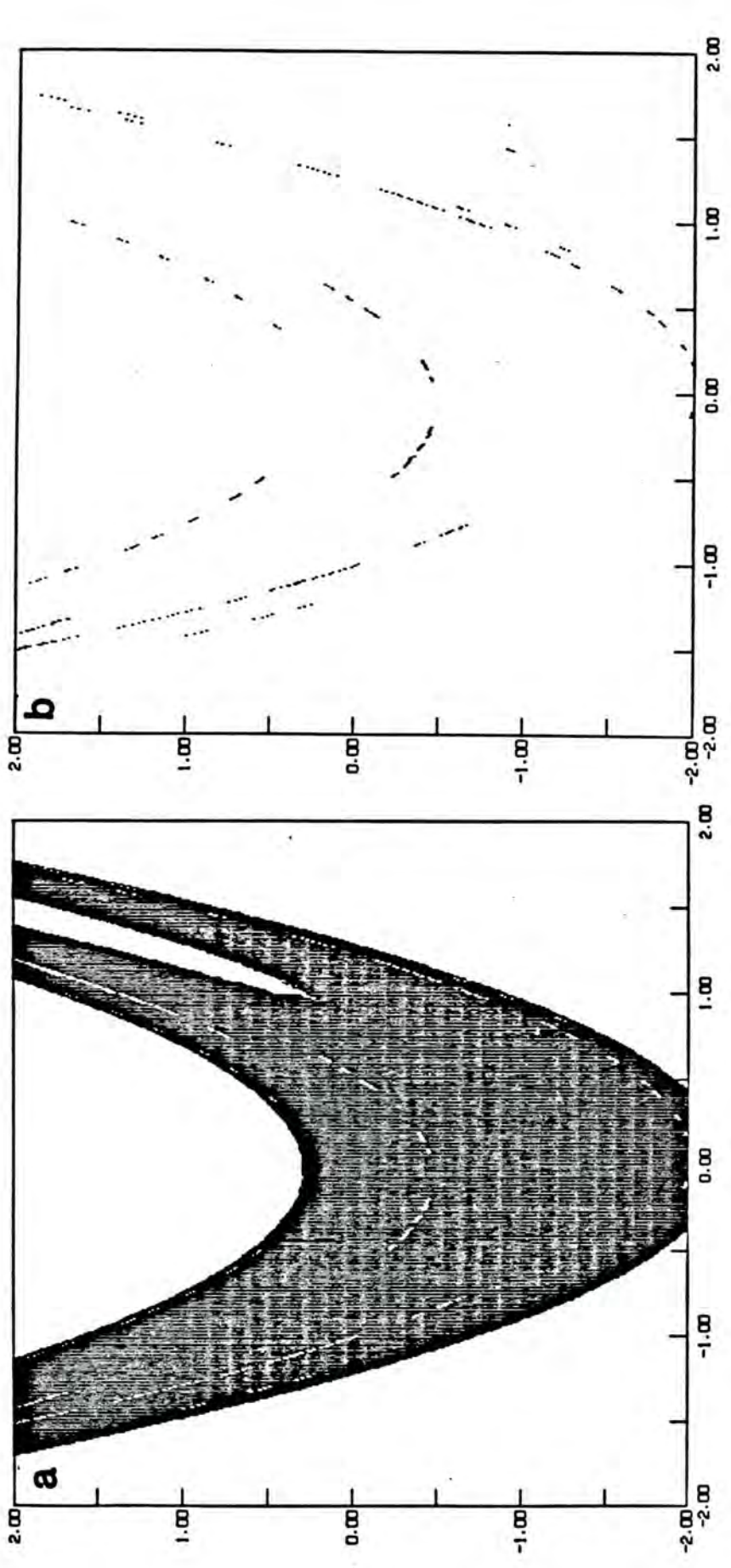

Figure 1

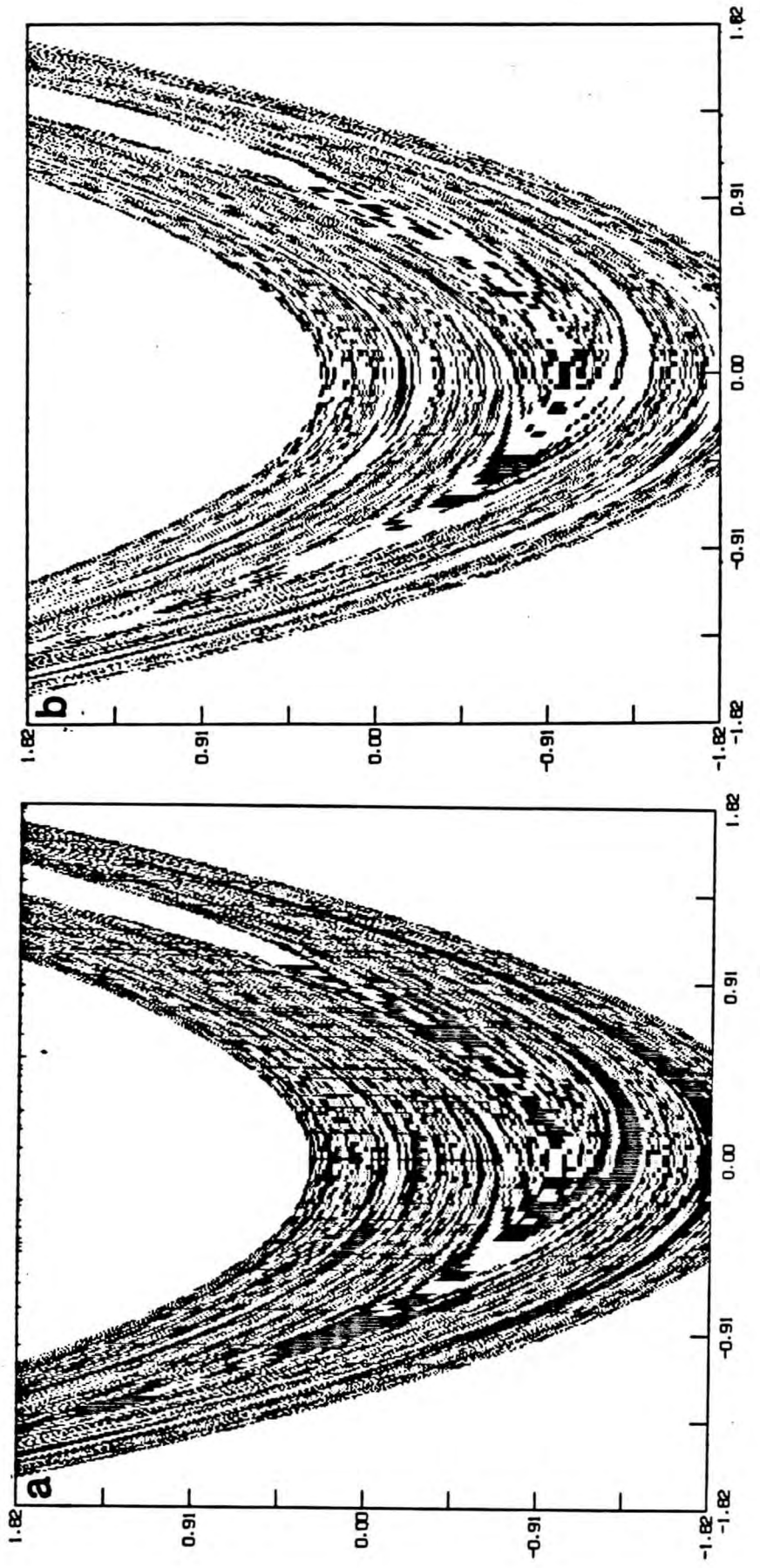

Figure 2

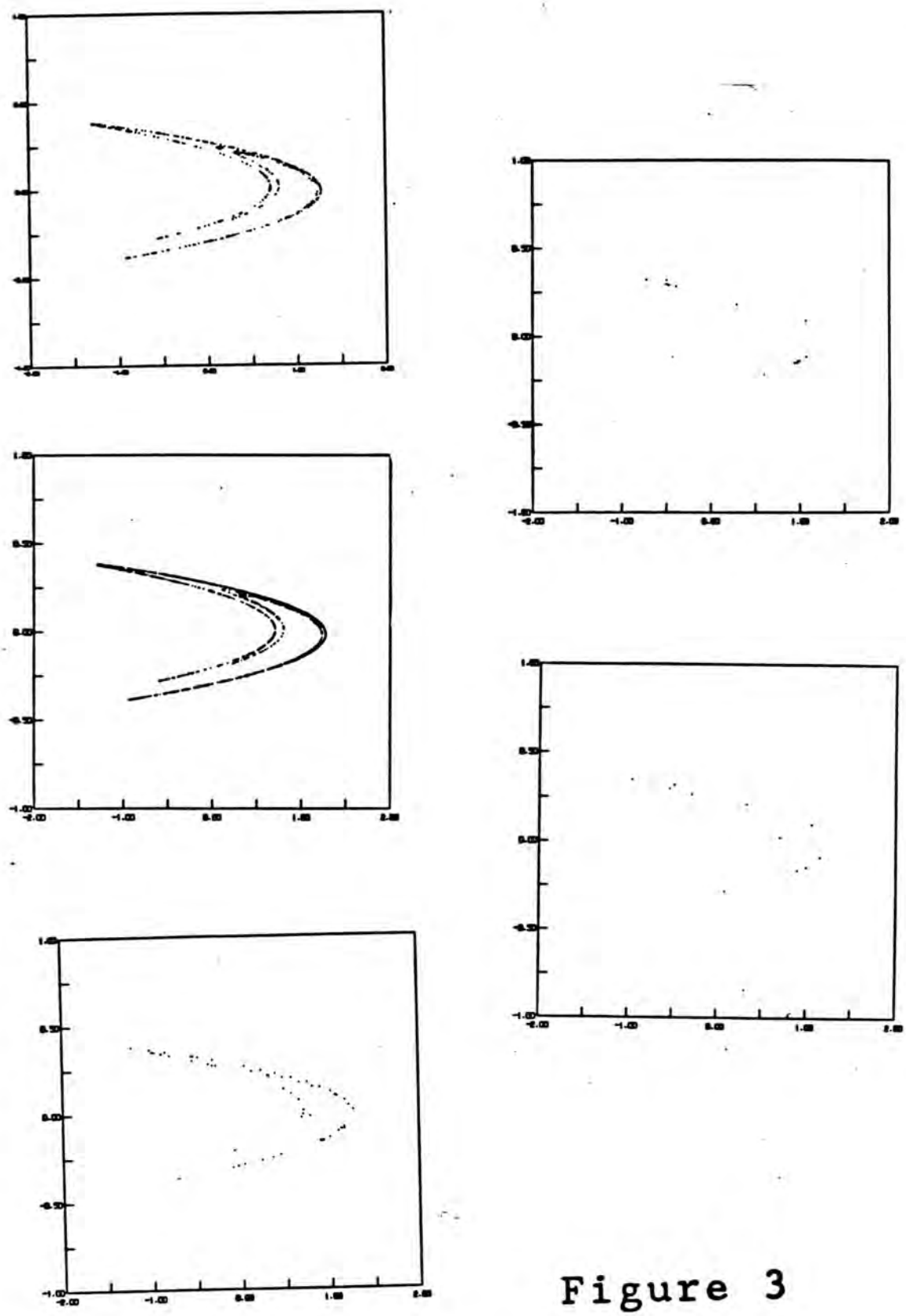

Figure 3

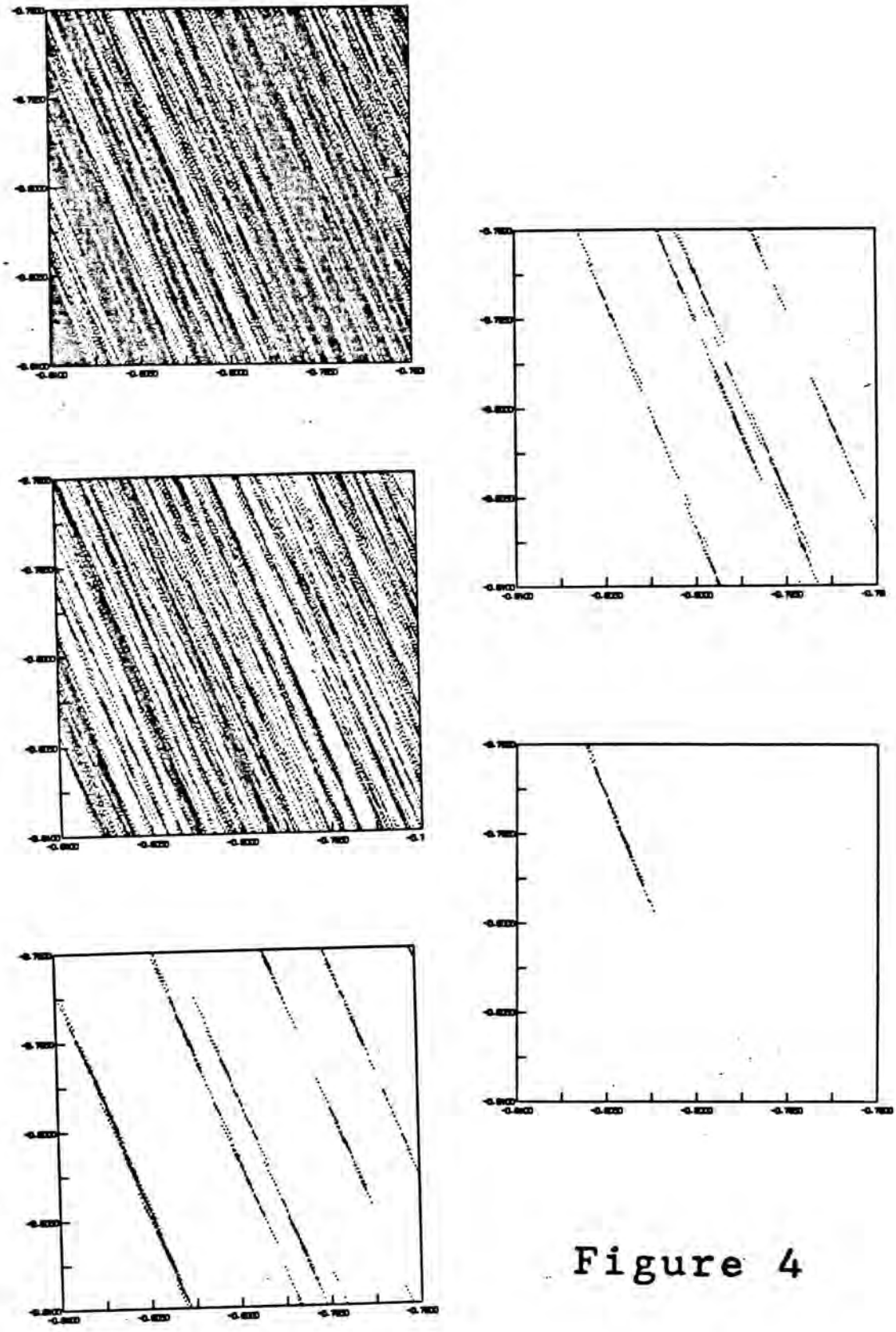

Figure 4

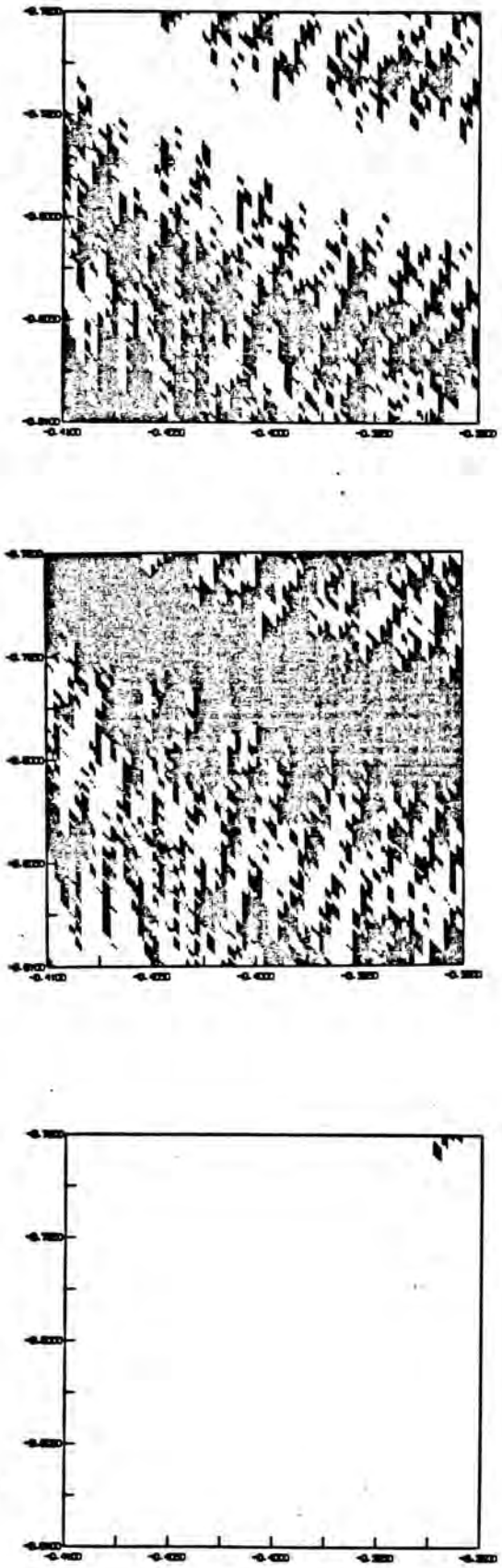

Figure 5

TABLE A1.1

$\aleph$	Number of Initial Conditions	Number of Orbits	Orbit	Length	Relative Probability
10	508	3	A	7	.95
			B	2	.04
			C	1	.01
50	1352	2	A	15	>.999
			B	1*	<.001
100	55863	2	A	25	.996
			B	1†	.004
101	52831	3	A	9	.998
			B	2	.002
			C	1†	<.001
110	59176	4	A	7	.663
			B	4	.320
			C	13	.016
			D	1†	<.001
1,000	19468	7	A	190	.483
			B	202	.412
			C	102	.092
			D	7	.006
			E	2	.004
			F	10	.003
			G	7	<.001
5,000	85096	7	A	253	.717
			B	341	.129
			C	320	.125
			D	21	.011
			E	13	.006
			F	61	.006
			G	9	.005
10,000	10185	6	A	504	.584
			B	1376	.397
			C	14	.013
			D	58	.005
			E	1†	.001
			F	20	<.001

* fixed point with $x < 0$
† fixed point with $x > 0$

TABLE A1.2

Machine	Representations	Number of Initial Conditions	Number of Orbits	Orbit	Length	Relative Probability
AMDAHL V6[a]	32 bit	20,000	7	A	4472	0.5490
				B	5690	0.2133
				C	224	0.1595
				D	1432	0.0401
				E	4735	0.0261
				F	816	0.0119
				G	25	0.0001
LSI 11/23[b]	32 bit	40,000	10	A	8557	0.4421
				B	1073	0.4005
				C	5827	0.1215
				D	3987	0.0343
				E	21	0.0008
				F	770	0.0004
				G	72	0.0001
				H	34	0.0003
				I	1	1 case†
				J	156	1 case†
IBM PC/XT[c]	32 bit††	1680	4	A	19229	0.8861
				B	2469	0.0761
				C	2239	0.0338
				D	488	0.0042

† an integer in this column indicates the number of initial conditions tested which evolved onto the orbit.

†† the 8087 chip computes 60-bit results with rounding, whereas the Amdahl truncates; this finer resolution may account for the lengthier orbit.

[a] See Struble (1975) for details.

[b] See DEC (1982) for details.

[c] See IBM (1984) for details.

Chapter II Analysis of Dimensionality

Introduction

Over the past 30 years, many methods have been developed to estimate the number of active degrees of freedom present in an empirical data set and, thereby, its topological dimension. Early algorithms were advanced by psychologists in order to quantify relationships between psychological observables (see Shepard 1962 a,b). These methods, similar to principal component analysis, suffer from the assumption that there is only linear structure in the data. Shepard and Carrol (1966) introduced a generalization assuming only local linearity (see also Fukunage and Olsen, 1971). From these beginnings various procedures were developed and applied to problems in signal processing and pattern recognition. Operationally, these methods may be separated into two groups. Members of the first class examine eigenvalues of some characteristic matrix such as the covariance matrix, constructed from the entire data set. An example of this type is singular systems analysis (see Bertero and Pike, 1982). Methods of the second class examine the scaling properties of a point set (vectors); an example of this type is the nearest neighbor method of Pettis *et al.* (1979), who also provide a comparison between the two methods. In general, those interested in dynamical systems theory have tended toward methods of the second type. Approaches include the direct application of box-counting ideas discussed in Chapter 1 (Mandelbrot, 1977; Russel *et al.* 1980), examination of the number of near neighbors as a function of distance

(Termonia and Alexandrowicz, 1983), and measurement of the correlation integral (Grassberger and Procaccia, 1983; see also §2.2). Multilinear regression techniques have been applied to determine the local structure of reconstructed attractors by Froehling *et al.* (1981). An additional approach for chaotic systems is to relate the dimension of the trajectory to the Lyaponov exponents of the flow via the Kaplan-Yorke conjecture (Kaplan and Yorke, 1979, see e.g. Lichtenberg and Lieberman, 1983, 394).

Recently, Broomhead and King (1986) proposed a procedure to determine the "qualitative information" contained in experimental data. Based on the theory of singular systems theory (see Pike, 1984), the Broomhead-King procedure estimates several parameters (the embedding dimension, noise level, eigenvectors) of a dynamical system from a time series. The Broomhead-King method is presented in §2.1 and applied to the Moore-Spiegel system. Anomalous results for the embedding dimension imply the method is not reliable in its present form. Through straightforward examples, these results are shown to be consistent with the conjecture that the estimate provided by the Broomhead-King method is related to the dimension of the space that the trajectory explores, not the dimension of the minimum embedding space.

Box-counting procedures that determine the fractal dimension of a data set are difficult to implement (Greenside *et al.*, 1982). An alternative to box-counting which provides a lower bound on the capacity (see §1.1) is the determination of the correlation exponent, ν. The favored method for this calculation is the Grassberger-

Procaccia algorithm (GPA, see Grassberger and Procaccia, 1983a,b). Our version of the GPA is introduced in §2.2 and used to demonstrate the lacunarity oscillation of Cantor sets in §2.3. We note that the presence of this oscillation may result in an incorrect interpretation of the correlation integral's properties.

The Grassberger-Procaccia algorithm has made it possible to calculate scaling exponents for many interesting systems. Implementation of the procedure is straightforward and there is strong enticement to treat it as a black box and process every available time series. In the final sections of this chapter, we demonstrate a lower bound on the amount of data required to unambiguously identify a correlation exponent of a given magnitude and we present supporting analytical arguments. It has been shown previously (Greenside *et al.*, 1982) that this amount increases exponentially with the dimension of the data set; here this growth is quantified and an additional, more restrictive bound is determined. In Figure 2.15 we present a disqualification table, which can assist in determining the significance of a particular result.

The phase space structure of an attractor is the true object of interest in many cases. The coordinates of the phase space trajectory of a numerical solution of a system of ODE's is known; experimentally neither these coordinates nor even the dimension of the phase space is known *a priori*. Packard *et al.* (1980) suggested that the phase space structure of an attractor could be determined from the time series of a single observable by calculating the derivatives of the measured variable and analyzing the trajectory in

this state space. A second approach, less sensitive to operational noise, was discussed by Takens (1981). In Takens' approach, the elements of the reconstruction vectors are consecutive values of the observable separated by a given delay time. Given a time series of measurements equally spaced by some sampling time τ_s

$$x(t_0),\ x(t_0+\tau_s),\ x(t_0+2\tau_s),\ x(t_0+3\tau_s),\ \ldots\ ,$$

the n-dimensional reconstruction consists of vectors

$$\mathbf{X}(t) = \{x(t),\ x(t+\tau_d),\ \ldots,\ x(t+n\tau_d)\}$$

where the delay time τ_d is an integral multiple of τ_s. Simply put, Taken's theorem states that a complete knowledge of the phase space variables is not required to reconstruct the attractor, that the reconstruction may be done in delay coordinates of a single observable, and that for ideal data, the result is not dependent on the delay time chosen.

For real data, the lack of complete precision places a lower bound on the delay time, measurements separated by less than this bound reflect only the operational noise in the analysis. In general, short delay times tend to project the data onto the diagonal which may then bias dimension calculating algorithms toward low values. When long delays are used, the decay of correlations may result in an overestimate of the scaling exponents. Determining the optimal delay for a given data set is a subject of current research; two methods to automate this choice involve either the first zero of the autocorrelation of the signal or the first minimum of its mutual

information (Fraser and Swinney, 1986). Signals of interest often have oscillating structure in their autocorrelation function and determination of the mutual information is a CPU intensive calculation. For low-dimensional reconstructions, when a signal is reconstructed in three-dimensional space (or four if a section is taken), it is useful to plot the data for several delay times and visually evaluate the constructions obtained.

Several delay reconstructions of the time series of z from the Moore-Spiegel system are shown in Figures 2.1 and 2.2. Each reconstruction is a collection of single points on the plane. The periodic nature of the T=10.0 trajectory is evident in Figure 2.1a. The trajectory is one-dimensional; it is self-intersecting in this two-dimensional reconstruction due to projection effects at this choice of delay time. The true phase space trajectory is a one-dimensional limit cycle in a three-dimensional space; a typical reconstruction in three-dimensional space would consist of a one-dimensional curve which did not self-intersect. Figure 2.1b is a similar reconstruction from a chaotic time series obtained with T = 36.0. Here, no simple structure is visible; as additional points are included, some sheetlike structures are implied as the figure generally blackens implying that the trajectory has a dimension of at least two. In Figure 2.2, several reconstructions of the T = 26.0 case are provided for different choices of delay time.

Once a delay time and an embedding dimension are chosen, the time series becomes a static object which may be treated by the methods of chapter 1, or the Grassberger-Procaccia algorithm. Before applying

these methods, we investigate a recent proposal to estimate the embedding dimension and optimal delay time.

SECTION 2.1 The Broomhead-King Procedure

In this section we review the Broomhead-King procedure and apply the method to the Moore-Spiegel system in several parameter regimes. These examples demonstrate that the method fails to accurately estimate the embedding dimension of the system. The similarity of the eigenvectors generated by a diverse set of examples is noted. These examples include both periodic and strange attractors, and the similarity of the eigenvectors indicates that they do not provide a customized set of coordinates for the reconstruction of attactors.

For band limited data, Broomhead and King examine the structure of the trajectory over time scales less than some window, τ_w, given by

$$\tau_w = \tau^* = 2\pi/\omega^* \tag{2.1}$$

where ω^* is the highest frequency which contains "significant power" in the Fourier spectrum of the time series. In many cases this definition of ω^* is sufficiently ambiguous to hamper the application of the method.

For a given τ_w, the structure of the trajectory within this window is reflected by the eigenvalue spectrum of the n x n covariance matrix of the trajectory, $\Xi(n)$, given by

$$\Xi(n) = \frac{1}{N} \begin{bmatrix} \sum_{i=1}^{N} x_i\, x_i & \sum_{i=1}^{N} x_i\, x_{i+1} & \cdots & \sum_{i=1}^{N} x_i\, x_{i+n-1} \\ \sum_{i=1}^{N} x_{i+1}\, x_i & \sum_{i=1}^{N} x_{i+1}\, x_{i+1} & \cdots & \sum_{i=1}^{N} x_{i+1}\, x_{i+n-1} \\ \vdots & & & \\ \sum_{i=1}^{N} x_{i+n-1}\, x_i & \sum_{i=1}^{N} x_{i+n-1}\, x_{i+1} & \cdots & \sum_{i=1}^{N} x_{i+n-1}\, x_{i+n-1} \end{bmatrix} \tag{2.2}$$

where

$$x_i = x(t_0 + (i-1)\,\tau_s)$$

and

$$\tau_s = \frac{1}{n}\,\tau_w \tag{2.3}$$

The idea here is that the structure of the trajectory at a given scale τ_w is examined in greater detail with increasing n. Once n exceeds the embedding dimension of the trajectory, the eigenvectors of Ξ divide into two sets: those which describe the trajectory and are characterized by "large" eigenvalues, and those which result from uncertainty (either in the observations or the analysis) whose eigenvalues correspond to numerical zero's. If this were the case, the algorithm would provide three useful parameters: an upper bound on the dimension of the system, the noise level, and an optimized set of coordinates (the eigenvectors of Ξ) with which to reconstruct the

attractor. Note that since τ_s varies with n, a different series is used for each value of n. Broomhead and King consider n = 3,4,5,7,9,13,and 25. Construction of the covariance matrix is simplified somewhat by the choice $n = 2^j$ with j = 1,2,3, and so on. With these choices for n, each x series may be chosen from the same data set and the full resolution of the time series is used.

The spectrum of Moore-Spiegel Case III, T=36.0, is relatively flat for $\omega > 0.128$. Adopting this value as ω^* provides our first example. The normalized eigenvalue spectrum of a 40,000 point time series (τ_s = 0.002) is shown in Figure 2.3. The n eigenvalues, σ_i, are first placed in descending order and then plotted against $\frac{i}{n}$ for n = 4,8,16,32 and 64. The eigenvalues for each n are joined by a solid curve to ease identification. In Figure 2.3a, the first four eigenvalues appear to be above the "noise floor." Although the phase space of the Moore-Spiegel system is three-dimensional, this seems a reasonable estimate of the embedding dimension. Figure 2.3b shows the eigenvectors corresponding to the first 12 eigenvalues from a Broomhead-King analysis. When the analysis is repeated using only 30,000 points, the eigenvalue spectrum and first 6 eigenvalues change only slightly. As τ_w is decreased, fewer of the eigenvalues retain significant power; this is to be expected since for τ_w sufficiently small, the change in x will be small when compared to any noise in the system or the analysis; the power will be concentrated in a single eigenvalue corresponding to a constant x eigenvector. It is important to make the "correct" choice of ω^*. As noted by Broomhead and King for the Lorenz case, the eigenvectors resemble orthogonal

polynomials. We have observed eigenvectors with this same structure and ordering for many of the systems we have analyzed. This distinctive structure may assist in identifying the significant eigenvalues; qualitatively, the numerically zero eigenvalues correspond to less ordered looking eigenvectors.

Similar results for the T=10.0 series are shown in Figure 2.4. Here however, the trajectory lies on a one-dimensional limit cycle, the periodicity of which is evident from an examination of the Fourier series or the time series itself. The procedure fails to distinguish between this periodic orbit and the chaotic one. The T=10.0 time series is not band limited; its periodicity is evident at all scales in the Fourier spectrum. The analysis used a time window determined from the highest frequency containing power in excess of the equivalent white noise spectrum.

To simplify matters, consider the system

$$x(t) = A \sin(\omega_1 t) + B \sin(\omega_2 t) + C \sin(\omega_3 t) + \epsilon \, Pr(t)$$

where the function Pr(t) represents a p-random "noise" term. Pr(t) is evenly distributed between zero and one, the constant ϵ is used to adjust the strength of the noise. Consider the choice

$$A = 1.0 \qquad B = 2.0 \qquad C = 1.5$$

with

$$\omega_1 = \frac{4}{3}\,\omega_2 = \frac{10}{18}\,\omega_3$$

For $\epsilon = 0$, and τ_w less than 2π divided by the highest frequency above the white noise limit, six large eigenvalues are observed. For nonzero ϵ the signal becomes bandlimited. With $\epsilon = 10^{-2}$ and $\tau_s = 0.04$, the whitened spectrum at high frequencies indicates $\tau^* \approx 0.128$. The singular spectrum and eigenvectors of this case are given in Figure 2.5. We conclude that, as formulated, the method does not provide a reasonable estimate of the embedding dimension; while the rank of Ξ does provide an upper bound on M, it may vastly overestimate M.

Another algorithm advanced to study the intrinsic dimensionality of a data set examines how the number of nearest neighbors scales as a function of separation (Pettis *et al.*, 1979). This method has been applied to dynamical systems by Termonia (1983, see also Gluckenhammer, 1984). We shall not discuss this method other that to note that it is sensitive to noise in the distribution. For low-dimensional objects, an estimate of the noise level is available from a calculation of the correlation integral (Grassberger and Procaccia, 1983 b, also §2.2). As is shown in §2.4, this estimate is no longer available for high dimensional embeddings. Analysis of the covariance matrix, however, may be of use in estimating the noise level and hence the meaningful separation scales to be considered in a nearest neighbor computation.

SECTION 2.2 The Grassberger-Procaccia Algorithm

Box counting algorithms suffer from a host of maladies. One of the most serious is the prohibitively large quantities of computer memory required to partition embedding dimensions greater than three (Greenside *et al.*, 1982). While virtual computer storage has increased the range of these methods (Giorgilli, 1986), following chaotic trajectories on a grid stored in virtual memory has been implicated as a cause of thrashing[1] (N. Habra, personal communication). Secondly, since d_0 depends only on the geometry of the set, determining the fractal dimension requires a knowledge of the low probability features of the set requiring 'long' runs. At some level, the structure of low probability features is of less importance to the physics of the problem than the general structure of the probability distribution. While the information dimension is sensitive to the probability distribution, it also suffers the problems of box-counting; indeed the same difficulty is encountered in the calculation of $f(\alpha)$ as presented by Hasley *et al.* (1986). (An alternative method has recently been advanced by Pawelzik and Schuster, 1987).

To circumvent these difficulties, Grassberger and Procaccia (1983a) introduced the correlation integral

---

[1] Thrashing is said to occur in computers with virtual storage when the resources expended on overhead far exceed those used for calculations, caused, in this case, by a great deal of disk access.

$$C_2(\ell) \equiv \frac{1}{N^2} \sum_{i=1}^{N} \sum_{j=1}^{N} \Theta(\ell - |x_{ij}|) \tag{2.5}$$

where N is the number of points in the set, $\mathbf{x}_{ij}$ is the vector separating the i^{th} and j^{th} points, and Θ is the Heavyside function. For fractal sets Grassberger and Procaccia (1983a,b) show

$$C_2(\ell) \sim \ell^{\nu} \tag{2.6}$$

where ν is called the correlation exponent. As it turns out, ν is equal to the generalized dimension d_2 (Hentschel and Procaccia, 1983, see also §1.3), and therefore provides a lower bound for the fractal dimension. Since the correlation exponent is sensitive to the probability distribution on the object; high probability regions are more heavily weighted than those of low probability and a good estimate of ν may be obtained without knowledge of the fine structure of the latter.

The direct evaluation of equation (1.8) for a many point approximation of the set in question provides an accurate method for determining ν. This is demonstrated in Figure 2.6 for the middle thirds Cantor set. An alternative method restricting the sum over j to a smaller number of "randomly" chosen base points, increases the accessible N for given computer resources thereby extending the range of length scales over which $C_2(\ell)$ may be calculated, but losing its fine structure.

A brief comment on the optimal implementation of the above methods is in order. As noted in Appendix A of Grassberger and Procaccia

(1983), execution time is significantly reduced when the logarithm is approximated by reading the exponent directly from memory. Computers generally represent real numbers in a hexadecimal format with exponent and mantissa juxtaposed within one or more words (for details of IBM machine architecture see Struble, 1975). The trick is to approximate the base-16 logarithm by the exponent alone, ignoring the contribution of the mantissa. While this does save time, its cost in resolution is great. We introduce an alternative method, binning the separation data in a (very large) integer array. The latter method yields very high resolution at the largest scales, revealing details of the fine structure of the oscillatory component (see §1.2) to be discussed in the following section. We have also investigated a method which reads the exponent and the first few bits of the mantissa and then estimates the logarithm using a look-up table for the contribution of the mantissa. The execution time required here was approximately a factor of three less than that required to evaluate the logarithm. The fastest method we have found is to use integer binning in conjunction with the Euclidian sup norm (the maximum component of the separation vector). The optimization problem is important in that the algorithm is presently limited by the amount of data that can usefully be considered.

Procedures that evaluate ν via Equations 2.5 and 2.6 are generically referred to as the Grassberger Procaccia Algorithm (GPA). The principle difficulty of the GPA is that it is an N^2 algorithm; the number of calculations required to determine $C_2(\ell)$ increases as the square of the number of data points. Coupled with the

exponential increase in the amount of data required to describe a surface for increasing dimension, reliable estimates of dimension via GPA are restricted to sets of small ν ($\nu \lessapprox 5$). This limitation is quantified in §2.5. In Chapter 3 we suggest an algorithm whose computational time consumption scales as the number of points in the set and apply it to several examples.

Scaling representative of an attractor may also be biased in the reconstruction if the orbit is sampled too frequently; doing so results in a large contribution to $C_2(\ell)$ from dynamically correlated points (exaggerating the one-dimensional nature of small segments of the trajectory). The effect has been investigated by Theiler (1986).

Several things are done in the next 3 sections: we illustrate the GPA on Cantor sets where the embedding dimension is known *a priori*. The oscillatory component of scaling in these sets arises in a natural way. Next, additional effects which arise when analyzing real data are discussed for a simple model and the Moore-Spiegel system. Finally, arguments are presented which quantify the amount of data required to use the method.

SECTION 2.3: Evaluating Correlation Exponents of Simple Fractal Sets

In this section the GPA is applied to fractal distributions where the embedding dimension is known. This is the case for a physical distribution (a coastline or the large scale distribution of visible matter in the Universe) or the solution to a system of ODE's. Our first examples will be strictly self-similar Cantor sets such as the

middle thirds set discussed in Chapter 1. Cantor sets are the simplest self-similar sets with *noninteger* dimension. A strictly self-similar Cantor set may be approximated to arbitrarily high resolution in the following manner:

1) divide the unit interval in R^1 into s equal subintervals
2) delete all but r of the subintervals
3) record the endpoints of each subinterval as the members of this approximation to the set (without double counting)
4) iterate this procedure on each of the remaining subintervals until the desired accuracy is achieved.

After N iterations of this procedure, the approximation consists of $2r^N$ points[2]. A set constructed in this way may be designated by an s-digit binary number with r ones and s-r zeros, the zeros being located at the positions where segments were deleted. The middle thirds set is then designated as 101.

In these cases a great deal of information is available from the outset. The set may be embedded in 1 dimension; for the Nth order approximation, the ratio of the outer cutoff to the inner cutoff is r^N and any operational uncertainty may be kept below this threshold. The specific cases described here are the sets 101, 101010001 and 101001001, which will be called sets I, II, and III respectively. All three sets are homogeneous fractals of dimension

$$d_q = d_{HB} = d_2 = \frac{\log 2}{\log 3}$$

---

[2]The total number of points will be less than $2r^N$ if any two segments are contiguous; we have also assumed that the first and final segments are retained.

for all q.

A graph of log $C_2(\ell)$ versus log ℓ for set I is shown in Figure 2.7. The oscillatory component of $C_2(\ell)$ for each of the three sets is evident. To examine it more closely we approximate $\psi(\ell)$ as

$$\psi(\ell) \approx \nu \log_2 \ell - \log_2 C_2(\ell). \qquad (2.7)$$

The results for each of the three sets are shown in Figures 2.8 and 2.9. Computed estimates of the correlation exponent and period of $\psi(\ell)$ for each set are provided in the figure. They are determined by a least square fit to a range of data that is a multiple of log σ. The oscillations reflect the manner in which the structure of the set changes over a range of log σ. For set I, r=3 and the change is regular. Sets II and III are indistinguishable from set I by their d_q, but are easily distinguished from set I and each other by the structure of $\psi(\ell)$; note especially that the asymmetry of set II is reflected in Figure 2.9 b.

The origin of the oscillation in strictly self-similar sets may be easily understood. Using set I as an example, for every structure (e.g. point pair of separation) observed at scale ℓ, exactly two such structures will be observed at scale $\ell/3$, hence the details of the scaling structure which form the oscillations are strictly periodic. Appendix 2 demonstrates that these oscillations are strictly log-periodic and provides a handy construction mechanism for the study of the residual. The oscillation itself has structure on all scales and appears self-similar. More correctly, it is self-affine in that there is an arbitrary (unit dependent) factor that relates $\psi(\ell)$ to ℓ.

The fine structure of $\chi(\ell)$ depends on the statistical quantity

measured. In these cases, where it is determined from $C_2(\ell)$ for sets embedded in one dimension, χ reveals the lacunarity of the underlying set; a large range of χ with slope $-d_2$ indicates the absence of pairs of points which are separated by a distance in this range, or equivalently, the presence of lacuna of scale ℓ in the underlying set. For inhomogeneous fractals, the lacunarity interpretation of the $C_2(\ell)$ oscillation is less useful at large scales. An alternative is discussed in Chapter 5.

Guckenheimer (1984) noted the departure from linear scaling caused by the oscillations and questioned whether this "logarithmic correction" might limit the accuracy with which dimensions may be calculated. In Chapter 3, we take advantage of the regularity of the oscillation to increase the accuracy of such calculations.

Consider the Poincaré sections of the T=36.0 Moore-Spiegel system (Figures 1.8); each section contains approximately 10^4 points. The correlation integral of these data are shown in Figure 2.10 with $\psi(\ell)$ below. While there is an indication of an oscillation, the data are insufficient to identify it unambiguously. In these cases, as in the dissipative Hénon map (Equation 1.19) the oscillations are damped at large scales due to the interplay of many regions. The important point here is that deviation from linear scaling is expected; the residual of a linear least squares fit of $\log C_2(\ell)$ to $\log \ell$ is a poor measure of the quality of the scaling.

The best fit values in this case are

$$\nu_x \approx 1.08 \qquad (10^{-1.5} < \ell < 1)$$
$$\nu_v \approx 1.10 \qquad (10^{-2.5} < \ell < 1)$$

where the subscript denotes the section taken: x = position and v = velocity . Since these sections come from the same attractor, their correlation exponents should be equal.

We have looked for the $\psi(\ell)$ function for several scaling distributions found in nature, generally without success. These are described in Chapter 4. An exception is found in the statistics of fluid turbulence. Here the oscillatory component of the scaling can be established in the cascade models (Novikov, 1964; Smith *et al.* 1986); it has been suggested (Smith *et al.*, 1986) that this oscillation is compatible with recent observations of the velocity structure functions of turbulence (Anselmet *et al.*, 1983). Similarly, velocity reconstructions of some turbulence data show the oscillations (Van de Water, 1987). The remainder of this chapter focuses on the difficulties of applying the GPA to more realistic data sets.

Section 2.4: Scaling limits in a Nonlacunar Set

In this section we address the question: given an ideal data set of unknown geometry, what is the minimum amount of data required to determine the correlation exponent of the set to within a desired degree of accuracy using the Grassberger Procaccia algorithm. The discussion centers upon the GPA determination of ν in sets for which no oscillation is visible. As mentioned above, this currently includes most attractors reconstructed from experimental time series. The "size" of a data set will be a central issue throughout this

section and is defined by the length of the time series and the optimal delay time, not the sampling rate. Thus the size will reflect the amount of information contained in the set.

Truly nonlacunar attractors do exist; a simple example is an attracting two torus. If the torus is covered densely and uniformly the $\psi(\ell)$ function of the correlation integral will tend to zero everywhere. It is this special case which is sometimes referred to as pure scaling; we will call this behavior linear scaling. In such a case, the prefactor A is a constant; and for $\ell \ll \ell_o$

$$\begin{aligned} \nu_s(\ell) &\equiv \frac{d \log C_2(\ell)}{d \log \ell} \\ &= d(\nu \log \ell + \log A)/d \log \ell \\ &= \nu \end{aligned} \tag{2.8}$$

where the subscript s emphasizes that we are not dealing with the limiting behavior. When working with digitized data, the derivative must be evaluated carefully.

Consider the general case of a time series embedded in an N-dimensional space. The dimension of the record is approximated by calculating the correlation exponent of the embedding. If the orbit of this system in its (unknown) phase space lies on an M-dimensional manifold and M is greater than N, the projection into E^N will be locally space filling. When this procedure is repeated for increasing N, the conventional expectation is that for small N (that is $N < M$), $\nu_s \approx N$ while once N exceeds M, ν_s approaches a constant value assumed to be the correlation exponent of the underlying set. This approach works well in many instances and its use has been suggested in the case of small data sets (Abrahamson *et al.*, 1985).

Our first example, perhaps the simplest dynamical system[3], is

$$\dot{x} = c \tag{2.9}$$

where c is a real constant. The system corresponds to a particle in steady motion along a linear path. When the motion is restricted to a finite interval (by, say, periodic boundary conditions), the trajectory consists of a line segment. The width of the well is taken as the unit of length and the sampling rate is chosen to cover the interval uniformly. Noise is introduced to system 2.9 by adding p-random numbers evenly distributed between 0 and ϵ to each data point.

The resulting time series is embedded in E^2 and $C_2(\ell)$ is calculated via the GPA; a graph of $\log C_2(\ell)$ vs $\log \ell$ is shown in Figure 2.11. The expected $N < M$ behavior of $\nu_s(\ell)$ is shown in Figure 2.12 where four distinct regions are visible. For separations less than the nearest neighbor distance ($\log\ell < -11$), the set scales as a collection of individual points and $\nu_s(\ell)$ is equal to zero. Similarly for ℓ greater than the diameter of the set ($\log\ell > 1.0$), the entire distribution will have been included, $C_2(\ell) = 1$, and $\nu_s(\ell)$ is again zero. For sufficiently long, sufficiently clean data records reconstructed with good delay times, two additional regions are found between these limiting behaviors. The first ($\log \ell \approx -7$), whose existence is due to noise or uncertainty in the measurements, will range from the nearest neighbor distance up to the magnitude of

---

[3]The alternative choice of simple harmonic motion yields a similar result, but the scaling structure is complicated either by projection effects (N=1)or modifications due to large scale structure (N=2).

the noise. (For white noise the upper limit of the noise range is this magnitude multiplied by the square root of the embedding dimension, corresponding to the diameter of a hypercube.) By definition, random fluctuations must not lie on a finite dimensional surface (if this was the case, they would not be independent) and are therefore expected to appear space filling in any embedding dimension. As a result, one expects $\nu_s(\ell)$ to be equal to M in this region. The region of greatest interest lies above the noise region. Here ($\log\ell \approx -3$) the value of the correlation integral is governed by the object and, for nonlacunar objects, $\nu_s(\ell) \approx \nu$. We reiterate that for lacunar objects, $\psi(\ell)$ is not zero and $\nu_s(\ell)$ need not equal ν.

$\nu_s(\ell)$ is estimated by determining the slope of the least squares fit over a window of width τ centered on $\log \ell$, thus τ represents the logarithm of the ratio of the largest ℓ scale to the smallest. The choice of τ depends on the uniformity of the data set; for completely nonlacunar data such as the cat map (see below), we have found $\tau = 2$ to yield good results. Within each power of τ, $\nu_s(\ell)$ is evaluated a number of times. These running averages are displayed in Figure 2.13 as "+" marks.

The minimum window size, τ_{min}, corresponds to the finest scale at which the value of $C_2(\ell)$ is determined. The disconnected points in Figure 2.13 represent $\nu_s(\ell)$ as calculated by this separation. Generally, these points fall about the curve computed with τ=2. The major deviations which occur at small scales result from the finite amount of data and the numerical resolution. For values of ℓ comparable with the nearest neighbor separation, the quantization

inherent in the correlation integral is observable. In this region, a small increment of ℓ introduces only a few additional separations into the sum; this results in discrete values in the change of $\log C_2(\ell)$ for each increment in $\log\ell$. Specifically

$$\delta_{ij} = \frac{\Delta \log C_2(\ell)}{\Delta \log \ell} = \frac{\log i - \log j}{N^2} \tag{2.10}$$

where

$$i = j, j+1, j+2, \ldots$$

and

$$j = 1, 2, 3, \ldots .$$

For each value of j, lines of δ_{ij} are observable in Figure 2.13. As ℓ increases j increases, and thus δ_{ij} decreases for a given value of i. For ℓ values in the scaling region, δ_{ij} is small and the pointwise value of $\nu_s(\ell)$ is in close agreement with the τ=2 value.

Rarely is the scaling region so distinct as it appears in Figure 2.12. Even when the system is ergodic and two-dimensional, the deviation of $\log C_2(\ell)$ from linearity may be large (an example is the standard map, see Appendix 5B). If $\nu_s(\ell)$ is to provide a good estimate of ν, τ must be enlarged or this method should be abandoned. On the other hand, though increasing the window reduces the fine structure in $\nu_s(\ell)$, it may also obscure the distinction between the noise region and the scaling region. Unless the noise level can be reduced significantly, the collection of additional data will not alleviate this problem, and this method will not yield a good estimate of ν.

When $\nu_s(\ell)$ has fine structure and the window size is large, the transition between the noise region and the scaling region becomes

indistinct. In the case of small data sets, it is crucial to determine which behavior is due to the data and which is due to the parameters of the data set (eg. the number of points). The large ℓ transition is investigated in the next section. Here we concentrate on distinguishing the scaling region from the noise. The point is that a truncated white noise signal will often appear to be scaling with an exponent less than E. Look again at the noise plateau of Figure 2.12. The mean value of $\nu_s(\ell)$ on the plateau is

$$\nu = 1.72 \qquad \begin{cases} \tau = 2.0 \\ \log \ell = -6.8 \end{cases} .$$

The data is embedded in a two-dimensional space, yet the noise plateau is significantly less than two. Either the noise is not space filling or the $\nu_s(\ell)$ calculation is faulty. The dilemma is resolved by increasing the magnitude of the noise term until it dominates. The plateau value of $\nu_s(\ell)$ is then computed as a function of the size of the data set for several low dimensional embedding spaces. As a result we are able to quantify when a data set is "small" as a function of the embedding space dimension.

These results are summarized in Figure 2.14, which shows the τ=2 plateau of $\nu_s(\ell)$ for several data set sizes. The data consists of p-random numbers generated by the additive congruent method[4] (see Carnahan *et al.* 1969) evenly distributed on the interval [0,1]. The series is then embedded in three-dimensional space. In the figure,

---

[4]A delay of at least 2 was used for all embeddings with this generator as fine structure in $\nu_s(\ell)$ was found when consecutive values were taken.

$\nu_s(\ell)$ is plotted against log ℓ; the number of points in the set increases by a factor of two between each realization. For small N the plateau is poorly defined and estimated by the greatest $\tau = 2$ value of $\nu_s(\ell)$ - a procedure which overestimates the value of $\nu_s(\ell)$. For a given embedding dimension E, we define a small data set as one in which the value of $\nu_s(\lambda)$ for p-random data is less than 0.90 E.[5] Thus any data set with $N \leq 2^{12}$ is small when embedded in 3 dimensions. It is not our claim that a data set of this size is sufficient, only that with a smaller set one cannot distinguish the dynamical system in question from white noise. For example, the departure of the mean slope of the correlation integral computed from a 1000 point data set from E = 3 by 15% is not evidence of an underlying low-dimensional structure.

A more common approach with experimental results is to embed a series of a given length into successively higher dimensions and to interpret the deviation of ν_s from E as a sign of fractal structure. The observations above apply even more strongly for large E values and sets reconstructed from a time series; the relevant comparison is not to E but to ν_s for a random data set of the same length. To ease this comparison, we have amalgamated the results of a variety of p-random computations to produce Table 2.1 . Here the value of maximum $\nu_s(\ell)$ is calculated as a function of N and E. For large enough E (for any N), the plateau narrows; the $\tau = 2$ and $\tau = 10$ maximum $\nu_s(\ell)$ values are given. Note this comparison with white

---

[5]Note that with the 10% limit it is not possible to distinguish the geometry of a smooth limit cycle from that of a fractal attractor for dimension exceeding ten.

noise is most reasonable when there is no correlation between successive point in the reconstruction; comparison with an appropriate red noise signal would yield a stricter, more useful bound.

Section 2.5: Edge effects as Strict Limits to Dimension Calculation

Given that there seem to be serious difficulties implementing the GPA with small data sets, we present an analytic argument to support this numerical result. First consider a slight modification of an argument due to Alan Wolf (personal communication, 1986; see also Wolf, 1984). In order to determine a scaling exponent one requires a certain range over which the data approximate some power law. Denoting the upper and lower limits of this region by ϵ_{hi} and ϵ_{low}, the requirement is then

$$\frac{\epsilon_{hi}}{\epsilon_{low}} \geq R \qquad (2.11)$$

where R (the range of scales) remains to be chosen. The largest conceivable choice for ϵ_{hi} is the diameter of the set. Considering an M-dimensional unit cube,

$$\epsilon_{hi} = \sqrt{M} \qquad (2.12)$$

With e_{low} determined through Equation 2.11, a lower limit on the number of points may be determined by assuming a uniform density at this separation. Then

$$\epsilon_{low} = N^{-1/M} \qquad (2.13).$$

Solving for N

$$N = \epsilon_{low}^{M} = (R/\epsilon_{hi})^{M} = (R/\sqrt{M})^{M}.$$

When present, the oscillations place a lower bound on R; R must be an integer multiple of the period of the oscillation. In practice Wolf found a Q of 30 to be required; it was with the hope of lowering this data limit that Wolf examined the Lyaponov exponents of dynamical systems. At present, it appears a similar limit may be required in the calculation of these exponents as well.

We now demonstrate a stronger bound on ϵ_{hi}, resulting in an increase of N(M), due to the equal weighing of points near the surface of the object. Such an effect was predicted by Guckenheimer (1984). Consider a one-dimensional unit cube made up of points uniformly distributed on the unit interval[6] as in the system given by Equation 2.9. The correlation integral is

$$C_2(\ell) = 2\ell - \ell^2 \qquad 0 \le \ell \le 1 \tag{2.15}$$

Due to the complete uniformity of this example, the set is nonlacunar; thus no oscillatory corrections are present and one may approximate ν by $\nu_s(\ell)$. Substituting Equation 2.15 into Equation 2.8 we have

$$\nu_s(\ell) = (1 - \ell/2 + O(\ell^2)) \qquad \text{for } \ell < 1. \tag{2.16}$$

As ℓ approaches one, ν_s becomes a poor estimator of ν. This is intuitive, as ℓ approaches one, more and more of the points lie

---

[6] This argument followed from a discussion with J. Theiler during the Los Alamos Summer School in Nonlinear Science, 1986

within ℓ of both endpoints) and scale as isolated points; for ℓ greater than one, $C_2(\ell)$ is a constant. For ν_s to be accurate to within 10% requires $\ell \leq 0.1$.

For an M-dimensional hypercube

$$C_2(\ell) = \ell^M(2 - \ell) \tag{2.17}$$

and

$$\nu_s(\ell) = M\ (1 - \ell/2\ + O(\ell^2)). \tag{2.18}$$

The argument may be made exact by using the Euclidean sup (ℓ_∞) norm. For a uniformly filled hypercube, $C_2(\ell)$ is equal to the probability that two randomly chosen elements will be separated by a distance less than ℓ. In the one dimensional case (the unit interval), this probability is equal to the fraction of the area of the unit square which is bounded by the lines $x - y = \ell$ and $y - x = \ell$. That is

$$P(|x-y|<\ell) = \ell\ (2 - \ell) \qquad \text{for } 0 \leq \ell \leq 1.$$

This is equivalent to Equation 2.15. For an M dimensional cube, the probability that two points are separated by a distance less than ℓ is equal to the probability that each of the elements of the separation vector is less than ℓ. Since these are independent for points chosen at random

$$C_2(\ell) = (\ell\ (2 - \ell))^M \tag{2.19}$$

and

$$\nu_s(\ell) = M[\ 1 - \ell/(2 - \ell)]. \tag{2.20}$$

Note that $\nu_s(\ell)$ always underestimates ν and define a quality factor, Q, such that $\nu_s(\ell) > Q\ \nu$. Using Equation 2.20 to define ϵ_{hi} for a

given value of Q and the minimum number of uniformly distributed points requires as a function of R and Q is given by

$$N = \left[\frac{R\ (2 - Q)}{2\ (1 - Q)} \right]^{M} \qquad (2.21)$$

In particular, assuming R = 4 is sufficient to determine a value of ν_s within 5% of ν yields

$$N = 42^{D}$$

Even with this conservative value of R, the number of points required increases so rapidly as to make application of the Grassberger-Procaccia algorithm impractical objects with dimensions greater than approximately 5.

The large scale transition is examined using Arnold's cat map [Arnold and Alvez, 1968]. The cat map is a two-dimensional, area preserving iterative map of the unit square onto itself. Given by

$$\begin{bmatrix} x_{n+1} \\ y_{n+1} \end{bmatrix} = \begin{bmatrix} 1 & 1 \\ 1 & 2 \end{bmatrix} \begin{bmatrix} x_n \\ y_n \end{bmatrix} \quad \text{mod } 1$$

it is both ergodic and mixing. Consider the embedding of the series $x_1, x_2, x_3, \ldots$ with delay 1 in two-dimensions[7]. In the range

---

[7] embedding this series in higher dimensional spaces results in a sheet like structure which obscures the boundary effects to be demonstrated here; the question as to whether similar effects might occur in experimental data is open.

($.01 < \ell < 1$) $\nu_s(\ell)$ as calculated by Equation 2.18 agrees well with the $r=2$ value of ν determined from a 2^{14} point data set.

We emphasize again that we have used simple objects - cubes of uniform density. Indeed, hyperspheres are the least sensitive objects to this edge effect. With complicated objects the effect should be more pronounced. There exist certain density distributions which minimize this effect. Objects of this category have been constructed and studied by Theiler (1986); however, to assume their existence in any given experimental setting is unwarranted.

Finnally note that the minimum number of points given by Equation 2.21 assumes a uniform covering of the entire set. For data from a time series, this quantity is related to the ratio of the length of the series to the reconstruction time, not the sampling rate. At some point, increasing the sampling rate does not effect the size of the data set.

Appendix 2: Explicit construction of the Cantor Oscillation

The simple structure of Cantor sets permits a straightforward recursive construction of $C_2(\ell)$, and thereby $\chi(\ell)$, to arbitrarily high accuracy. For concreteness we will examine the 101 set. The argument is easily extended. Consider the most developed oscillation at every finite approximation to the set, that is $C_2(\ell)$ over the interval $1/\sigma \leq \ell \leq 1$.

$C_2(\ell)$ is completely specified by the location of its discontinuities, x_i, and their strengths, w_i. The function is generated in a manner which parallels the method for constructing Cantor sets (see §1.2). The following notation allows us to deal with two sets of integers, simplifying and speeding numerical implementation of the method. The N^{th} approximation of the set will consist of $n = 2^{N+1}$ points and there will be a discontinuous increase in $C_2(\ell)$ at the 3^N values of ℓ given by

$$ {}^{N}x_i = \frac{\alpha_i}{3^N} $$

and the magnitude of the i^{th} discontinuity will be

$$ {}^{N}w_i = \frac{\beta_i}{2^{N+1}} $$

for $\quad i = 0,1,2,\ldots,3^N.$

The problem is now reduced to finding the two sets of integers α_i and β_i. The correlation integral may then be evaluated by calculating

$$C_2(\ell) = \frac{1}{N^2} \sum' \beta_i$$

where Σ' is a sum over all i such that

$${}^N x_i \leq \ell$$

or, equivalently

$${}^N \alpha_i \leq 3^N \ell \ .$$

For N = 1, the four point approximation to the set yields

$$\begin{aligned} {}^1\alpha_0 &= 0 \\ {}^1\alpha_i &= i \qquad\qquad i = 1,2,3 \\ {}^1b_0 &= 4 \\ {}^1b_i &= 2(4 - i). \end{aligned}$$

At each generation, there exists at least one pair of points separated at every integer multiple of the smallest separation. Thus

$${}^N\alpha_i = i. \qquad\qquad i = 0,1,\ldots,3^N$$

The ${}^N\beta_i$ are slightly more complicated. The destruction operator may be thought of as introducing fine scale structures in the N+1st generation with twice the weight of the corresponding structure of the Nth generation on ($0 \leq \ell \leq 1$). If the Nth generation is considered as a 3^N digit binary integer with 1's corresponding to points, the Nth generation structure in the range $1/3 \leq \ell \leq 1$, is

equal to the number of 1 bits remaining after a left shift of α_i bits and logical AND operation on the binary representation of the set; this results in a simple growth and decay process of the N + 1st generation β's in this range. At the point $\ell = 1/3$, both processes contribute. In symbols

$$
{}^{N+1}\beta_i = \begin{cases} 2\,{}^{N}\beta_i & i = 0,1,\ldots,k-1 \\ 2\,{}^{N}\beta_i + 2 & i = k \\ {}^{N}\beta_{2k-i} & i = k+1,k+2,\ldots,2k-1 \\ 2\,{}^{N}\beta_0 & i = 2k \\ {}^{N}\beta_{i-2k} & i = 2k+1,2k+2,\ldots,3^N \end{cases}
$$

where $k = 3^{N-1}$.

FIGURE CAPTIONS

Figure	Caption
2.1	Delay reconstruction of z(t) from the Moore-Spiegel system with the parameter values R=100.0 and (a) T=10.0,(b) T=36.0. In both cases τ_d = 0.20 .
2.2	The effect of varying the delay time is shown in reconstructions of a single time series of z from the Moore-Spiegel system in the case R=100.0 and T=26.0. The delay time increases with each panel, specifically (a) τ_d=0.20,(b) τ_d=0.40,(c) τ_d=0.80,(d) τ_d=1.60 .
2.3	The (a) normalized eigenvalues and (b) corresponding eigenvectors generated by the Broomhead-King procedure applied to a time series from the Moore-Spiegel system in the case R=100.0 and T=36.0 . In (b) the eigenvalue corresponding to each eigenvector is printed above each panel.
2.4	As in Figure 2.3 for the case T=10.0 . Here the attractor is periodic.
2.5	As in Figure 2.3 for the system of three period harmonic oscillations with noise described in the text.
2.6	A linear plot of the correlation integral as a function of ℓ for the set 101.
2.7	The graph of log $C_2(\ell)$ as a function of log(λ) for set 101.
2.8	$\psi(\ell)$ for the set 101.
2.9	$\psi(\ell)$ for the sets (a) 101010001 and (b) 10100101.
2.10	The (a) correlation integral and (b) $\psi(\ell)$ for a surface of section of the Moore-Spiegel system.
2.11	The correlation integral for a one-dimensional object.
2.12	$\nu_s(\ell)$ for the set of Figure 2.11.
2.13	$\nu_s(\ell)$ as in Figure 2.12. Here the δij structure is shown.
2.14	$\nu_s(\ell)$ plateaus for an increasing numbers of points. The individual curves are labeled by the number of points in

the source data set. Note the slow increase in the maximum value.

Table 2.1 Disqualification table showing the results of embedding white p-random noise.

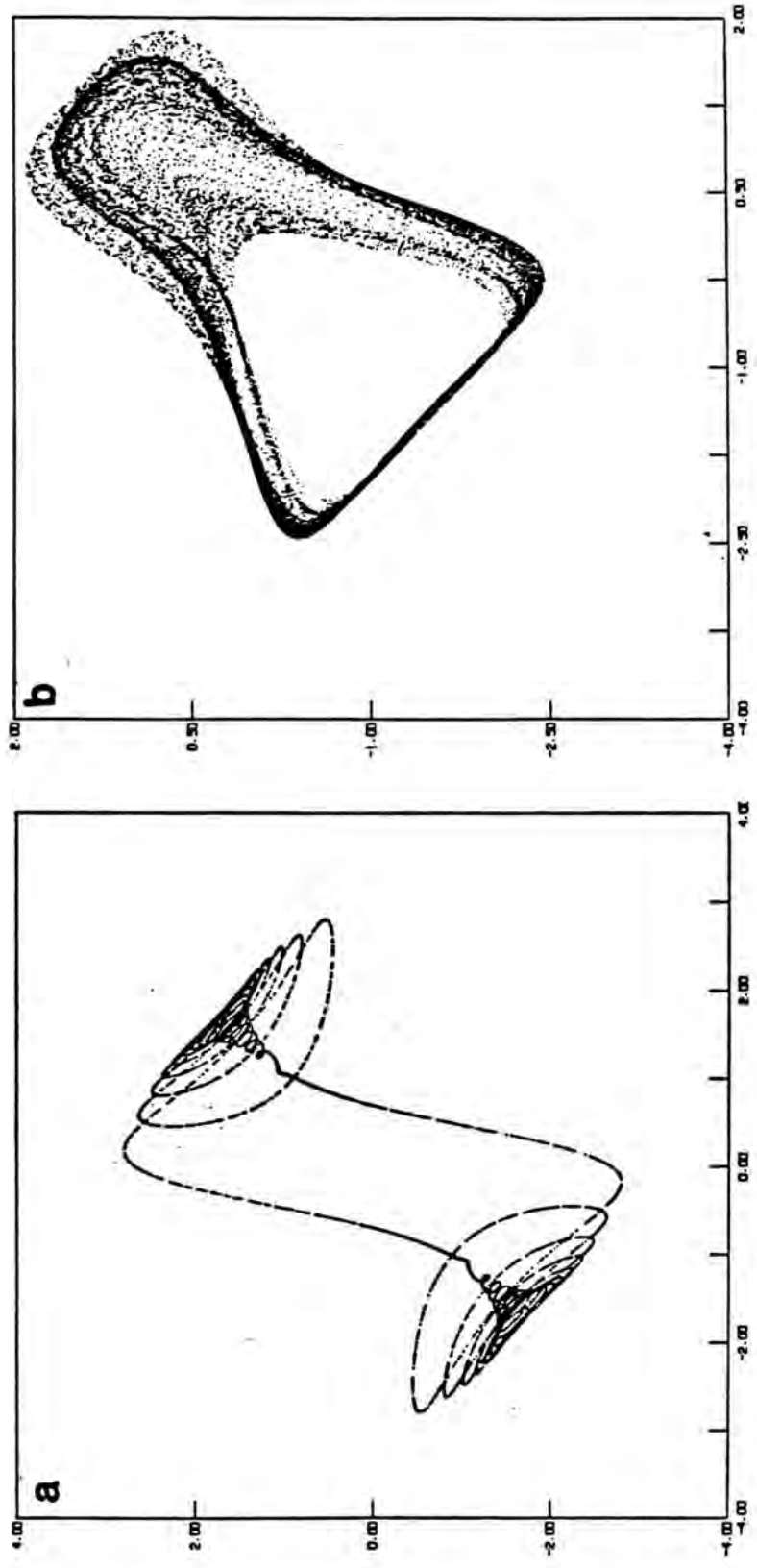

Figure 1

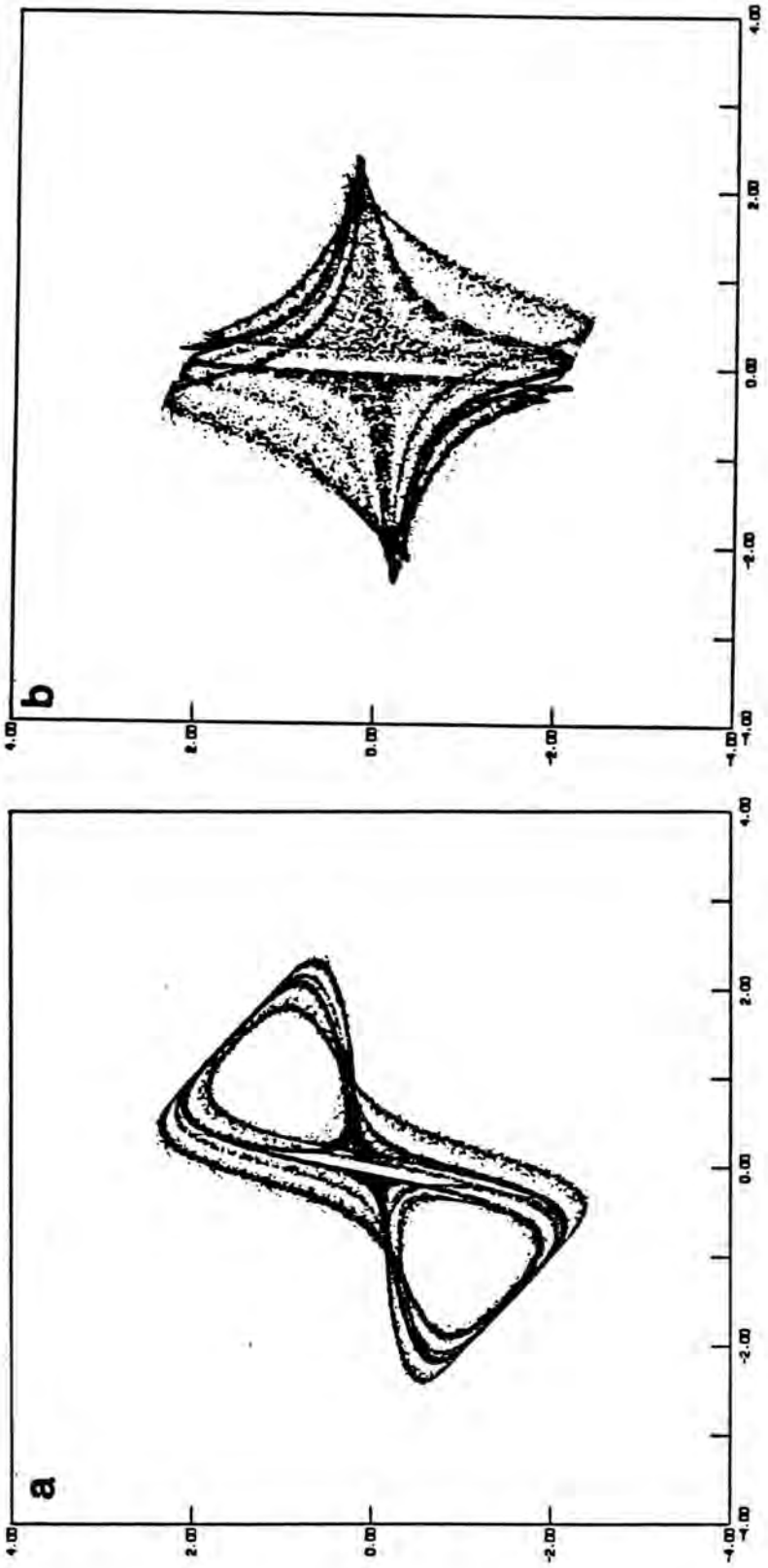

Figure 2

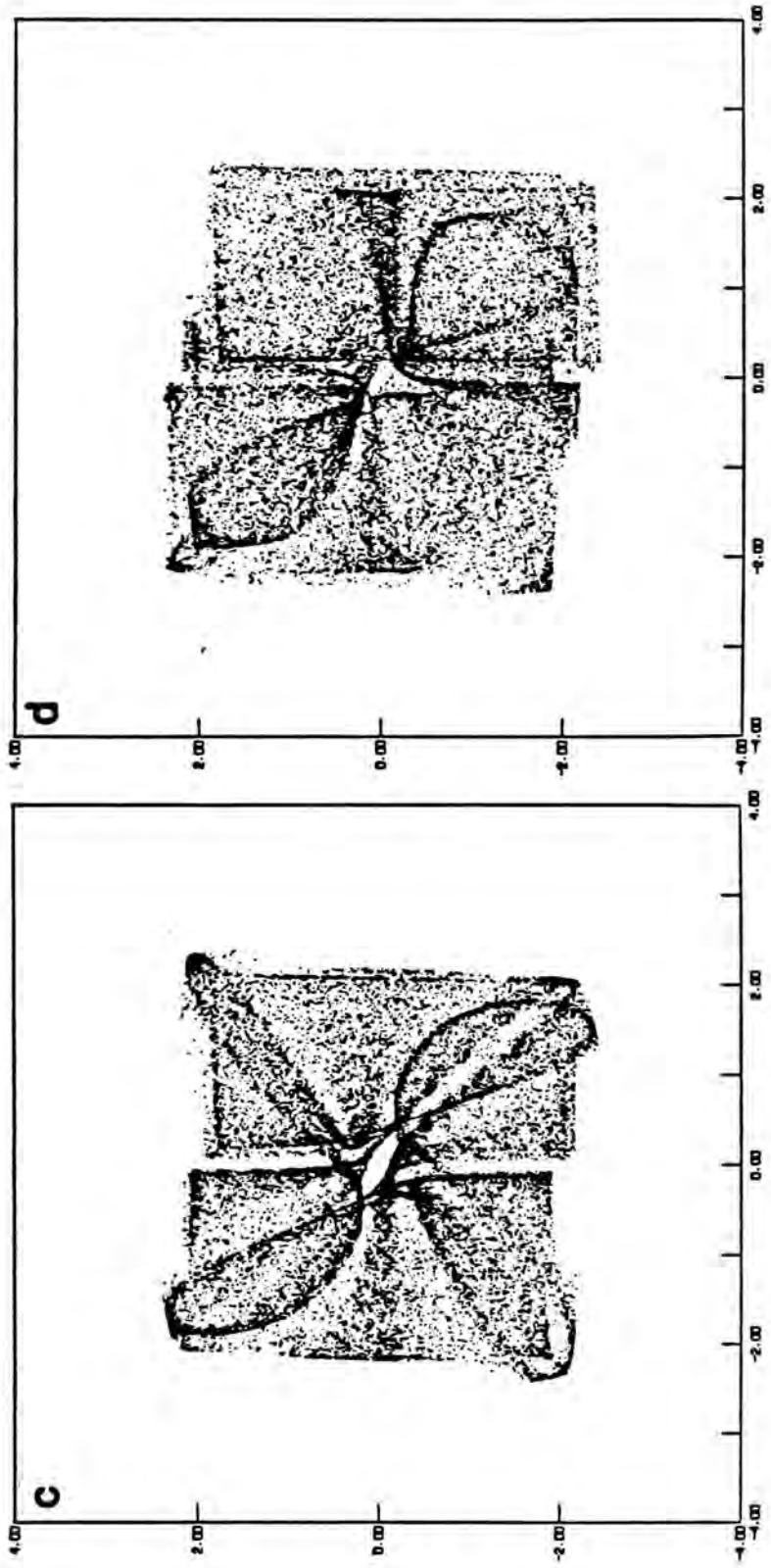

Figure 2

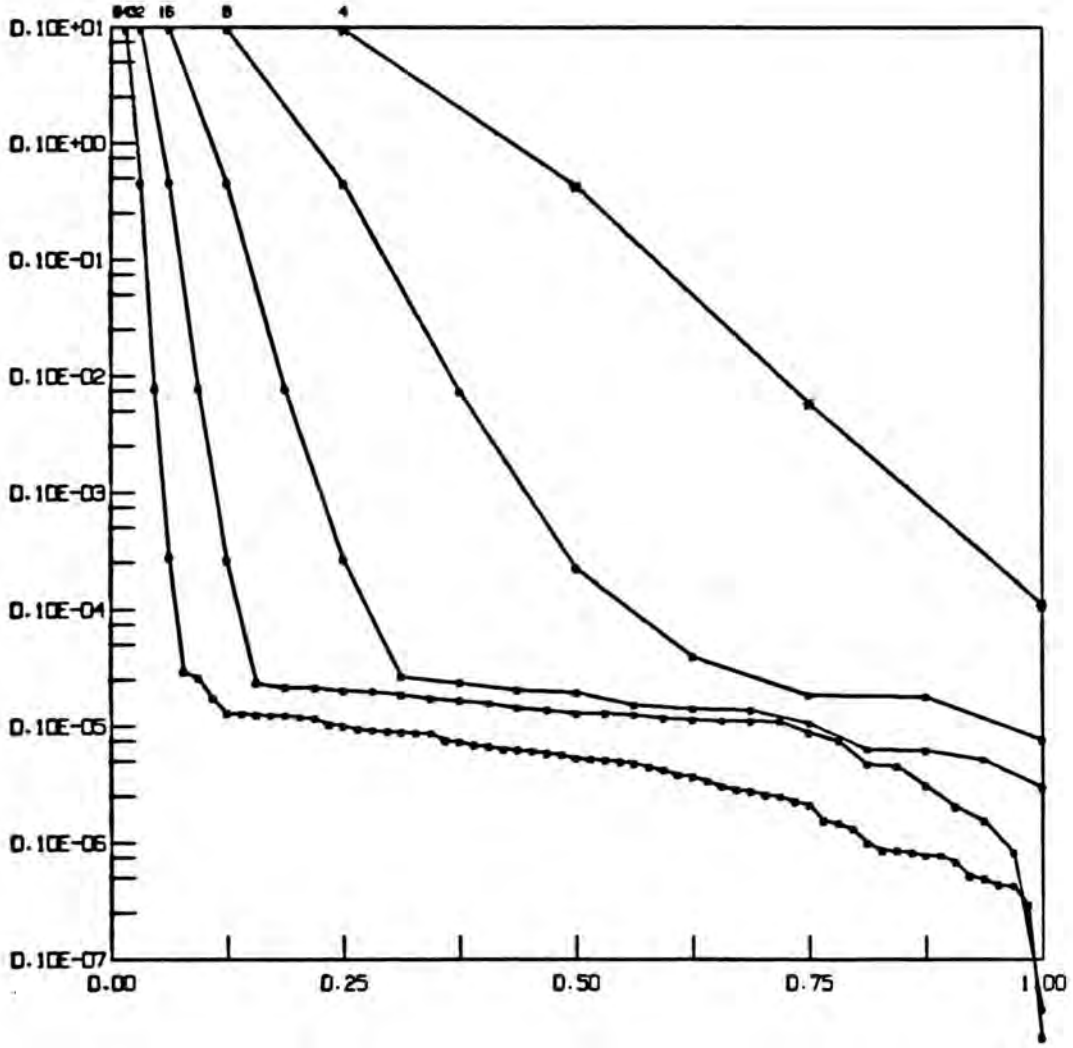
32
16
8
4
0.10E+01
0.10E+00
0.10E-01
0.10E-02
0.10E-03
0.10E-04
0.10E-05
0.10E-06
0.10E-07
0.00
0.25
0.50
0.75
1.00

Figure 3a

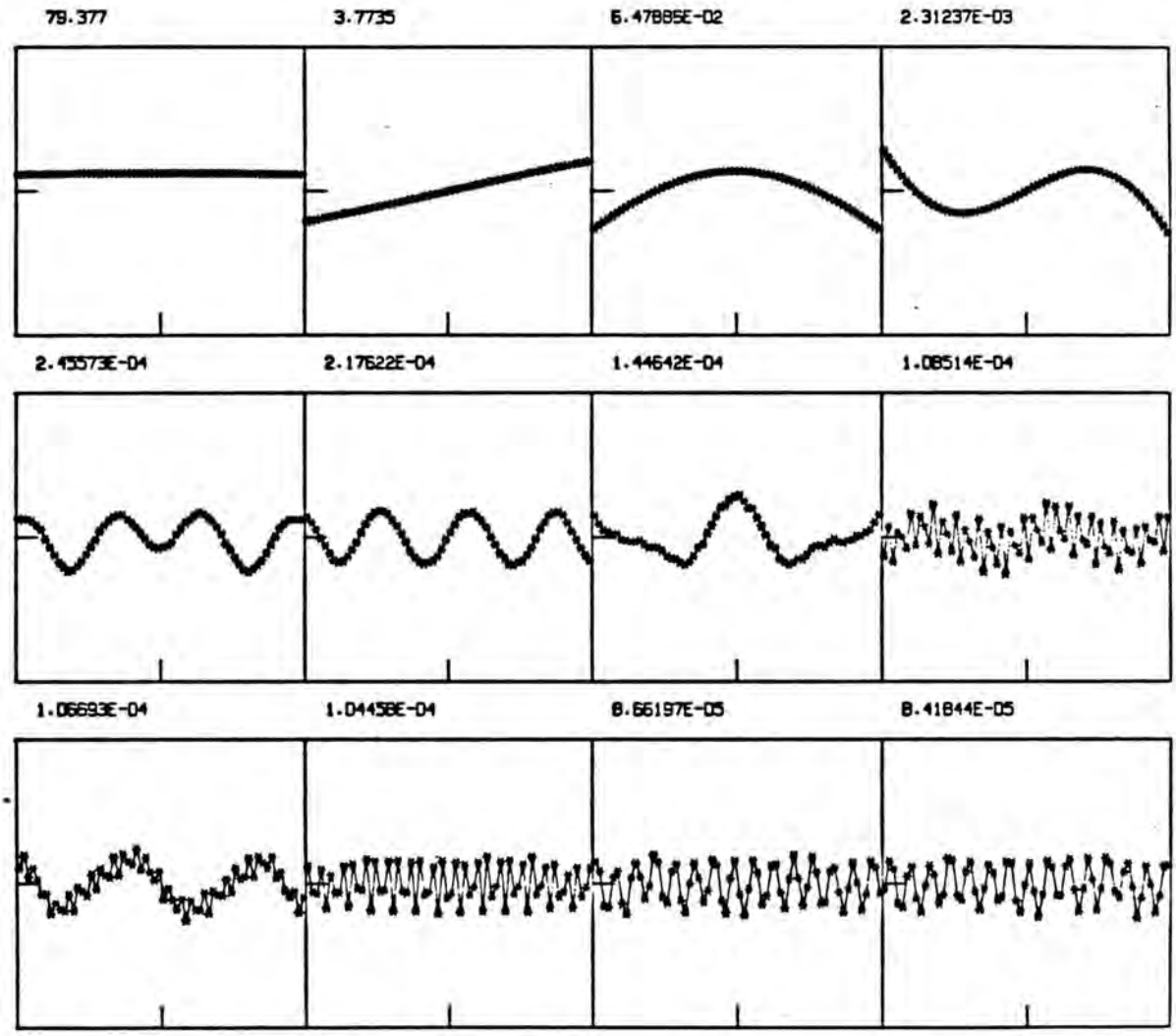
79.377
3.7735
6.47885E-02
2.31237E-03
2.43573E-04
2.17622E-04
1.44642E-04
1.08514E-04
1.06693E-04
1.04458E-04
8.66197E-05
8.41844E-05

Figure 3b

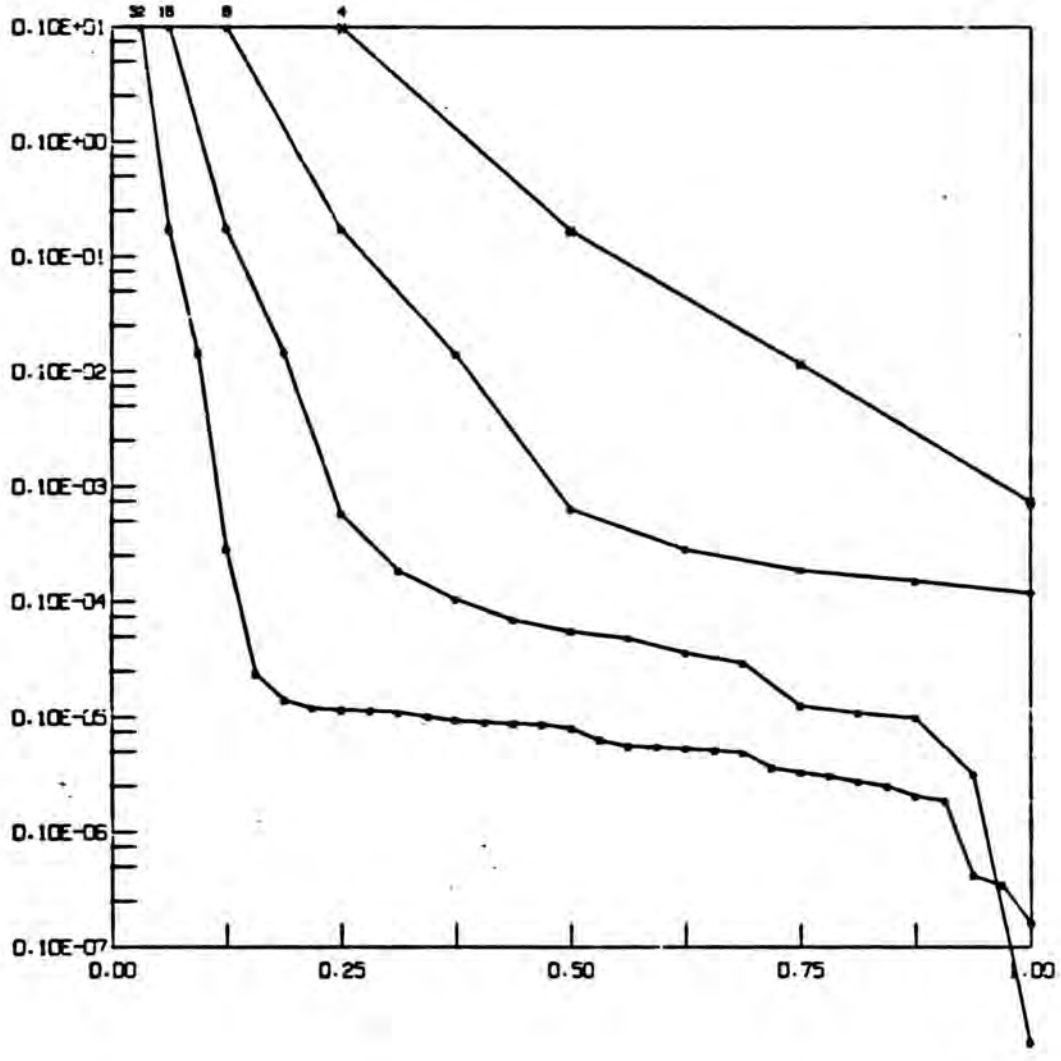
32
16
8
4
0.10E+01
0.10E+00
0.10E-01
0.10E-02
0.10E-03
0.10E-04
0.10E-05
0.10E-06
0.10E-07
0.00
0.25
0.50
0.75
1.00

Figure 4

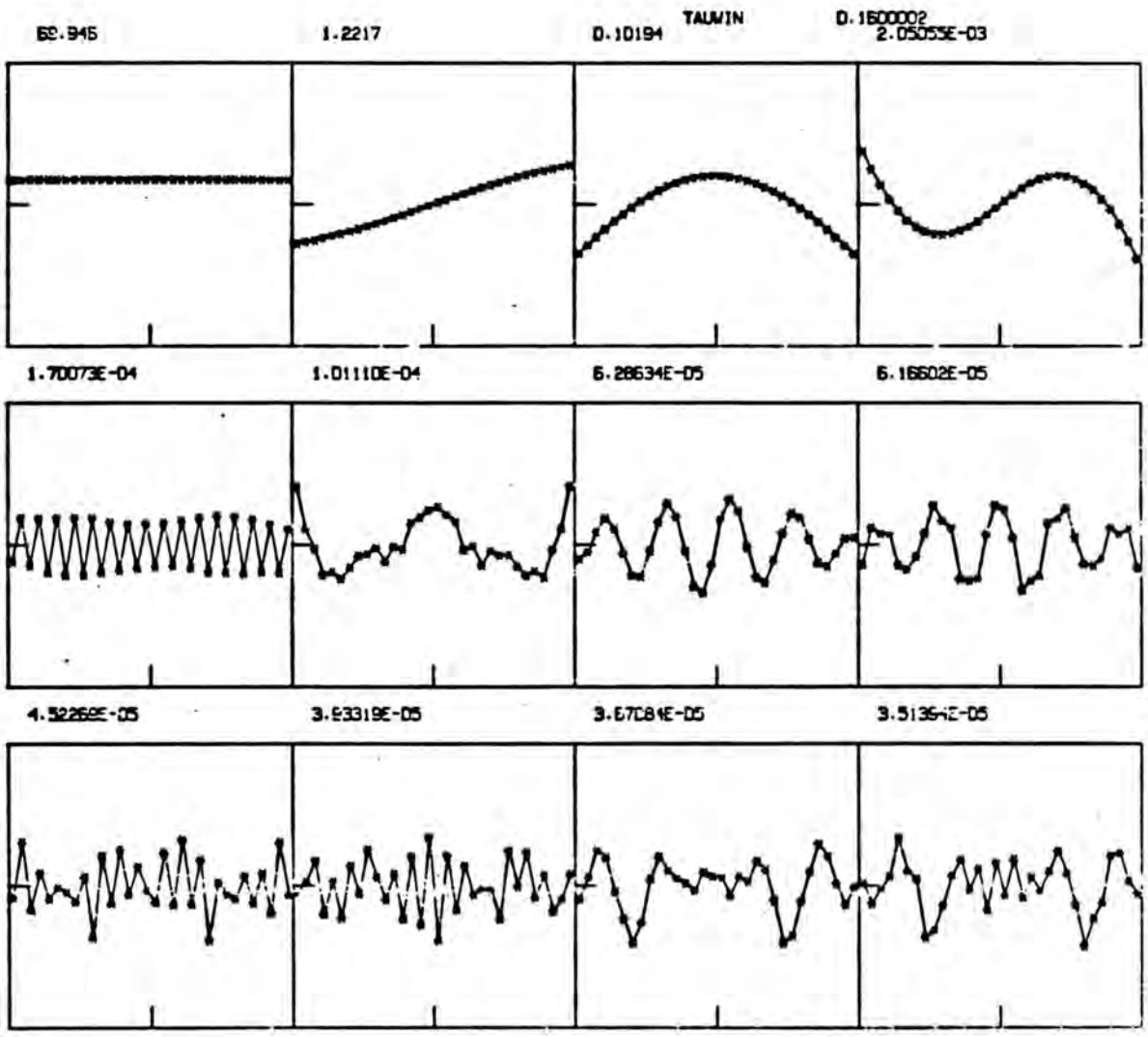
69.945
1.2217
0.10194
TAUWIN
0.1600002
2.05055E-03
1.70073E-04
1.01110E-04
6.28634E-05
6.16602E-05
4.52269E-05
3.93319E-05
3.67084E-05

Figure 4

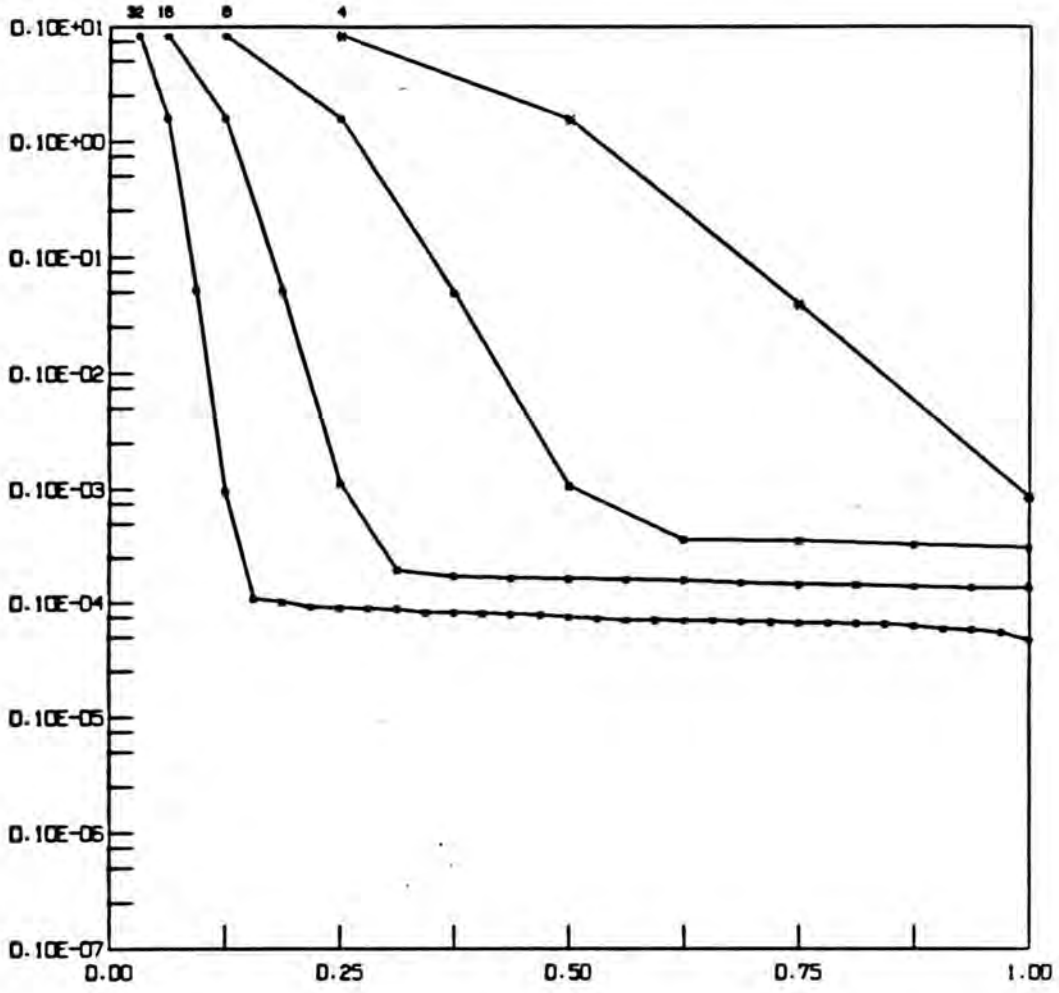
32
16
8
4
0.10E+01
0.10E+00
0.10E-01
0.10E-02
0.10E-03
0.10E-04
0.10E-05
0.10E-06
0.10E-07
0.00
0.25
0.50
0.75
1.00

Figure 5

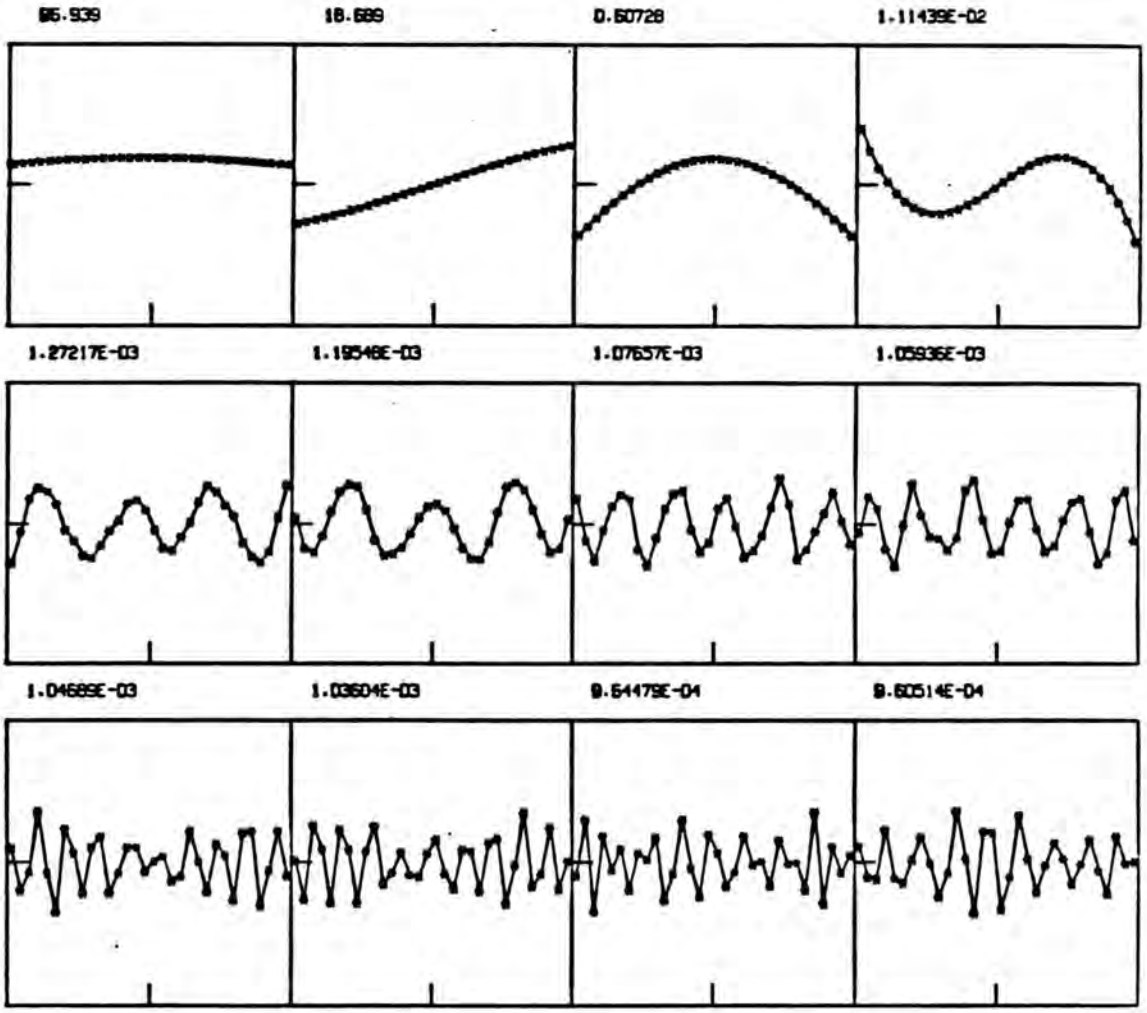
86.939
18.689
0.60728
1.11439E-02
1.27217E-03
1.19548E-03
1.07657E-03
1.05936E-03
1.04689E-03
1.03604E-03
9.64479E-04
9.60514E-04

Figure 5

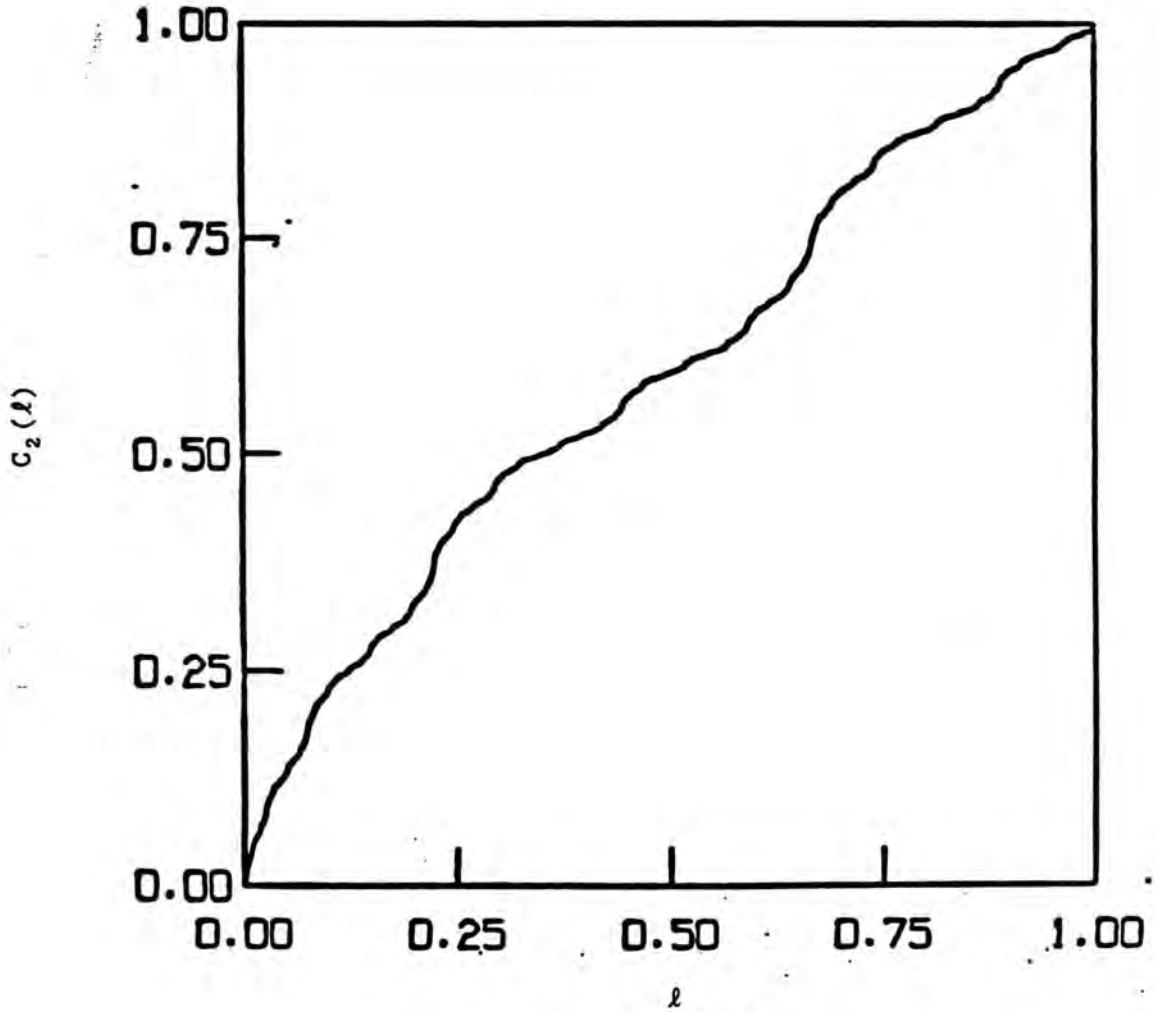

Figure 6

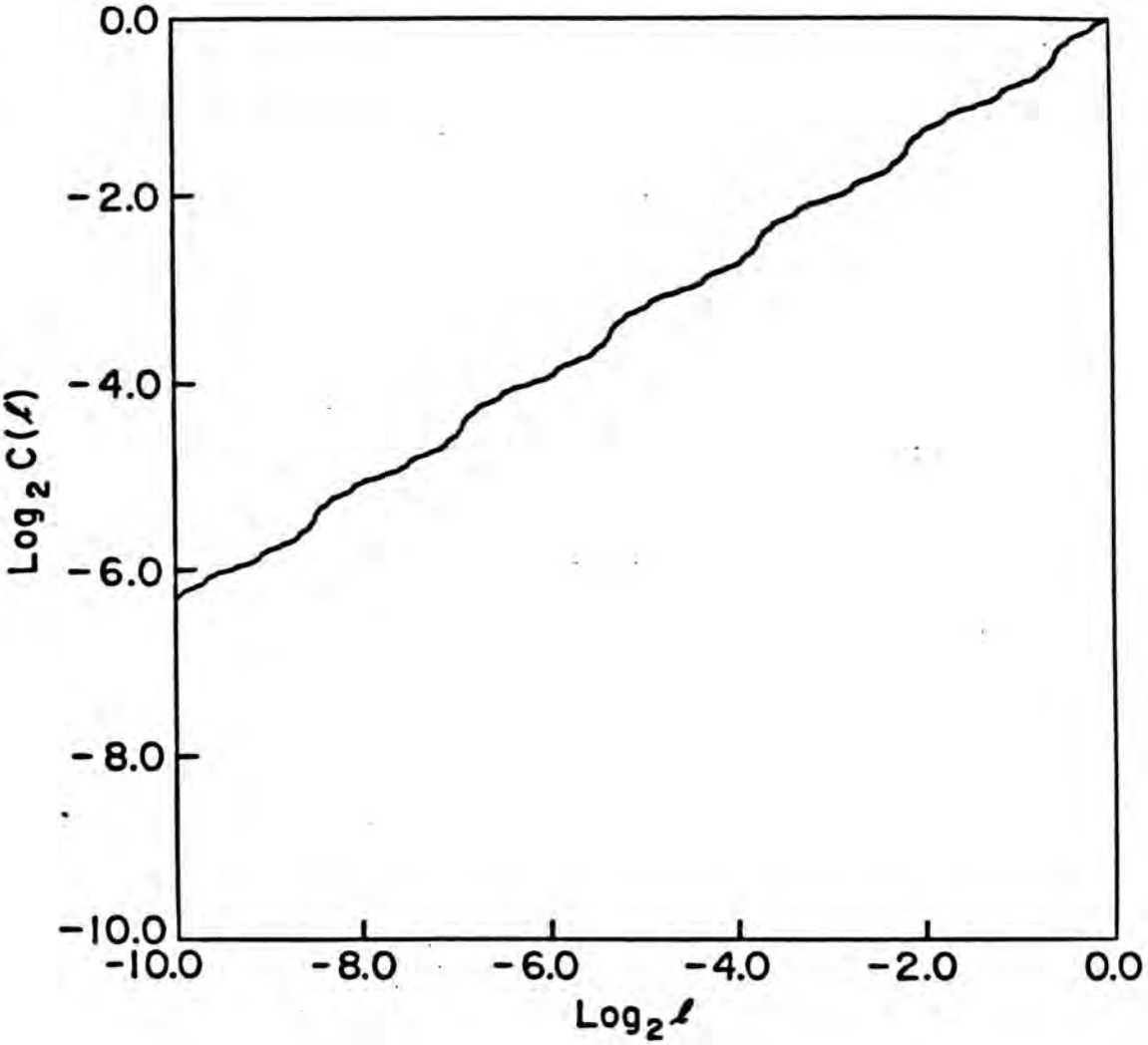

Figure 7

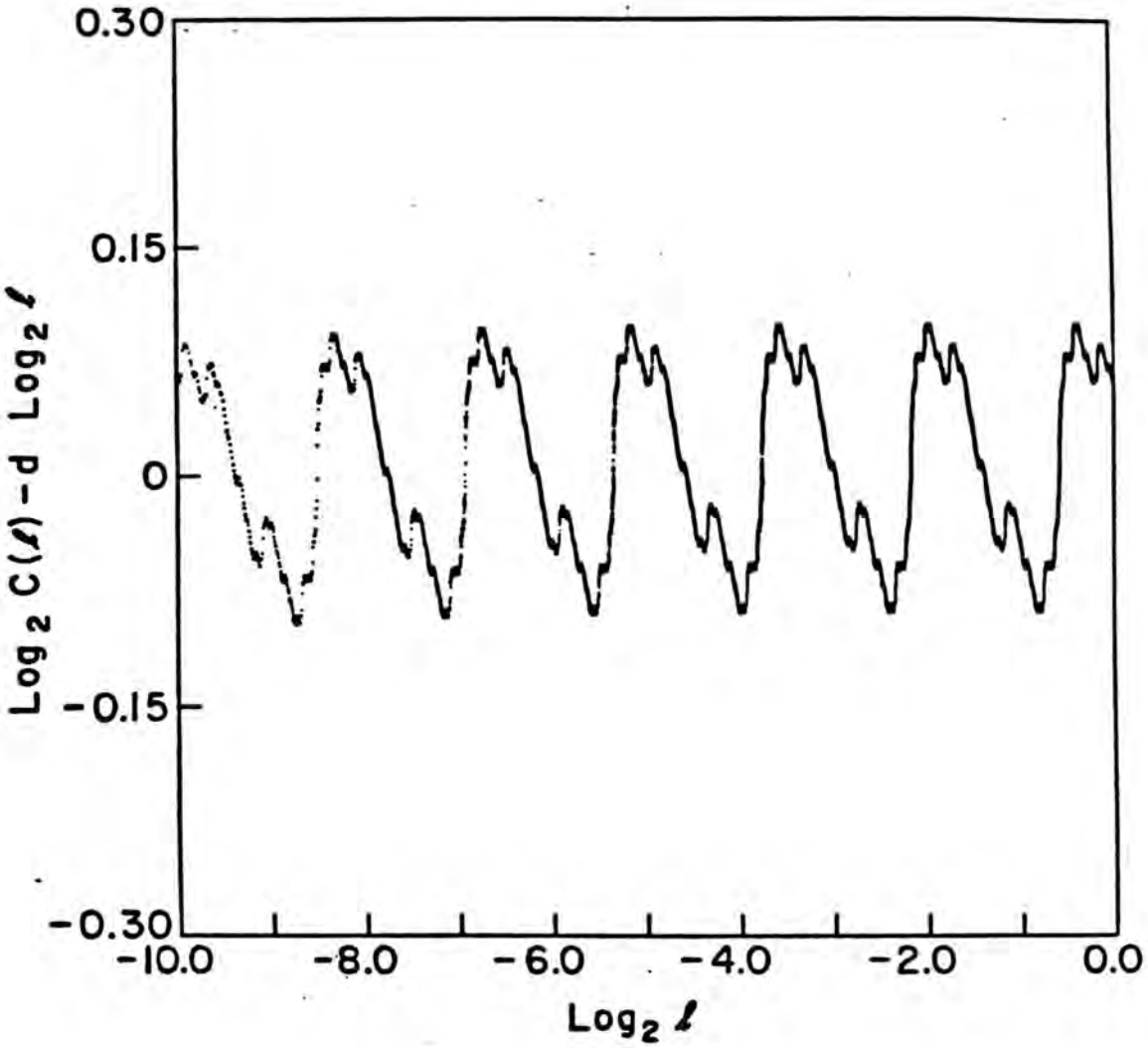

Figure 8

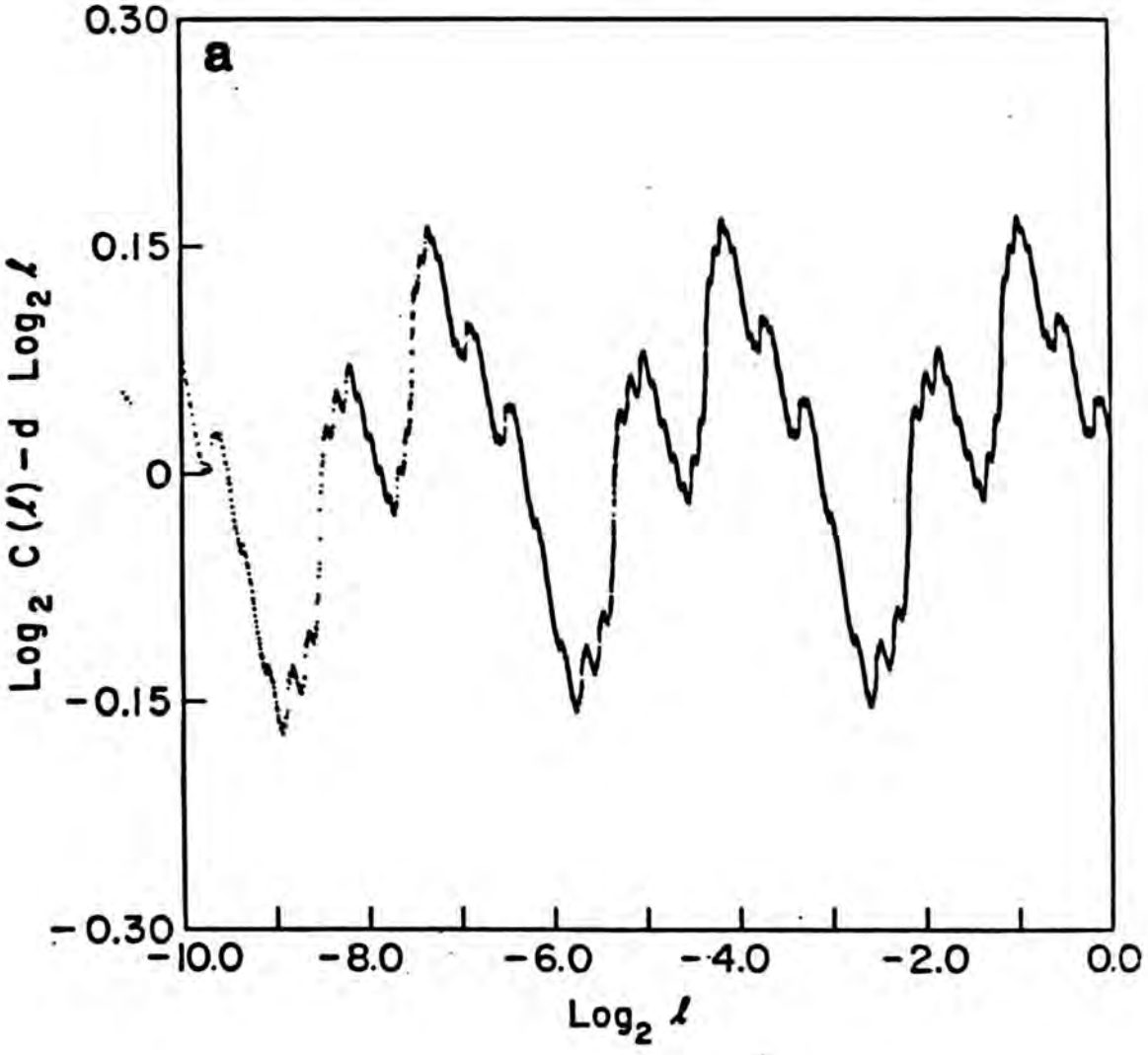

Figure 9

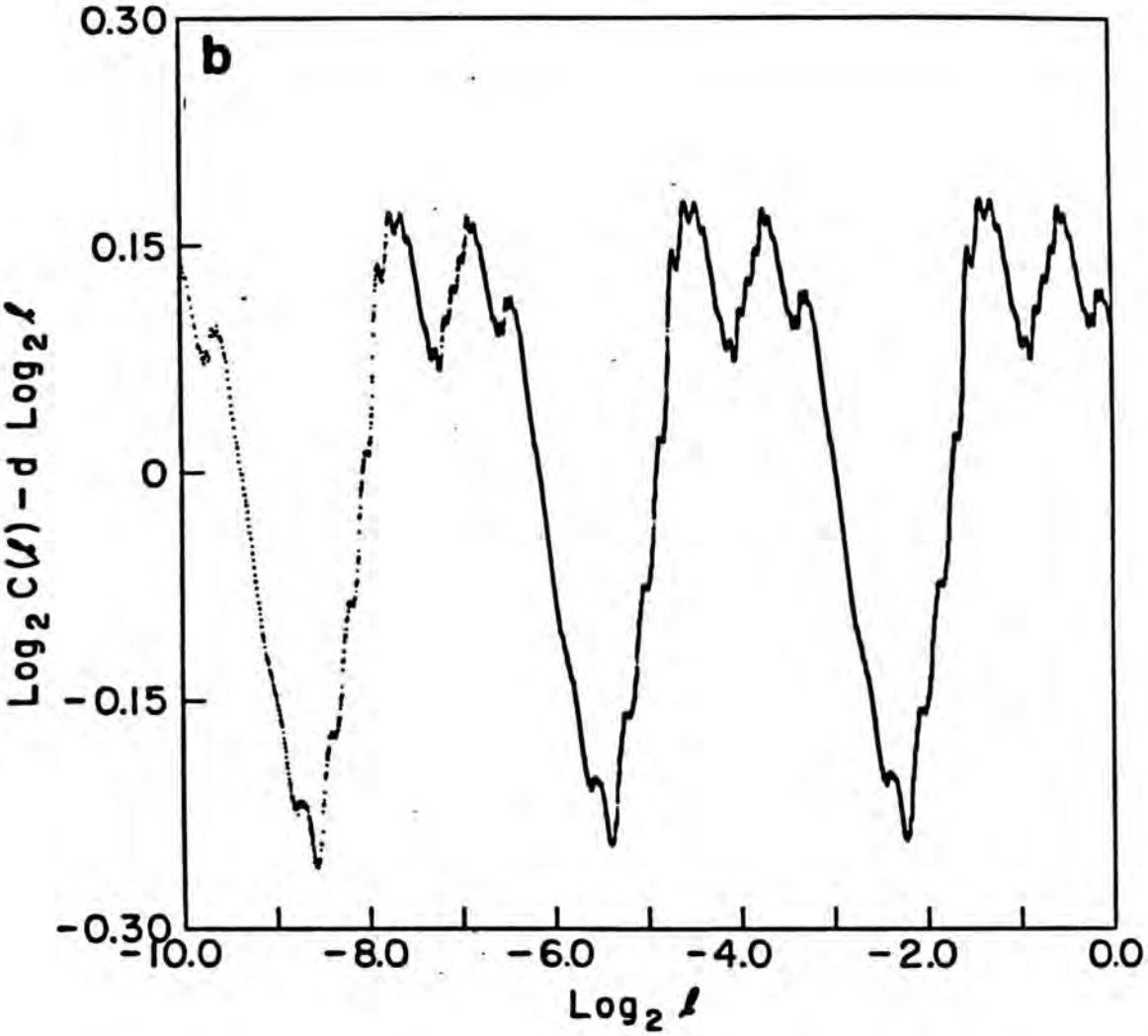

Figure 9

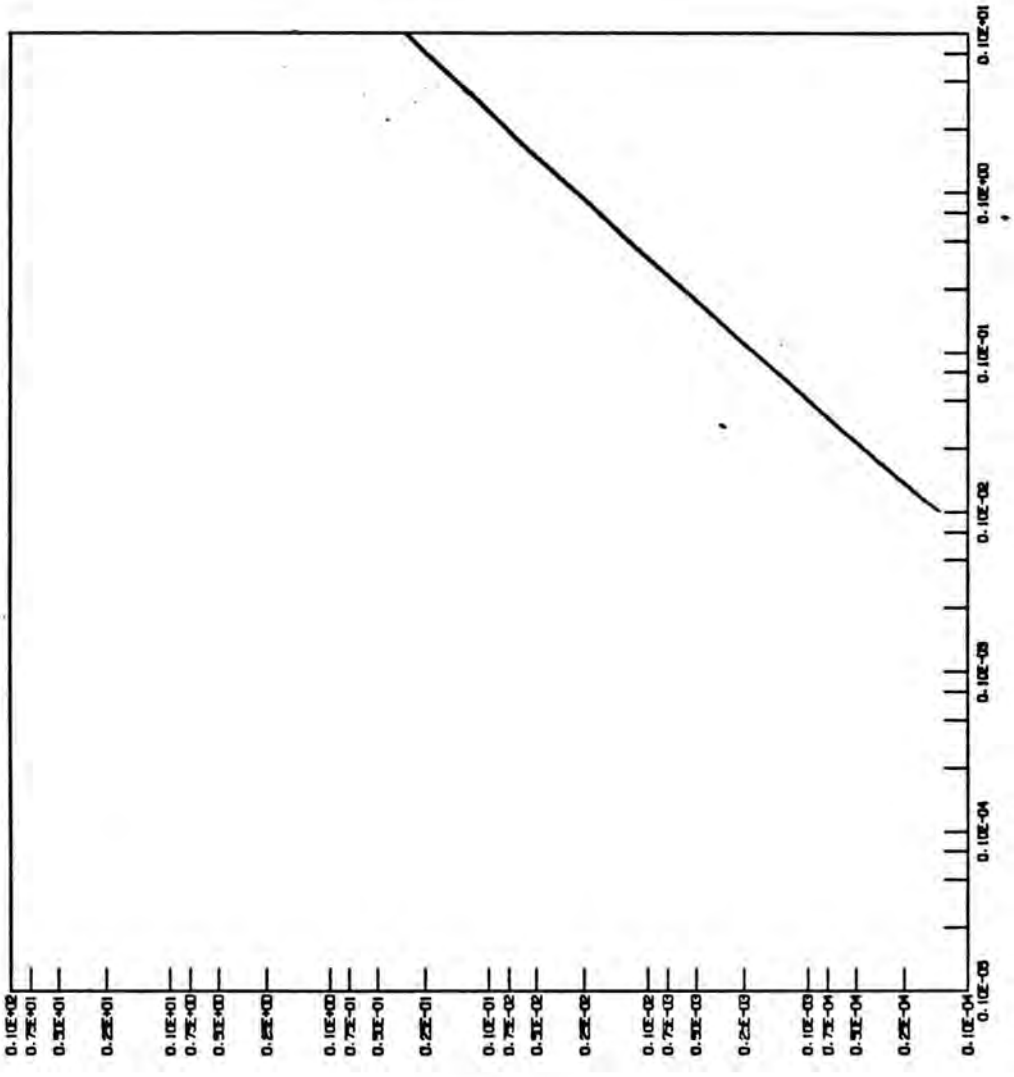

Figure 10

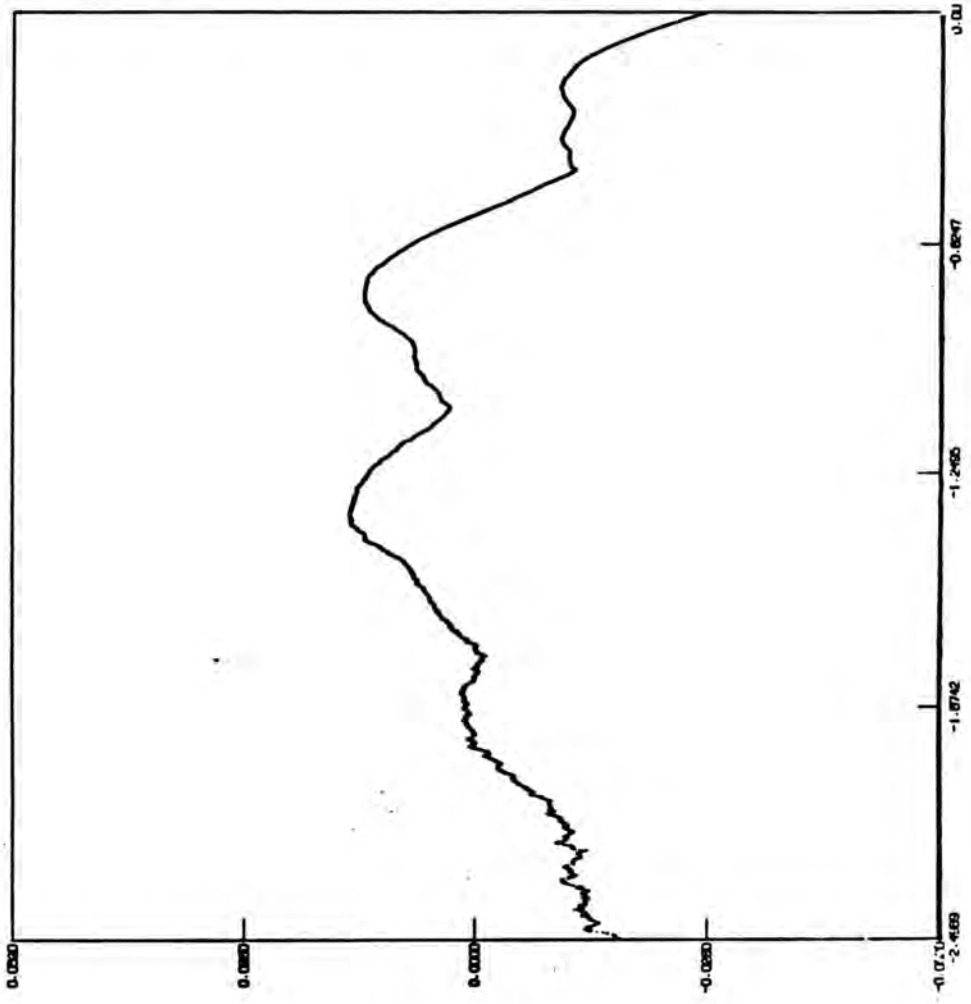

Figure 10

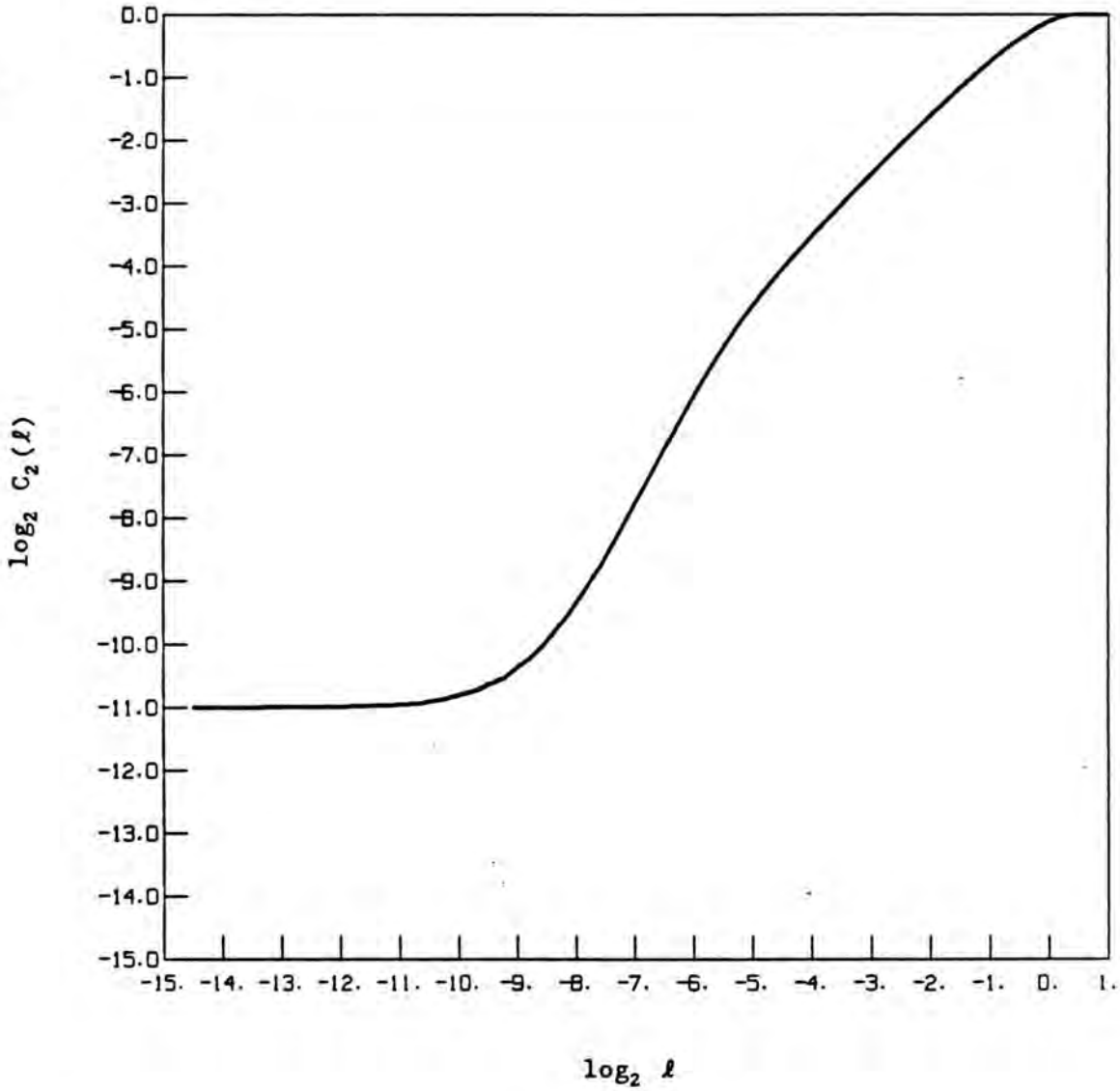
0.0
-1.0
-2.0
-3.0
-4.0
-5.0
-6.0
-7.0
-8.0
-9.0
-10.0
-11.0
-12.0
-13.0
-14.0
-15.0
log2 C2(ℓ)
-15. -14. -13. -12. -11. -10. -9. -8. -7. -6. -5. -4. -3. -2. -1. 0. 1.
log2 ℓ

Figure 11

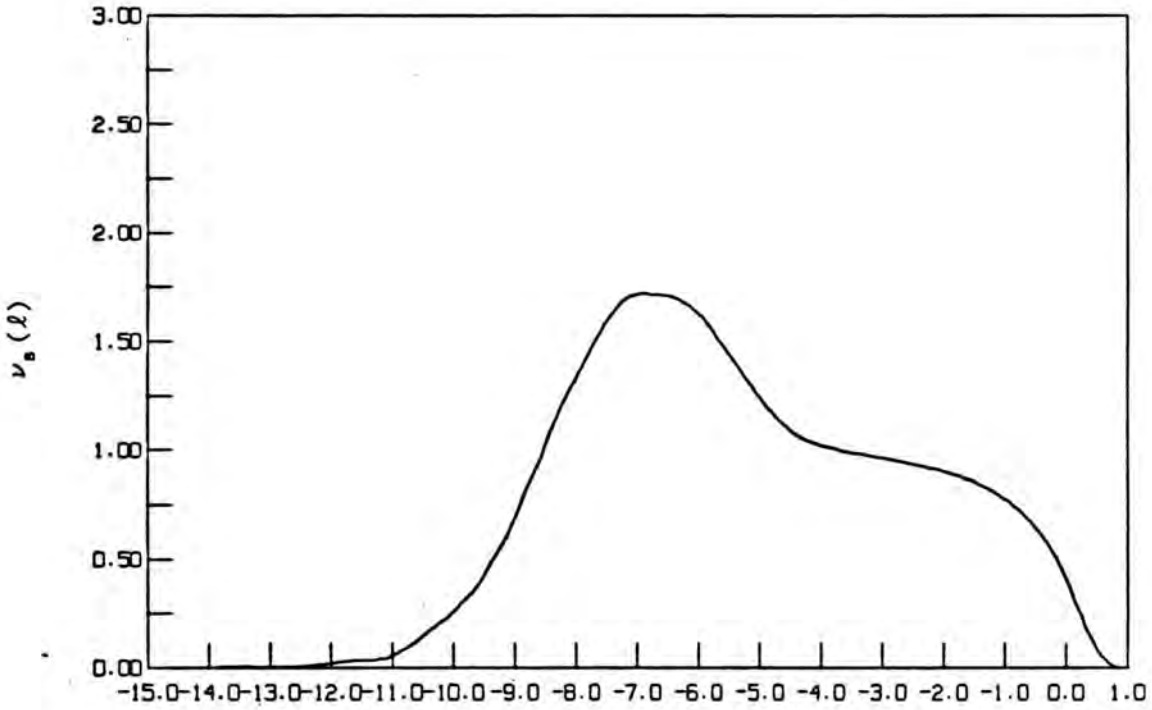
3.00
2.50
2.00
1.50
1.00
0.50
0.00
$\nu_s(\ell)$
-15.0 -14.0 -13.0 -12.0 -11.0 -10.0 -9.0 -8.0 -7.0 -6.0 -5.0 -4.0 -3.0 -2.0 -1.0 0.0 1.0

Figure 12

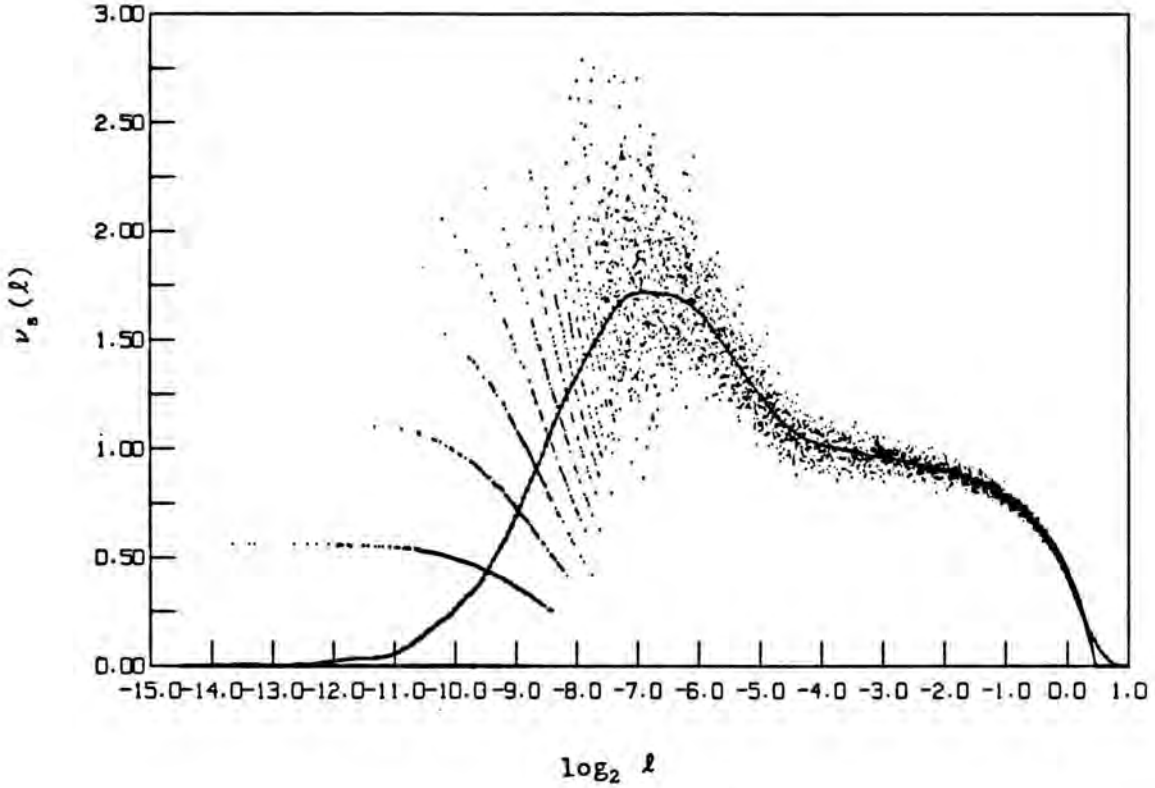
3.00
2.50
2.00
1.50
1.00
0.50
0.00
$\nu_s(\ell)$
-15.0 -14.0 -13.0 -12.0 -11.0 -10.0 -9.0 -8.0 -7.0 -6.0 -5.0 -4.0 -3.0 -2.0 -1.0 0.0 1.0
$\log_2 \ell$

Figure 13

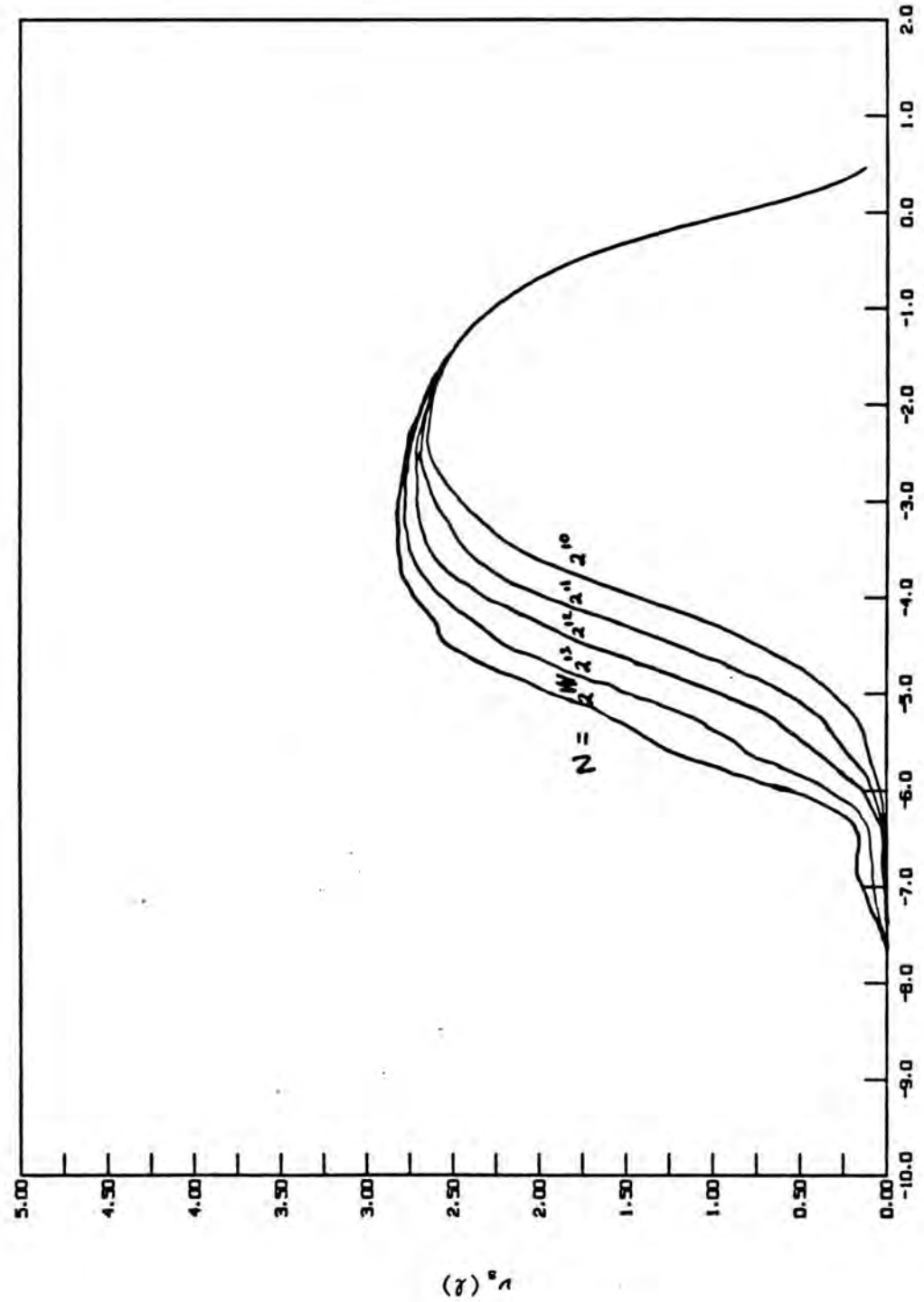
$v_2(\ell)$
5.00
4.50
4.00
3.50
3.00
2.50
2.00
1.50
1.00
0.50
0.00
-10.0
-9.0
-8.0
-7.0
-6.0
-5.0
-4.0
-3.0
-2.0
-1.0
0.0
1.0
2.0
$\log_2 \ell$
$N = 2^{13}/2^{12}, 2^{11}, 2^{10}$

Figure 14

Table 2.1

EMBEDDING DIMENSION	2^8	2^9	2^{10}	2^{11}	2^{12}	2^{13}	2^{14}
6	4.27	4.58	4.85	4.95	5.06	5.16	
	3.03	3.36	3.68	3.89	4.11	4.28	
5	3.72	3.92	4.10	4.16	4.28	4.46	
	2.87	3.17	3.43	3.64	3.80	3.98	
4	3.12	3.26	3.40	3.45	3.55	3.61	
	2.63	2.84	3.05	3.18	3.30	3.41	
3	2.45	2.54	2.64	2.69	2.73	2.79	2.83
	2.24	2.36	2.50	2.58	2.65	2.72	2.75
2	1.75	1.79	1.85	1.87	1.90	1.92	
	1.67	1.75	1.81	1.84	1.87	1.90	
1	0.957	0.973	0.971	0.987	0.987	0.988	
	0.937	0.955	0.965	0.972	0.980	0.985	

Number of Data Points

CHAPTER III The Oscillatory Component of Scaling

Introduction

The calculation of scaling exponents is becoming a common tool with which to analyze systems which display complex behavior. Several difficulties remain in processes for the determination of the scaling exponents of inhomogeneous fractal sets.[1] Included are (1) the lack of reliable error estimates, (2) the intrinsic N^2 nature of the much-used Grassberger-Procaccia algorithm (GPA), and (3) the box-counting limitations of current $f(\alpha)$ schemes. In addition, there are no reliable schemes for calculating d_q for large negative q; global methods have difficulty determining the properties of the least dense singularities. In this chapter we present a new method which alleviates the first two of these difficulties and may assist in solving the third. In Section 3.2 we demonstrate that the log-periodic ψ functions discussed in Chapters 1 and 2 originate from an oscillatory component in the general solution to the scaling equation. The main result of this chapter is a new characterization of the local scaling structure of fractal sets, focused, in the case of strange attractors, on the unstable periodic orbits. Using the periodicity (in log ℓ) of the ψ function, one may compute a reliable estimate of a local scaling exponent; this is illustrated in Section 3.3. This procedure is the first to supply meaningful error statistics on the exponent. Since only the local structure is considered, bounds on $d_{-\infty}$ are available. Computationally, the time

---

[1] Definitions of the quantities discussed here are to be found in Chapter 1.

required by the algorithm goes as the number of points. The procedure may be interrupted to examine intermediate results and then restarted easily.

It is generally believed that the singular structure of strange attractors is closely related to the set comprised of all (unstable) periodic orbits. For the flows in a three-dimensional phase space such as the Lorenz and Moore-Spiegel systems, these (closed) trajectories have been investigated by Baker *et al.* (1971). In a time series generated by a weakly chaotic system, a trajectory is often observed to alternate (irregularly) among several cycles; these cycles resemble the periodic orbits. A comprehensive discussion of the importance of periodic orbits to the dynamics of the Lorenz system is given by Sparrow (1982). This behavior can be seen in the Moore-Spiegel attractor (Figure 1.3b), where the trajectory exhibits characteristics of one of several distinct motions between each crossing of the z=0 plane. In a two-dimensional mapping (or surface of section) the periodic orbits are isolated points. A method for determining both the periodic and near periodic points for 2-D mappings has been introduced by Cvitanović and Gunaratue (in preparation). If the singular structure is completely determined by the periodic points, it should be possible to determine the scaling structures of a set using the methods introduced in this chapter. A discussion of how this might be done is given in Section 3.5.

This chapter is structured as follows: in Section 3.1 we define the local correlation integral or Cantor function. Section 3.2 then demonstrates its application to familiar fractal sets; oscillatory

components of the Cantor function of those sets are observed and shown to arise from the general solution to the scaling equation. This departure from linear scaling is then utilized in Section 3.3 to determine the scaling exponents of the Feigenbaum set, where some of the scaling exponents may be computed analytically. The method is applied to a strange attractor from the Hénon system in Section 3.4. In § 3.5 we outline a procedure to relate these new scaling exponents to global quantities and discuss implications for $f(\alpha)$. The importance of the oscillations in physical systems is discussed in Chapter 4, where their implications for fractal models of turbulence and experimental observations are shown.

Section 3.1 : The Local Correlation Integral

In this section we introduce the local correlation integral and relate it to the full correlation integral. Consider a distribution of points, perhaps fractal, in E^n, the Euclidean space of dimension n. Define the local correlation integral or Cantor function, $C_1(\mathbf{x},\ell)$, of the set of $\mathbf{X}$ as

$$C_1(\mathbf{x},\ell) = \frac{1}{N} \sum_{i=1}^{N} \Theta(\ell - |\mathbf{x}_i - \mathbf{x}|) \qquad (3.1)$$

where $\mathbf{x}$ is a vector in E^n, N is the number of points in the set, $\mathbf{x}_i$ is the position vector of the i^{th} point, and Θ is the Heavyside

function. In order to get a feel for the scaling properties of $C_1(\mathbf{x},\ell)$, we examine its behavior in several familiar geometries. In each case we assume that N is sufficiently large that there exists a range of scales between the inner and outer cutoff; it is in this range that the scaling behavior is observed. The discrete nature of the sets may be made explicit by including a density factor in the equations below; this is omitted in the interest of clarity. All lengths have been normalized by the outer cutoff. In the following cases the set is considered to lie in E^3.

If **X** consists of an isolated point located at **x**,

$$C_1(\mathbf{x},\ell) = 1 = \ell^0 . \qquad \mathbf{x} \in \mathbf{X}$$

Alternatively in the case **X** is a line

$$C_1(\mathbf{x},\ell) = 2\ \ell^1 \qquad \mathbf{x} \in \mathbf{X};$$

when **X** is a plane

$$C_1(\mathbf{x},\ell) = \pi\ell^2 \qquad \mathbf{x} \in \mathbf{X};$$

and when **X** is the full 3-dimensional space

$$C_1(\mathbf{x},\ell) = \frac{4}{3}\ \pi\ell^3 \qquad \mathbf{x} \in \mathbf{X}.$$

In each case

$$C_1(\mathbf{x},\ell) = A\ \ell^{\mu} \tag{3.2}$$

where μ is equal to the topological dimension of the object. In these nonlacunar, Euclidean examples, the various definitions of dimension given in Chapter 1 correspond to the same numerical value and A is a constant. Note that, in general, μ is not equal to d_1.

Now consider $C_1(\mathbf{x},\ell)$ for sets of fractional Hausdorff dimension.

First, the 101 Cantor set: Figure 3.1a shows $C_1(\mathbf{x},\ell)$ for a 2^{10} point approximation of the 101 set about $\mathbf{x} = 0$. This is a classic devil's staircase (a curve of zero derivative everywhere except at points corresponding to members of the Cantor set itself). As ℓ approaches zero, $C_1(0,\ell) \sim \ell^d$ where $d = \log 2/\log 3$ is equal to the Hausdorff dimension of the underlying set. Figure 3.2 shows log-log plots of the local correlation integral for (a) the 101 Cantor set about $\mathbf{x} = 0$, (b) the $\log(4)/\log(3)$ Koch curve (see Mandelbrot, 1977, Chapter 2) about $\mathbf{x} = (\sin(\pi/3)/3,0)$, and (c) for the Hénon attractor about its unstable fixed point $\mathbf{x}_{us}$. The topological dimension of the Cantor set is zero, while that of the Koch curve is one; the topological dimension of the Hénon attractor appears to be one, but no proof of this is available (Farmer, 1982). In each case μ exceeds the topological dimension of the set, implying that the sets are fractal over the range of scales considered.

In Figure 3.3 the local correlation integral of the 101 Cantor set is plotted for several values of $\mathbf{x}$. The vertical offset of each base point is proportional to its distance from the origin. For these choices (see below), the scaling of $C_1(\mathbf{x},\ell)$ at small ℓ is independent of $\mathbf{x}$. Observation at macroscopic scales and the presence of the finite inner cutoff will introduce a dependence on the particular choice of $\mathbf{x}$. Both the strength and weakness of the local correlation integral lies in this $\mathbf{x}$ dependence; when evaluated at a "dynamically" interesting point, $C_1(\mathbf{x},\ell)$ yields important information unavailable in the correlation integral $C_2(\ell)$ (defined below). The lack of dependence of μ on $\mathbf{x}$ for approximations to the 101 set is due to the

uniformity of this set; for certain elements of a homogeneous fractal there exists an effective outer cutoff inside which $\mu = d_0$. For the 101 set this cutoff, when it exists, is the largest power of 1/3 which evenly divides $|x|$. If the set is approximated using the decimation procedure of §2.3, a point which is first recorded in the N^{th} generation scales with $\mu=d_0$ for all $(\ell < (1/3)^N)$. For members of the set whose symbolic representation does not terminate in a repeated symbol, no such bound exists. Simply put, if a point is an end point of a reduced image of the full set, it will scale like x=0 for sufficiently small ℓ.

To relate the Cantor function, $C_1(x,\ell)$, to the correlation integral, $C_2(\ell)$, recall the definition of the correlation integral (Equation 2.5) for a set of N points embedded in E^N.

$$C_2(\ell) = \frac{1}{N^2} \sum_{i=1}^{N} \sum_{j=1}^{N} \theta(\ell - x_{ij}) \tag{3.3}$$

where

$$x_{ij} = |x_i - x_j|$$

is the separation of the i^{th} and j^{th} points. $C_2(\ell)$ is simply the integral of $C_1(x,\ell)$ taken over all members of the set. That is,

$$C_2(\ell) = \frac{1}{N} \int C_1(x_i,\ell) \ \delta^n(x - x_i)\, dx \tag{3.4}$$

where the x_i are the elements of the set and δ^n is the n dimensional Dirac delta function. A summation of the repeated index is implied. For sets whose topological dimension is zero, the integral of equation 3.4 reduces to a sum over the elements of the set.

As noted in Chapter 2, the double sum in Equation 3.3 makes computation of the correlation integral difficult for large N. This difficulty is alleviated in the computation of the Cantor function. Evaluating $C_1(\mathbf{x},\ell)$ differs fundamentally from restricting the summation over i in $C_2(\ell)$ to a small number of randomly selected points in that $C_1(\mathbf{x},\ell)$ is evaluated at specific, dynamically significant points.

Section 3.2: Intrinsic Oscillations in Statistics on Fractal Sets

The self-similar nature of fractals implies the presence of log periodic oscillations about the mean scaling behavior of the local correlation integral. These oscillations may be observed in Figures 3.2. Computing the linear least squares fit of log $C_1(\mathbf{x},\ell)$ as a function of log ℓ for the 101 Cantor set data of Figure 3.2a yields a slope:

$$\mu = 0.630931 \quad \text{for} \quad \frac{1}{2}\left(\frac{1}{3}\right)^6 < \ell < \frac{1}{2} \quad .$$

A regular oscillation, periodic in log ℓ, is apparent in the graph of the deviation from the linear trend in each of the examples in Figure 3.2. The oscillation in the scaling of log $C_1(\mathbf{x}_{us},\ell)$ for the Hénon attractor is considered in Section 3.4.

Such oscillatory corrections have been anticipated and observed by other authors. The earliest reference of which we are aware was by De Bruijn (1948), who discusses log-periodic oscillations in the context of a number theoretic partition problem. An oscillatory

factor of this type was noted by E.A. Novikov (in a footnote of Novikov, 1966) in his model of turbulence. It was this model that laid the foundation for future self-similar mathematical models of turbulence, in which the implication of an oscillatory term was lost. In the late 1960's, de Vaucouleurs (1970, 1971) postulated an oscillatory correction to the "clumpyness" of the mass distribution in the universe. These two topics are treated more fully in Chapter 4. Badii and Politi (1985) found the oscillations in their analysis of the Zaslavski attractor using a method based on mean nearest neighbor distances. They surmised the oscillations were intrinsic to fractal sets.

An oscillatory term is to be expected from the general solution to the scaling equation (Smith, Fournier, and Spiegel, 1986). It may be used to advantage when determining scaling parameters and ignored only at the peril of the investigator.

Consider a statistical moment $C(\ell)$ on the set **X** where C depends on a separation scale ℓ. As our notation indicates, both C_1 and C_2 are examples. A self-similar fractal set may be expected to satisfy the scaling law

$$C(\ell) = \frac{1}{\rho} \; C(\sigma\ell) \tag{3.4}$$

for some ρ and σ. The usual power law

$$C(\ell) = A \; \ell^{d}, \tag{3.5}$$

where

$$d = \frac{\log \rho}{\log \sigma} \tag{3.6}$$

and A is a constant is only a particular solution of Equation 3.4.

The general solution is

$$C(\ell) = \chi\left(\frac{\log \ell}{\log \sigma}\right) \ell^{d} \tag{3.7}$$

where χ is a periodic function of period one. The general solution shows the possibility of oscillations observed in the scaling of strictly self-similar sets and in many numerical experiments. Identifying $1/\sigma$ with the similarity ratio, we find agreement of the periodicity with the textbook examples.

In strictly self-similar fractals the presence of oscillations is assured. In more general fractals, scaling is expected only in an asymptotic sense. The observed oscillations are first corrections to the $d_0 \log \ell$ term in the series for $C(\ell)$; that is, as ℓ approaches zero, we have

$$\log C(\ell) = d_0 \log \ell + \psi(\log \ell/\log \sigma) + \ldots \tag{3.8}$$

where ψ is a periodic function of period one. In inhomogeneous fractals the double average in the correlation integral may tend to wash out the oscillations at large scales if the lacunarity is not uniform over the set. For instance, at $\ell \approx 1$ (standard units) in the Hénon attractor, $C_2(\ell)$ is not dominated by the frequently shown Cantorial sections, but by the more heavily weighted gossamer (linear) portions; the amplitude of ψ is small. A deviation from a smooth power law relationship between the number of grid boxes that contain a portion of the attractor and the box size at small scales

has been observed by Cawley and York (1986, preprint), who point to the need for good error determination. Following their suggestion, we will indicate the range of ℓ considered when an exponent is determined by a linear least square fit of $\log C(\ell)$ on $\log \ell$.

In the limit of small ℓ, $C_2(\ell)$ should be governed by the oscillation of the most frequently visited region of the attractor. One advantage of examining $C_1(\mathbf{x},\ell)$ is that the fine structure of a region is immediately available without the interference of other portions of the attractor. For strictly self-similar, homogeneous fractals such as the Cantor sets above, the phase of the oscillation is locked in place by the stringent requirements of homogeneity. In those instances, the oscillation is easily accessible in both $C_2(\ell)$ and $C_1(\mathbf{x},\ell)$.

In addition to providing a new handle on the physics of a problem, the presence of an oscillation holds practical consequences in calculating scaling exponents. These are most strongly expressed when the amplitude of the oscillation is large and its period is long compared to the available data. At such times the oscillation introduces a strong bias into the measurement; a good example is found in the Zaslavsky attractor (Zaslavsky, 1978; see also Badii and Politi, 1985 and Grassberger and Procaccia, 1983b). It is not possible to determine the exponent of a data set via standard techniques unless the range of available data is greater than the period of the oscillation. When the range is less than a period, the exponent may appear to be "scale dependent"; such an insufficiently resolved fractal set may be confused with a multi-fractal set (see

Section 4.4).

Section 3.3: Oscillatory Component of Scaling in Inhomogeneous Fractals

In the next two sections we determine μ for two inhomogeneous fractal sets. While we shall use the Feigenbaum set and the Hénon attractor as examples, the method should be useful in the analysis of many fractal sets and attractors in general, and in the analysis of some experimental results. In the latter, its usefulness will vary with the quality of the reconstruction. At present, most attractors which are reconstructed from experimental time series are formed using a delay time related to the first zero of the autocorrelation function. When this method is used to determine the delay time, the reconstruction process tends to squash the folded portions of the attractor. As Fraser and Swinney (1986) have pointed out, the autocorrelation reflects the linear dependence of the data, while the mutual information measures the general dependence. (See Fraser and Swinney, 1986 for definitions and an application to experimental data.) Their alternative method of choosing a delay time by minimizing the mutual information yields a reconstruction with a much more self-similar appearance. We conjecture that an improved reconstruction will expose the presence of the oscillation in many physical systems. Judging from Figure 1 of Fraser and Swinney (1986), the oscillation may already be visible in the data from the Belousov-Zhabotinskii reaction.

Our first example is generated by the logistic map

$$x_{i+1} = 4\lambda\, x_i\, (1-x_i). \tag{3.9}$$

There are many introductions to this mapping, due to its widespread application. See, for instance, May (1986), Feigenbaum (1980), and Cvitanović (1983). A general treatment of maps on the unit interval is given by Collet and Eckmann (1980). The familiar bifurcation tree for this map is shown in Figure 3.4. This plot is constructed by iterating the map 2^{10} times starting from $x_0 = \frac{1}{2}$ for each of 800 values of λ on the interval $0.625 \leq \lambda \leq 1.0$. Treating the first 2^8 values of x as transient, we plot the remaining points. The map shows "attracting" orbits of varying period with λ. The values at which the orbital period doubles from 2^n to 2^{n+1} are related geometrically by

$$\delta_F = \lim_{n\to\infty} \frac{\lambda_{n-1} - \lambda_n}{\lambda_n - \lambda_{n+1}} \approx 4.6692016 \tag{3.10}$$

while ratio of successive branch splittings (see Figure 3.4) at λ_n and λ_{n+1} scale as

$$\alpha_F = \lim_{n\to\infty} \frac{\epsilon_n}{\epsilon_{n+1}} \approx 2.502907875 \ . \tag{3.11}$$

The infinite period orbit at $\lambda = \lambda_\infty \approx 0.837005134$ which contains the point $x = \frac{1}{2}$ is known as the Feigenbaum set. Interest in this set comes, in part, from the many observations of period doubling in nature; Cvitanović (1983, Table 9.1) tabulates the values of α_F and

δ_F obtained from experimental observations of ten systems. Libchaber *et al.* (1986) have measured $f(\alpha)$ for the equivalent set reconstructed from a convection experiment and found close agreement with that of the logistic map.

The Hausdorff dimension of the Feigenbaum set has been calculated by Grassberger (1982) as

$$d_{HB} = 0.5381 \pm 0.0006 \quad .$$

Hentschel and Procaccia (1983) calculate the generalized dimensions

$$d_0 = 0.537 \qquad d_1 = 0.518 \qquad d_2 = 0.501 \quad ,$$

while Grassberger and Procaccia (1983) report

$$\nu = d_2 = 0.500 \pm 0.005 \quad .$$

Our calculation of $C_2(\ell)$ for a 2^{13} point approximation of the Feigenbaum set yields a linear least squares fit of $\log C_2(\ell)$ to $\log(\ell)$ with slope

$$\nu = 0.496 \qquad \text{for } 10^{-3} < \ell < 10^{-3}\,\alpha^6 .$$

Structure in the departure from linear scaling is shown in Figure 3.5a where we plot $(\log C_2(\ell) - \nu \log \ell)$ as a function of $\log \ell$. The first 8 iterations are shown in Figure 3.5b. Since the pattern of future iterates is known, Halsey et al. (1986) compute

$$d_{+\infty} = \frac{\log 2}{\log \alpha_F^2} \approx 0.37775$$

and (3.12)

$$d_{-\infty} = \frac{\log 2}{\log \alpha_F} \approx 0.75551 \quad .$$

In obtaining the results below, we analyzed a 2^{19} point approximation of the set. $C_1(\frac{1}{2},\ell)$ is shown in Figure 3.6a. Here we see regular oscillation with a period approximately equal to α_F. Removing the mean slope over scales $(0.1/\alpha_F^6)$ to 0.1 yields the oscillation shown in Figure 3.6b, and a value

$$\mu(x_0) = 0.754. \quad ((.1/\alpha_F^6) < \ell < .1) \quad .$$

Since $x_0 = \frac{1}{2}$ is located in the least dense region of the set, we expect $\mu(x_0) = d_{-\infty}$. Next, we consider the densest region of the set which is located near the first iterate of x_0 under the map, $x=x_1$: $C_1(x_1,\ell)$ is shown in Figure 3.7; the oscillation here has period α^2. This is a result of the flipping of the set between adjacent factors of α_F; for an identical orientation of the set, two generations are required (see Feigenbaum, 1980).

The oscillatory component of $C_1(x_1,\ell)$ is shown in Figure 3.7b, where the linear component removed had slope

$$\mu(x_1) = 0.370 \quad ((.1/\alpha_F^6) < \ell < .1) \quad .$$

Similarly

$$\mu(x_2) = 0.380 \quad .$$

Here we note $\mu(x_1) \approx d_{+\infty}$, a reasonable correspondence in that x_1 is in the densest region of the set. Now consider x_i for $i > 2$, at scales

$$\ell_y \leq (1/\alpha)^a \tag{3.13}$$

where

$$a = [\tfrac{1}{2} \log(i) + 1].$$

Since x_i is located at an end point of the local image of the set, it will scale as either x_1 or x_2, both of which have $\mu \approx d_{+\infty}$. By understanding the manner in which these regions are coupled, and the crossover between the two, one should be able to calculate d_2 directly from $d_{\pm\infty}$.

Section 3.4: Observing the Oscillatory Component in a Strange Attractor

In this section we examine the local scaling structure of the Hénon attractor. Following a brief review of the mapping, the local correlation integral is evaluated about an unstable periodic point of the mapping. The periodicity of the ψ function is then used to determine a μ at this point.

The Hénon mapping represents the most general one-to-one quadratic mapping with constant Jacobian. The map is given by

$$\begin{aligned} x_{n+1} &= 1 - a\, x_n^2 + y_n \\ y_{n+1} &= b\, x_n \end{aligned} \tag{3.14}$$

and its Jacobian is:

$$J = \begin{vmatrix} \delta\ (x_{i+1},\ y_{i+1}) \\ \hline \delta\ \ (x_i,\ \ y_i) \end{vmatrix} \qquad = -b.$$

This system has been most thoroughly studied for the parameter values a=1.4 and b=0.3. For this parameter choice $|J| < 1$; thus, areas contract under the action of the map. There are no attracting fixed points, yet many initial conditions remain near the origin indefinitely; it is generally believed that the long-time evolution of these initial conditions is governed by a strange attractor. 2^{20} iterations of such an initial condition are shown in Figure 3.8a. The region centered on the unstable fixed point discussed below is shown in increasing detail in 3.8b-e. The large scale structure of the attractor is shown in Figure 1.10.

Once a mapping is chosen and the parameter values are set, it remains to pick a value of $\mathbf{x}$ about which to evaluate $C_1(\mathbf{x},\ell)$. A natural choice is a fixed point of the mapping. Fixed points satisfy

$$x^* = 1 - ax^{*2} + y^*,$$
$$y^* = bx^*$$

or

$$x^* = \frac{-(1-b) \pm \sqrt{(1-b)^2 + 4a}}{2a} ,$$

$$y^* = bx^* .$$

Let x_+ denote the fixed point whose location is given by the positive root and x_- the point corresponding to the negative. For our choice of parameters, both fixed points are real. The stability of a fixed point is determined by linearizing the map about that point and determining whether small displacements grow. For the Hénon map

$$\begin{pmatrix} \delta x^1 \\ \delta y^1 \end{pmatrix} = \begin{pmatrix} -2ax^* & 1 \\ b & 0 \end{pmatrix} \begin{pmatrix} \delta x^0 \\ \delta y^0 \end{pmatrix}$$

where δx^0 and δy^0 represent the initial deviation from (x^*, y^*) and a superscript 1 indicates the value of the variable after one iteration. Solving for the eigenvalues, we find

$$\lambda_1 = -ax^* + \sqrt{a^2x^{*2} + b} \qquad \hat{e}_1 = \begin{pmatrix} 1 \\ \frac{b}{\lambda_1} \end{pmatrix}$$

$$\lambda_2 = -ax^* - \sqrt{a^2x^{*2} + b} \qquad \hat{e}_2 = \begin{pmatrix} 1 \\ \frac{b}{\lambda_2} \end{pmatrix} .$$

Consider x_+ where

$x^* = 0.63135448...$

$y^* = 0.18940634...$.

We obtain

$$\lambda_1 = 0.15594632...$$

$$\lambda_2 = -1.92373886...$$

and

$$\hat{e}_1 = \begin{bmatrix} 1.0 \\ -\lambda_2 \end{bmatrix} \qquad \hat{e}_2 = \begin{bmatrix} 1.0 \\ -\lambda_1 \end{bmatrix}$$

where we have used the fact that

$$\lambda_1 \lambda_2 = -b.$$

Since $\lambda_2 < -1$, $\mathbf{x}_+$ is unstable and a point will alternately move from one side of $\mathbf{x}_+$ to the other, relative to $\hat{e}_2$. Almost all initial conditions near $\mathbf{x}_+$ will move away along $\hat{e}_2$ increasing their distance from $\mathbf{x}_+$ by a factor of $|\lambda_2|$ per iteration. At $\mathbf{x}_+$, the unstable manifold lies along $\hat{e}_2$. Since $|\lambda_1|$ is less than one, there exists a stable manifold which lies along $\hat{e}_1$. Points which fall exactly on the stable manifold approach $\mathbf{x}_+$ asymptotically. A similar analysis shows $\mathbf{x}_-$ is also unstable.

In Figure 3.9 we present the results of a calculation of $C_1(\mathbf{x},\ell)$ using a 2^{24} iteration run. The mean scaling behavior and oscillation are evident. The flattening of the curve at small ℓ indicates that there is insufficient data to describe the attractor at separations ℓ less than 10^{-4}. A least squares fit to the data over the range ($10^{-4} < \ell < 0.06$) provides an initial estimate $\mu = 1.319$. Removing this trend yields the first approximation of $\psi(\ell)$, which is shown in Figure 3.10. Inspecting the residual we suspect that μ has been

underestimated due to a bias from the small ℓ points. The error in μ is minimized by fitting an integer number of oscillations. In general, a function of the delayed difference, $f(\psi(\ell) - \psi(\ell-\mathbf{x}))$, may be used to obtain an estimate of the period; in this case, the period corresponds to the eigenvalue of the stable manifold of the fixed point. Once the linear features of the attractor are established by the dynamics (Figure 2.8a), one iteration of the map acting on this pattern will produce a similar pattern reduced by a factor of λ_1 and stretched longitudinally by a factor of λ_2.

Cawley and Yorke (1986 preprint) have pointed out that meaningful error estimates for dimension/exponent estimates are difficult to obtain. They show that the residual of the least squares fit is a poor indicator of the goodness of the estimate. We now see why this is true: the residual is a combined measure of the mean scaling and the magnitude of $\psi(\ell)$. Since the residual does not discriminate between the two, a set with a $\psi(\ell)$ function of large amplitude--such as the Zaslavsky attractor or the 100010101 Cantor set[2] -- will produce a "poor fit" when exact values of the scaling exponents are used. Worse still, if a small portion of the oscillation is

---

[2] In this Cantor set there are large bands of log ℓ in which no point pairs are separated by ℓ; these correspond to the "000" segments. In such a band the set scales as if it had dimension zero. Alternating regularly with these regions (in log ℓ) are "overpopulated" bands, so that the scaling over factors of the similarity ratio has exponent equal to the Hausdorff dimension. Similarly, the Zaslavski attractor resembles a collection of linear bars of finite width; it scales with exponents near 1 at the outer scales, near 2 when at scales comparable to the width of the bars, and then near 1 again when the structure of individual bars is observed. In this case, the structure at smaller scales has not yet been confirmed.

analyzed, this residual may be (arbitrarily) small, while the estimate of the scaling exponent is incorrect by a great deal. This is a fundamental difficulty in the determination of scaling exponents; for a reliable estimate to be made an indication of the of the structure of smaller scales is needed. Although not conclusive, an oscillatory component provides such evidence. The oscillations are robust, and their appearance is an indicator that the scaling region has been reached.

To obtain a qualified estimate of μ, we examine the fine structure of $C_1(\mathbf{x}_{us}, \ell)$. Instead of evaluating Equation 3.1 directly, we record the number of points whose separation from $\mathbf{x}_{us}$ is between ℓ_i and $\ell_i + \Delta\ell$ (similar to the method applied to the correlation integral in Chapter 2). A typical calculation uses 100,000 bins to record these separations. The Cantor function $C_1(\mathbf{x}, \ell_j)$ is calculated as the normalized sum over bins 0 to j.

We estimate μ from the statistics of $\hat{\mu}(\ell)$,

$$\hat{\mu}(\ell_j) = \frac{\log C_1(\mathbf{x}, s\ell_j) - \log C_1(\mathbf{x}, \ell_j)}{\log s} \qquad (3.15)$$

where s is the period of the oscillation. In practice, the value of ℓ_j is chosen aligned with the bins and the value of $C_1(\mathbf{x}, s\ell_j)$ is interpolated (on a logarithmic scale, the bin density is much greater at this separation). The calculation is repeated for a number of different ℓ_j's (typically several thousand) spanning one period of the oscillation. The error in μ is determined from the scatter of these estimates; $\hat{\mu}(\ell)$ for the Hénon case is shown in Figure 3.11,

along with the oscillation. Each tick mark on the vertical $\hat{\mu}$ scale corresponds to one standard deviation of the distribution. For the Hénon attractor about x_{us} we find

$$\mu = 1.347 \pm 0.003$$

where the uncertainty corresponds to one standard deviation of $\hat{\mu}$. It is evident from Figure 3.11 that the scatter is biased in sign and concentrated in the fine structure regions of the oscillation -- this is a direct result of the inner cutoff. $\hat{\mu}(\ell)$ shows a self-similar structure which may be taken into account. The bias of $\hat{\mu}(\ell)$ is even more pronounced in the Feigenbaum set (see Figure 3,11'). Here we have

$$\mu(x_0) = 0.75511 \pm 0.002 \quad .$$

If in place of the mean we consider the distribution of the first 10% of the data (in the flat region of $\hat{\mu}$), we have

$$\mu(x_0) = 0.75551 \pm 0.00001 \quad .$$

Returning to the Hénon case and interpreting Equation 3.6 with $d \rightarrow \mu$ and $\sigma \rightarrow \lambda$ yields an effective filling factor ρ of

$$\rho = 2^{\mu \log \lambda_1} \approx 0.082 \ .$$

This means we expect each blowup in Figure 3.8 to contain a twelve-fold increase in the number of points (corresponding to $1/\rho$). The observed ratios are $r_{ab} = 12.40$; $r_{bc} = 12.89$; and $r_{cd} = 12.22$ where the subscripts denote the two frames considered.

The Cantor function evaluated about an unstable period 2 point is shown in Figure 3.12. The periodic structure is evident. Similar structure has been observed about higher order periodic points.

How is μ related to the more popular scaling exponents? First, μ

provides a bound on $d_{-\infty}$. Specifically

$$d_{-\infty} \geq \max\ (\mu(x)) \ . \tag{3.16}$$

This inequality follows from the sensitivity of d_q to the distribution on the object. $d_{-\infty}$ reflects the scaling structure of the least dense singularities of the set; each value of μ reflects the properties of one (or more) members of the set, thus relation 3.16 follows.

If the singular spectrum is dependent on the periodic orbits, then the details of $f(\alpha)$ may vary when evaluated on different Poincaré sections. The number of intersections that a given unstable periodic orbit makes with a surface of section varies with the surface taken and since $f(\alpha)$ is sensitive to the distribution of singularities, details of $f(\alpha)$ for a given attractor may vary from section to section. It is shown in Chapter 4 that $f(\alpha)$ of a self-similar set may be altered by projection. This is true even in the case that the topological dimensions of the two Euclidean spaces (the original embedding space and the space into which the projection is made) are greater than the Hausdorff dimension of the set. If $f(\alpha)$ is to provide a useful characterization of a system it may be important that the full embedding space be used, or the section chosen with care.

Section 3.5: Conclusions

To conclude we recall the relation of $C_1(\mathbf{x},\ell)$ to $C_2(\ell)$. For a given set **X**, consisting of N points,

$$C_2(\ell) = \frac{1}{N} \sum_{i=1}^{N} C_1(\mathbf{x}_i, \ell) \qquad \mathbf{x}_i \in \mathbf{X} \qquad (3.17)$$

this implies

$$A(\ell)\ell^{\nu} \propto \sum_{i=1}^{N} \alpha_i(\ell)\, \ell^{\mu_i} \qquad (3.18)$$

The point is that, since the sum of power laws is not, in general, a power law, the α_i contain information about the scaling. If the global scaling at small ℓ is dominated by the set of unstable periodic points, the number of terms in the sum is reduced.

The relative strengths of the α_i cannot be fixed, otherwise $\nu = \max(\mu_i) \approx d_{-\infty}$ for ℓ sufficiently small. This requires that the dynamics renormalize the α_i as additional points are considered so that Equation 3.18 holds. We are currently studying the manner in which this balance is maintained.

FIGURE CAPTIONS

Figure	Caption
3.1	The Cantor function of the 101 set about x=0. Note the linear coordinate axes.
3.2	The Cantor functions on a log-log scale for the (a) 101 set at x=0, (b) $\frac{\log 4}{\log 3}$ Koch curve, and (c) Hénon attractor about the unstable fixed point $\mathbf{x}_{us}$.
3.3	$C_1(\mathbf{x},\ell)$ for the 101 set evaluated at several $\mathbf{x}$ values.
3.4	Bifurcation tree for logistic map.
3.5	An approximation of the Feigenbaum set generated by recording the first 2^{13} iterations of the point $x = \frac{1}{2}$ under the logistic map with $\lambda = \lambda_\infty$.
3.6	(a) $C_1(\frac{1}{2},\ell)$ for the approximation to the Feigenbaum set (see Figure 3.5) and (b) $\psi\ (x_0,\ell)$ for this set.
3.7	(a) $C_1(\mathbf{x}_1,\ell)$ for the approximation to the Feigenbaum set (see Figure 3.5) and(b) $\psi\ (x_1,\ell)$ for this set.
3.8	The structure of the Hénon attractor near x_{us}. Each panel is a close up of the preceding panel. Each panel is centered on the unstable fixed point and the scale of each panel is a factor of λ larger than the preceding.
3.9	The local correlation integral, $C_1(\mathbf{x}_{us},\ell)$, evaluated for a 2^{24} point approximation of the Hénon attractor.
3.10	The first approximation of $\psi(\mathbf{x}_{us},\ell)$ determined by removing the linear trend computed from $C_1(\mathbf{x}_{us},\ell)$ first approximation.
3.11	(a) One cycle of $\psi(\mathbf{x}_{us},\ell)$ for the Hénon mapping. (b) The matching value of $\hat{\mu}(\ell)$, the ℓ axis is displaced from (a) by one cycle.

3.11′ (a) One cycle of $\psi(\mathbf{x}_0, \ell)$ for the Feigenbaum set
(b) The matching value of $\hat{\mu}(\ell)$, the ℓ axis is displaced from (a) by one cycle.

3.12 $C_1(\mathbf{x}_{\text{period } 2}, \ell)$ for the Hénon mapping

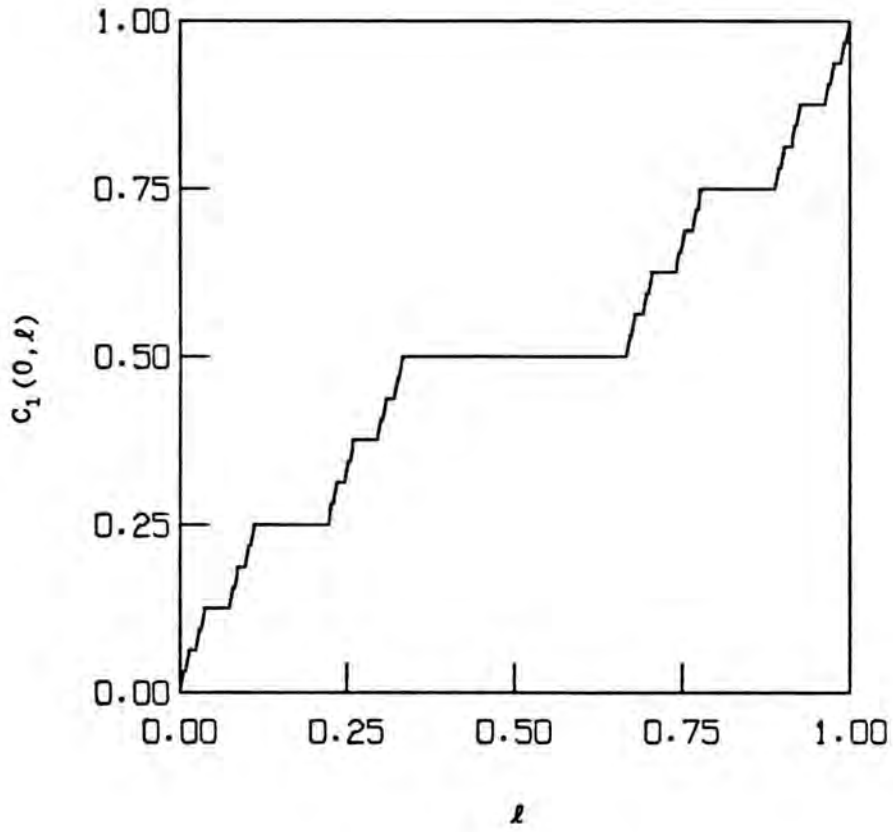

Figure 1

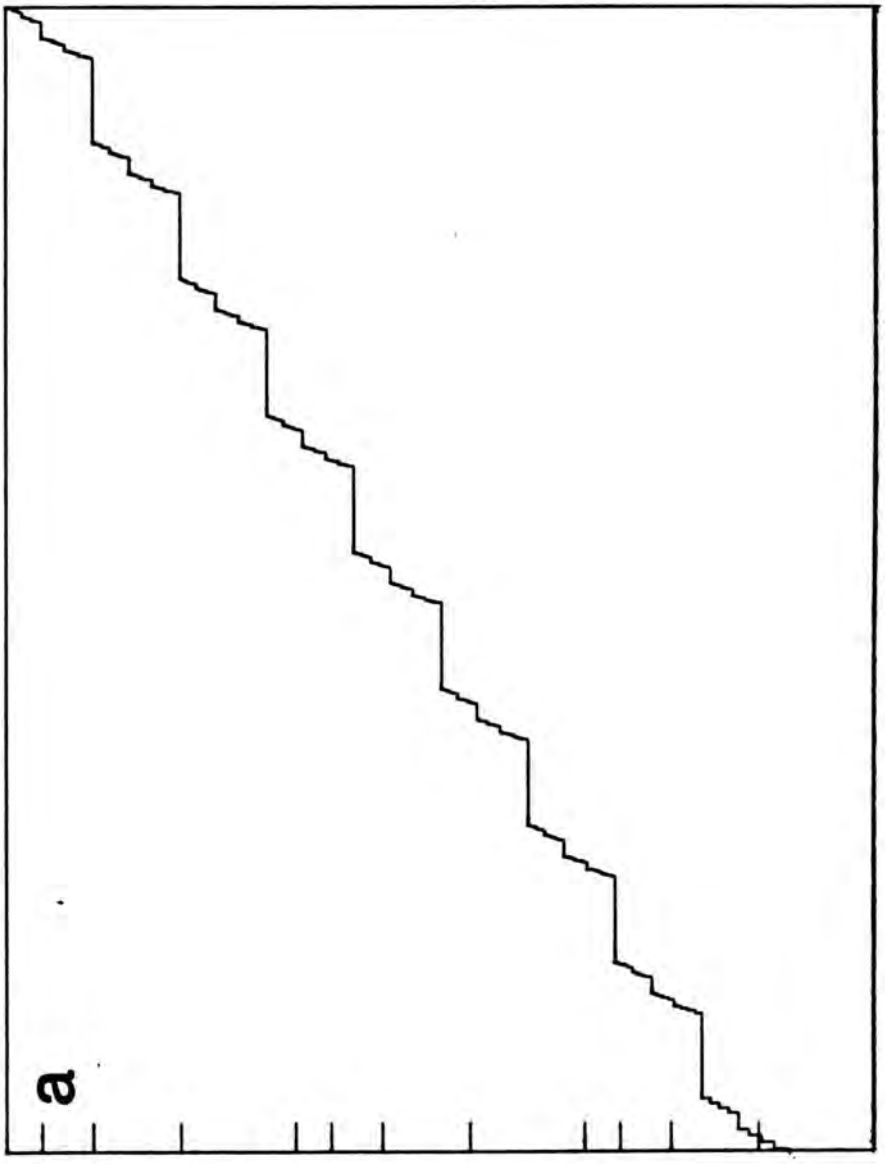

Figure 2

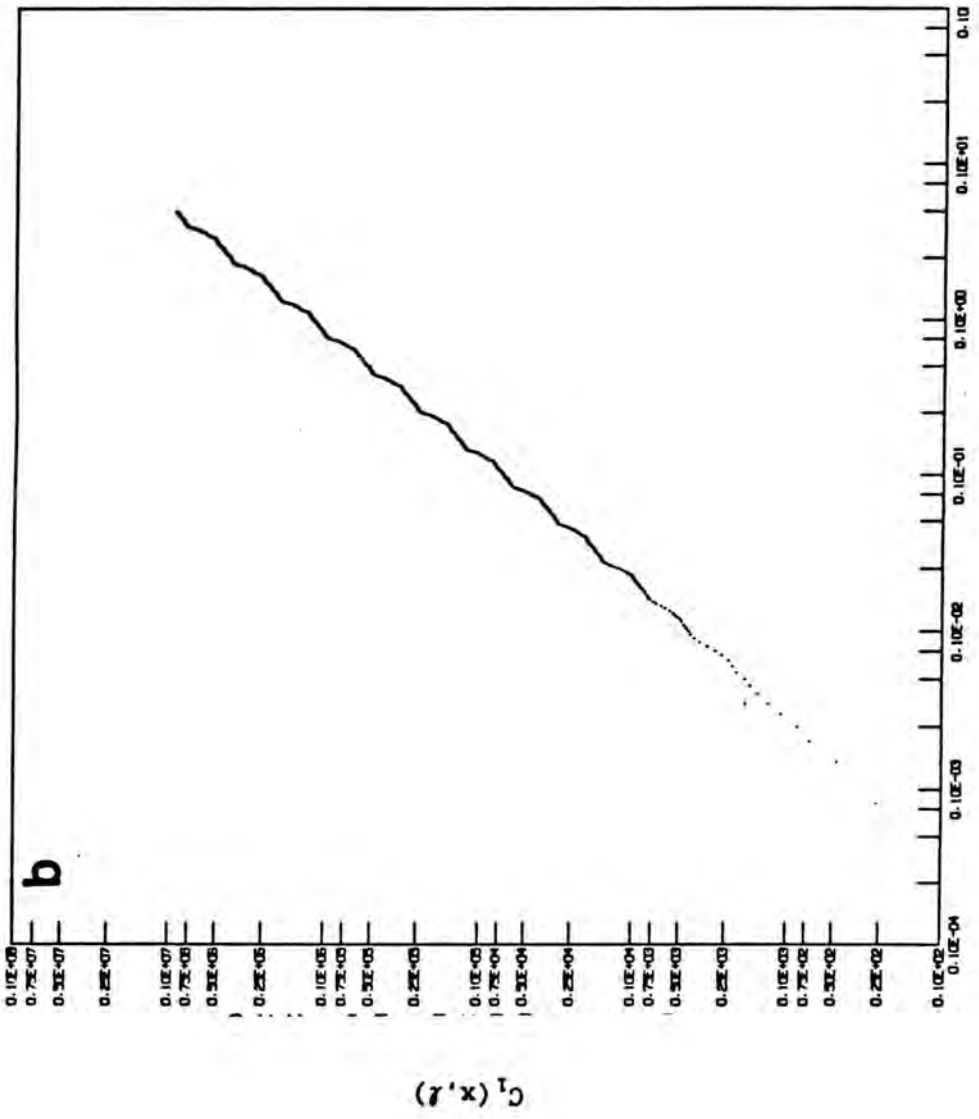

Figure 2

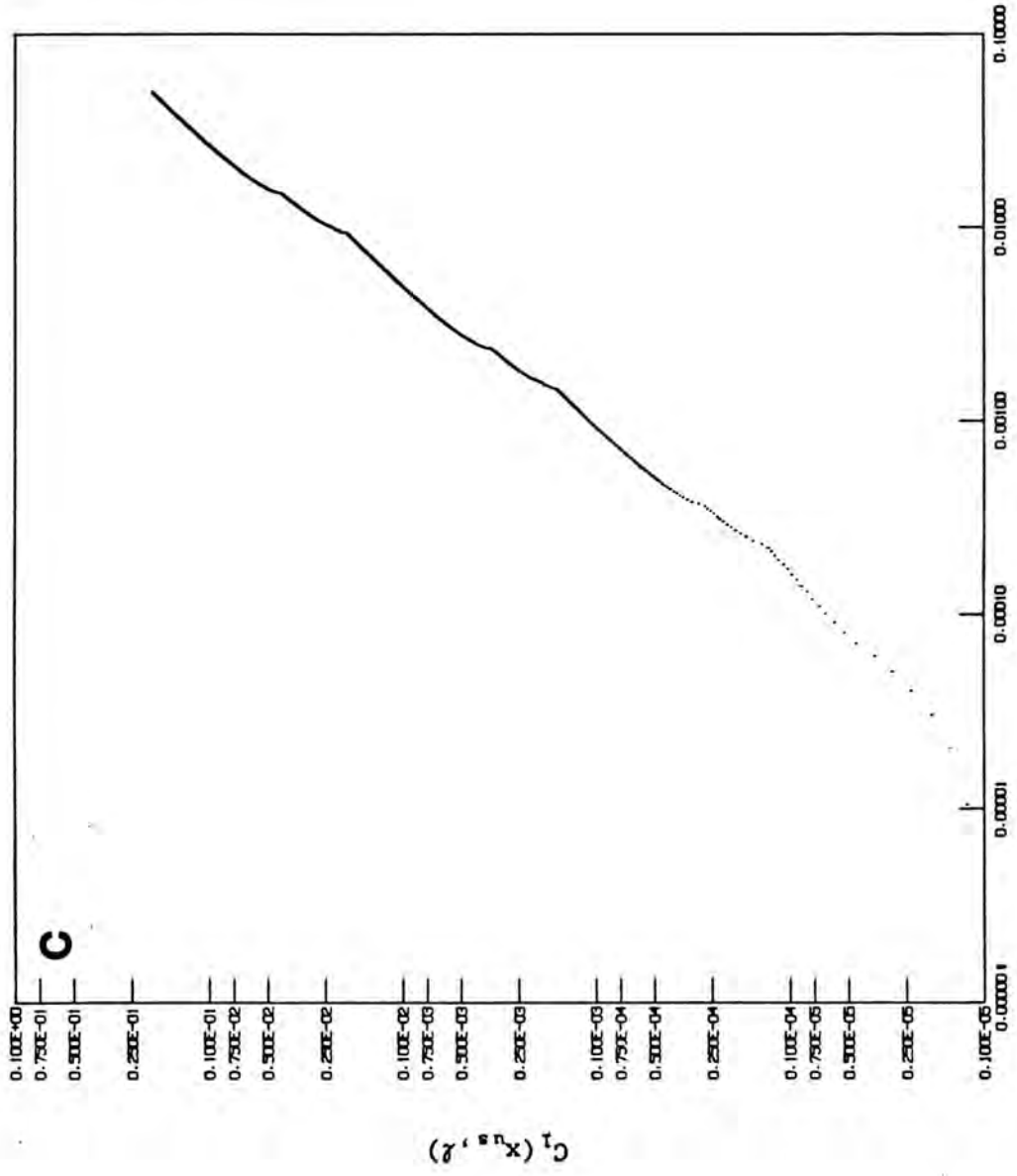
C
$C_1(x_{us}, \ell)$
ℓ
0.10E+00
0.75E-01
0.50E-01
0.25E-01
0.10E-01
0.75E-02
0.50E-02
0.25E-02
0.10E-02
0.75E-03
0.50E-03
0.25E-03
0.10E-03
0.75E-04
0.50E-04
0.25E-04
0.10E-04
0.75E-05
0.50E-05
0.25E-05
0.10E-05
0.00001
0.00010
0.00100
0.01000
0.10000

Figure 2

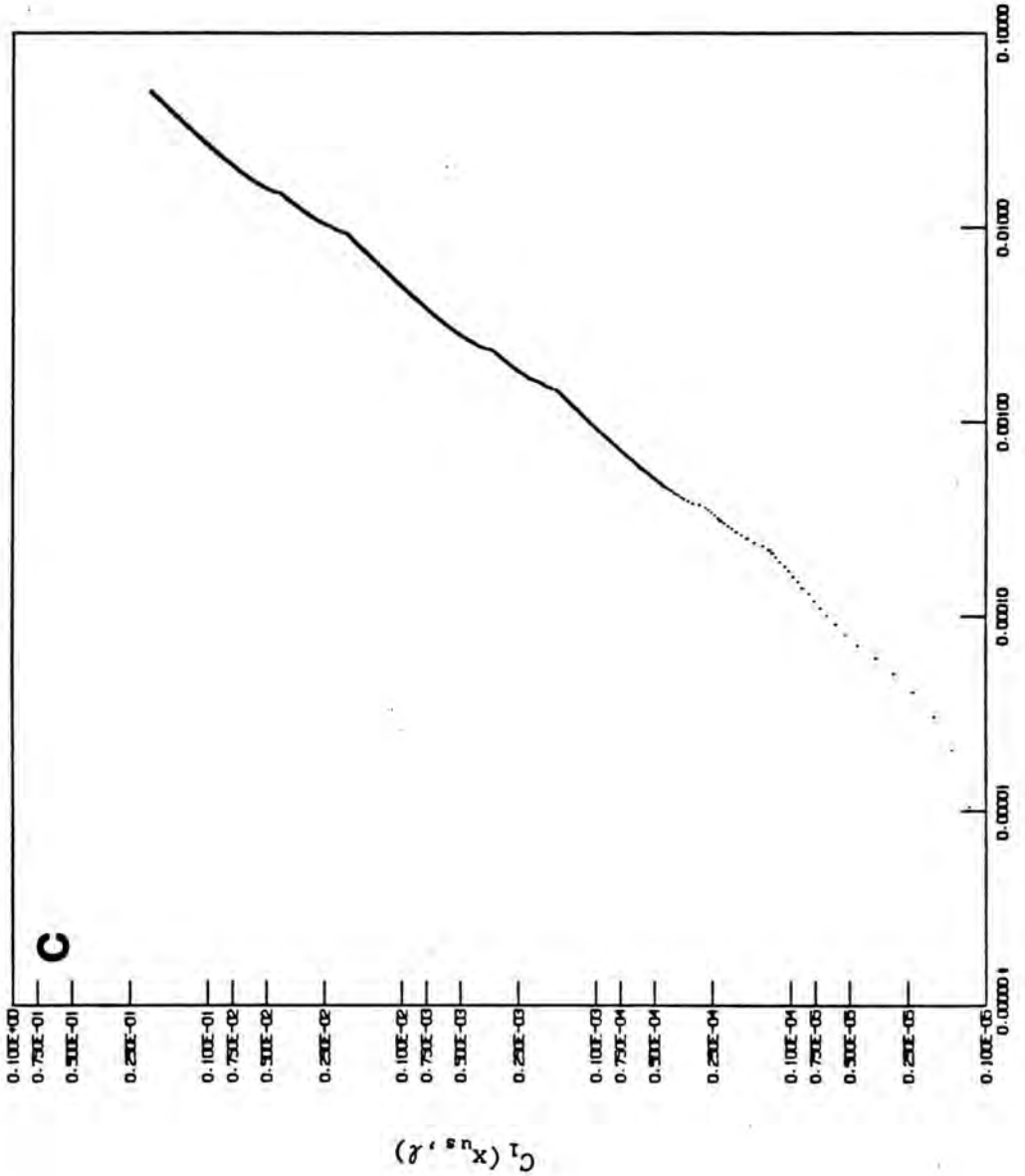
C
$C_1(x_{us}, \lambda)$
λ
0.10000
0.01000
0.00100
0.00010
0.00001
0.100E+00
0.750E-01
0.500E-01
0.250E-01
0.100E-01
0.750E-02
0.500E-02
0.250E-02
0.100E-02
0.750E-03
0.500E-03
0.250E-03
0.100E-03
0.750E-04
0.500E-04
0.250E-04
0.100E-04
0.750E-05
0.500E-05
0.250E-05
0.100E-05

Figure 2

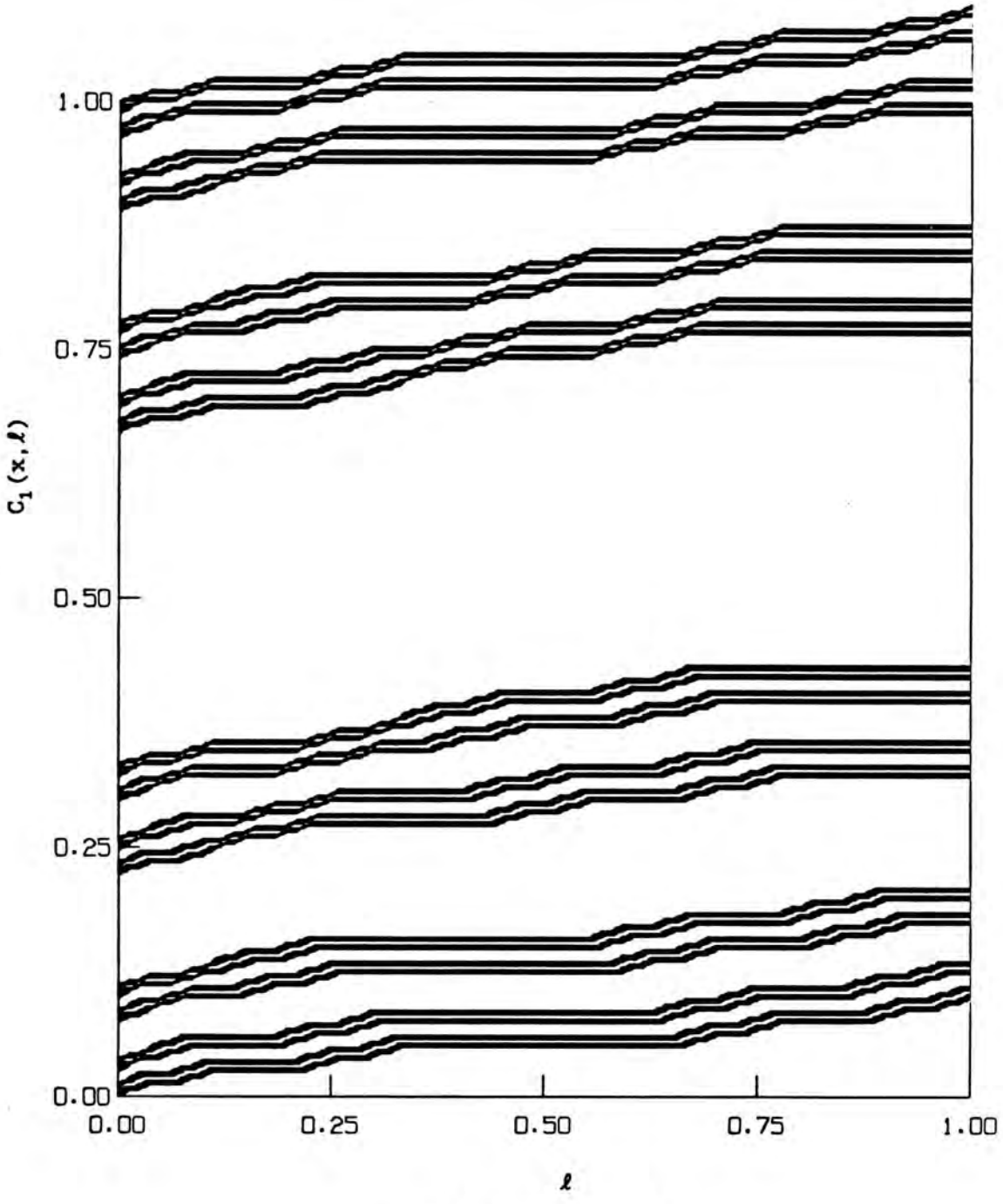

Figure 3

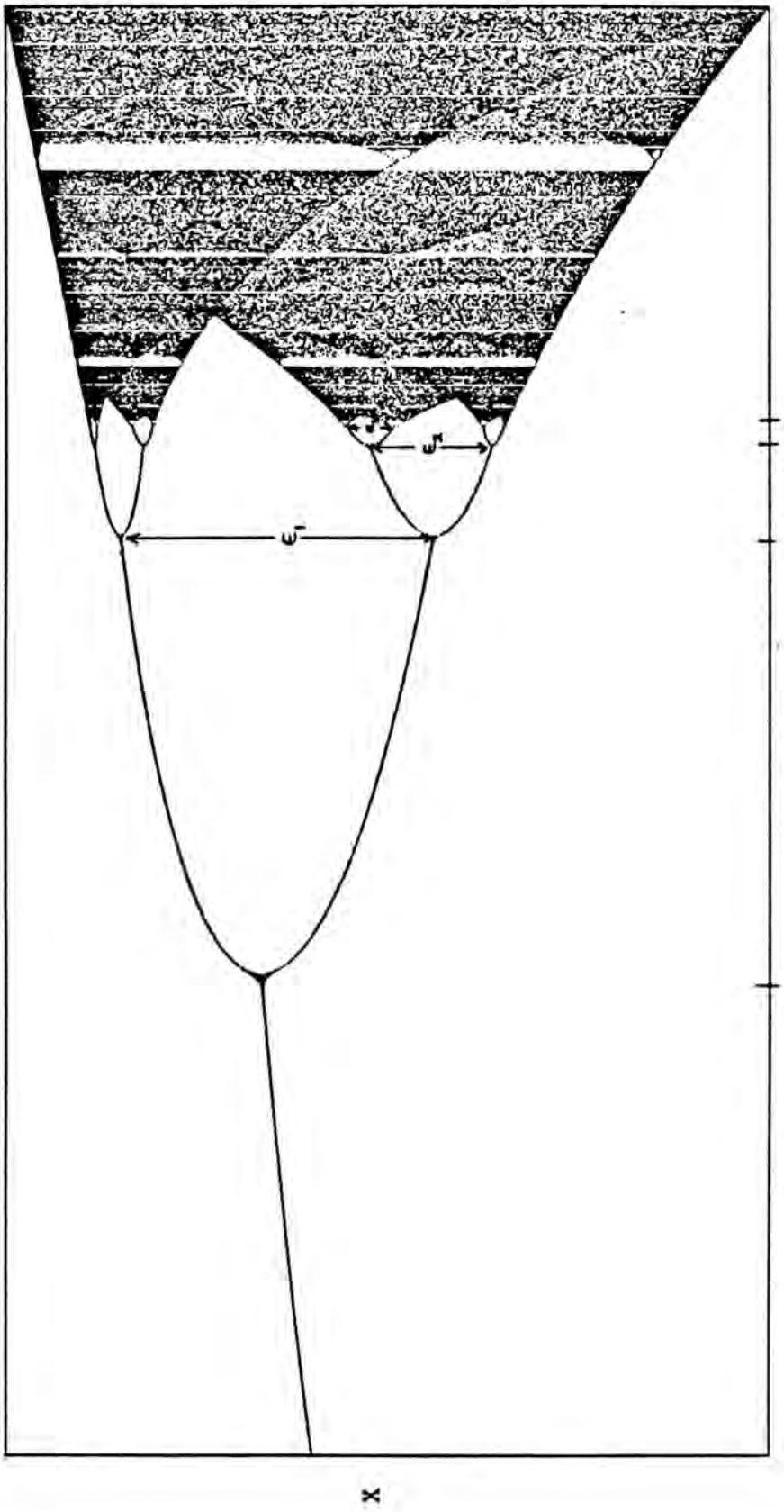

Figure 4

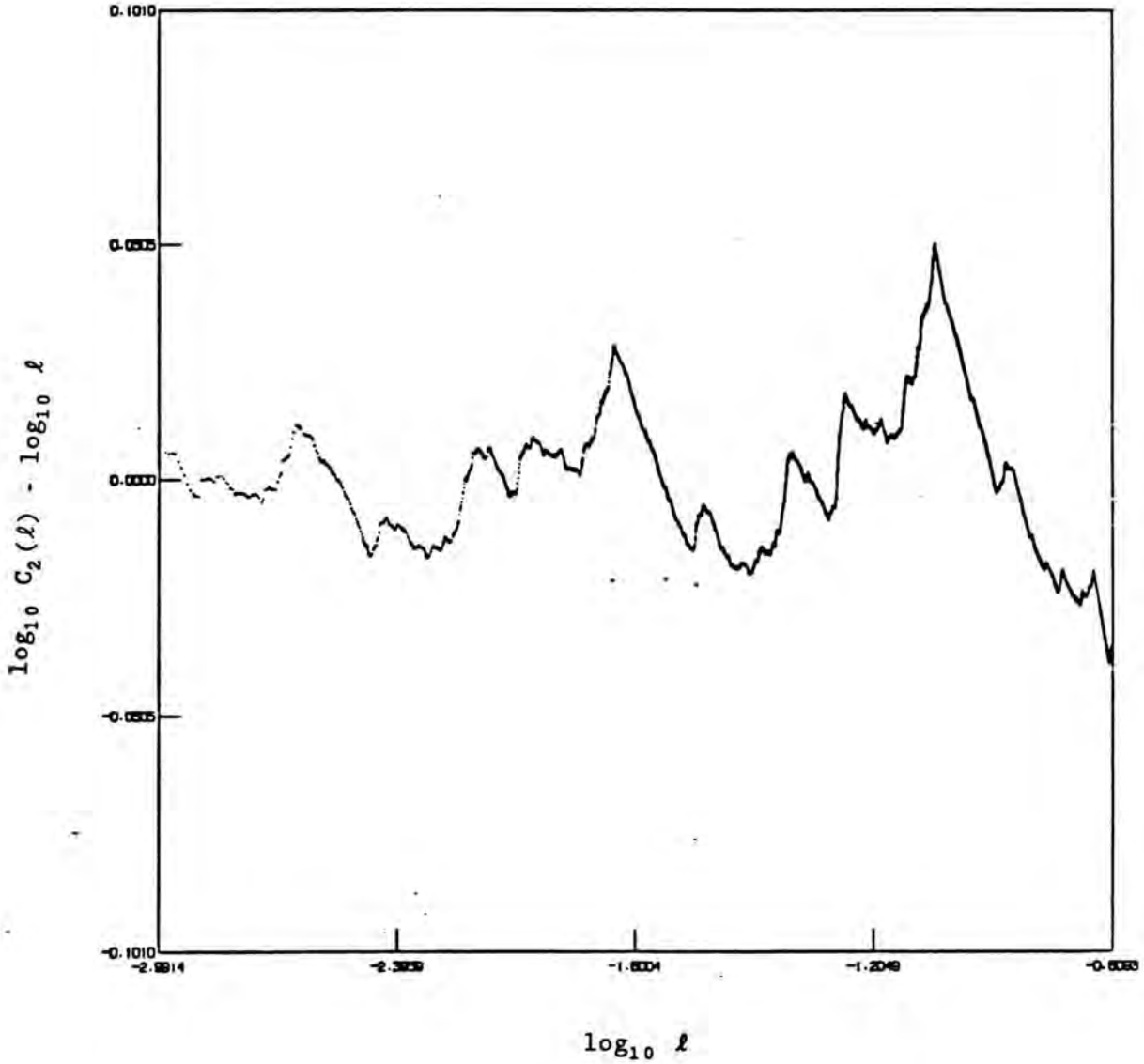
0.1010
0.0000
-0.1010
-2.9814
-2.3959
-1.8004
-1.2049
-0.6093
log10 C2(ℓ) - log10 ℓ
log10 ℓ

Figure 5 a

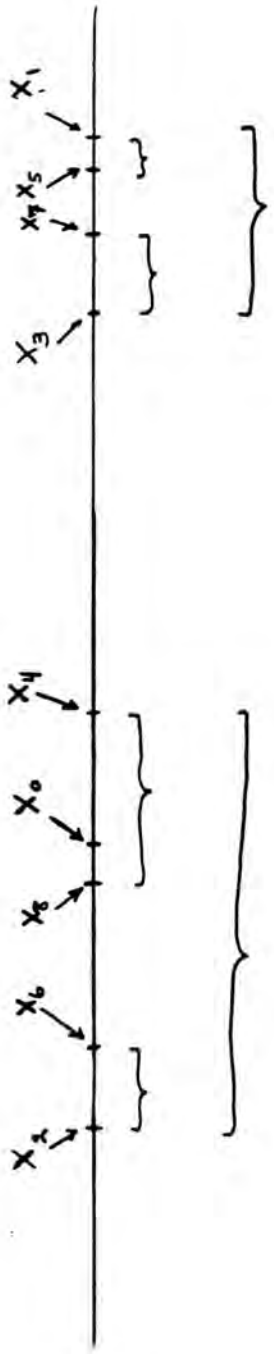

Figure 5 b

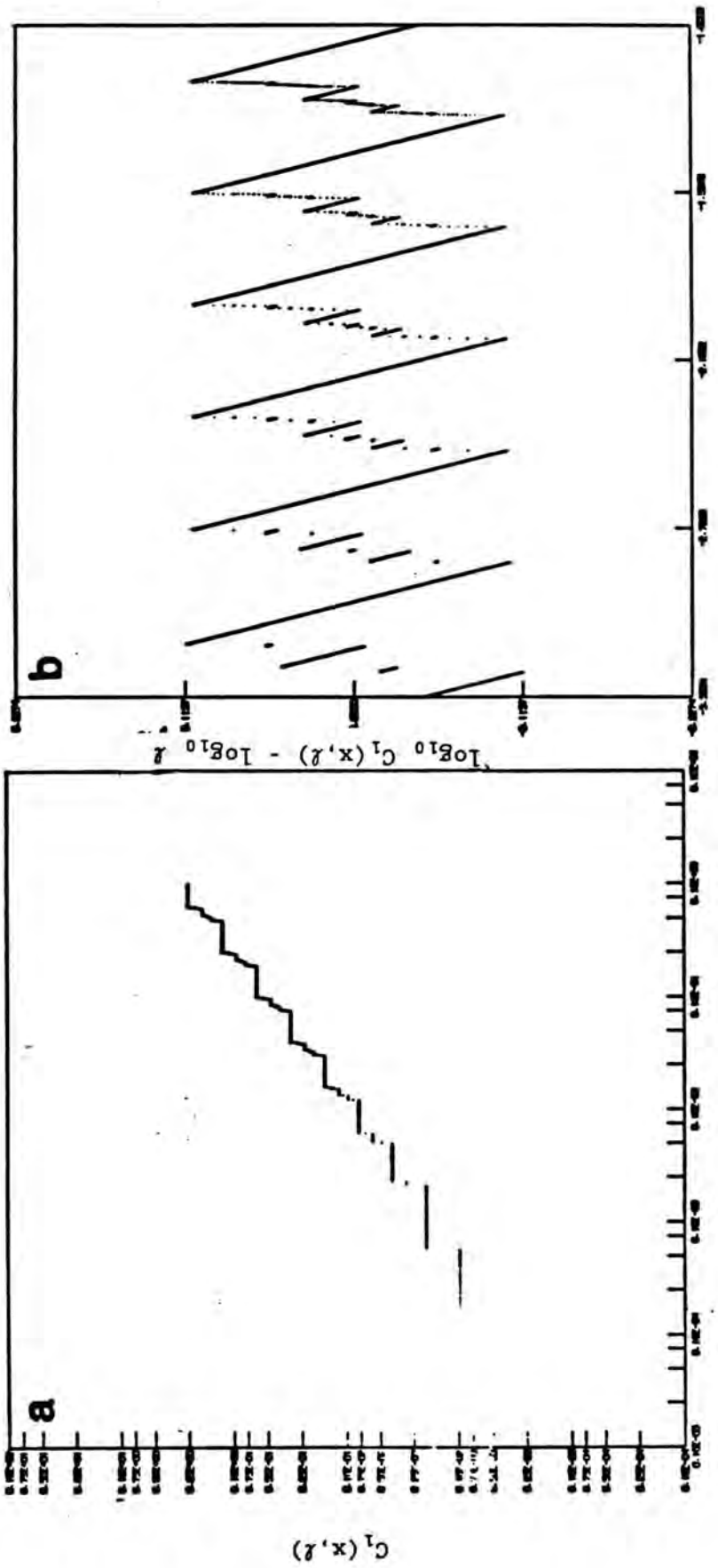
a
b
$C_1(x,\lambda)$
$\log_{10} C_1(x,\lambda) - \log_{10} \lambda$
$\log_{10} \lambda$
λ

Figure 6

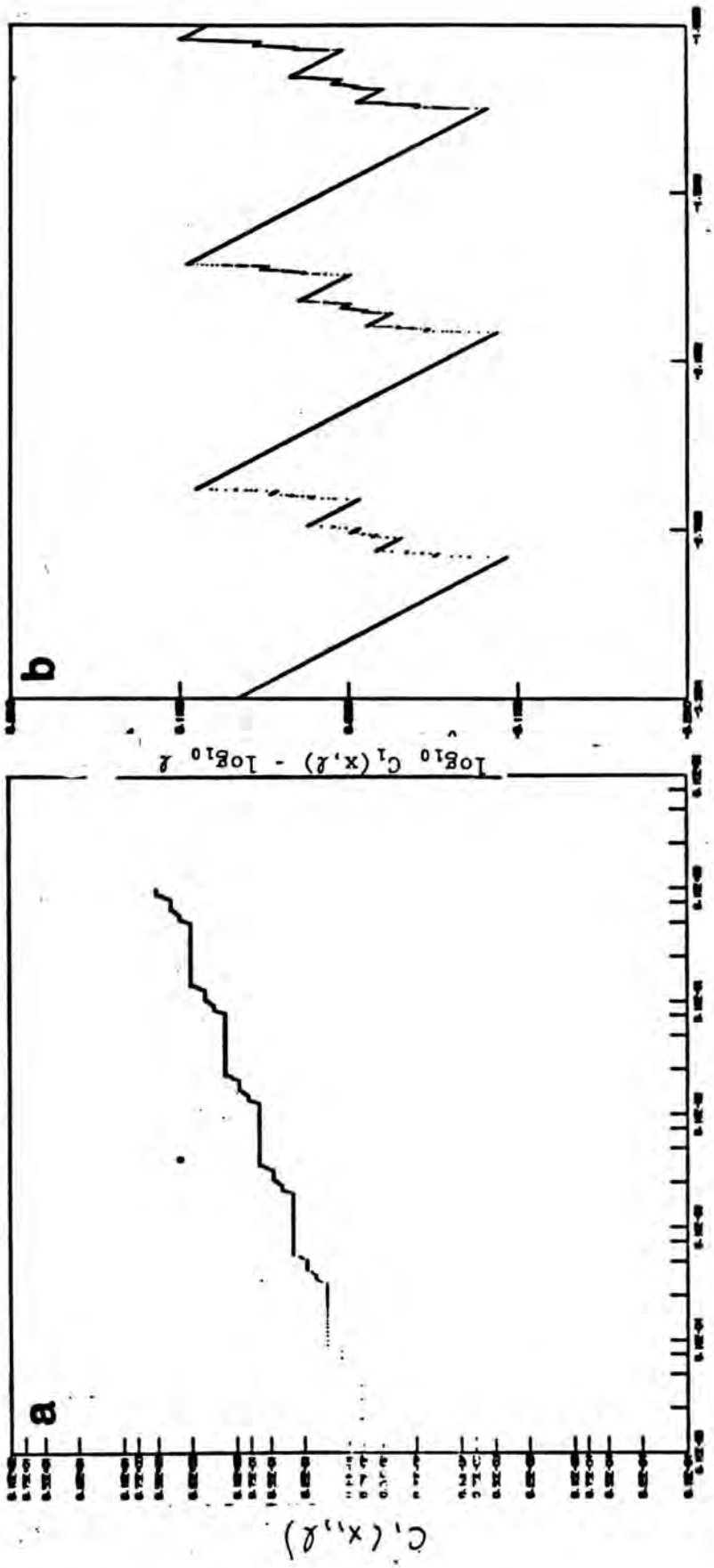

Figure 7

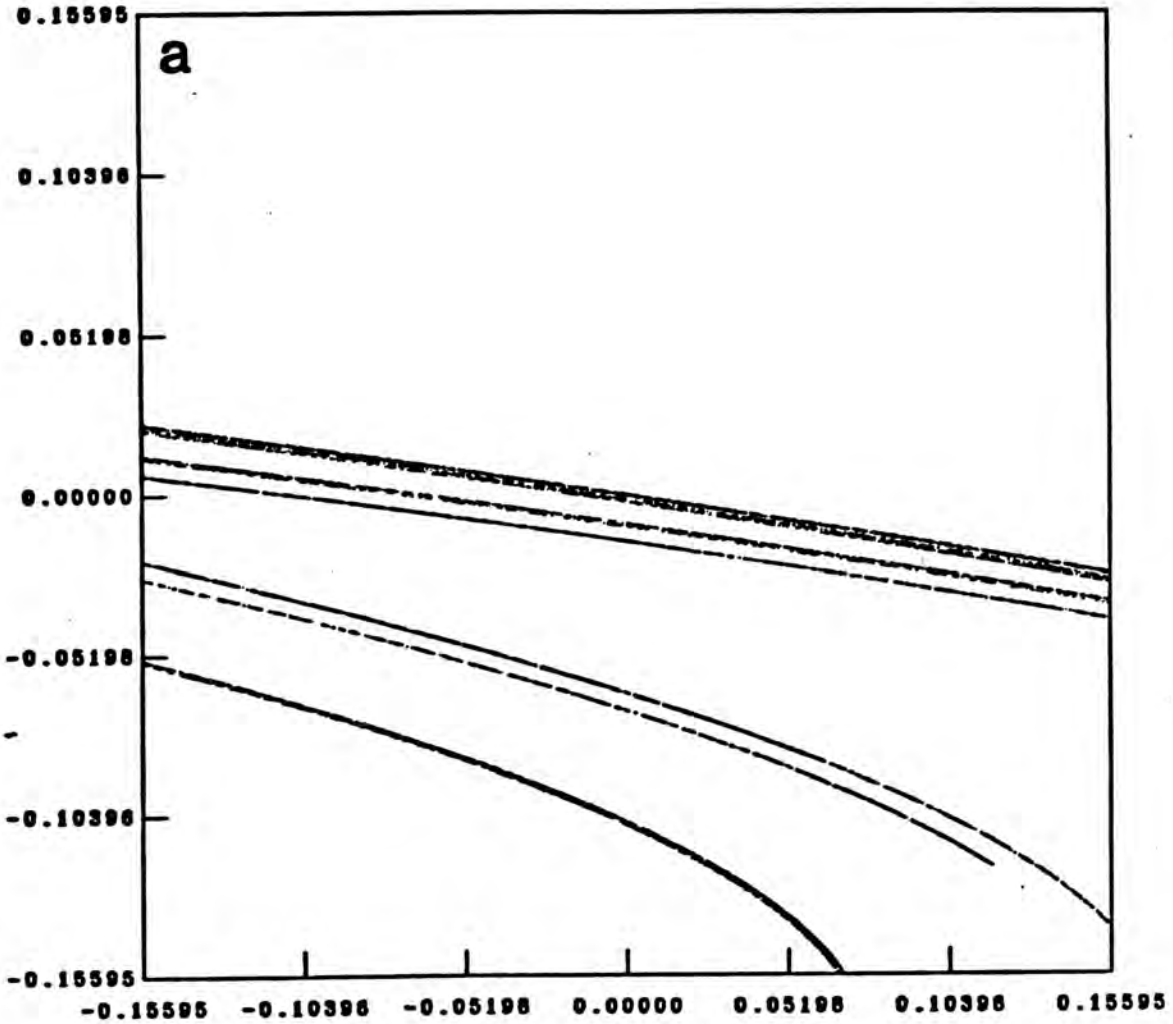
a
0.15595
0.10396
0.05198
0.00000
-0.05198
-0.10396
-0.15595
-0.15595
-0.10396
-0.05198
0.00000
0.05198
0.10396
0.15595

Figure 8

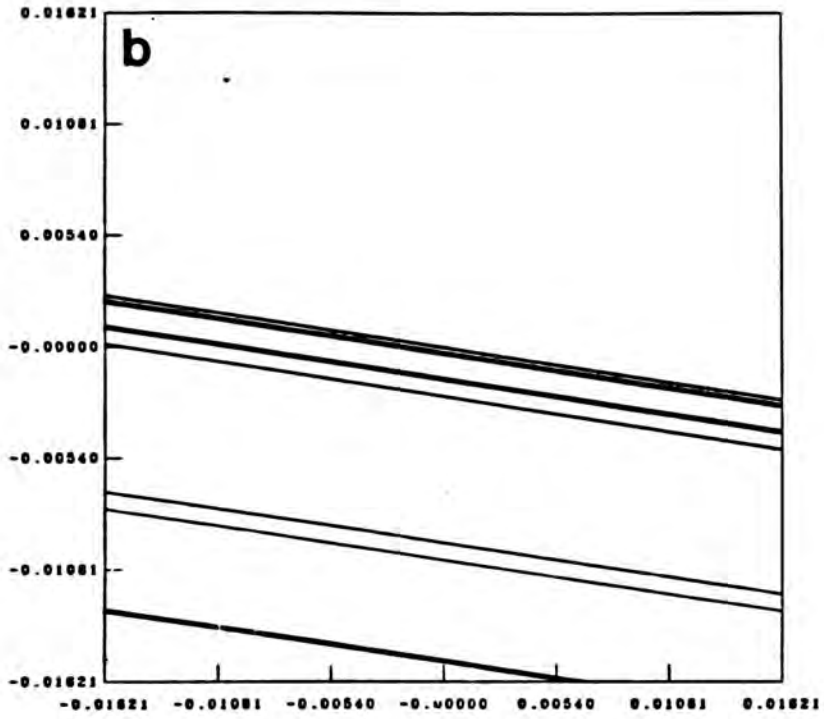
b
0.01621
0.01081
0.00540
-0.00000
-0.00540
-0.01081
-0.01621
-0.01621 -0.01081 -0.00540 -0.00000 0.00540 0.01081 0.01621

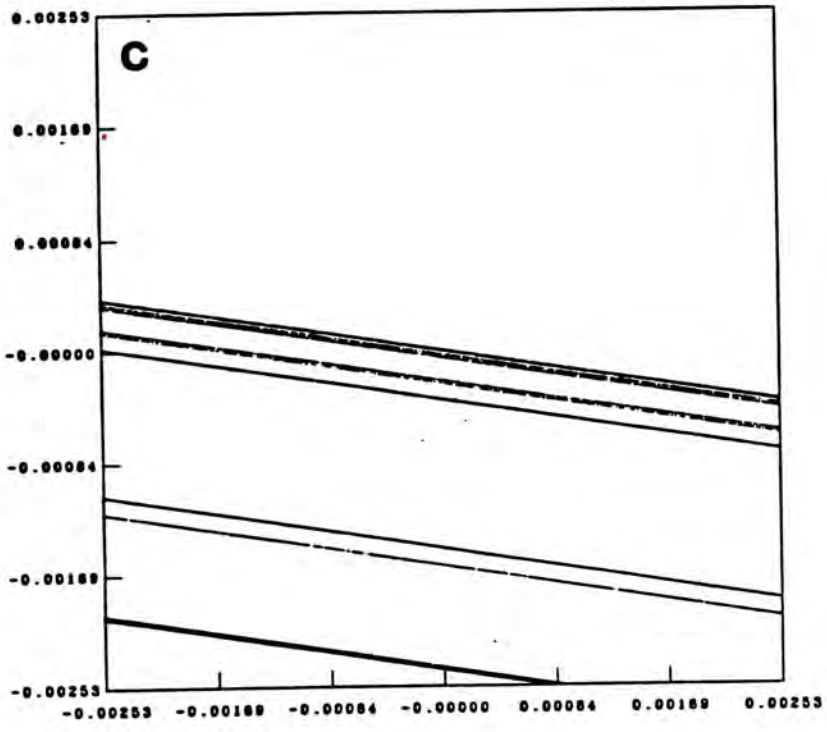
c
0.00253
0.00169
0.00084
-0.00000
-0.00084
-0.00169
-0.00253
-0.00253 -0.00169 -0.00084 -0.00000 0.00084 0.00169 0.00253

Figure 8

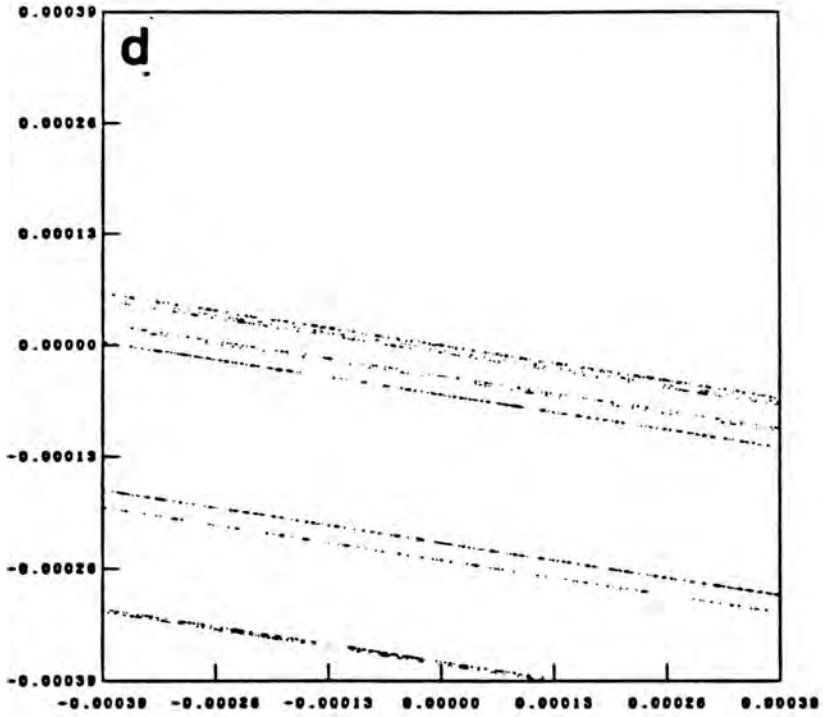
d
0.00039
0.00026
0.00013
0.00000
-0.00013
-0.00026
-0.00039
-0.00039 -0.00026 -0.00013 0.00000 0.00013 0.00026 0.00039

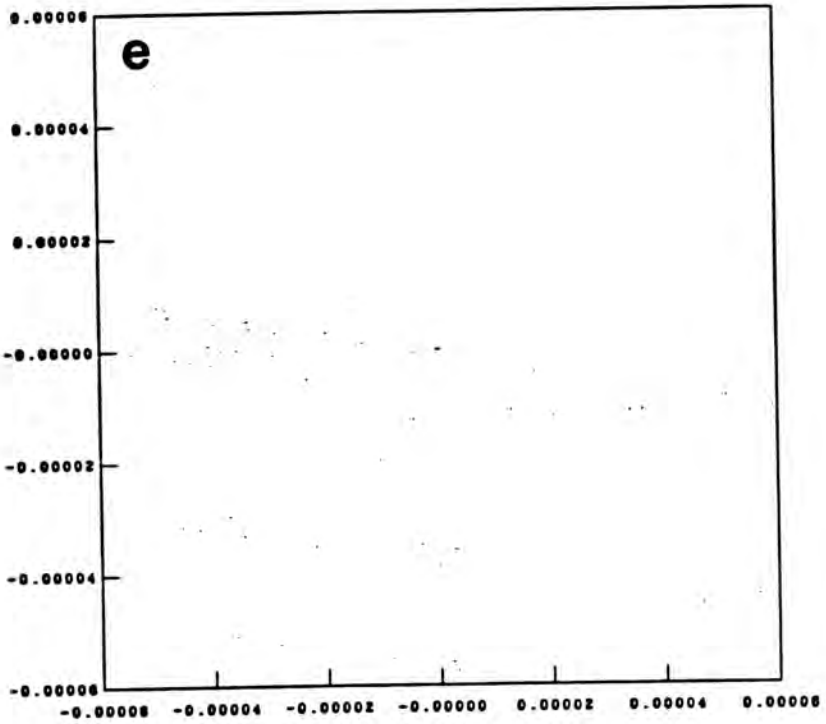
e
0.00006
0.00004
0.00002
-0.00000
-0.00002
-0.00004
-0.00006
-0.00006 -0.00004 -0.00002 -0.00000 0.00002 0.00004 0.00006

Figure 8

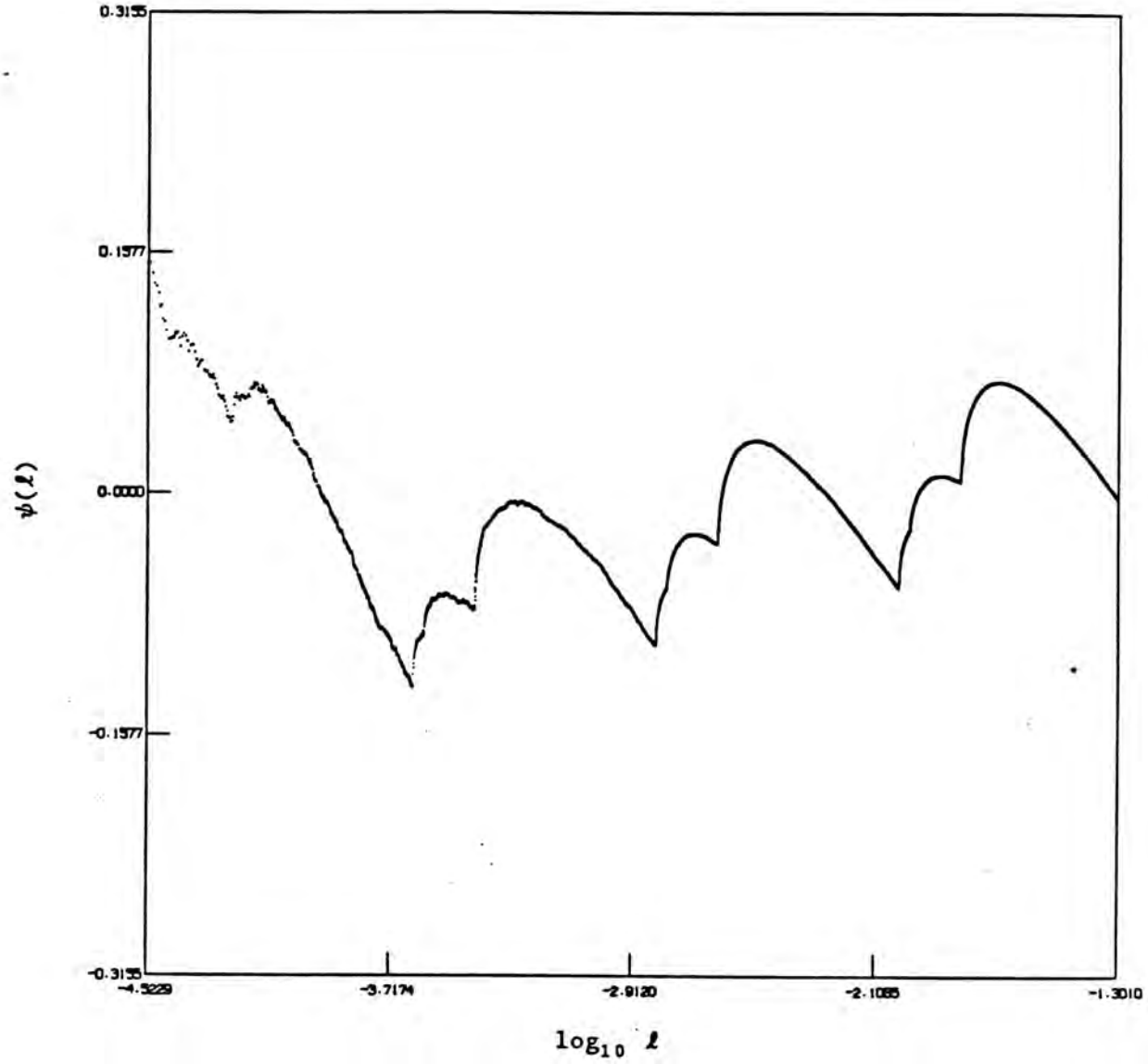
0.3155
0.1577
0.0000
-0.1577
-0.3155
$\psi(\ell)$
-4.5229
-3.7174
-2.9120
-2.1065
-1.3010
$\log_{10} \ell$

Figure 10

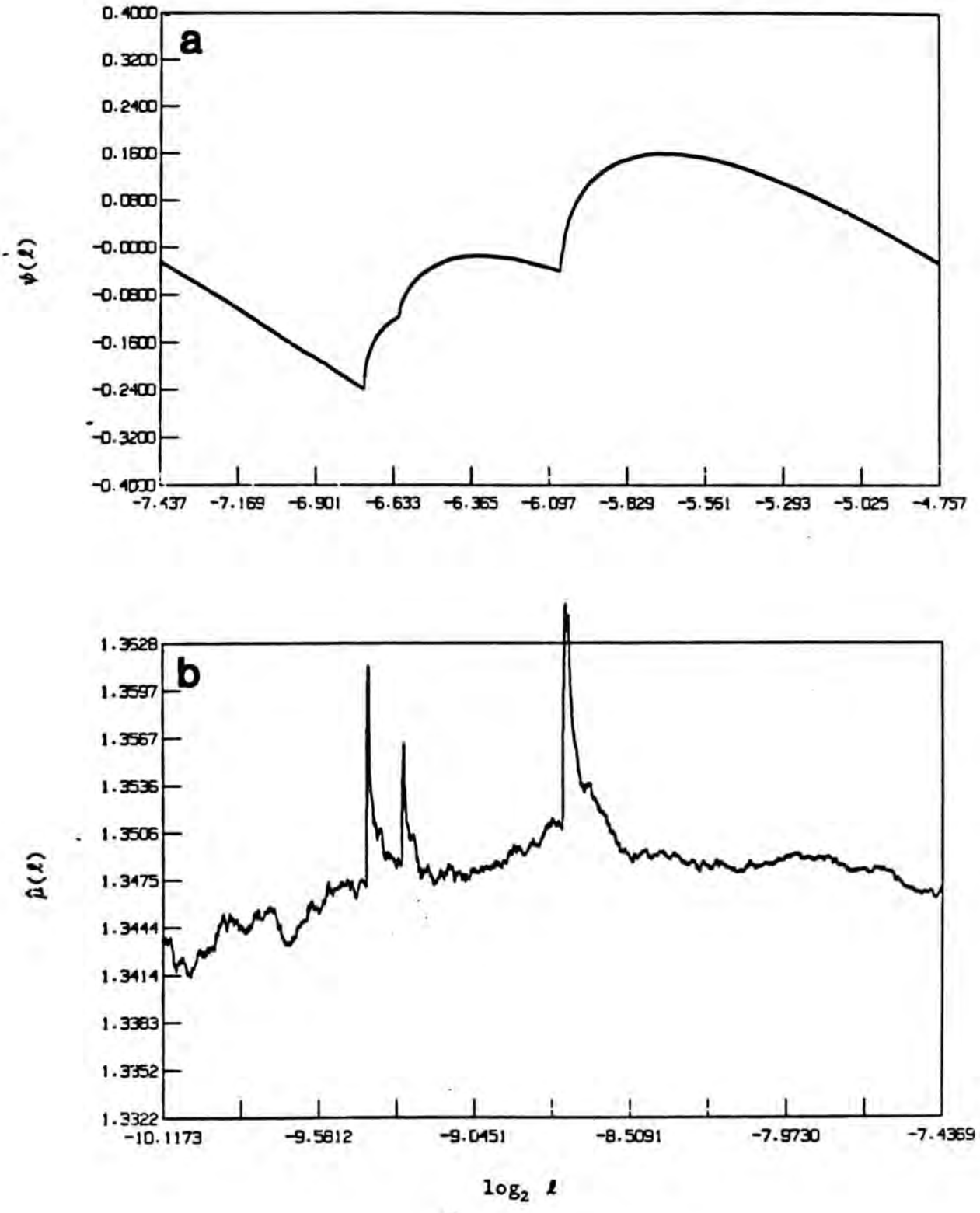
a
0.4000
0.3200
0.2400
0.1600
0.0800
-0.0000
-0.0800
-0.1600
-0.2400
-0.3200
-0.4000
ψ(ℓ)
-7.437
-7.169
-6.901
-6.633
-6.365
-6.097
-5.829
-5.561
-5.293
-5.025
-4.757
b
1.3528
1.3597
1.3567
1.3536
1.3506
1.3475
1.3444
1.3414
1.3383
1.3352
1.3322
μ̂(ℓ)
-10.1173
-9.5812
-9.0451
-8.5091
-7.9730
-7.4369
log2 ℓ

Figure 11

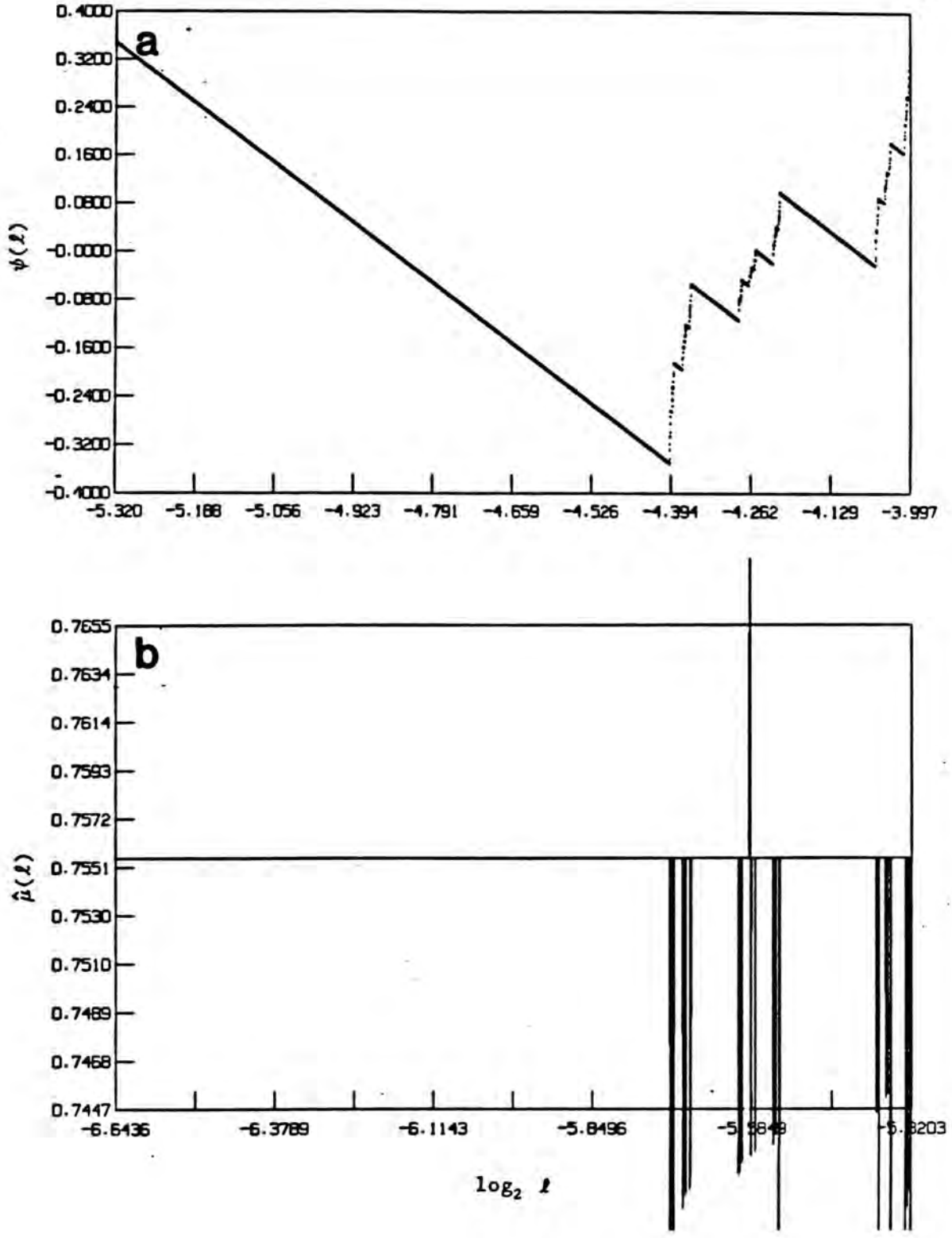
a
0.4000
0.3200
0.2400
0.1600
0.0800
-0.0000
-0.0800
-0.1600
-0.2400
-0.3200
-0.4000
ψ(ℓ)
-5.320
-5.188
-5.056
-4.923
-4.791
-4.659
-4.526
-4.394
-4.262
-4.129
-3.997
b
0.7655
0.7634
0.7614
0.7593
0.7572
0.7551
0.7530
0.7510
0.7489
0.7468
0.7447
μ̂(ℓ)
-6.6436
-6.3789
-6.1143
-5.8496
log2 ℓ

Figure 11'

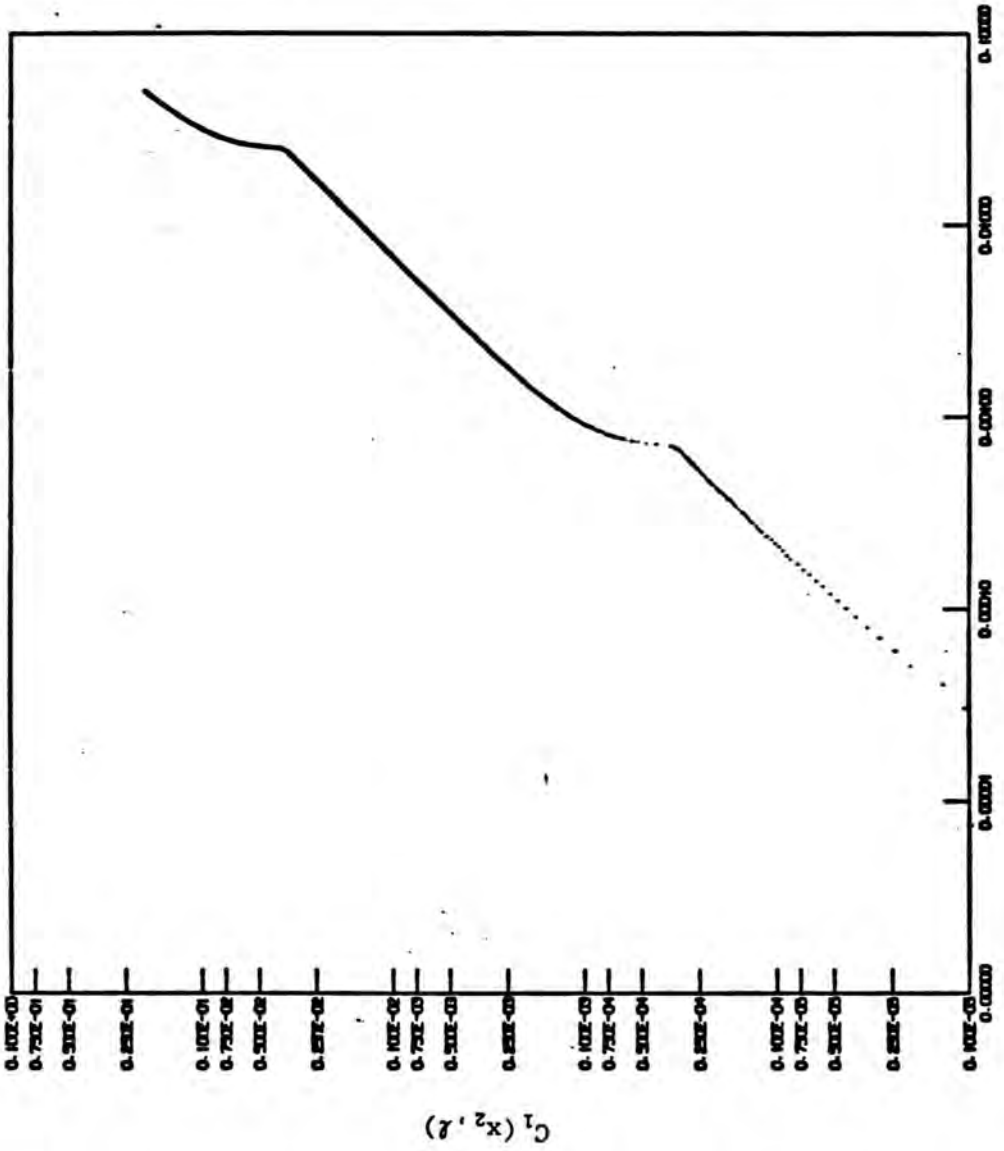

Figure 12

CHAPTER IV Lacunarity in Nature

The concept of self-similarity has received widespread use in a variety of disciplines. Inherently self-similar models have been constructed for the investigation of cosmology (e.g. Fournier, 1907), diffusion limited aggregation models of dielectric breakdown (Sander, 1987), and cascade theories of fluid turbulence (Novikov, 1966; Mandelbrot, 1974). The intrinsic oscillations in the scaling of fractal structures which appear in many of these models will be useful in making the comparison of theory with experiment. In this chapter we will investigate the lacunarity oscillations in the first and third of the examples mentioned above.

Turbulence has been called "the unsolved problem of classical physics" (Cvitanović, 1984). Here we are concerned with a subclass of this problem: the description of three-dimensional, fully developed fluid turbulence. The meaning of these adjectives is made clear below. In the first part of this chapter we demonstrate the role of the oscillation in the β model of fully developed fluid turbulence due to Frisch, Sulem, and Nelkin (1978). We show, via the β model, that oscillations in the scaling statistics are expected as a consequence of the fractal nature of turbulence; predict how the ψ functions of different moments of the velocity distribution are related; and interpret a new scaling parameter for turbulence. Several reasons motivate our choice of the β model. The derivation of the β model is straightforward and the origin of the oscillatory ψ function fits neatly into its development (Smith *et al.*, 1986). Secondly, recent observations by Anselmet *et al.* (1984) are

compatible with and even suggest the existence of an oscillation of reasonably large amplitude in the velocity structure functions of turbulent flows. Finally, other investigators have interpreted the change of slope of the statistical moment versus the logarithm of length scale as an indication of multi-fractal behavior. We do not believe this is always a correct interpretation and demonstrate a characteristic which may distinguish multi-fractal scaling from scaling with an oscillation.

The first part of this chapter is organized into four sections. Section 4.1 contains a brief review of the terminology and phenomenology of the study of turbulence. In Section 4.2 the standard derivation of the β model is presented. Section 4.3 provides a generalized derivation in which the oscillation is seen to arise naturally, notes the favorable comparison with experimental results, and contrasts the behavior of statistics on a multi-fractal and a fractal.

The second portion of this chapter contains an investigation of scaling arguments in cosmology. The distribution of visible matter is non-uniform at scales up to at least 50 megaparsecs (Lapparent, 1986). Evidence for the nested behavior of this distribution (at least at small scales) is stronger than in the case of turbulence. In Section 4.5, the Fournier universe is used to show the implications of viewing a nested scaling structure in projection. Dynamical considerations are noted through the Kida equation and a new generator of such distributions is discussed in Section 4.5. After noting the effects of projection in Section 4.6, an analysis

of current observations is presented in Section 4.7.

Part I Lacunarity in Fluid Turbulence

Section 4.1: Characteristics of Turbulence

Richardson (1922) was the first to propose that a turbulent flow field could be envisioned as a collection of eddies of all sizes. Richardson's observation was that an active region of size ℓ is spatially composed of several smaller more intensely active regions. The distribution of the largest structures is neither spatially nor temporally uniform. Hot wire anemometer measurements of turbulent velocity fields by Batchelor and Townsend (1947) quantified this behavior which they termed "intermittency." A typical velocity trace recorded at a fixed position in a turbulent flow reveals long periods of quiescence interrupted by irregularly spaced bursts of activity; this behavior is the distinguishing characteristic of intermittency in turbulence. Intermittency is a property of small scales; active bursts are not space-filling. The behavior of a temporal trace is related to spatial intermittency through to the mean advection of this flow: it is assumed that the active regions that are carried past the fixed detector provide a good representation of the flow's characteristics. Landau (1944) suggested that the transition to turbulence could be understood as the activation of more and more Fourier modes; while this model of the transition to turbulence is not universally excepted, the swirls visualization has become the textbook model of fully developed turbulence (Landau and Liftshitz, 1979 §31).

Consider a fluid in turbulent motion: if the flow is to maintain itself, the constant dissipation of energy by viscosity at the smallest active scales, must be balanced by an inflow of energy. It is often the case that this source introduces energy into the system at large scales. In a turbulent energy spectrum (see e.g. Tenekes and Lumley, 1972) a range of wave numbers over which the energy scales as the 5/3 power of the wave number is often observed. This was predicted by Kolmogorov (1941) on the basis of dimensional arguments. This inertial range corresponds to length scales ℓ such that

$$\ell_o \gg \ell \gg \ell_d \tag{4.1}$$

where ℓ_o is the scale at which energy is introduced into the system; ℓ_d is the scale at which viscous damping becomes important. As emphasized by Frisch and Morf (1981), the scales below ℓ_d do not constitute a strictly damping region; both damping and inertial effects play a part at these scales.

The goal is to follow the path of the energy introduced into the system as it cascades to smaller length scales (larger wave numbers) and is eventually dissipated by viscosity. We will frame our picture in wave number space (k-space) and consider the energy contained in "eddies of size ℓ", or equivalently, the energy in a thin spherical shell of k space with radius $k = 2\pi/\ell$. Kolmogorov assumed the energy cascade was local in this space, passing from one shell to the next until the dissipative range was reached at large k. This assumption is often considered equivalent to saying that energy is transferred only between eddies of similar sizes. Note that in this picture an

eddy is something other than a blob of swirling fluid with a characteristic size ℓ. There are special cases in which the swirling blob picture may be shown to have its energy concentrated in a fairly narrow band of k values near ℓ^{-1} (see, e.g. Beran (1968), 344); Townsend (1956) relates the spatial structure to the k spectrum for several simple distributions. Nonetheless, the energy in eddies of size ℓ is the energy in a region of k space defined by an integral over the entire spatial domain.

Turbulence is considered fully developed once a dynamic equilibrium is established and the energy dissipated by viscous forces, E, in some characteristic time of the system, t, is equal to the rate at which it is introduced into the system. Denoting this quantity by ϵ, we have

$$\epsilon \equiv \frac{E}{t} = \nu \langle (\nabla v)^2 \rangle \tag{4.2}$$

where $\langle \ldots \rangle$ denotes ensemble average and ν is the viscosity of the fluid.

Scaling behavior in fluid motion is not unexpected. It is easily seen (eg. Benzi et al., 1984 or Frisch, 1983) that the Navier-Stokes equations for the velocity fields $\mathbf{v}(\mathbf{x})$ of a viscous fluid (with to no external force)

$$\partial_t \mathbf{v}(\mathbf{x}) + (\mathbf{v}(\mathbf{x}) \cdot \nabla)\, \mathbf{v}(\mathbf{x}) = -\nabla p/\rho + \nu \nabla^2\, \mathbf{v}(\mathbf{x}) \tag{4.3}$$

are formally invariant under the scale transformations

$$r \to \sigma r,\ v \to \sigma^h\, v,\quad t \to \sigma^{1-h}\, t,\quad \nu \to \sigma^{h+1}\, \nu;\ \sigma > 0. \tag{4.4}$$

For arbitrary values of h. In the above ρ is the density and p the pressure.

Under this transformation, the energy dissipation scales as is

$$\epsilon \rightarrow \sigma^{3h-1} \epsilon$$

With the assumption that the relevant nonlinear interactions are local in k space, the invariance of the energy dissipation

$$\sigma^{3h-1} \epsilon = \epsilon \quad \Rightarrow \quad h=1/3. \tag{4.5}$$

In this case,

$$\lim_{\Delta x \to 0} \frac{\Delta v}{\Delta x^h} = \lim_{\Delta x \to 0} \frac{v(x) - v(x+\Delta x)}{(\Delta x)^{1/3}} = 1 \tag{4.6}$$

and, therefore, the velocity gradient is singular. Kolmogorov (1941) originally assumed that the set of singular points was space filling. In an attempt to understand the spatial intermittency of turbulence, Landau (1944) pointed out that if the set of singular points had a dimension less than three, the energy dissipation would be a fluctuating quantity in space. Novikov and Stewart (1964) provided the first self-similar mathematical model of the energy cascade. These ideas were extended by Kraichnan and culminated in the β model of Frisch, Sulem and Nelkin (1978).

The difference between turbulent and laminar flow is often visually apparent. The complexity of a turbulent field suggests a statistical description, such as the energy spectrum. Some experiments seek to provide a detailed history of individual fluid elements. One approach is to follow the path of a "passive tracer" suspended in the fluid and reconstruct the fluid motion from that of the tracer. The composition of the tracer may vary considerably; Richardson and Stommel (1948) used parsnips to follow eddy motion on the surface of a river, while a line or sheet of hydrogen bubbles is

often used to trace motions within a fluid system. In turbulent flows, fluid lines are expected to grow exponentially (Corrsin, 1950; see also Cocke,1969). Sreenivassen *et al.* (1986) follow a line of hydrogen bubbles in a turbulent shear flow, measuring its length as it is advected downstream. The line is stretched and folded by the flow, and fractal structures are observed to develop. The task is then to relate the fractal distributions of the tracer to the motion of the host fluid. In Chapter 5, it is shown that while exponential growth of a material line of a tracer is a necessary condition for turbulence, such observations are not sufficient to infer turbulent flow. It is demonstrated that such tracer distributions may develop very complex, self-similar structure in very simple, non-turbulent flows; exponential growth of a material line does not imply turbulence. The development of this self-similar structure has been recently observed in a surface flow by Chaiken et al.(1986,1987).

When describing the velocity field, the moments of the velocity distribution (called the velocity structure functions) provide a common vehicle for the presentation of experimental results and their comparison with theory. In a homogeneous, isotropic flow, the p^{th} order velocity structure function is defined as

$$S_p(\ell) \propto \langle (\delta v(\ell))^p \rangle = \langle (v(\mathbf{r} + \ell) - v(\mathbf{r}))^p \rangle \qquad (4.7)$$

where $\mathbf{r}$ represents a point in the flow and ℓ defines a separation vector. For isotropic turbulence, all orientations of $\mathbf{r}$ and ℓ are considered and the average is taken over physical space. For a jet

flow (e.g. Anselmet *et al.*, 1984) only the component of the velocity parallel to the mean flow is considered and the displacement is likewise taken only in this direction. High order structure functions are often normalized by the second order moment, forming the nondimensionalized structure functions,

$$a_p(\ell) = \frac{S_p(\ell)}{[S_2(\ell)]^{p/2}} \tag{4.8}$$

In the inertial range, the structure functions are observed to scale as a power of ℓ. Differences in the relationship between exponents of different moments provide a method to distinguish between models experimentally. In Kolmogorov's 1941 theory, the structure functions are independent of p in the inertial range. As shown below, the β model implies a linear dependence on p while the lognormal model (Kolmogorov, 1962) has a quadratic dependence. Anselmet et al.'s experiments fall between the last two, but in the high order moments, the dependence appears to depart from linearity.

The β model has spawned a host of more realistic progeny including the α model (Lovejoy, private communication) and the random β model (eg. Benzi *et al.*,1984). The results of our own generalization may be straightforwardly (if not easily) applied to the more modern versions. The main point of this chapter is that in addition to the mean scaling, the fractal nature of turbulence implies an oscillatory behavior in the $S_p(\ln(\ell))$. This result was foreseen by Novikov (1964).

Section 4.2 : The β Model

The β model considers the energy cascade of a three dimensional flow. Consider starting with an active region at the outer length scale, ℓ_o. The region is divided into λ^3 smaller subregions representing eddies "nearby" in k-space. The original active eddy feeds its energy into N active eddies of size $\ell_1 \approx \ell_o/\lambda$. Figure 4.1 attempts to show this schematically. After n generations, there are N_n active 'n-eddies' of scale ℓ_n where

$$\ell_n = \lambda^{-n} \ell_o \tag{4.9}$$

Frisch *et al.* (1978) take λ equal to 2, our departure from their notation stems from a desire to track the role of this parameter. Kolmogorov's space-filling model corresponds to the case where all λ^{3n} n-eddies are active. In the β model, N is less than λ^3 – not all of the subregions are active – and the cascade continues only within a fraction of the space. In this model, the small scale activity is forced to be nested within larger active regions.

Denoting the active fraction at each step of the cascade as β, we find

$$\beta(\lambda) = (N/\lambda^3) \tag{4.10}$$

In order to compute the structure functions for the β model, it is necessary to determine the typical velocity difference across a region of size ℓ. After n generations, the fraction of the original volume occupied by active eddies is

$$\beta_n(\lambda) = (N/\lambda^3)^n$$

$$= \lambda^{-(3-D)n}. \qquad (4.11)$$

These n-eddies will contain an energy per unit mass

$$E_n \approx \beta_n(\lambda)\, v_n^2 \qquad (4.12)$$

where v_n is the typical velocity difference at scale ℓ_n. Taking an energy transfer time, t_n, to be on the order of the eddy turnover time, ℓ_n/v_n, we obtain the energy transfer rate

$$\epsilon_n = E_n/t_n$$

as

$$\epsilon_n \approx \beta_n(\lambda)\, v_n^3/\ell_n. \qquad (4.13)$$

Imposing equilibrium in the energy transfer rate ($\epsilon_n = \epsilon$ for all n) then yields

$$v_n \approx \epsilon^{1/3}\, \ell_n^{1/3}\, \beta_n(\lambda)^{-1/3} \qquad (4.14)$$

In Frisch et al (1983), $\lambda = 2$ and β_n takes the form

$$\beta_n(\lambda) = \beta^n \quad , \quad \beta = N/2^3 \leq 1 \qquad (4.15)$$

Assuming

$$N = \lambda^D = 2^D,$$

they find

$$v_n \approx \epsilon^{1/3}\, \ell_n^{1/3}\, (\ell_n/\ell_o)^{(3-D)/3} \qquad (4.16)$$

where D is the Hausdorff dimension of the set of singularities of the velocity field and is related to the number of offspring through

$$D = \log_\lambda N = \log_2 N \tag{4.17}$$

A value of D less than three implies the set of singularities is not space filling and hence spatial intermittency.

Now consider the velocity structure function of β model flows. The evaluation Equation 4.7 requires the average velocity difference as a function of space. In the β model, the velocity difference across an active region of scale ℓ_n is simply $v_n(\ell_n)$. Only a fraction $\beta_n(\lambda)$ of the total volume is active; the remainder is inactive and therefore does not contribute to the average. The p^{th} order structure function is

$$\begin{aligned} S_p(\ell_n) &= \langle\, \delta v_n(\ell_n)^p \rangle \\ &\approx \beta_n(\lambda)\, \langle\, \delta v_n(\ell_n)^p \rangle_{active} \\ &\approx \beta_n(\lambda) v_n(\ell_n)^p \end{aligned} \tag{4.18}$$

where $\langle \ldots \rangle_{active}$ means the average is taken only over active regions. Substituting from Equations 4.15, 4.16 and 4.17, the structure functions are

$$S_p(\ell_n) \approx \epsilon^{p/3}\, \ell_n^{p/3} \left[\frac{\ell_n}{\ell_o} \right]^{\zeta_p}$$

where

$$\zeta_p = \frac{1}{3}\,(3-D)(3-p). \tag{4.19}$$

Similarly, the dimensionless structure functions are

$$a_p(\ell_n) \approx \left[\frac{\ell_n}{\ell_o} \right]^{\xi_p}$$

where

$$\xi_p = (3-D)(2-p)/2. \tag{4.20}$$

The slope of the β model structure functions varies linearly with

the order of the moment. This is the result of Frisch *et al.*

Section 4.3: β Model Oscillations

We return now to the velocity equation (4.14) and repeat the analysis retaining λ explicitly. In doing so, we will observe that while the scaling remains independent of λ a generalized similarity ratio is introduced. At this point $\beta_n(\lambda)$ is defined only at $\ell = \ell_n$. We want to transform β into a function for arbitrary ℓ. First recall that for an arbitrary magnification α, the general solution to a scaling for a set of dimension d and similarity ratio σ implies

$$C(\alpha\ell) = \alpha^d\ C(\ell)\ \exp\{\psi(\log(\alpha\ell)/\log(\sigma)) - \psi(\log(\ell)/\log(\sigma))\}$$

where $\psi(\log(\ell))$ is a periodic function of period one (for $\alpha = m\sigma$ and integer m we recover $C(\alpha\ell) = \alpha^d\ C(\ell)$).

Generalizing Equation 4.11 we have

$$\beta_n(\lambda) \rightarrow \beta(\lambda,n) = \lambda^{-n(3-D)}\ \exp\left\{ f\left[-n\ \frac{\log(\lambda)}{\log(\mathcal{L})} \right] - f\left[\frac{\log(\ell/\ell_o)}{\log(\mathcal{L})} \right] \right\} \tag{4.21}$$

where $f(\log\ell)$ is a ψ function with period $\log \mathcal{L}$.

Solving Equation 4.9 for n, we find

$$n = -\ \frac{\log(\ell/\ell_o)}{\log(\lambda)} \tag{4.22}$$

where we have dropped the subscript on ℓ along with the restriction

to integer n. Substitution of this expression into Equation 4.21 yields the desired expression for β as a continuous function of ℓ. Specifically

$$\beta(\ell) = \left(\frac{\ell}{\ell_o} \right)^{-3+D} \exp \left\{ f \left[\frac{\log(\ell/\ell_o)}{\log(\mathcal{L})} \right] - f \left[0 \right] \right\} \tag{4.23}$$

where λ has cancelled and a new length ratio $\mathcal{L}$ characteristic of the flow has entered. With this form for β, the velocity becomes

$$v(\ell) = \epsilon^{1/3} \ell^{1/3} \left(\frac{\ell}{\ell_o} \right)^{(3-D)/3} \exp \left\{ -\frac{1}{3} \left\{ f\left[\frac{\log(\ell/\ell_o)}{\log(\mathcal{L})} \right] - f\left[0 \right] \right\} \right\} \tag{4.24}$$

and the oscillatory correction is present in the structure function as

$$S_p(\ell) = \epsilon^{p/3} \ell^{p/3} \left(\frac{\ell}{\ell_o} \right)^{\zeta_p} \exp \left\{ \left[\frac{3-p}{3} \right] \left\{ f\left[\frac{\log(\ell/\ell_o)}{\log(\mathcal{L})} \right] - f\left[0 \right] \right\} \right\} \tag{4.25}$$

and

$$a_p(\ell) = \left(\frac{\ell}{\ell_o} \right)^{\zeta_p} \exp \left\{ \frac{2-p}{2} \left[f\left[\frac{\log(\ell/\ell_o)}{\log(\mathcal{L})} \right] - f\left[0 \right] \right] \right\} \tag{4.26}$$

If the intermittent nature of turbulence is due to a self-similar structure, we expect there to exist oscillations about the mean scaling of the velocity structure functions. We reiterate here that these oscillations are a result of the fractal nature of the system, not a particular result of the β particular model used. Observing the oscillation may prove quite difficult; yet such an observation would be very valuable in that it would provide additional parameters in the description of turbulent flows. Since the energy cascade is

not strictly local in k space, one might interpret ℓ as an indicator of the range over which eddies interact; specifically, the logarithm of the ratio of the outer radius to the inner radius of the k shells which are coupled to the wave number in question.

While Equation 4.25 does not determine the amplitude or period of the oscillation, it does predict a relationship between the oscillations observed in structure functions of various orders; specifically that their periods are equal and their amplitudes determined by the extreme values of ψ. The β model ψ function yields

$$\text{range of } |\psi_p(\ell)| = \left(\frac{2-p}{2}\right) |f_{max} - f_{min}| \qquad (4.27)$$

In the β model, the magnitude of ψ increases linearly with p. A central assumption here is that the singularities of the set are governed by a single self-similar set, which may be described by a single dimension and one basic ψ function. The comparison with multi-fractals is given below.

Oscillations have been observed in the structure functions of shear jet turbulence in a recent experiment by Anselmet *et al.* (1983). They note "oscillations, which are only weakly manifested for n = 10 and 12, are rapidly amplified at larger n," where n is the order of the moment. From their Figure 13, we judge the period of oscillation appears to take on the same value for each moment. Independently of Anselmet, van der Water *et al.* (1987) have observed what they believe to be a robust oscillation in the reconstructed attractor from the velocity measurements in a turbulent (air) boundary layer.

The source of these observed oscillations has not been

established. They may result from factors other than those discussed here. Nonetheless, oscillatory corrections are expected if the fractal on which the set of dissipation lives is lacunar, and will assist in determining the characteristics of that set. It has been suggested that the oscillation provides an insight much more deeply coupled to the underlying physics than the mean scaling. Indeed, Novikov (1986) has remarked that linearly scaling models should be classified as "pre-models": such models are wrong. The physics is to be found in understanding the deviations from pure scaling.

The term "multi-fractal" was coined by Frisch and Parisi (1983) to describe a set constructed from a combination of fractal sets each of differing Hausdorff dimension. The relevance of multi-fractals to turbulence arises in the limit of zero viscosity. In this limit, the Navier-Stokes equations (4.3) are invariant under transformations 4.4 for any value of h. Assuming that singularities of different orders do exist, different moments of the velocity structure functions will be sensitive to the distribution of different sets of singularities (see Frisch and Parisi for more details). This would result in a deviation of the slope of S_p vs ℓ with increasing p. Such a decrease is observed by Anselmet, although it is small compared to the error estimates.

If the scaling of different moments are governed by independent fractal distributions, each may have its own $\mathcal{L}$. In the β model above, only one set is considered and a single dimension and ψ function are predicted. Experimental discrimination of multi-fractal scaling may prove very difficult; individual sets should dominate

only at small separations. If such sets have different dimensions, the arguments above establishing a unique period for all moments should fail; conversely the observation of a single period would then cast doubt on a multi-fractal interpretation.

Can a homogeneous fractal masquerade as a multi-fractal? Yes. If the range of observation covers only a portion of an oscillation of a homogeneous fractal, the variation in ψ may be misinterpreted as a change in the mean slope. The two cases may be distinguished by increasing the range of observations, a difficult task at best.

The change in slope of a given moment may increase at small scales either as a results of seeing a set with a higher dimension in projection or following the oscillation of a homogeneous fractal. Once the domain of the higher dimensional set is entered, it is hard to leave (without invoking a conveniently located inner cutoff). If the slope is observed to decrease toward smaller scales, it seems more plausible to attribute the change to a homogeneous oscillation.

Part II: Cosmic Lacunae

Self-similar structures have a long history in astronomy; the large scale distribution of matter in the Universe inspired one of the first self-similar models of nature. At the turn of this century, Fournier (1907) proposed a strictly self-similar mass distribution as a solution to Olber's paradox. The model describes a hierarchial universe, ordered at all scales though homogeneous at none. The dynamics and evolution of such a distribution have also been

discussed by Hoyle (1953). Our interest in the distribution originated in the hope of observing the oscillatory component of the scaling by examining the angular position of galaxies on the sky. The existence of such an oscillation was proposed by de Vaucouleurs (1970, 1971), who conjectured that the structure of the cosmos results in a clustering hierarchy of visible matter such that the number of clusters or aggregates of a given mass follows a scaling law, complete with a superimposed oscillation periodic in the logarithm of the length scale. While more modern distributions have been advanced (see Mandelbrot, 1977), the two primary features are demonstrated nicely in Fournier's example. With this simple model, the observational consequences of fractal distributions are explored and the effects of projection on the d_q spectrum are noted. Next, the arguments of Kida are applied to model the dynamics of the cosmic cascade. Such processes typically give rise to distributions with self-similar geometry. A method for constructing such distributions is introduced to show that a complex array of filaments and voids appear in these simple cascade models. The chapter is concluded with a report of the correlation integral of nearby galaxies as a function of angular separation. No oscillation is found.

Section 4.4: The Fournier Universe

The Fournier universe consists of a structured hierarchy, each generation of which consists of seven "stellar aggregates" located at the vertices and center of a regular octahedron (see Figure 4.2).

The model, a Cantor set embedded in three dimensions, is a homogenous fractal of topological dimension zero; with a similarity ratio equal to 1/7 and a filling factor of 7, its capacity dimension is equal to one.

Consider an n^{th} generation aggregate (n-aggregate) of scale ℓ_n. If $N(\ell_n)$ represents the number of n-aggregates observed, then

$$N(7\ell_n) = 1/7\ N(\ell_n)$$

$$N(\ell) = \chi(\log\ell)\ \ell^{d_o} \quad \text{with } d_o = 1$$

and we have the gist of de Vaucouleurs' intuition with this simple model.

The dynamics of these hierarchial models is described as a fragmentation cascade from an initially uniform density distribution. In the present case we consider a co-moving domain of the Hubble flow, specifically a box, B, whose sides define an outer scale ℓ_0. We shall assume ℓ_0 sufficiently small that a Newtonian theory is applicable. During the first step of cascade, the initially uniform density of B clumps into aggregates of size ℓ_1; the cascade continues, the n^{th} generation consisting of N_n n-aggregates of size ℓ_n. For ℓ_{n+1} sufficiently less than ℓ_n, the impression of each generation remains observable. The population dynamics of such a process are described by the Kida equation

$$\frac{dN_n}{dt} = -\frac{N_n}{\tau_n} + \left(\frac{\ell_{n-1}}{\ell_n}\right)^{\kappa} \frac{N_{n-1}}{\tau_{n-1}} \qquad (4.28)$$

where there are N_n n-aggregates with a lifetime τ_n and each n-aggregate produces $\left(\frac{\ell_n}{\ell_{n+1}}\right)^{\kappa}$ (n+1)-aggregates.

We make the following assumptions:

(1) The ratio of the characteristic lengths scale of n-aggregates to that of (n+1)-aggregates is a constant, β, independent of n; for contraction $\beta > 1$. That is

$$\ell_n = \beta \ell_{n+1} \qquad \text{For all n.}$$

(2) The characteristic time for each n-aggregate is much less than the Hubble time, and scales as a power of the relevant characteristic length. Assuming some outer time scale T we have

$$\tau_n = T\ \ell_n^{\eta} \ .$$

The additional assumption that the cascade has "run its course" before the current epoch implies

$$\frac{dN_n}{dt} = 0$$

so that

$$N_n = \left(\frac{\ell_{n-1}}{\ell_n} \right)^{\kappa-\eta} N_{n-1} \tag{4.29}$$

with solution

$$N_n = \ell_n^{-d}\ \chi \left(\frac{\log \ell_n}{\log \beta} \right)$$

where

$$d \equiv \kappa - \eta$$

and χ is periodic with period one. Suggested values of d range from one to three; while β has been argued on various "physical" grounds

to be equal to 5 by Hoyle (1953), equal to 7 by Fournier (1909), and equal to 10 by de Vaucouleurs (1971).

While we expect only the n-aggregates to be visible, one may include the exchange of mass with an invisible background. The assumption that this interaction is also scaling gives

$$M_n = \Phi\, M_{n-1} \tag{4.30}$$

where M_n is the totality of mass in n-aggregates and the interaction term Φ is

$$\Phi = \left(\frac{\ell_{n-1}}{\ell_n} \right)^{\mu} \tag{4.31}$$

In the absence of interactions with the background μ is zero; currently we cannot determine even the sign of μ.

If there is an interaction with a background mass, one would expect to detect it in the mass distribution among n-aggregates. Since

$$M_n = \rho_n \ell_n^{\,3}\, N_n$$

the density between different generations is related through

$$\rho_n \ell_n^{\,3-d} = \rho_{n-1}\, \ell_{n-1}^{\,3-d} \left(\frac{\ell_{n-1}}{\ell_n} \right)^{\mu}$$

where the rescaling of lengths by a factor of β eliminates any contribution from χ.

Substituting we find

$$\rho_n = \left(\frac{\ell_{n-1}}{\ell_n} \right)^{3-d+\mu} \rho_{n-1}$$

or

$$\rho \sim (\ell)^{-(3-d+\mu)}$$

With the additional assumption that the background mass is distributed uniformly, we have

$$M_n \sim \ell^{d-\mu} N_n = \ell_n^{-\mu} \chi(\log \ell). \qquad (4.32)$$

The participation of the hidden mass is revealed in the mass distribution of the n-aggregates provided the hidden mass interacts more or less as above.

Section 4.5: A Geometric Construction

The Kida equation describes the dynamics of the cascade process; it suggests the structure will be fractal. We now introduce a generator for the construction of particular geometries. The procedure is straightforward and includes several distributions considered by other investigators as special cases. Despite the simplicity of the construction, the results have rich probability distributions. The output of this process could serve as the basis for Universe simulations similar to those of Soneira and Peebles (1978) who used nested, random distributions.

In the present case, begin by choosing a set of N 3-vectors g_i and a 3 x 3 generating matrix $G_{ij}(\sigma,\theta,\varphi)$ of the form

$$G = \sigma \begin{bmatrix} \cos(\theta) & -\sin(\theta) & 0 \\ \sin(\theta) & \cos(\theta)\cos(\varphi) & -\sin(\varphi) \\ 0 & \sin(\varphi) & \cos(\varphi) \end{bmatrix} . \qquad (4.33)$$

The zeroth generation consists of the 2N points ${}^0s_j$, located by

$${}^0s_j = \begin{cases} + g_j & j = 2i \\ - g_j & j = 2i + 1 \end{cases} . \qquad i = 1, 2, \ldots, N \quad (4.34)$$

Defining the vectors $g_i^1 = G\, g_i$, we get the first generation

$${}^1s_j = \pm g_i \pm g_k^1 \quad \text{all combinations of } \pm . \qquad (4.35)$$

Repeat the procedure with $g_i^2 = G\, g_i^1$ to form ${}^2s$. And so on. A set s is formed <u>with retention</u> if, at each generation, the set includes the union of all previous generations. Usually this will not be the case; only the new members of the n^{th} generation will be used in future iterations of the cascade as indicated in Equation 4.35 above.

Five iterations with the particular choice $\sigma = 1/7$, $\theta = 0$, $\varphi = 0$ with N = 3 and

$$g_i = \left\{ \begin{bmatrix} 1 \\ 1 \\ 0 \end{bmatrix} , \begin{bmatrix} 1 \\ -1 \\ 0 \end{bmatrix} , \begin{bmatrix} 0 \\ 0 \\ \sqrt{2} \end{bmatrix} \right\}$$

produces the distribution shown in stereograph 1. Formed with retention, this is the Fournier Universe. By adjusting σ, the capacity dimension of the set may be altered to yield any value between zero and three. When the measure is distributed uniformly in each generation, all the D_q are equal and $f(\alpha)$ is constant.

Section 4.6: Projection Effects

A complete three-dimensional view of the local matter distribution in the Universe is currently unavailable to the observer. More accessible data consists of the angular position of galaxies as points on the celestial sphere. To simulate this in the Fournier case, position an observer at a 5^{th} generation point O. The observer at O records the distribution shown in equal area projection in Figure 4.3. A set mundane and intrinsically uniform as the Fournier universe yields many apparent structures in projection. Considering the correlation integral as a function of the angular separation ξ, the observed scaling has a large oscillatory component.

The effects of projection are more easily visualized by considering the members of the set which fall within the horizontal mid-plane of an octahedron (Figure 4.4). This set, called the equatorial section by Fournier, is also a homogeneous fractal; the filling factor is changed to five; thus

$$d_0 = d_q = \frac{\log 5}{\log 7} .$$

Since the similarity ratio is invariant under this procedure, the period of a ψ function of the set will not change. The two-dimensional equivalent to projection onto the sky is projection onto a circle, of consideration of only the angular position, ξ. Locally, in angle, the set will appear as if projected onto a line. Assuming the coordinate system shown in Figure 4.4, projection onto the x (or y) axis gives $\rho = 3$, $\sigma = 5$ while projection onto the line $x = -y$ yields $\rho' = 3$, $\sigma' = \sqrt{2}\,\sigma$; a homogeneous fractal when viewed in this

projection, may have a non-trivial d_q spectrum.

For non-zero values of θ and φ, these structures are apparent in the unprojected distribution. In the case $\varphi = 0$, $N = 1$ with

$$g = \begin{pmatrix} 0 \\ 1 \\ 0 \end{pmatrix}$$

the set lies in the z=0 plane. With the identification

$$s = \sigma\, e^{i\theta}$$

this set corresponds to the objects studied by Barnsley. In his notation the set consists of all points

$$\pm 1 \pm s \pm s^2 \pm \ldots .$$

Several probability distributions for this situation are shown in Plate 1; specifically, the cases $\theta = 23$ degrees, $\sigma = 0.90$, 0.93, 0.96, and 1.00 times the $\sqrt{2}/2$. The point illustrated here is that very complex conglomerations of filaments and voids are expected in fractal distributions.

Section 4.7 : Observations

Recent observations reinforce the view that the visible matter in the Universe is distributed in a very nonuniform manner. In the slices in which unprojected three dimensional data are available (see Lapparent, 1986), large voids are observed. These are presumably cross-sections of huge, relatively empty bubbles. While spherical projection of a distribution in 3-d may disturb the d_q spectrum, the simple examples above suggest that an oscillatory component may remain observable. The presence of an oscillation in the cosmic

distribution of visible matter would provide yet another new universal number – the period of the oscillation. In order to search for such an oscillation, we have examined the Zwicky and Shane Wirtanen catalogs. Analysis of the Zwicky catalog consisted of the direct evaluation of the correlation to a statistical sample of 3333 galaxies supplied by Groth. We determine

$$\nu = 1.8 \qquad \text{in the range} \quad 0.05 < \xi < 1.0 \ .$$

No significant oscillatory component was found.

We also considered determining the d_q from the Shane Wirtanen survey (see Peebles, 1973). Here we have not yet successfully dealt with the problem of variations from one plate to the next (this structure is apparent in color projections of the relative density) and the difficulty of taking into account the overlap of the plates.

Figure Captions

4.1 The β model picture. This figure illustrates nested regions of activity. Each active region of size ℓ is composed of three smaller, more intensely active regions.

4.2 A three generation (7^3 point) approximation of the Fournier universe. In this model, matter is nested in a strictly self-similar hierarchy.

4.3 An equal area projection of the data in Figure 4.2 as viewed from the point $(\sigma + \sigma^4, \sigma - \sigma^4, \sqrt{2}\ (-1 - \sigma^2 - \sigma^5))$ looking in the direction of increasing z (upwards).

4.4 The "equatorial section" of the Fournier Universe, this section corresponds to the z=0 plane.

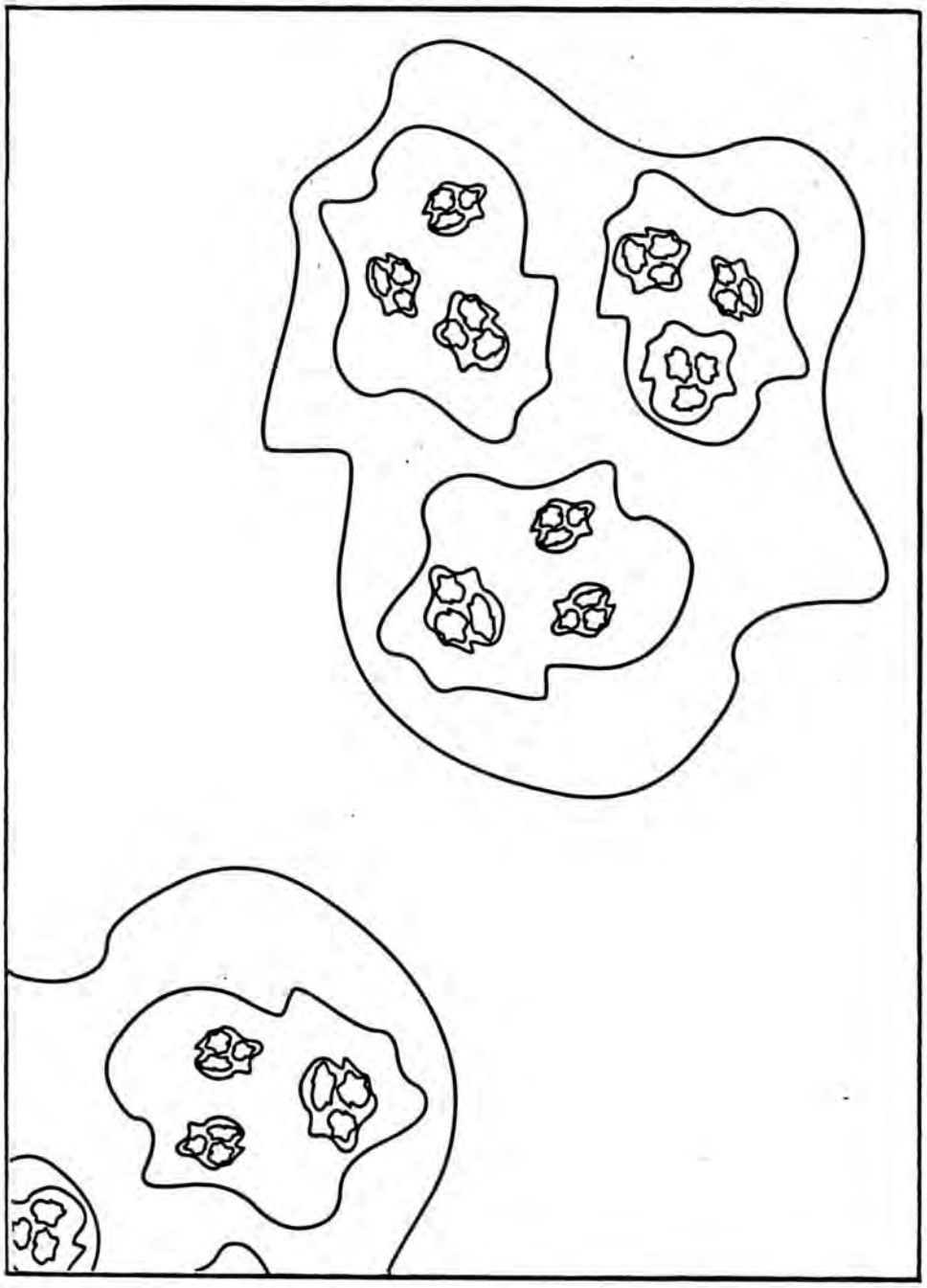

Figure 4.1

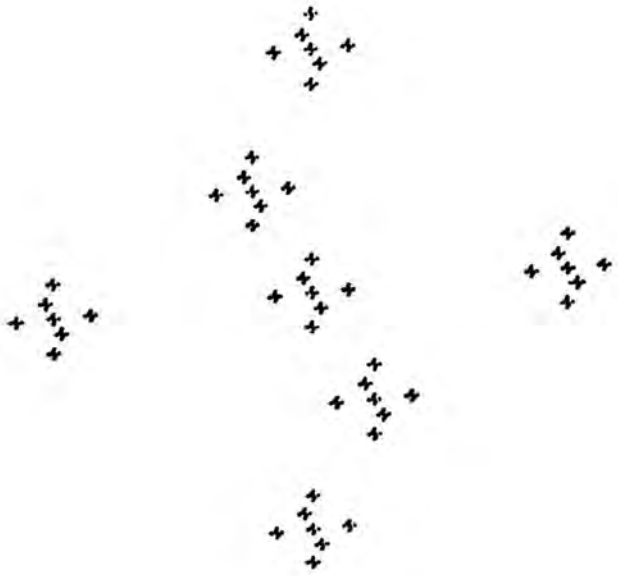

Figure 4.2

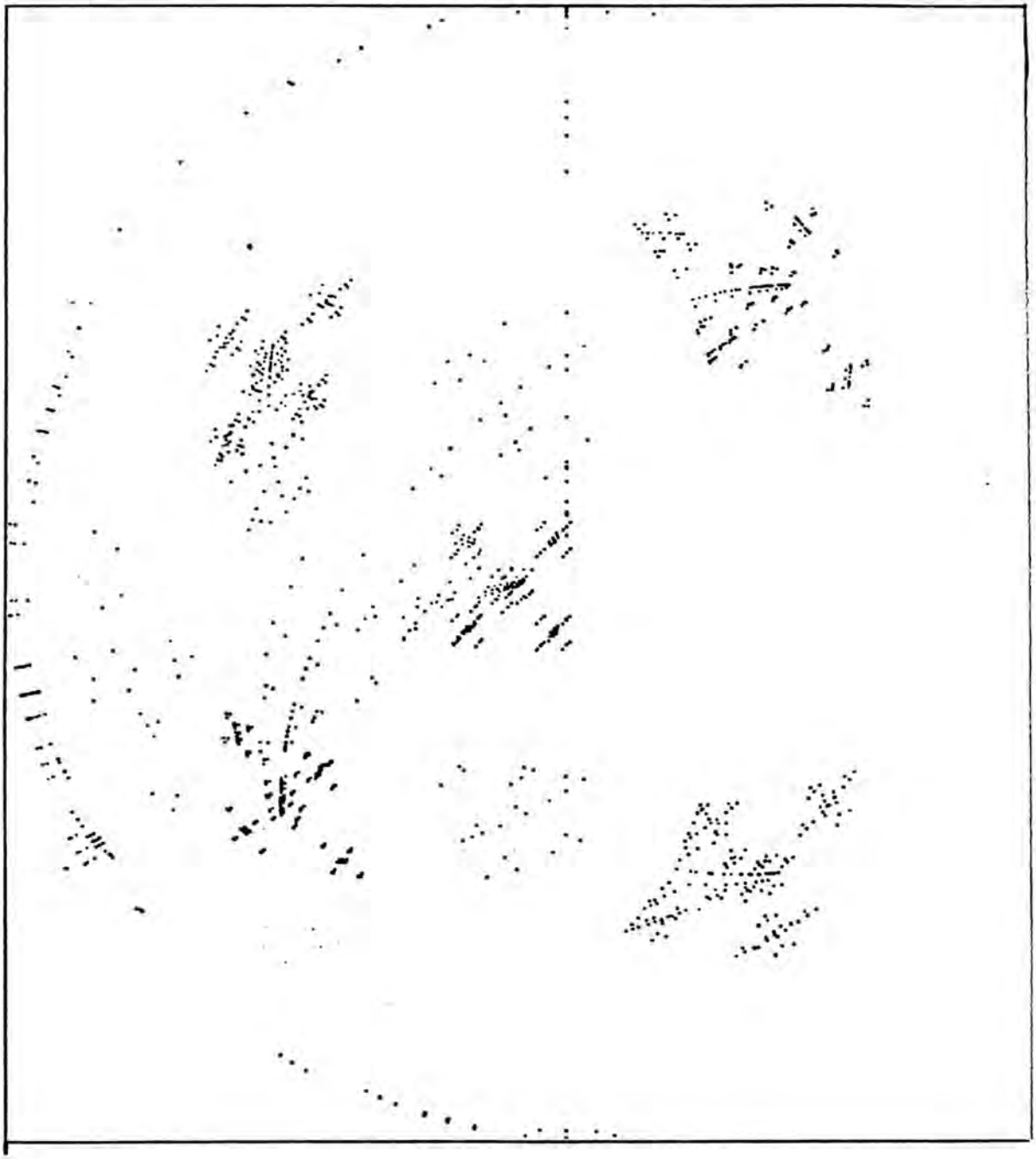

Figure 4.3

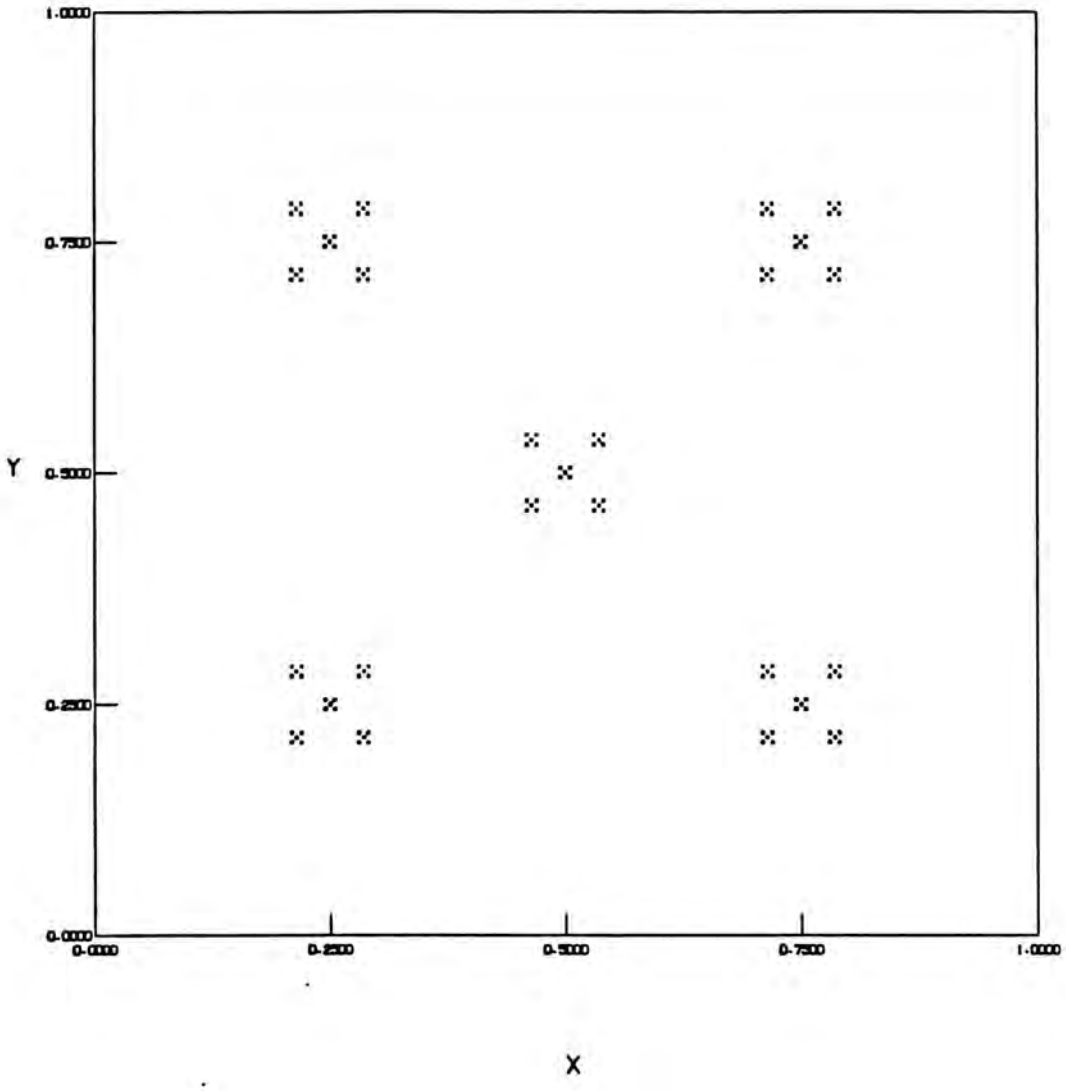
1.0000
0.7500
0.5000
0.2500
0.0000
Y
0.0000
0.2500
0.5000
0.7500
1.0000
X

Figure 4.4

Chapter 5 PARTICULATE DISPERSAL IN A TIME-DEPENDENT FLOW

Introduction

In this final chapter we develop a model for the motion of tracer particles suspended in a time dependent flow. The model demonstrates the stability of the suspension of negatively buoyant particles to time dependent perturbations and the exponential growth in the length of a tracer line in a nonturbulent flow field. Treated as a dynamical system, the model equations differ from those discussed in chapters 2 and 3 due to their area conserving property. Examination of sedimentation in this model reveals highly structured probability distribution which we believe are a generic feature of area preserving maps and flows. A discussion of the accumulation of probability density with several area preserving maps is given in Appendix 4 while a mapping for the model discussed in this chapter is developed in Appendix 3.

The behavior of particles suspended in a moving fluid is of interest in many areas of geophysics; in some problems, a better understanding of this behavior is a prerequisite for further progress. Three examples in which this phenomena is relevant are: (1) precipitation formation and the lifetime of volcanic aerosols in the atmosphere (Rogers, 1976), (2) suspension of plankton in the sea (Stommel, 1949), and (3) the evolution of growing crystals in a convecting magma chamber (Huppert (1984), Maxey and Corrsin (1986)). In each of these realizations, negatively buoyant particles may remain in suspension for a time far exceeding naive dimensional calculations and it is this aspect of the problem which we intend to

study here.

As an initial step toward understanding such phenomena, we examine the motion of particles in a simple laminar flow which is periodic in time. Stommel (1949) developed the theory for the case of steady rolls while experimental investigations of a similar steady flow field have been performed by Tooby *et al.* (1977). Recently, experiments by Gollub (1987) have probed particle behavior in a time-dependent convective flow similar to the flow considered here. The correspondence between a time-dependent surface flow and an area preserving mapping has been developed by Chaiken et al. (1986, 1987). In Chaiken et al.'s experiments, the correspondence between the laboratory flow and the mapping is sufficiently accurate that the mapping may be used to predict features of the flow.

The motions of fluid particles in time-dependent flows have been studied by Aref (1984), who has modeled the stirring of a tank of fluid by alternately flashing, point vortices. The novelty of our approach is to allow a simple two-dimensional incompressible flow to become periodic in a smooth manner (Smith, 1984). Since the velocity field is completely determined as a function of position and time, the phase space is effectively three-dimensional, the lowest dimension permitting chaotic behavior. Such behavior is in fact observed. In addition to regions of retention and simple fallout, regions of chaotic particle motion are observed. The presence of chaotic motion holds deep implications for the sedimentation properties of the system. In the physical surface flow studied by Chaiken et al. (1986,1987), chaotic motion is observable through the

rapid evolution of tracer distributions. These effects are relevant in many fluid systems.

Section 5.1 Steady Background Flow

Consider small bodies immersed in a fluid whose motion is described by a stream function $\Psi(x,y,t)$. The particle motion is governed by Newton's second law which takes the form

$$\begin{aligned} m\,\ddot{x} &= -6\pi a\mu(\dot{x} - \Psi_y) \\ m\,\ddot{y} &= -6\pi a\mu(\dot{y} + \Psi_x) - m'g \end{aligned} \tag{5.1}$$

where a is the particle radius, μ the viscosity of the fluid, g the acceleration of gravity, m the mass of the particle and the effective mass, m′ adjusted for buoyancy effects, is given by

$$m' = \frac{4}{3}\,\pi\, a^3\,(\rho - \rho_f),$$

where ρ is the particle density and ρ_f the density of the fluid. The coordinate system is defined with the y axis vertical.

If particle inertia is negligible, the particle trajectories also follow a stream function. That is, the trajectories are solutions of

$$\begin{aligned} \dot{x} &= \varphi_y \\ \dot{y} &= -\varphi_x \end{aligned} \tag{5.2}$$

where the particle stream function is

$$\varphi(x,y,t) = v_s x + \Psi(x,y,t) \tag{5.3}$$

and v_s, the Stokes velocity, is given by

$$v_s = \frac{m' g}{6\pi a \mu} = \frac{2a^2(\rho - \rho_f)g}{9\mu} \quad . \tag{5.4}$$

The Stokes velocity is the terminal velocity obtained by a particle in free fall through a quiescent viscous fluid.

The reduced equations 5.2 define a Hamiltonian dynamical system with one degree of freedom. The particle stream function φ is the Hamiltonian; its x and y location form a conjugate coordinate momenta pair. When φ is independent of time, topological constraints prevent trajectories in such a system from displaying chaos. A time-dependent stream function corresponds to a nonautonomous Hamiltonian system; this case resembles a system with a three-dimensional phase space. Such a system admits qualitatively different (particle) trajectories.

The effect of steady convective rolls on the motion of a small, slowly sinking body was first investigated by Stommel (1949), who was intrigued by the observation that the yield of plankton tows taken along the direction of the wind was much more variable than that of tows taken perpendicular to the wind. Long cellular rolls generated by wind stresses (Langmuir, 1938) are often observed in oceans and lakes where they are made visible by floating debris trapped above subduction zones. Treating the plankton as negatively buoyant point masses, Stommel considered a vertical cross-section taken parallel to the direction of the wind. In this cross-section, the flow is approximately two-dimensional; treating it as such, Stommel chose the stream function

$$\Psi(x,y) = A \sin x \sin y \quad . \tag{5.5}$$

Streamlines of this flow are shown in Figure 5.1. A similar flow field is associated with the first unstable mode of Rayleigh-Bernard convection (Chandrasekar, 1961). Substitution of Equation (5.5) into (5.3) yields Stommel's result: a stream function for the particle motion of

$$\varphi(x,y) = A \sin x \sin y + v_s x \quad . \tag{5.6}$$

In order to examine how the system behaves for a variety of parameter values, we normalize the Stokes velocity by the maximum fluid velocity and obtain

$$\gamma = \frac{v_s}{A} \quad . \tag{5.7}$$

Particles for which $\gamma = 0$ are neutrally buoyant and they follow the streamlines of the fluid. All particles for which $\gamma > 1$ fall through the cells with horizontal displacement (in the x direction) as shown in Figure 5.2. The sinking particles have minimum vertical velocity in regions of maximum upward fluid velocity, this increases their residence time in the area, and hence their horizontal displacement due to the horizontal component of the velocity of the background flow. A similar type of behavior occurs for particles with $\gamma < -1$, which rise through the cells. For an intermediate value, $-1 \leq \gamma \leq 1$, there exists a region of retention in which particles will execute closed orbits, remaining suspended in the cell. The boundary of this region is delineated by the largest closed orbit within the cell; here, the particle stream function has the same value it takes along the cell border. In the steady case, this orbit is

infinitesimally close to the upward flow at the cell boundary. Motion along the cell boundary corresponds to separatrix motion in a pendulum.

Stommel concluded that this simple picture explained why the plankton tows in the direction of wind were less variable than those taken across the wind. The large variations in yield observed in tows taken parallel to the rolls distinguish those that sample a region of retention from those that are taken in relatively plankton-free regions between them. Tows perpendicular to the rolls sample both the plankton-dense and plankton-free regions and hence are more uniform.

Without loss of generality, we consider only negatively buoyant particles which are initially within the cell with a fluid stagnation point at $x = 3\pi/2$, $y = 3\pi/2$ (the upper right quadrant of Figure 5.1). Denote the stagnation point of the particle motion by x_s. At this point the fluid velocity is upward in direction and equal in magnitude to the settling velocity of the particle. Therefore

$$x_s = \sin(\gamma) \tag{5.8}$$

For a given value of γ, the orbit of a retained particle is uniquely identified by the location of its right most crossing of the line on which the horizontal (x) component of the fluid velocity vanishes (that is, the line $y = 3\pi/2$). The value of x at this point is denoted x_r. In steady flows, paths of particles with different initial positions do not cross unless they follow the same streamline (the phase space is two-dimensional).

Trajectories are determined by integrating equations (5.6)

numerically with a sixth order Runge-Kutta scheme using subroutine DVERK from the International Mathematics and Statistics Library (IMSL, 1978). Integration of trajectories in the steady flow is straightforward. The time steps used were typically on the order of $\Delta t = 0.01$. Trajectories of integrable orbits were not sensitive to the precise value of Δt near this choice.

First consider particles located within a region of retention. Figure 5.3 shows the period of the particle orbit as a function of x_r for several values of γ. Near the fluid stagnation point ($x = 3\pi/2$, $y = 3\pi/2$), fluid parcels (and $\gamma = 0$ particles) are in solid body rotation with period $P = 2\pi$. The orbital period increases with increasing x_r, becoming infinite for a particle following the orbit along the ascending cell boundary. For a given value of γ, particles near the particle stagnation point have the minimum x_r and lowest period orbits. As γ increases, the period of these tightest orbits ($x_r \approx x_s$) also increases. All particles with $x_r > x_s$ are retained.

The increase of the minimum period with γ may be understood as follows. On translation of the origin to the fluid stagnation point, the particle stream function becomes

$$\varphi(x,y) = \cos x \cos y + \gamma x \quad . \tag{5.9}$$

Expanding the velocity in a Taylor series about the particle stagnation point $\mathbf{x}_s$, we have, to leading order,

$$\dot{x}(x,y) = \dot{x}(x_s,y_s) + (x - x_s) \left.\frac{d\dot{x}}{dx}\right|_{\mathbf{x}_s} + (y - y_s) \left.\frac{d\dot{x}}{dy}\right|_{\mathbf{x}_s}$$

$$\dot{y}(x,y) = \dot{y}(x_s,y_s) + (x - x_s)\left.\frac{d\dot{y}}{dx}\right|_{x_s} + (y - y_s)\left.\frac{d\dot{y}}{dy}\right|_{x_s}$$

or

$$\begin{aligned} \dot{\tilde{x}} &= -\kappa\,\tilde{y} \\ \dot{\tilde{y}} &= -\kappa\,\tilde{x} \end{aligned} \tag{5.10}$$

where

$$\begin{aligned} \tilde{x} &\equiv x - x_s \\ \tilde{y} &\equiv y - y_s \\ \kappa &= \cos(x_s) \end{aligned} \tag{5.11}$$

and $\mathbf{x}_s \equiv (x_s,y_s) = (\sin^{-1}(\gamma),0)$.

Particles near the particle stagnation point are in solid body rotation with period

$$P = \frac{2\pi}{\kappa} \tag{5.12}$$

This is the line in Figure 5.3. The cross marks along this line represent the locations of the stagnation points for numerical calculations with the parameter values specified in the caption.

In discussing sedimentation, it is useful to distinguish the particles which remain in the original cell from those which do not. A particle which passes through the bottom cell boundary is said to "fall out" of the cell, as opposed to a "retained" particle which does not cross a horizontal cell boundary. The horizontal motion of the particles is strictly that of the fluid; contours of zero horizontal fluid velocity (the lines $y = n\pi$, $n = 0,1,2,\ldots,$) are barriers which the particles cannot cross.

The symmetry of the flow field requires that the net effect of the fluid flow on the settling velocities, averaged over all space, is

zero. It is more interesting to examine the effect in the region of retention or the region of fallout separately. The area of the region of retention may be calculated as follows. Consider the region $0 \le x \le \pi$, $\pi \le y \le 2\pi$ (see Figure 5.2 a). Compute the area of the region of retention by integrating the contribution at each value of y from the point at which the streamline of value zero leaves the y axis until it returns. By symmetry this area is divided evenly by the line $y = 3\pi/2$. Thus

$$R_\gamma = \frac{2}{\pi^2} \int_{y_{min}}^{\frac{3\pi}{2}} dy \; x_{max}(y) \tag{5.13}$$

where x_{max} is defined by

$$\psi(x_{max}, y) = 0$$

or

$$\gamma \, x_{max} = -\sin(x_{max}) \sin(y). \tag{5.14}$$

The fraction of the cell occupied by the region of retention is shown as a function of γ is shown in Figure 5.4. As expected, the fraction of area in which the particles are retained decreases from one for neutrally buoyant particles to zero for particles whose Stokes velocity is equal to the maximum fluid velocity. The region contains half the cell area for

$$\gamma \approx .35 \; .$$

Section 5.2: Phase Wrapping

Before considering a time-dependent streamfunction, we examine the behavior of a cluster of particles introduced into the steady

flow of the type examined above. As a line of particles initially on the upper cell boundary (completely outside the region of retention) falls though a series of cells its length increases linearly with time. A line which is initially located entirely within the region is rolled up by the flow as shown in Figure 5.5. The density of particles, when projected onto a horizontal plane, will evolve as in the upper panels of Figure 5.6. Visible particles distributed in a fluid roll, when viewed from above, may take on the appearance of the lower panels of this figure. The well defined structures in the projected density mimic the familiar phenomenon of vortex roll-up in suitably dyed fluids.

A similar behavior has been discussed by Quin (1984) in a study of stellar dynamics. Quin follows the motion of stars from a light spiral disk as they interact with the gravitational potential of a massive elliptical galaxy. While shells are apparent in his simulations when the data are plotted in physical space (and in the observations), they are more striking when the data is viewed in a velocity-position space. For this reason Quin calls the phenomena phase wrapping.

Stommel motivated his original study with a discussion of patterns formed in the sea. As shown by the studies of Quin, the problem has implications over a large range of scales; it may bear on such questions as dune formation in shallow water beaches, though the inertial effects may be significant in such a case.

Section 5.3: Experimental Observations

The motion of small negatively buoyant spheres in an axisymmetric flow is easily observed in the laboratory.[1] An apparatus consisting of a cylindrical tank filled with a high viscosity fluid and mounted with its axis horizontal is sufficient. As the cylinder is rotated about its axis, the fluid quickly attains solid body rotation. Small spheres placed in the ascending flow are observed to follow nearly circular orbits about the particle stagnation point. If small air bubbles (which are positively buoyant) are present, they are observed to execute similar motion in the descending fluid on the opposite side of the tank. A detailed investigation of this type of system has been performed by Tooby, Wick, and Isaacs (1977), using a variety of test particles and rotation speeds. On time scales long relative to the fluid motions, the orbits evolve, the density and diameter of the test particle determining the specific manner in which its orbit evolves. The instability of closed orbits is due to inertial effects and the influence of the walls on finite diameter test particles. Particle-particle interactions are also observed to produce large perturbations in particle motions (J. Whitehead, private communication). In the cases of precipitation formation and magma crystal growth, the properties of a single particle change with time influencing the particle's motion, which in turn feeds back upon the particle's growth and the surrounding fluid. None of these

---

[1] The following observations were made with J. Whitehead and B. Frazel at the Woods Hole Oceanographic Institute (see Smith, 1984).

complicating effects were considered in section 5.2 nor will be in what follows.

Experimental techniques of flow visualization (e.g. Corrsin, 1950) rely on tracers assumed to be passive. The rate of growth of material lines in a turbulent flow is expected to be exponential and lead to the development of fractal structures (Sreenivasan and Meneveau, 1986). For nonideal tracers, these behaviors occur in an unsteady laminar flow (Smith and Spiegel, 1986), leading to the formation of self-similar distributions.

Section 5.4: Time Dependent Flows

To consider flows smoothly varying in time, we let

$$A(t) = 1 + \epsilon \sin(\omega t) \tag{5.15}$$

With this choice, the phase space of system 5.5 becomes three-dimensional and the possibility for chaotic behavior arises. One could consider more spatially complicated flows by superimposing additional periodic structure periodic with half the wavelength of this flow. Repeating the process with additional, smaller-length scales would yield a flow similar to the β model. As shown below, the particle patterns produced by the single length scale are already quite intricate.

The presence of chaotic motion is immediately felt in attempts at analytic solution through perturbative methods where the problem of small denominators destroys the convergence of the solution for many initial conditions (see Lichtenberg and Lieberman (1983)). Here, we

continue to study the system via numerical simulation.

In most instances, the trajectories in three dimensions are either projected onto a plane or a two-dimensional surface of a section is taken (see Chapter 1). The situation is simplified in our case because the flow is strictly periodic in time; stroboscopy at the frequency of the fluid motion is equivalent to taking a surface of section. Runge-Kutta integration schemes are ideally suited for this method. Even so, numerical integration is a resource consuming process. A two dimensional area preserving map able to simulate long evolutions efficiently was constructed for this system. This mapping is described in Appendix 3.

We consider the effect of small ϵ on the motion of a particle well within the region of retention for the corresponding $\epsilon = 0$ flow. For ϵ equal to zero, the particle moves on a roughly circular path. For small ϵ, the particle will, initially, oscillate about its steady flow orbit with frequency ω (see Figure 5.8a). The asymptotic stability of this motion for non-zero ϵ was not established until 1963 (see Moser, 1968); the nonlinearities involved make the question of the stability of this system similar to that of the three body problem.

For small ϵ, particles well within the region of retention display three distinct classes of motion. The first corresponds to oscillations about the steady flow path. When a trajectory of the type (e.g.: Figure 5.7a) is viewed in section, the orbit again fills out a closed curve as shown in Figure 5.7b. By strobing at different phases it is seen that the particle winds about on a torus in phase

space. A single point in phase space defines the future evolution of the system; thus when a torus is covered densely, all initial conditions within a torus remain within it. In section, the tori appear as closed curves; initial conditions within closed curves on a Poincaré section are trapped there. This intuitive result holds for two-dimensional tori in three-dimensional space and therefore our system. Note, however, that by the definition of topological dimension (see Poincaré's quote in §1.1) this argument fails in spaces of dimension greater than three, giving rise to a slow spreading of trajectories known as Arnold diffusion (Lichtenberg and Lieberman, 1983).

Viewed stroboscopically, the orbits of nonzero γ particles near their particle stagnation point will move through an angle $\Delta\theta_i$ between the $(i-1)^{th}$ and i^{th} recording and will, for $\Delta\theta$ sufficiently irrational, fill out a closed curve[2]. Initial conditions for which $\Delta\theta$ is a rational angle resonate with the strobing frequency so that a finite number of points are observed in a repeating sequence. For nonzero ϵ, not too large, the majority of particles of the first type continue to move on trajectories that are tori. Two different types of motion are observed for particles whose unperturbed period is near resonance with that of the fluid: one corresponds to motion on islands, the other to chaos. For the former, in each revolution about x_s, the particle follows one of several distinct pathways. Which path is executed depends on the phase of the flow as the

---

[2]If $\Delta\theta$ is not sufficiently irrational, the trajectory may describe a Cantor set.

particle crosses the x axis from below ($x > x_s$). This type of motion is shown in projection in Figure 5.8a. The clear regions shown remain clear, with the trajectory being restricted to, and slowly filling, the outlined region. In this example two revolutions about the stagnation point, one along each branch, occur in three cycles of the background fluid flow; the particle executes three revolutions about x_s until its crossing of the x axis occurs at approximately the same position and phase with respect to the fluid flow period. When such a trajectory is strobed at the fluid flow frequency, islands are observed (Figure 5.8b). Particle motion on these islands is stable. The particle visits every island in turn, slowly delineating each. Poincaré sections taken at different phases are shown in Figure 5.10. The islands slowly deform and rotate in the direction of particle motion until, one full fluid period later, particles initially on island 1 (2,3) have taken positions on island 3 (1,2). Recalling that these figures are cross-sections of a three-dimensional phase space, it is seen that this motion takes place on a torus which is stretched and twisted, closing on itself in three fluid periods. Particle paths wind around on this torus. Plotting t as z results in the three-dimensional reconstruction of Figure 5.9a, while the periodic boundary conditions are more naturally reflected in Figure 5.9b where the trajectory is shown in polar coordinates (r,θ,z) related to (x,y,t) by the transformation

$$\begin{aligned} r &= x + r_o \\ \theta &= \omega t \\ z &= y \end{aligned} \qquad (5.16)$$

where the constant displacement r_o is chosen relative to the point at which the trajectory crosses the line $y = {}^{3\pi}/_{2}$ at zero phase of the fluid. Initial conditions sufficiently inside or outside the island ring (relative to the particle stagnation point) wind about a single torus. Particles initially located between the islands at the same distance from the stagnation point are observed to display chaotic motion For sufficiently small ϵ, these trajectories remain in the vicinity of the island ring.

The general structure of this pattern is understood (see Lichtenberg and Lieberman, 1983). The particle stagnation point corresponds to a stable elliptic point. For nonzero perturbations, trajectories about the stagnation point which resonate from a series of elliptic and hyperbolic points. The (stable) elliptic points correspond to the centers of islands, the (unstable) hyperbolic points to chaotic regions. Surrounding each of these equilibrium points is another generation of elliptic and hyperbolic points. The cascade continues to all scales. For the simplest integrable orbit, each passage through the plane corresponds to a rotation about the particle stagnation point, θ grows in a regular manner, filling the interval $-\pi < \theta \leq \pi$ densely and variations in radius are small; as a function of θ, the radius is single-valued. In the island case, there are bands of values at which θ is never observed, $\mathbf{r}$ is a double-valued function of θ. In a chaotic trajectory on which the particle falls out of the cell. This results in values of $\mathbf{r}$ greater than $\sqrt{2}\pi$ and biases θ toward large angles and $\Delta\theta$ toward small values. For all chaotic trajectories, $\mathbf{r}$ is multi-valued function of θ.

The appearance of this structure corresponds to a qualitative change in the region of retention when the flow becomes temporally periodic. In the case of steady flow, particles arbitrarily near an up-flowing branch are retained, completing closed orbits. In a periodic flow, the region of retention detaches from the cell boundary. Particles initially in the band of separation will often remain in the cell for many revolutions, but (most) eventually fall out. For small ϵ, a particle oscillates about its equilibrium path. As long as these excursions are completely within the region of retention, the particle will remain in the cell. A particle which oscillates to a point outside the retention region may remain in the cell for a time, depending on where in the cell it is when it crosses the boundary. If the frequencies of these two oscillations are incommensurate, these particles will eventually cross the boundary near the bottom of their trajectories and fall out of the cell. For some initial positions, a resonance between the fluid oscillations and the particle motions occurs which tends to stabilize the particle, producing stable islands in the chaotic sea. Gaps corresponding to the location of this type of island chain are visible in several of the figures (eg. Figure 15). Figure 5.11 is a histogram of the frequency of various residence times, it is clear that particles take much longer to fall through a series of rolls than would be predicted from the steady case.

The strobed paths for a variety of initial positions are shown in Figure 5.12. Counting from the left, the first particle (1.1π, 1.5π) falls through the cell, oscillating about the strobed path shown.

This line presents a barrier which other particles do not cross; hence the open region in the lower left-hand side of the figure. (The motion of initial conditions in this open area is symmetrical with that of the trajectories shown.) As the initial position of the particle is moved to the right along $y = 3\pi/2$, the trajectory breaks up into islands, which in turn become part of the chaotic sea shown in the figure. Particles initially in this area are often trapped in a cell for many revolutions and then fall (drifting) through the next cell (and often several more) before becoming re-entrained. Embedded in this chaotic sea are regions avoided by the falling particle. The largest of such areas is the region of retention containing the particle stagnation point. Islands are observed in this and several other of the barren regions where the particle motion is such that they are stabilized against sedimentation as discussed above.

It is this stabilization which complicates the calculation of an average fallout velocity. In the vicinity of every island structure there exists a higher-order island chain, each member of which is surrounded by yet another chain. A particle in the chaotic sea which moves into the region will remain outside these islands but may remain in this "reef" for an extended period of time. When the probability distribution of a Poincaré section is viewed, the reef areas that have been visited stand out as regions of high probability. The long runs required to get reasonable statistics are more easily obtained with conservative maps. The structure of these strange accumulators is described in Smith and Spiegel (1987), which is reproduced here as Appendix 4.

The effect of increasing ϵ with fixed v_s is shown in Figures 5.13. Here, the area of the chaotic region is observed to grow with ϵ. Individual islands are observed to break up, allowing particles to pass within, but also forming the intricate reef regions of the accumulator. The evolution of the upper island of Figure 5.13b is shown in detail as ϵ increases in Figure 5.14.

For moderate values of δ, the chaotic region B occupies a large area of the section. The chaotic sea has holes on all scales corresponding to island chains. Sets like the shown in Figure 5.15 have been called fat fractals by Umberger and Farmer (1985), who proposed a scaling relation which can be used to estimate the total area visited by a chaotic trajectory.

Before considering the motion of swarms of particles, we note that particle motion at large ϵ is qualitatively different from that of small ϵ. Quasi-stable regions in a flow with large ϵ ($\approx$10.0) have been found where the particle revolution period is slightly less than half the fluid period. Such a particle, initially near the top of its orbit will be swept around by the strong flow, again to near the top of the cell, as the flow weakens it will sink down toward the cell center and then be swept around in the opposite direction sense by the second half cycle of the fluid flow. Often the radius of the particle from the stagnation point will increase until the particle falls out, however some initial conditions particles have been observed to be carried up above their initial points and then dropped back near their original position (and phase). In this manner, the particle is retained in the cell for the entire observation (= 300

fluid periods).

Figure 5.16 shows, at several different times, the locations of 513 $\gamma = 0.25$ particles that were initially spread along the line y=2.0 in the x interval (1.85, 1.90) as they evolved in a flow with $P = 4.5$ and $\epsilon = 0.50$. Particles from this interval are outside any region of retention; they spread in vertical extent, but stay within the original cell width. In the final frame, the particles are spread over 9 cells. In this case, the abscissa is the value of y (not mod 2). We wish to see whether a fractal structure develops. However, there are not enough points in Figure 5.16 to do this. In Figure 5.17, we show the results of a calculation designed to suggest the detail in the loops of Figure 5.16. In this calculation, the periodic boundary conditions in y are applied, showing only the upper half of a cell. There are long intertwined filaments extending into the lower half of the cell where the segment was stretched exponentially. This poses a resolution problem.

The complexity of this distribution is quantified by examining the vertical final separation of particles which were initially nearest neighbors. In Figure 5.18, we show the (scaled) y-coordinate of each particle as a function of x_0, the initial x-coordinate, for a sequence of times. Portions of these curves with very large slopes correspond to initial line segments of particles that have been stretched over many cell heights. The stretching and folding in x-y space of the original line of particles produces the self-similar structure seen in Figure 5.15. Braking the x_0 coordinate into steps of size Δx_0 and determining the length, L, of each curve as a

function of Δx_0, we fit L to the formula

$$L \propto (\Delta x_0)^{-\sigma}. \tag{5.17}$$

As a function of time, σ increases rapidly to a plateau. The precise form of this evolution depends on how we perform the calculations; the plateau at σ=0.76 is characteristic and appears to be independent of the initial particle density. This plateau does not survive indefinitely at fixed resolution. As expected, it persists longer if the initial density is higher. We estimate the value σ=0.76. We do not have a good way to determine the precision of this result but, on the basis of many such calculations, we would estimate that the internal errors are less than 10%. σ is not very sensitive to ϵ and γ for ϵ in the range 0.1 to 0.8. For ϵ less than about 0.1, the effect of time dependence is so weak that the particle spreading is very slow, while for large ϵ the integration time steps required become prohibitively small. As the scaling structure of Figure 5.19 develops, the length of the particle line increases rapidly. A plot of this length with time shows exponential growth (see Figure 5.20), though the fluid flow is not turbulent; exponential stretching of a material line of tracer is not a sufficient condition for turbulent motion in the host fluid.

Section 5.5: Conclusions

We have constructed a model for the behavior of particles

suspended in a time-dependent flow. It is observed that negatively buoyant particles may remain suspended in the flow for a time exceeding the estimate based on a sedimentation at the Stokes velocity. More relevant from a dynamical systems point of view is the observed self-similar inhomogeneities which develope and persist in the probability distribution of a single trajectory. The self-similar structure of these inhomogeneities pose another source of difficulty in determining the correlation integral from an experimental time series. Specifically, the application of the Grassberger-Procaccia algorithm to a finite sample of an trajectory which is (asymptotically) space filling in two dimensions may indicate a value of the correlation exponent which is significantly less than two.

Finally, it is demonstrated that a material line of tracers may develope a complex, self-similar distribution in a smooth flow field. The development of this pattern requires the rapid stretching and wrapping of the tracer line. The exponential growth of a tracer material line is not a sufficient condition for turbulent flow.

FIGURE CAPTIONS

Figure	Caption
1	Fluid streamlines of the steady flow corresponding to Equations 5.5. A streamline corresponds to a contour of streamfunction; each streamline shown is labeled with this value.
2	Particle streamlines in the steady flow case for several Stokes velocities as shown. Each streamline is labeled with the local value of the particle streamfunction.
3	The period of retained particle orbits as a function of initial position for several Stokes velocities.
4	Area of the region of retention as a function of γ.
5	Phase wrapping on a line of particles within the region of retention for the flow parameters ν = 0.2. The distributions correspond to times (a) t = 0, (b) t = 18, (c) t = 36, (d) t = 54.
6	The particle densities integrated vertically for the four states in the previous figure. The upper panels show the particle number explicitly while the lower panels are 'dust plots' simulating the appearance of suspended particles viewed from above.
7	A trajectory corresponding to motion on a torus (a) projected and (b) strobed.
8	A trajectory corresponding to motion on a period three island chain (a) projected and (b) strobed.
9	A three-dimensional reconstruction of the trajectory projected in Figure 8a. The reconstruction on the left shows the winding of the islands over one period of the background flow. On the right, time has been taken as an angular variable as described in the text. In this way the continuous nature of the trajectory is apparent.
10	Poincaré sections of the trajectory of Figure 8 taken at several phases. These section correspond

to planes of constant z in Figure 10 and show the islands at different phases.

11 A histogram of the residence times per cell for a particle in the chaotic fallout region. This trajectory was taken with P = 4.5, v = .25.

12 Strobed motions of six γ=0.25 particles in the time dependent Stomel flow, ϵ = 0.5, P = 4.5

13 Poincaré section of the γ=0.25 paths with P=4.5 and increasing ϵ, (a) ϵ=0, (b) ϵ=0.25, (c) ϵ=7.5.

14 The effect of increasing ϵ as shown in the "ear" region, γ = 0.25, P = 4.5.

15 An extended integration (3000 P) for seven initial conditions in the chaotic region; γ=0.25, P = 4.5.

16 Evolution of a line of particles initially on the upper boundary of a cell. In their initial configuration, the particles are labeled with letters alphabetically with increasing x coordinate. The position of the line is shown after (a) 2, (b) 5, (c) 6 (d) 7, and (3) 21 periods of the background flow.

17 A surface of section for the line of particles described in Figure 5.17. Only the upper half of the cell is shown.

18 Time development of a fractal showing the vertical displacement as a function of initial horizontal position at several times.

19 Final time sequence of Figure 19 at T=24 fluid periods.

20 Length of line segment as a function of time.

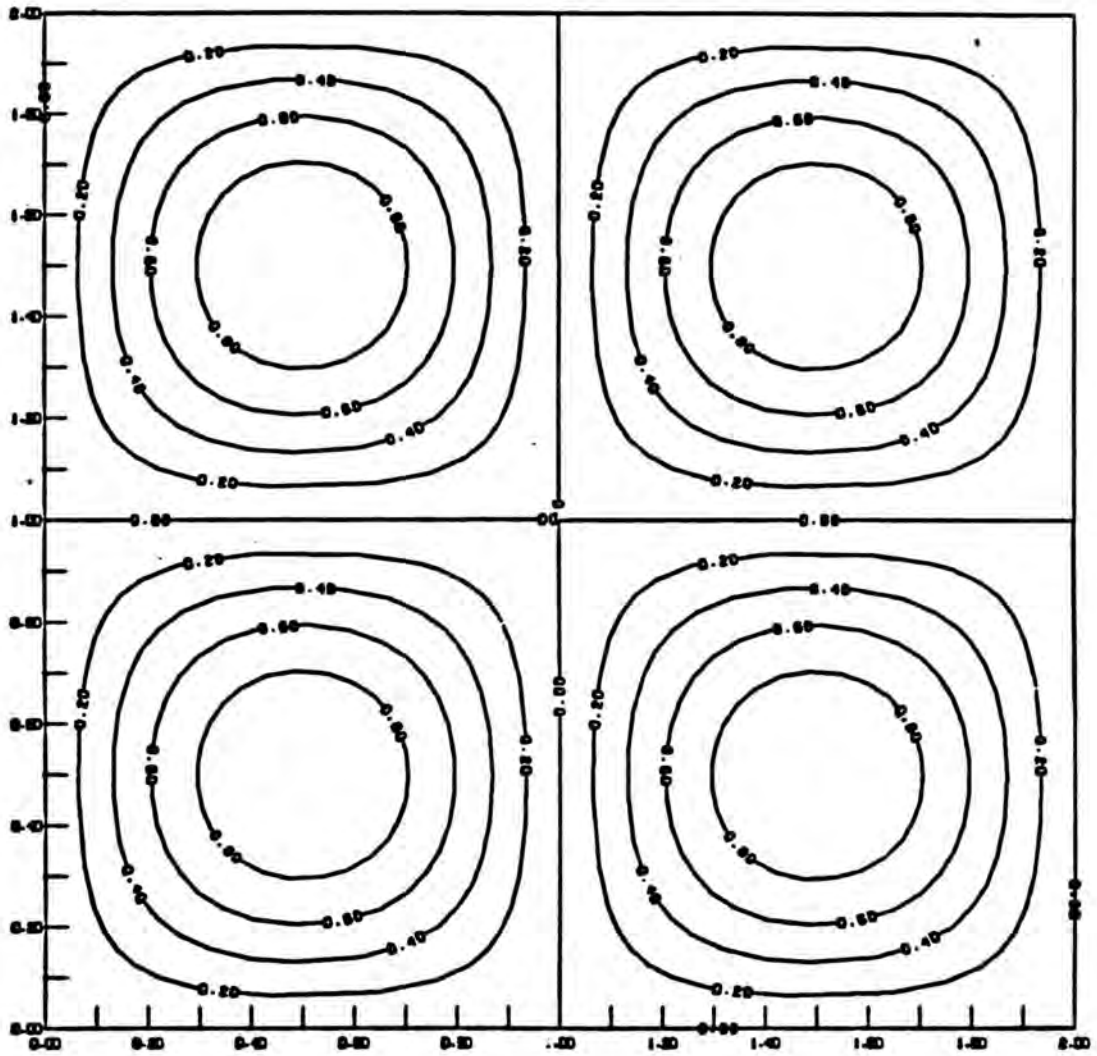

Figure 5.1

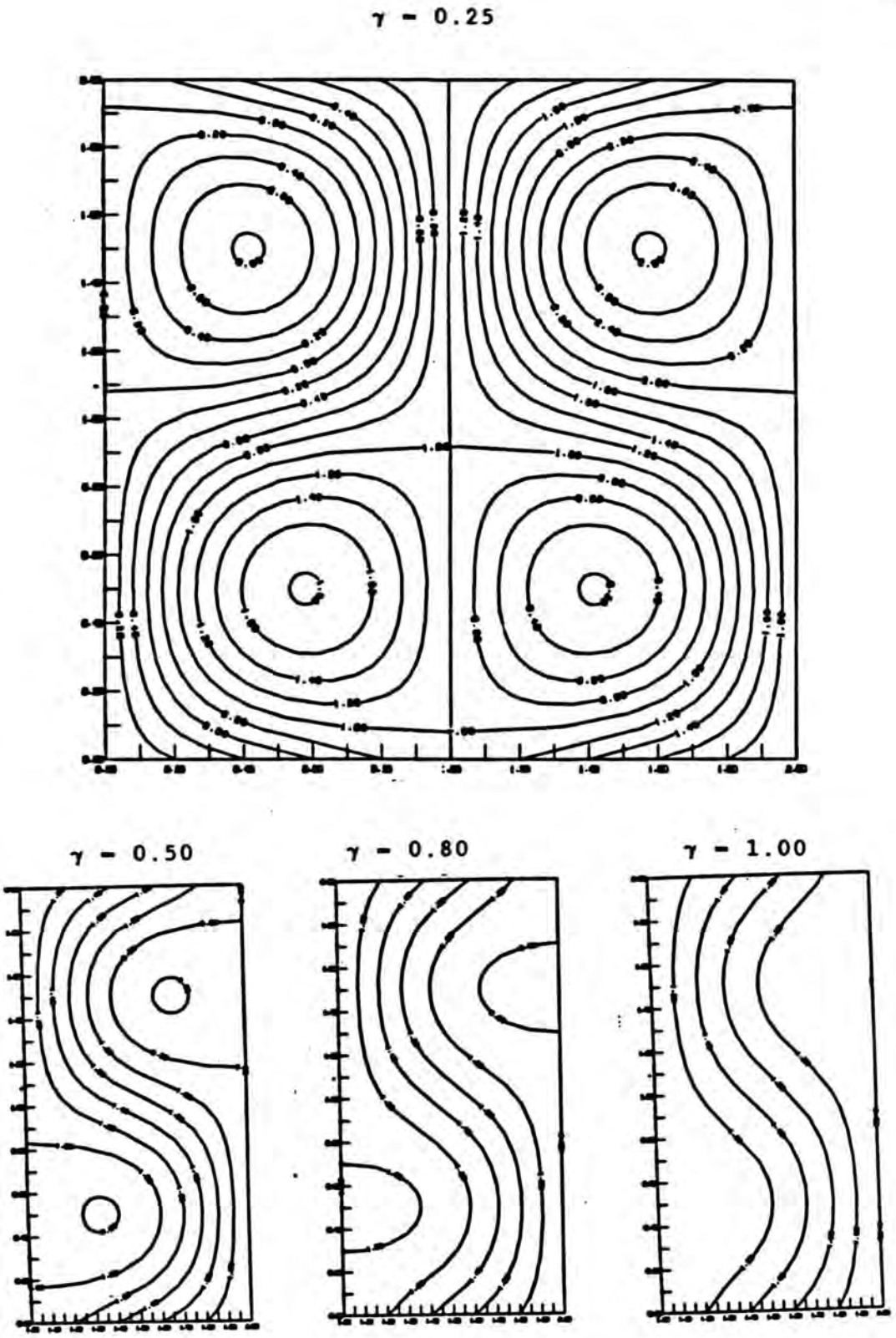

Figure 5.2

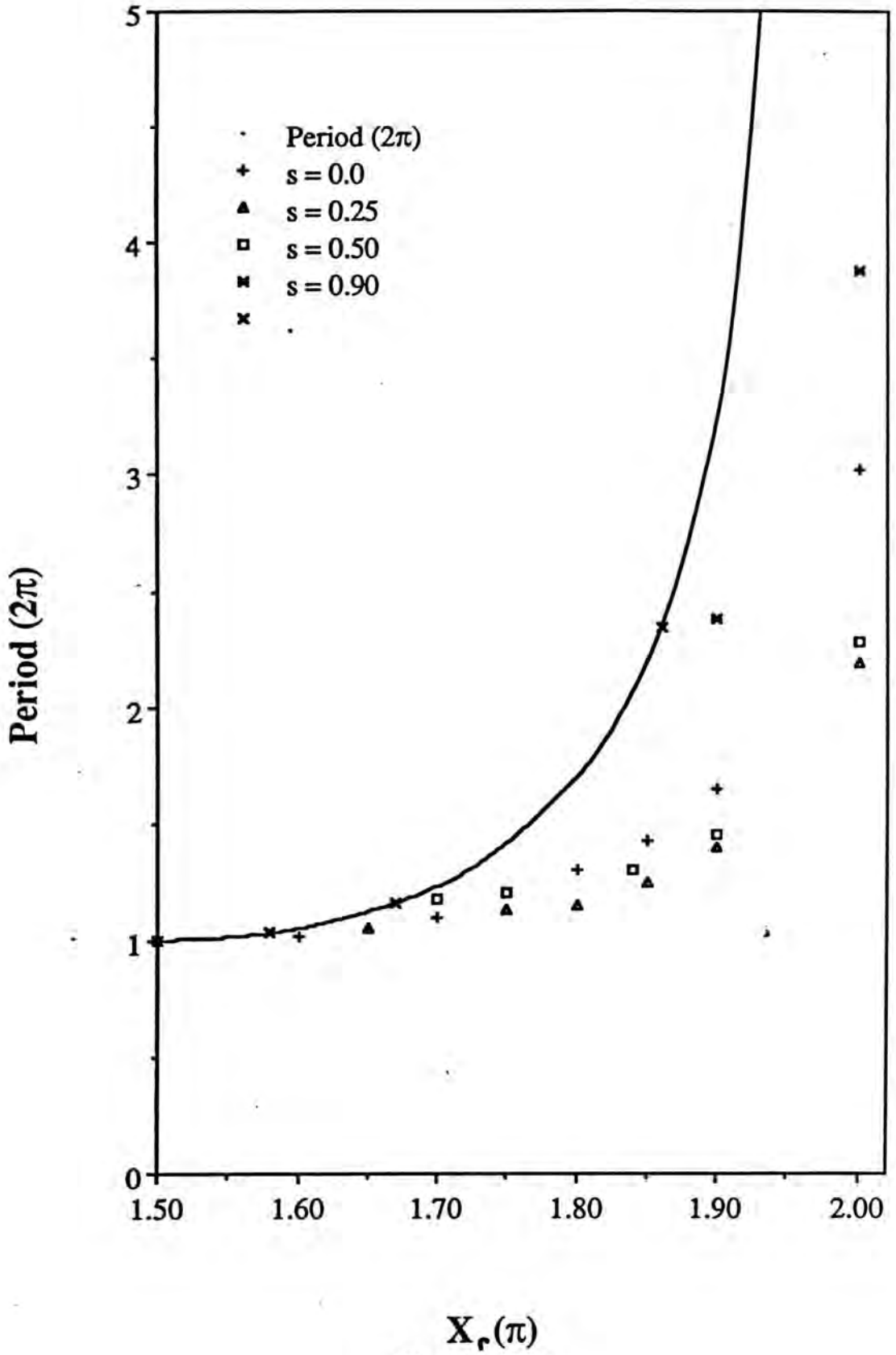
Period (2π)
s = 0.0
s = 0.25
s = 0.50
s = 0.90
Period (2π)
0
1
2
3
4
5
1.50
1.60
1.70
1.80
1.90
2.00
X_r(π)

Figure 5.3

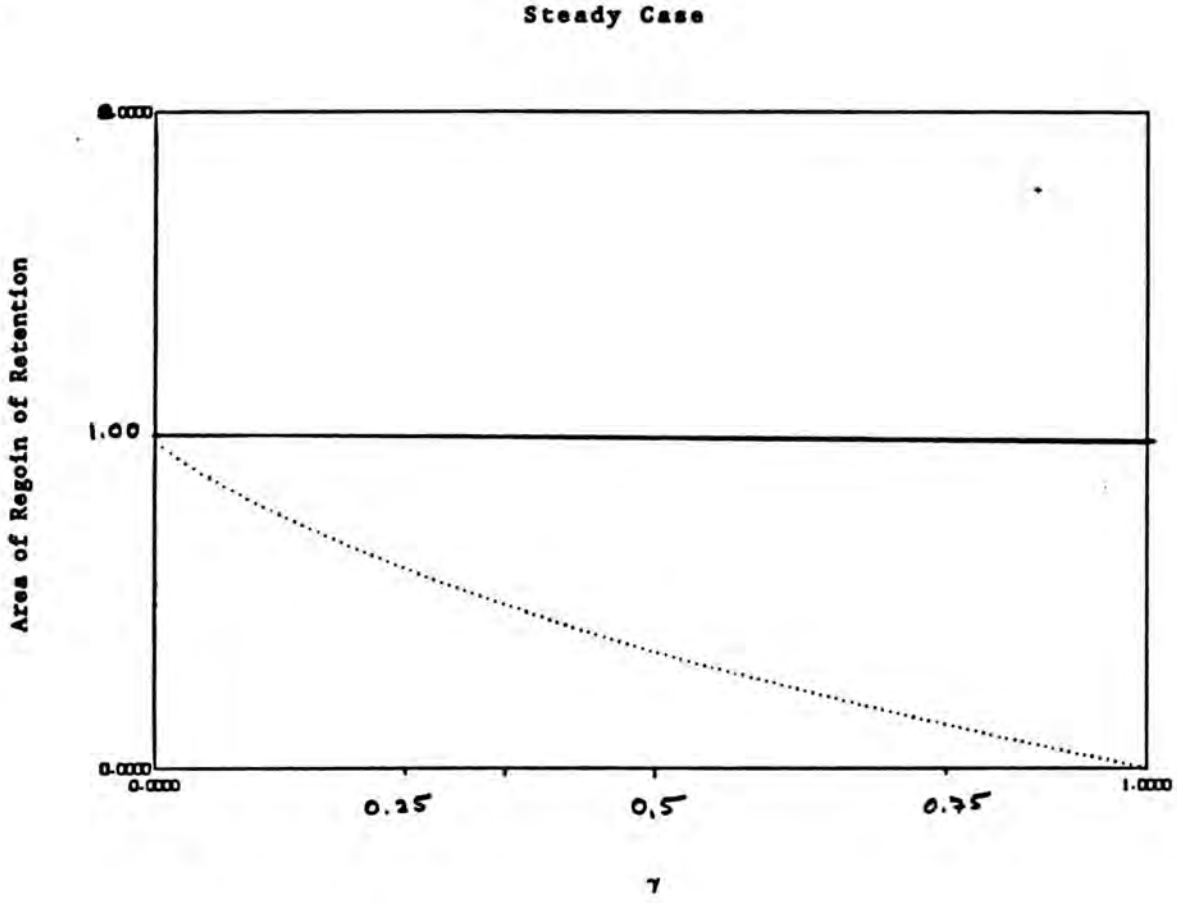
Steady Case
Area of Regoin of Retention
1.00
0.0000
0.0000
0.25
0.5
0.75
1.0000
τ

Figure 5.4

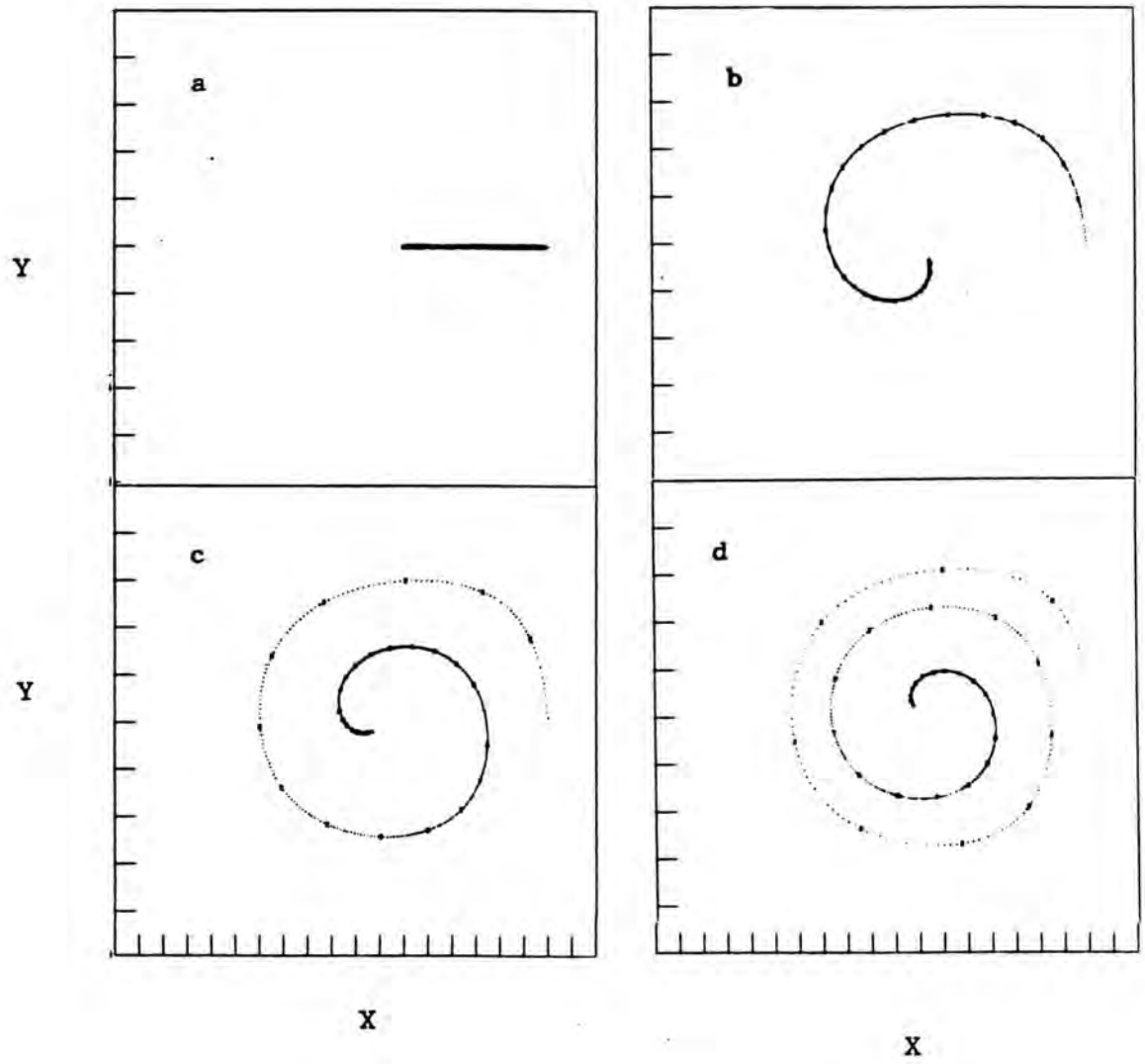

Figure 5.5

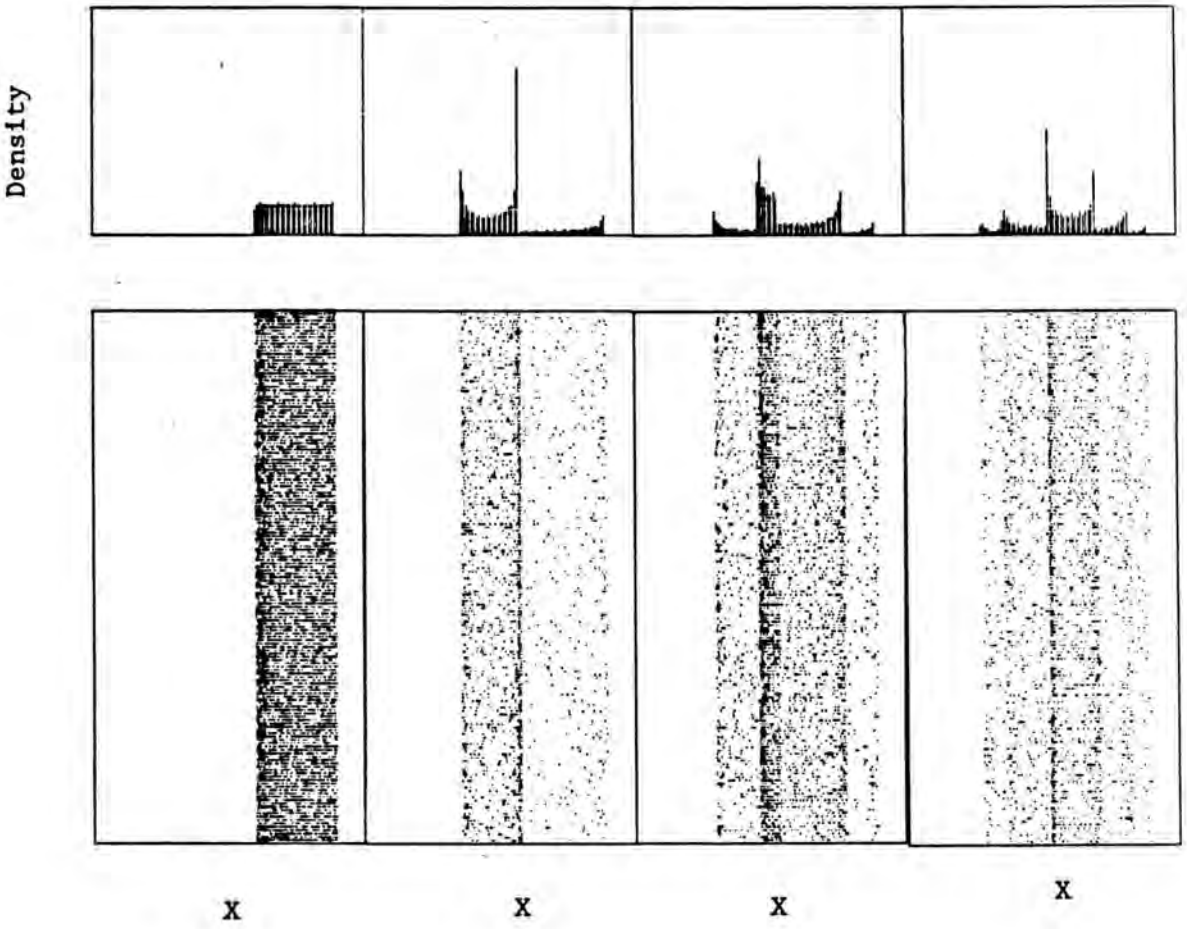

Figure 5.6

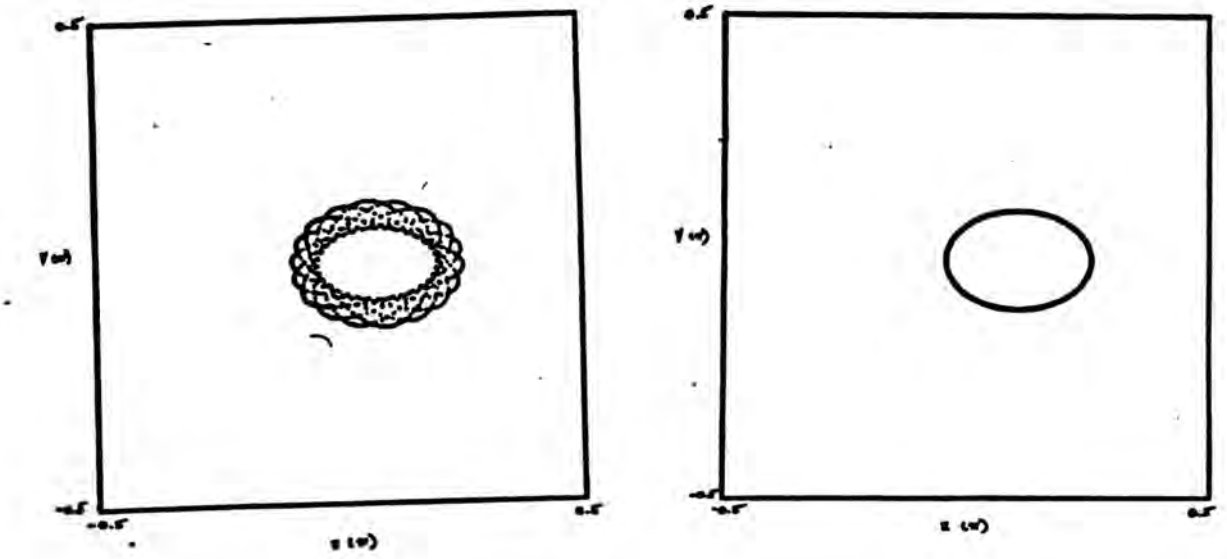

Figure 5.7

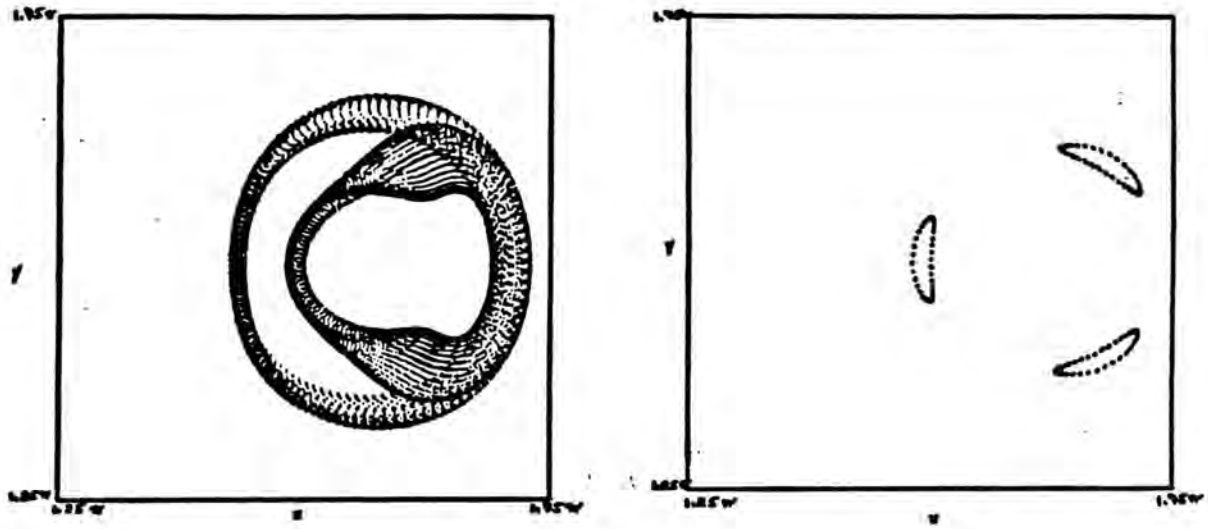

Figure 5.8

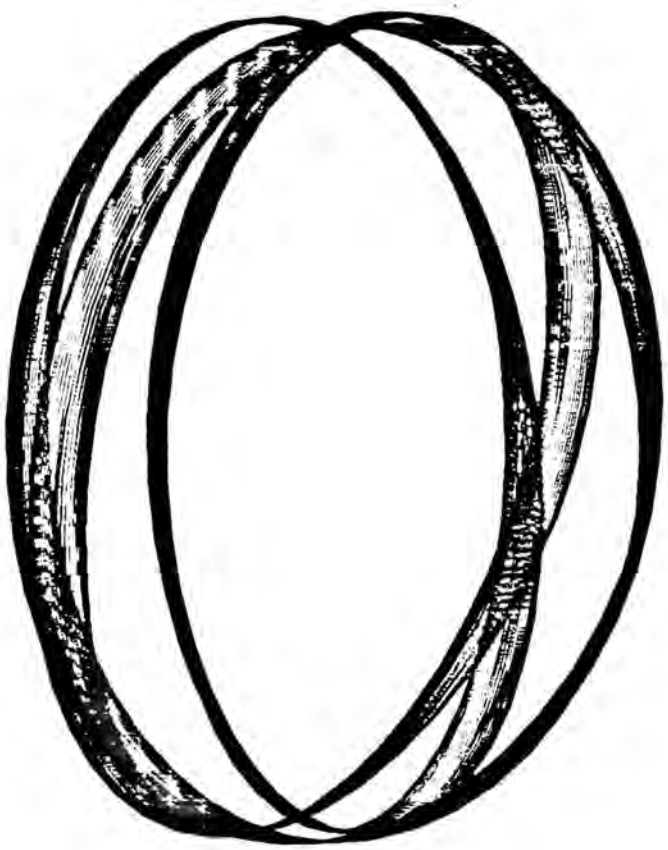

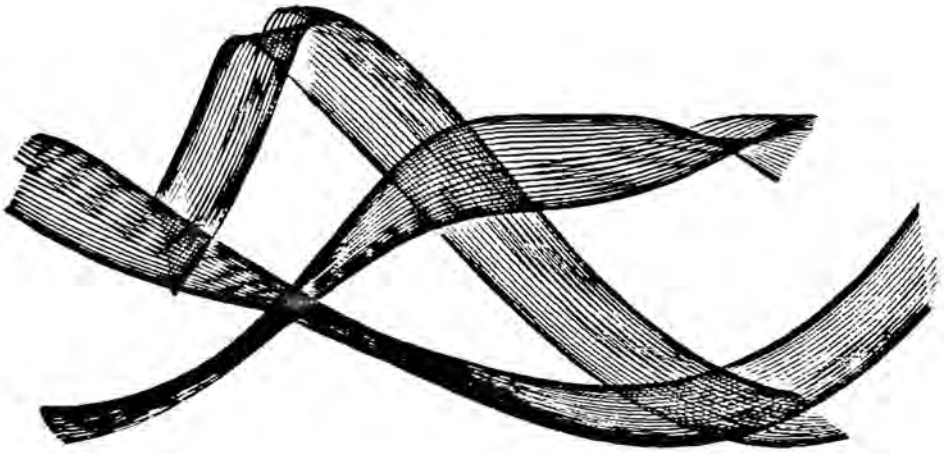

Figure 5.9

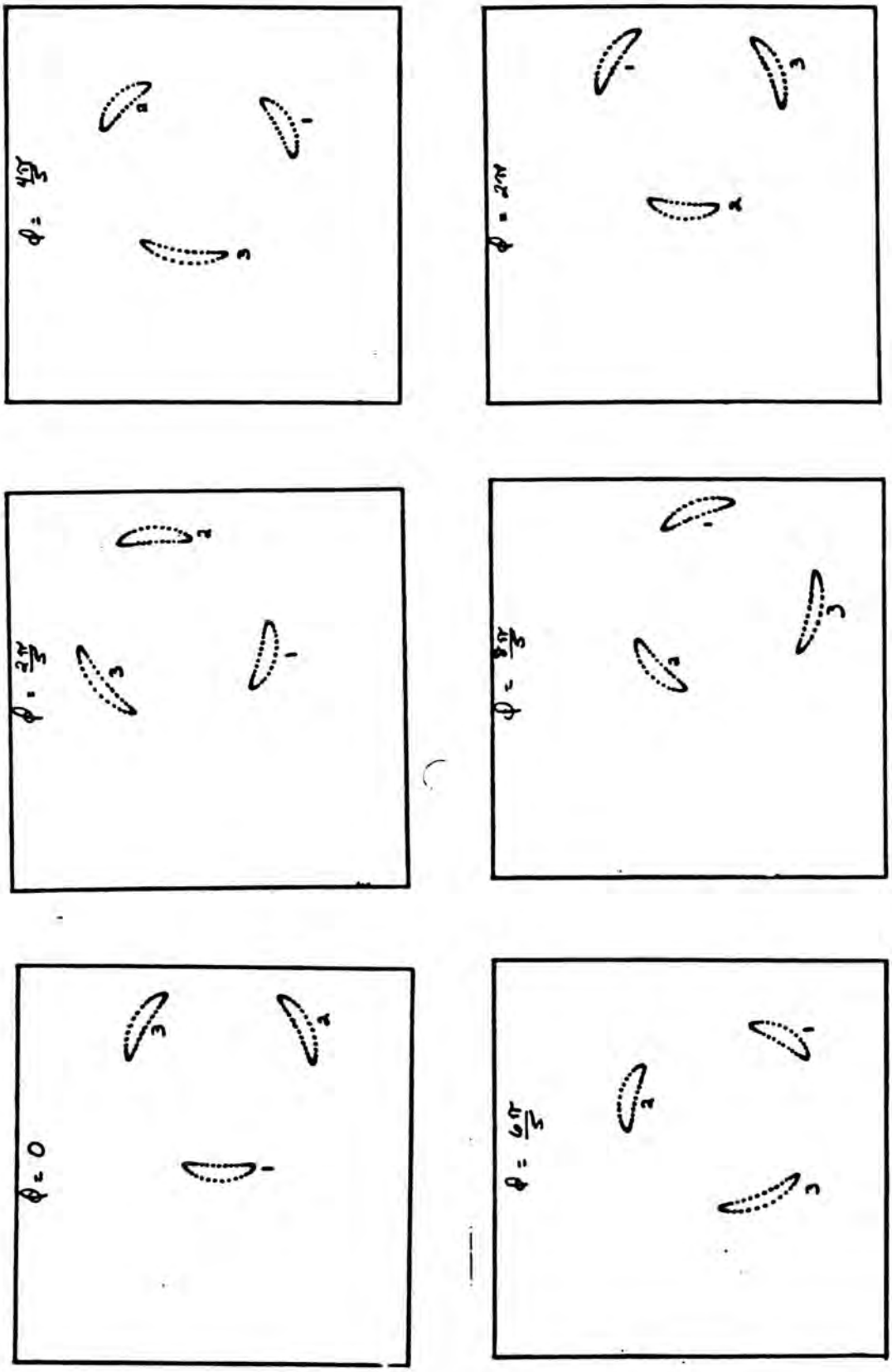
$\phi = 0$
$\phi = \frac{2\pi}{3}$
$\phi = \frac{4\pi}{3}$
$\phi = 2\pi$
$\phi = \frac{8\pi}{3}$
$\phi = \frac{10\pi}{3}$

Figure 5.10

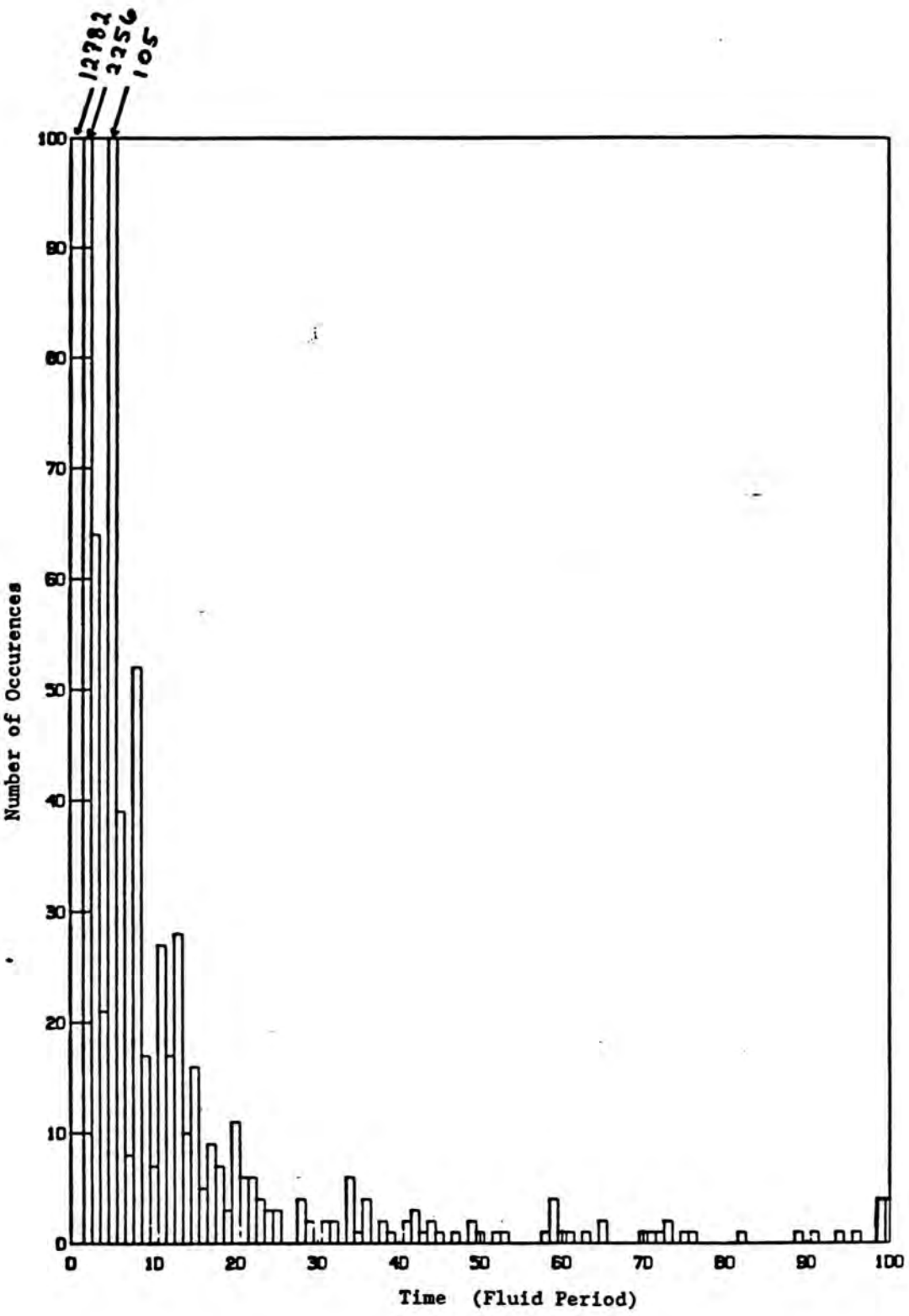
12782
3256
105
Number of Occurences
Time (Fluid Period)
0
10
20
30
40
50
60
70
80
90
100

Figure 5.11

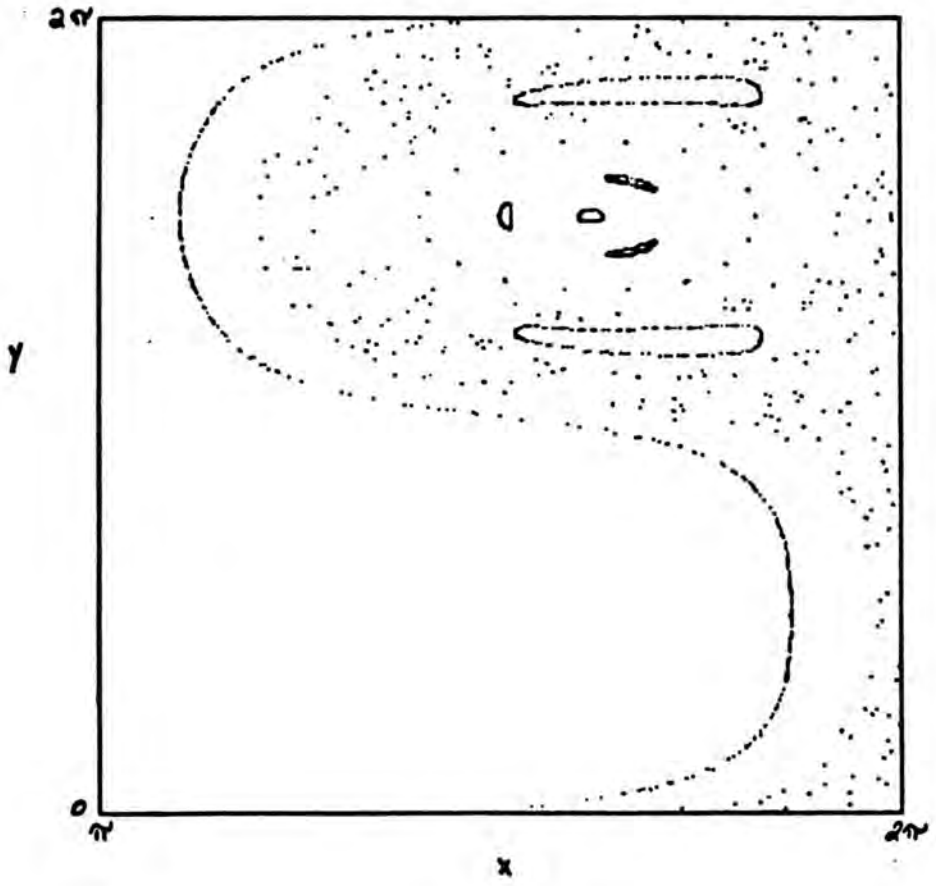

Figure 5.12

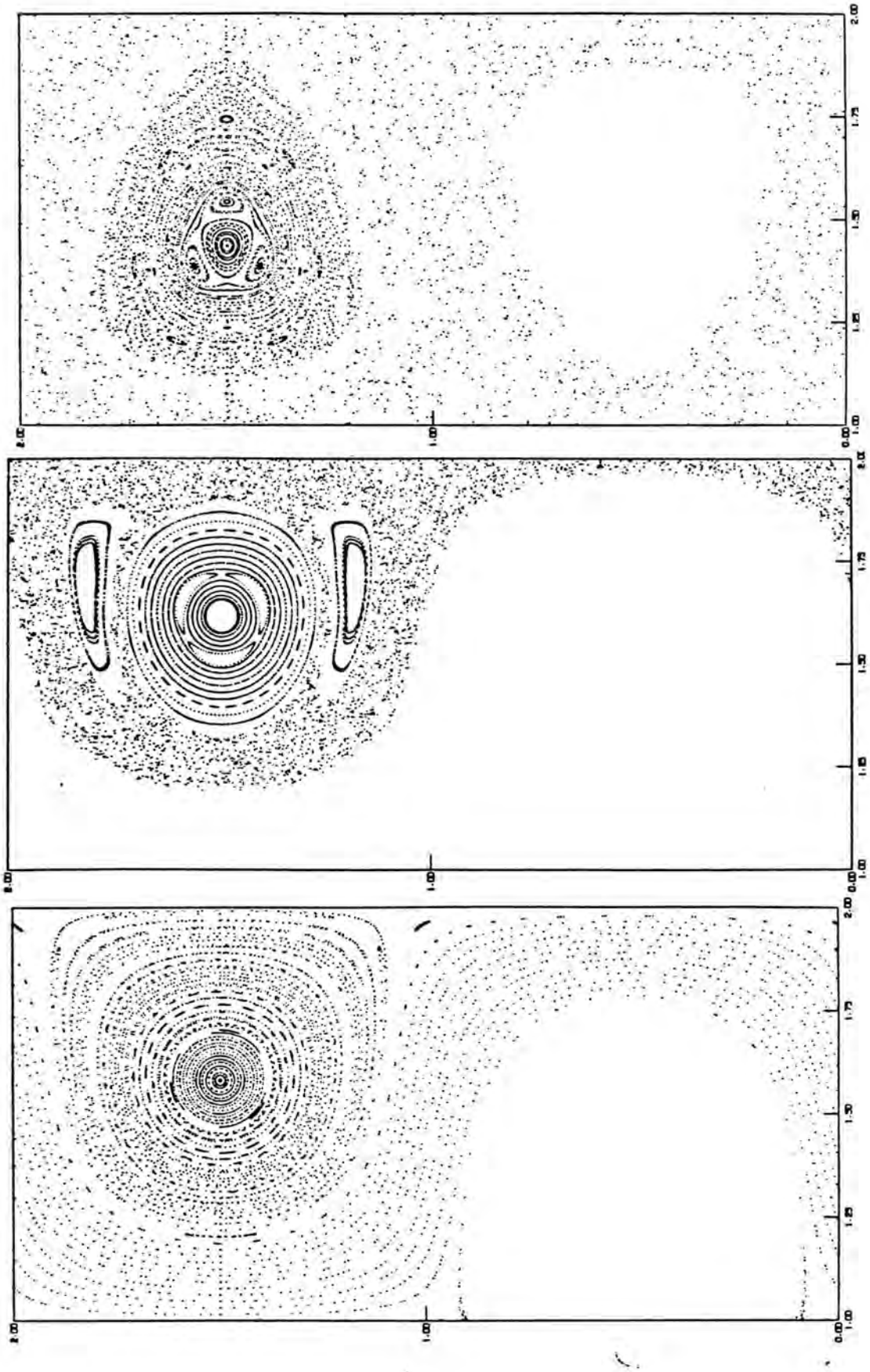

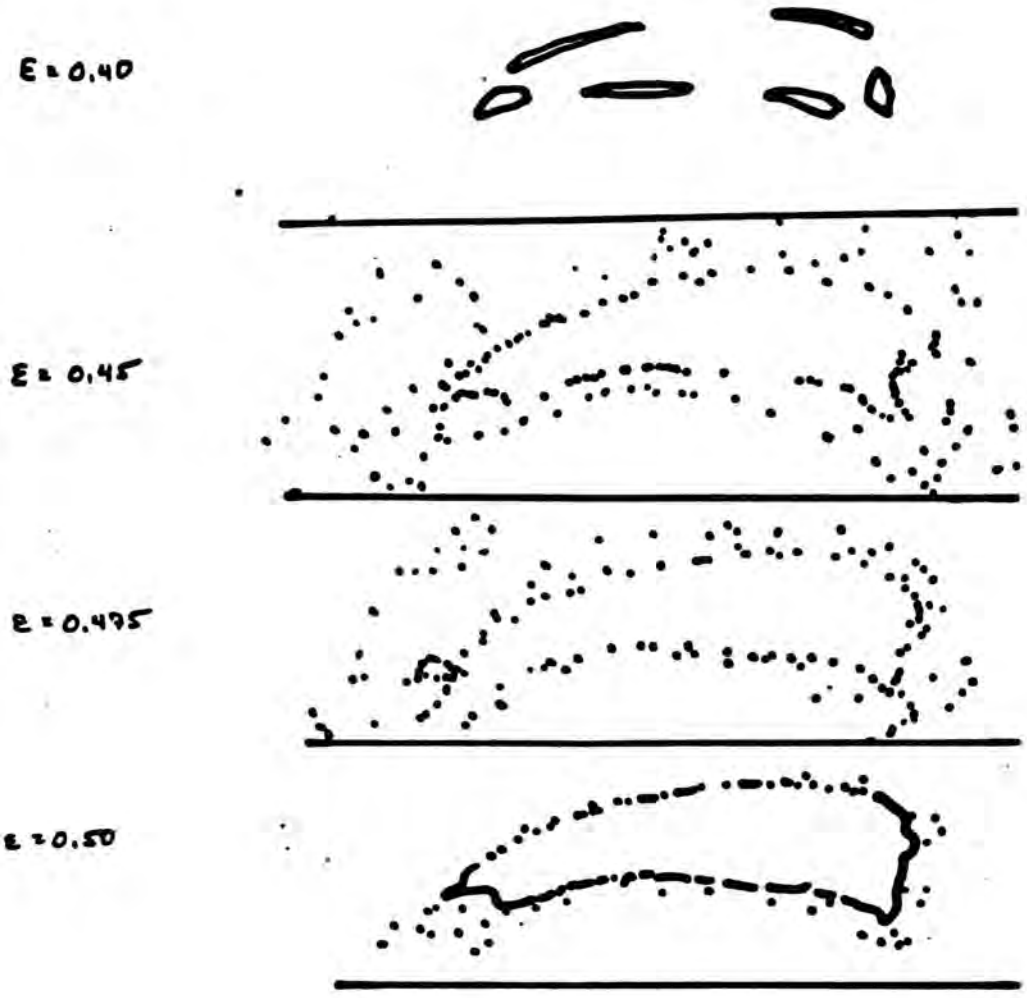

Figure 5.14

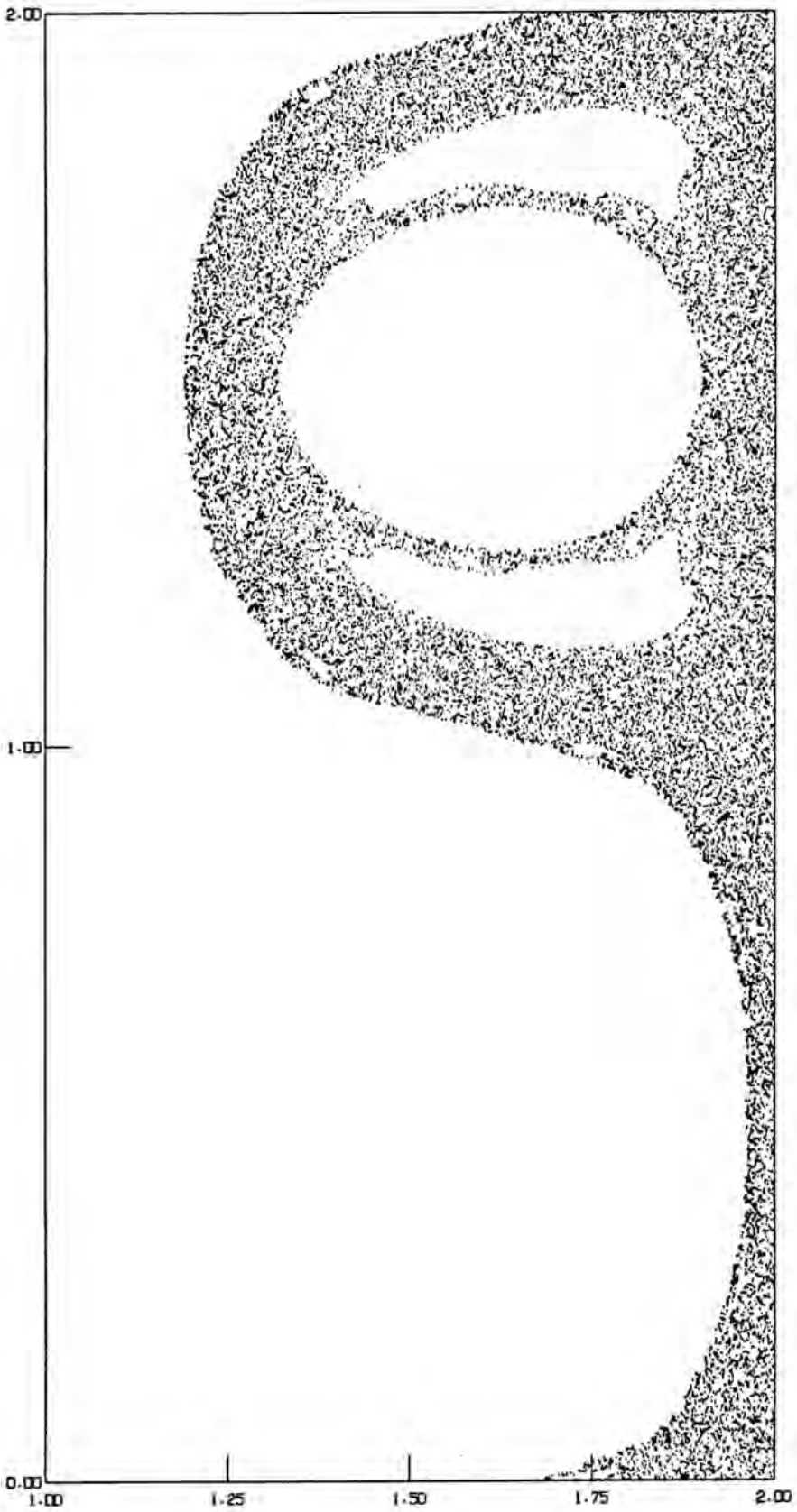

Figure 5.15

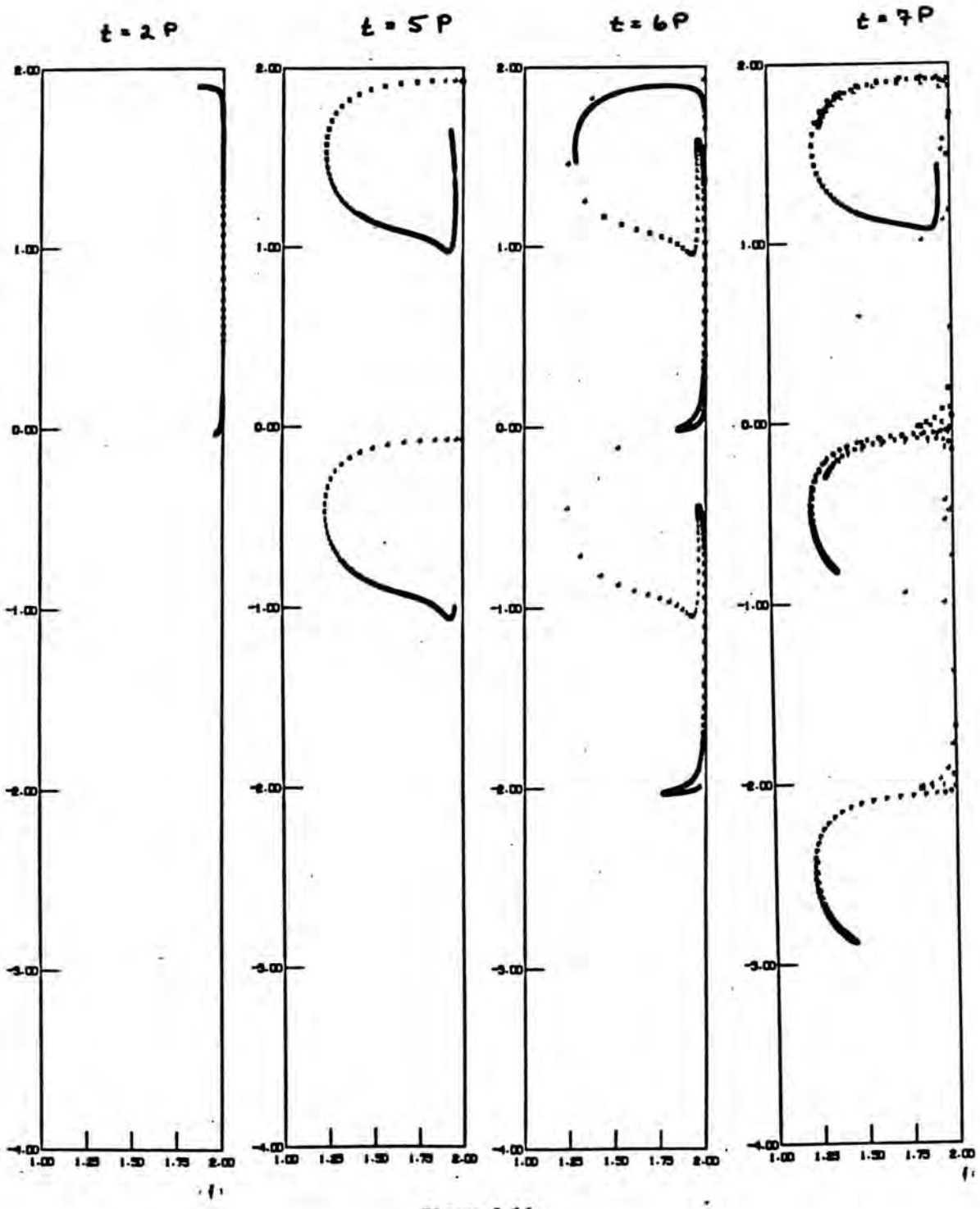

Figure 5.16

$t = 21\ P$

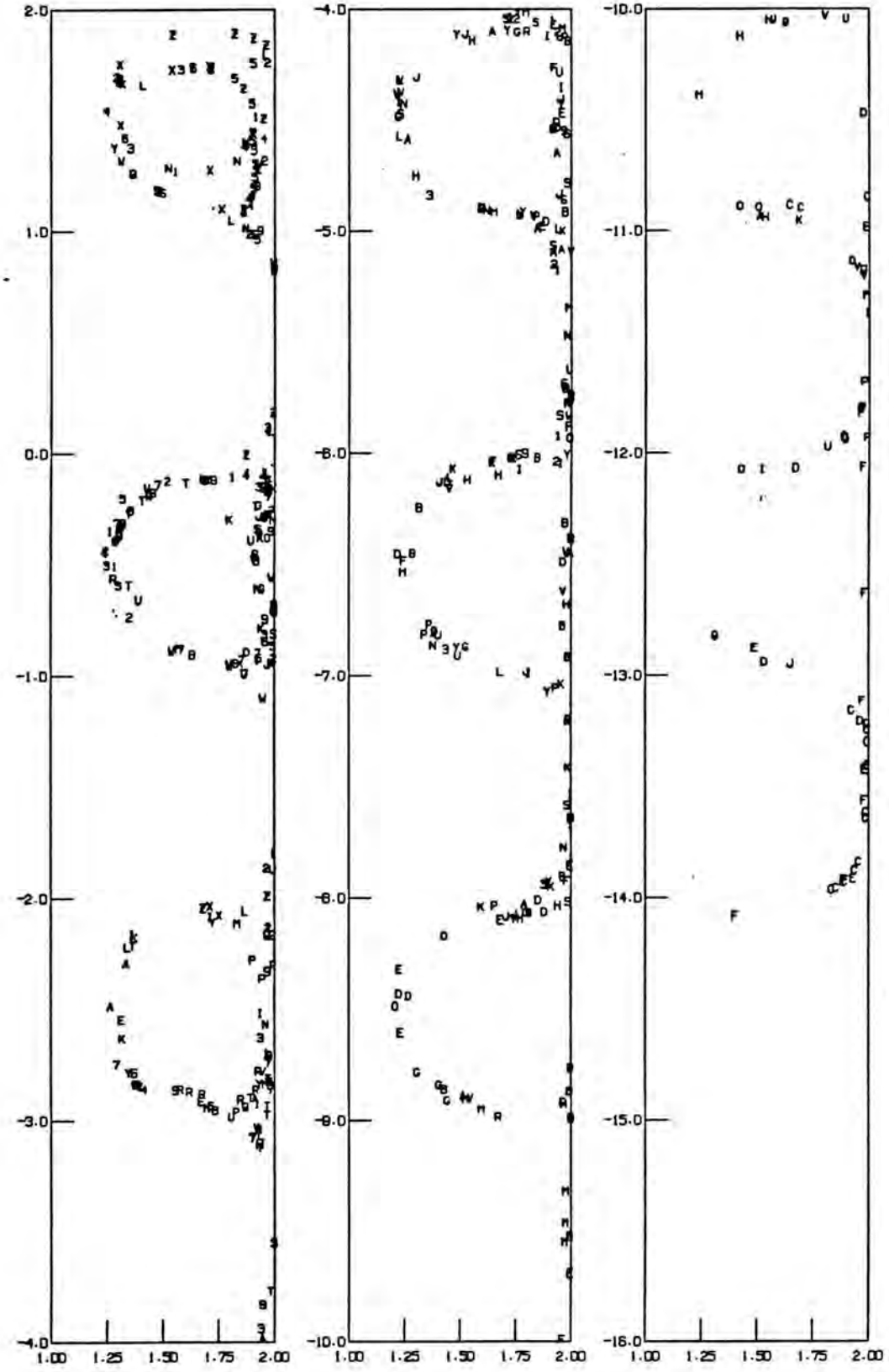

Figure 5.16

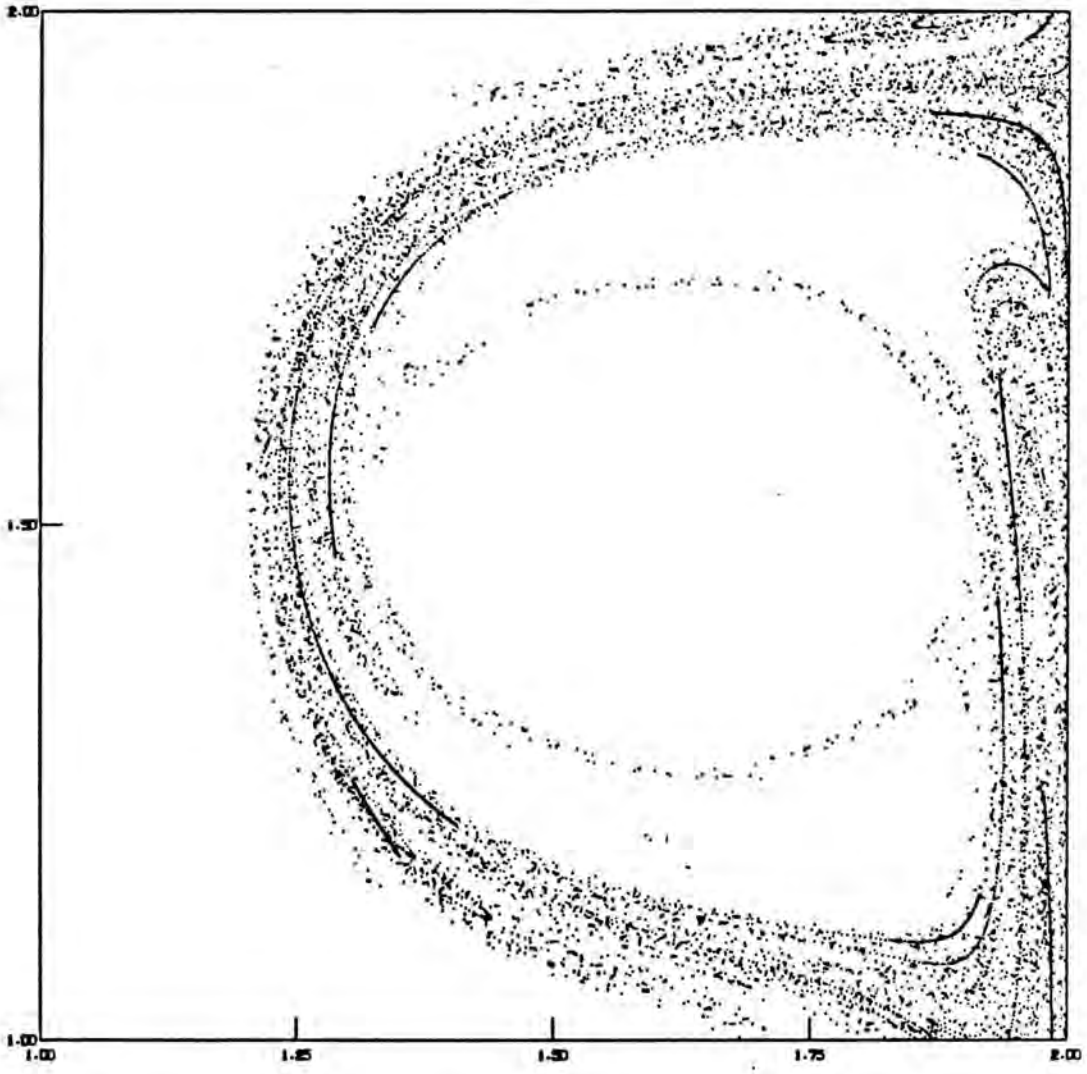

Figure 5.17

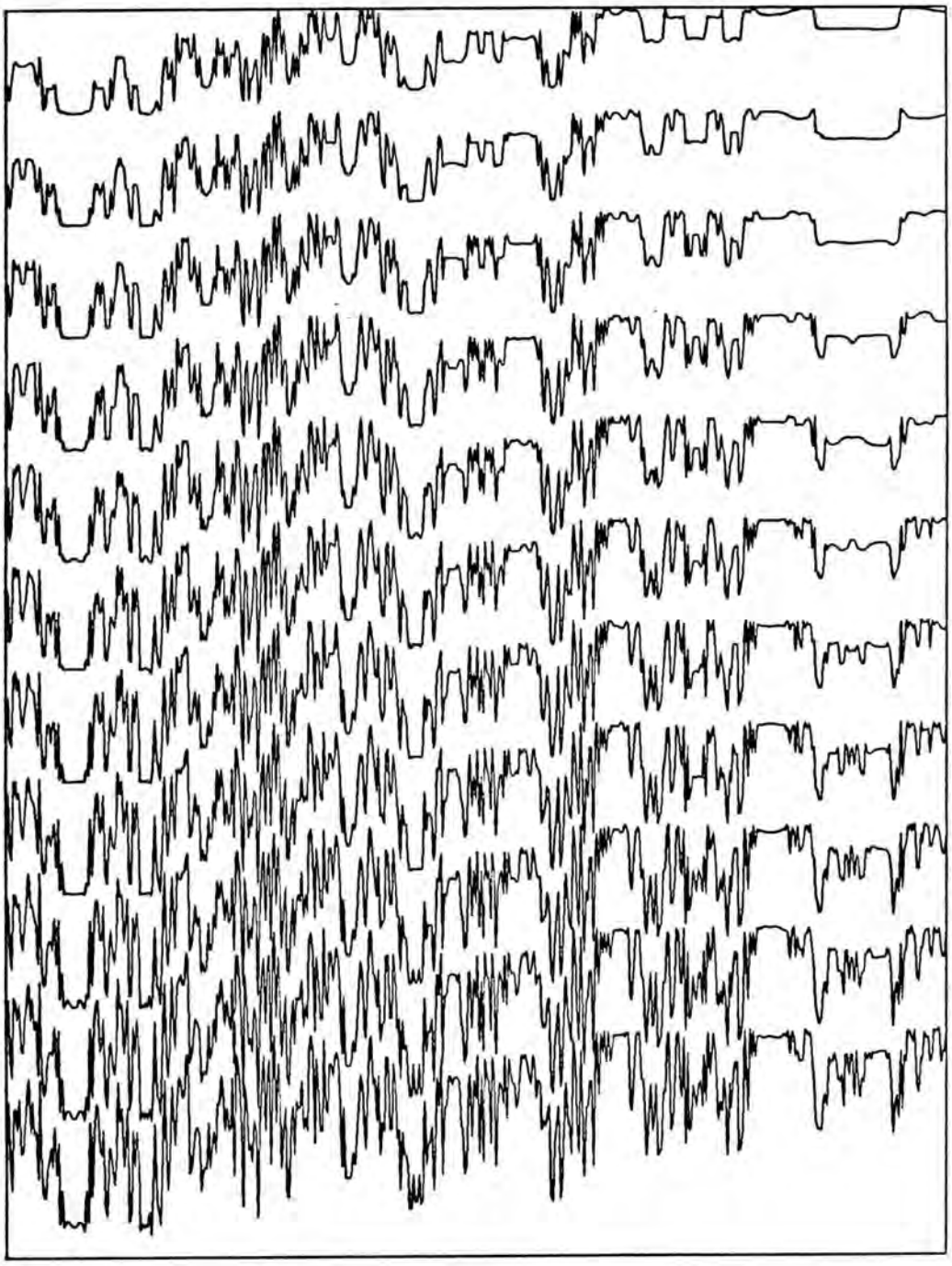

Figure 5.18

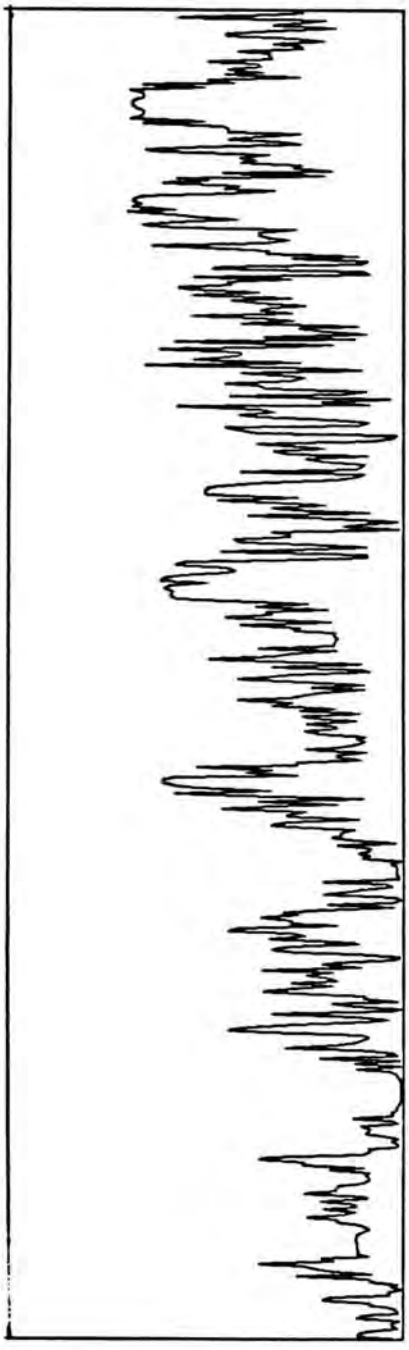

Figure 5.19

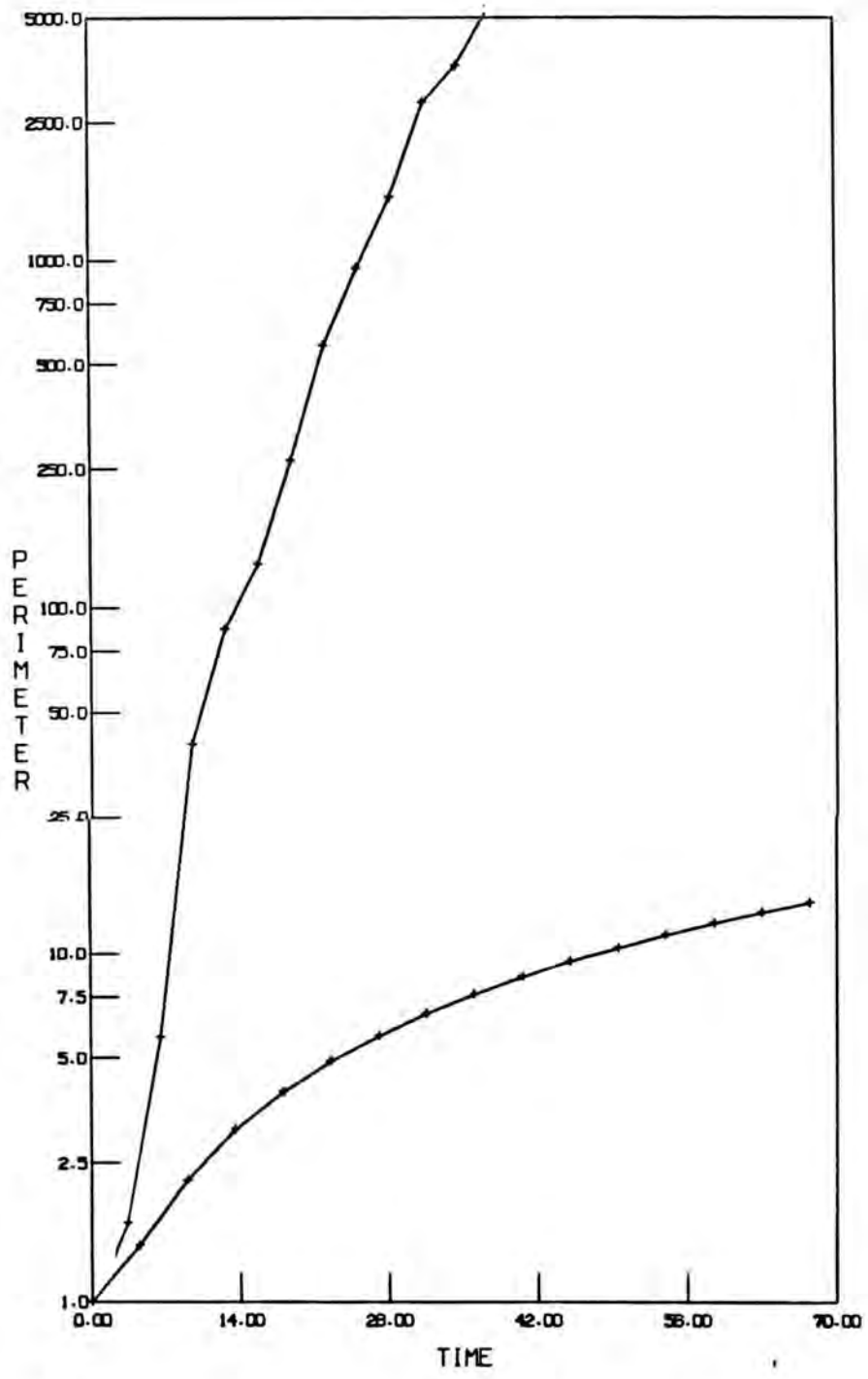
5000.0
2500.0
1000.0
750.0
500.0
250.0
100.0
75.0
50.0
25.0
10.0
7.5
5.0
2.5
1.0
PERIMETER
0.00
14.00
28.00
42.00
56.00
70.00
TIME

Figure 5.20

Appendix 3: An Class of Iterative Maps

In this appendix, we present a class of two-dimensional area preserving maps which simulate a surface of section for flows of the type discussed in Chapter 5. While it is not possible to predict a single chaotic trajectory, the general topological features of the phase space associated with a set of parameter values may be determined by integrating the equations of motion for a variety of initial conditions and studying the nature of the resulting trajectories. It was in this way that the surfaces of section presented in Chapter 5 were generated. Large amounts of computer resources are required to generate these sections; the motivation behind deducing a map is that such a map provides a method capable of quickly surveying the phase space for a variety of parameter values.

For the time-dependent flow described by Equations 5.5 and 5.15, a map accurate near the fluid stagnation point may be constructed as the composition of 4 simple maps; a twist, a vertical displacement, a lesser twist, and a second vertical displacement equal in magnitude to the first. The product of these maps is area preserving since each of the maps are area preserving individually. The amplitude of the flow is reflected by the strength of the twists while of oscillatory nature of the flow is shown in the difference between the two twists; the average magnitude of the modulation is added in the first twist and subtracted in the second. The vertical displacements reflect the magnitude of the Stokes velocity, v_s and the period of the flow, P. For clarity, we specify the twist maps (T_1 and T_3) in

polar coordinates, and the vertical displacements (T_2 and T_4) in cartesian coordinates.

$$T_1\ (r,\theta): \quad \begin{aligned} r' &= r \\ \theta' &= \theta + \tau_+\ F(r)/r \end{aligned} ,$$

$$T_2\ (x,y): \quad \begin{aligned} x'' &= x' \\ y'' &= y' - \delta_y \end{aligned} ,$$

$$T_3\ (r,\theta): \quad \begin{aligned} r''' &= r'' \\ \theta''' &= \theta'' + \tau_-\ F(r'')/r'' \end{aligned} ,$$

$$T_4\ (x,y): \quad \begin{aligned} x'''' &= x''' \\ y'''' &= y''' - \delta_y \end{aligned} ,$$

where

$$\tau_+ = \frac{P}{2}\ (1 + \bar{\epsilon})$$

$$\tau_- = \frac{P}{2}\ (1 - \bar{\epsilon})$$

$$\delta_y = \frac{v_s}{A}\ \frac{P}{2}$$

and

$$\bar{\epsilon} = \frac{2}{\pi}\ \epsilon\ .$$

The map is then

$$T(x,y) \equiv T_4 \cdot T_3 \cdot T_2 \cdot T_1\ .$$

A more compact form is obtained by considering the map as acting on the complex variable z where

$$z = x + i\,y.$$

In this case, this map composed of two complex maps

$$T^{\pm}(z) = \exp\{i\tau_{\pm}F(|z|)/|z|\}\; z - i\,\delta_y,$$

as

$$T(z) = T^{+} \cdot T^{-}.$$

A particular map of this class is determined by specifying the velocity function, F(r). We examined several functions, the simulations shown in the figures were obtained with

$$F(r) = \begin{cases} \sin r & r \leq \frac{\pi}{2} \\ 0 & r > \frac{\pi}{2} \end{cases}$$

where we have made the identification $r = |z|$. In each of the cases shown, the initial conditions are along a line of constant y, equally spaced in x. In Figure A3.1, the Stokes velocity is zero and the map reproduces the fluid streamlines of the equivalent flow. The correspondence between the mapping and the full flow is best where the streamlines agree, the poorest correspondence occurring at large r. As δ_y is increased, behaviors in qualitative agreement with the those of the full system are observed.

The major difficulty we found in matching the map to the flow of Chapter 5 was following the particles which passed through the boundaries in the mapping. In the illustrations periodic top and bottom conditions were imposed. Specifically, if at any time

$$y < -\frac{\pi}{2}$$

then

$$y \rightarrow y + \pi$$

$$x \rightarrow -x$$

These top and bottom conditions correspond to the stacked cells described in Chapter 5 where two vertically adjacent cells have been folded onto each other with a refection. Hence only a single square cell is shown. If a particle is displaced horizontally from the original "cell", that is if

$$|x| = \pi/2,$$

then the calculation is halted. With F9r) as above, the side boundaries are not crossed.

The mapping reflects the flow most accurately when the displacements due to the rotations are small relative to the cell height yet large relative to δ_y. This implies small values of P and v_s. Even in this case, particles which are far from their stagnation point sample regions of the mapping which do not accurately reflect the flow; this is especially true for particles which pass outside the circle $r = \pi/2$.

Qualitatively, the behaviors present in the flow are reflected in the mapping. For v_s equal to zero, the mapping yields circular trajectories as shown in Figure A3.1. For nonzero v_s, there exists a region of retention the area of which decreases as v_s increases. Some of the particles in the chaotic fallout region behave

differently than any particle in the full flow due to the reasons mentioned above. Figure A3.2 shows typical behavior for a moderate value of v_s; the chaotic fallout region contains integrable island chains, as in the full flow. Motion resembling that on a twisted torus is shown in Figure A3.3. In this case, bounded chaos is present as in the full flow. Finally, in Figure A3.4, a case with relatively large values of v_s and ϵ is shown. The large void region is the region of retention. The smaller lacuna represent regions of integrable fallout. Density variations in the chaotic sea are also apparent in the figure. This is evidence of strange accumulator behavior discussed in Appendix 4.

COMPLEX MAP
AMP = 0.3183
PERIOD= 1.0000
VSTOKE= -0.0100
EPS = 0.1000
NPOINT= 0
XO = 0.0100 0.1047
YO = 0.0000 0.0000

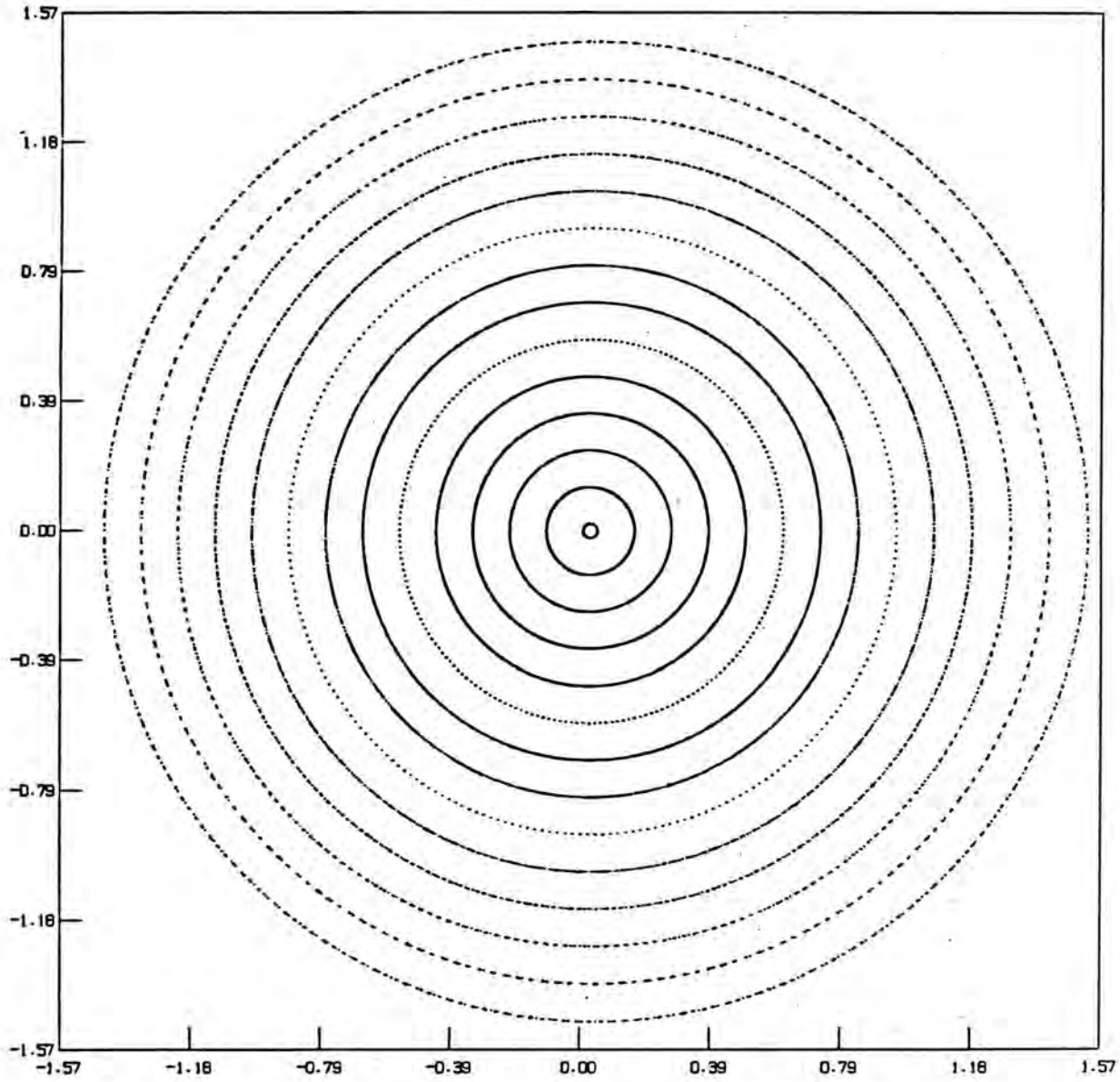

Figure A3.1

COMPLEX MAP
AMP = 0.3183
PERIOD= 1.0000
VSTOKE= -0.3000
EPS = 0.1000
NPOINT= 0
XO = 0.3047 0.1047
YO = 0.0000 0.0000

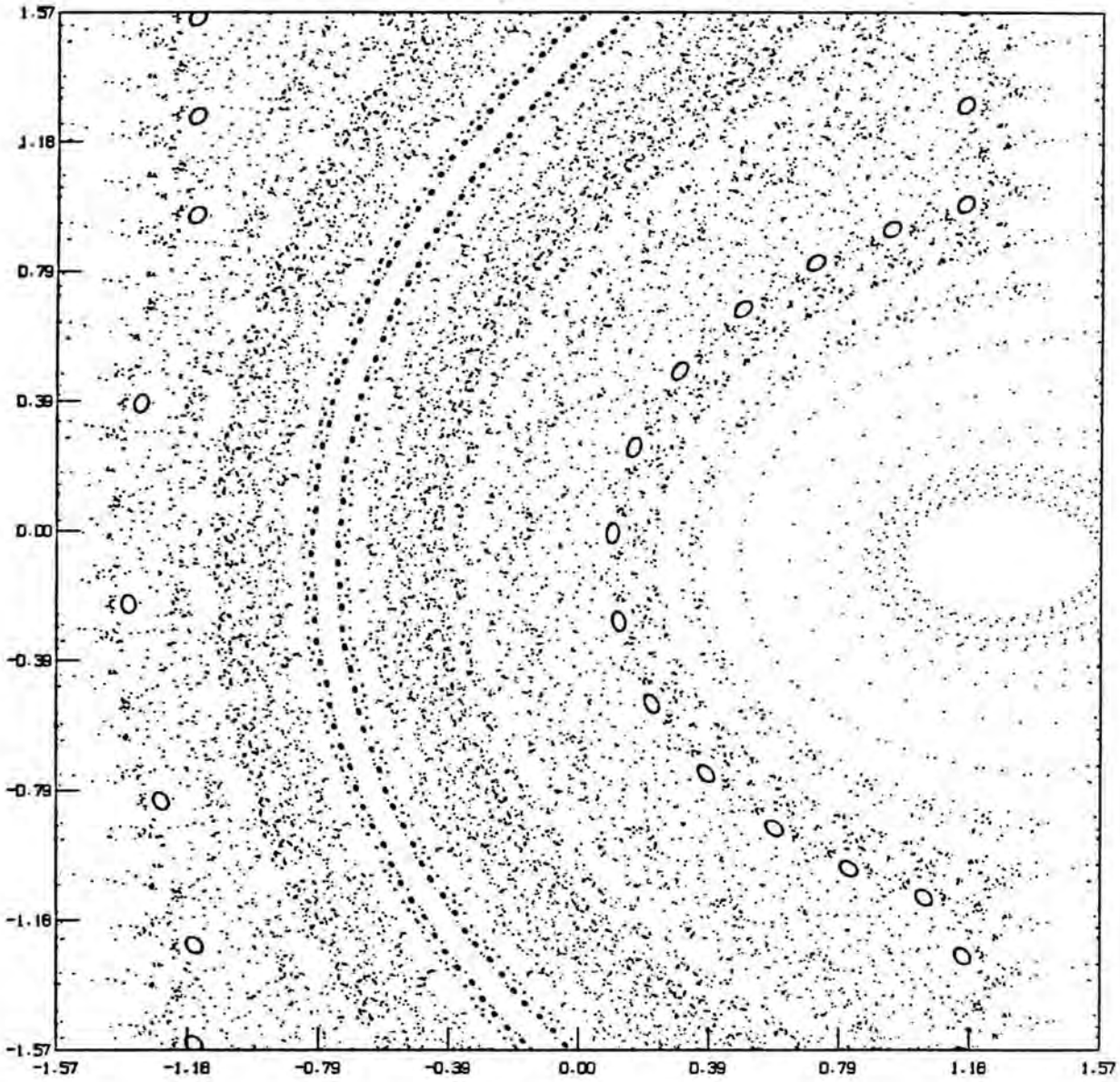

Figure A3.2

COMPLEX ANAMAP
TIME=

COMPLEX MAP
AMP = 1.0000
PERIOD= 4.5000
VSTOKE= -0.3000
EPS = 0.2000
NPOINT= 0
XO = 0.3047 0.1047
YO = -0.1500 0.0000

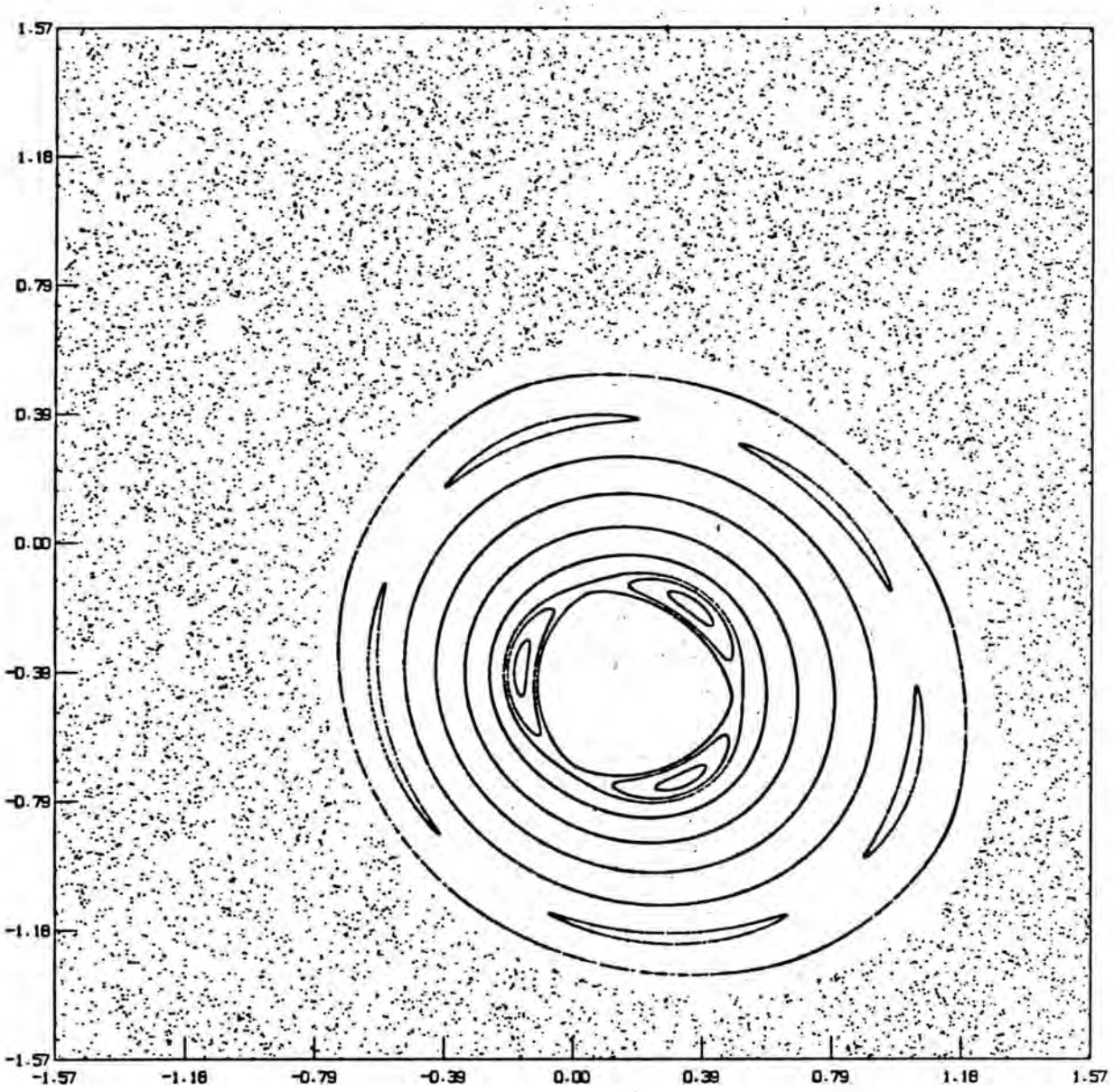

Figure A3.3

COMPLEX MAP
AMP = 1.0000
PERIOD= 4.5000
VSTOKE= -0.5000
EPS = 0.2000
NPOINT= 0
XO = 0.5236 0.1047
YO = 0.0000 0.0000

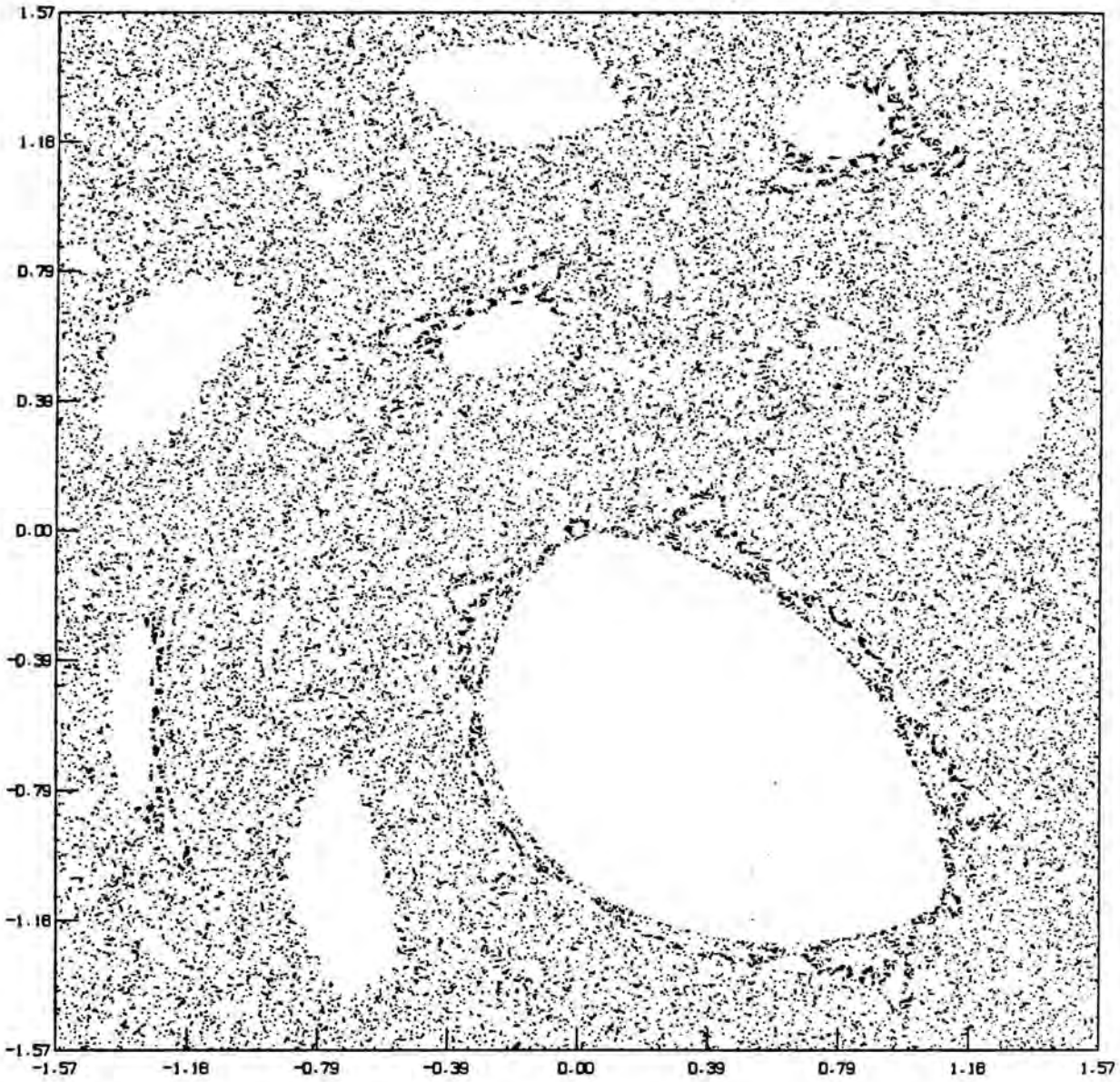

Figure A3.4

Strange Accumulators[a]

L.A. SMITH[b] AND E.A. SPIEGEL[c]

[b] *Department of Physics*
Columbia University
New York, New York 10027
and
NASA Goddard Space Flight Center
Institute for Space Studies
New York, New York 10025

[c] *Department of Astronomy*
Columbia University
New York, New York 10027

In astronomy, we see many irregular structures manifested in the form of strong inhomogeneities of physical variables like density, temperature, or magnetic field. The appearance of strong concentrations of these variables, in the presence of what frequently must be highly turbulent conditions, poses an interesting question whose answer probably lies in the nature of turbulence itself. Indeed, G.I. Taylor, seventy years ago, wrote that turbulence is the strong concentration of vorticity. How does this work?

Fluid dynamicists often refer to a mechanism that they call Batchelor-Prandtl expulsion to explain inhomogeneities; the nature of this process has recently been clarified by Rhines and Young[1]. Solar physicists know of the process as it applies to the development of magnetic inhomogeneities on the solar surface[2]. However, no unanimity seems to exist among solar physicists on the explanation of the fine-scale structures on the sun[3]. There even seems to be disagreement about the proper description of the topology of field lines.

Dynamical systems theory shows us a simple way to look at field lines that may teach us about their structures. Though the approach does not explain how such fields arise in hydromagnetics (MHD), it may nevertheless be valuable in thinking about the possibilities that confront us when we look at a complicated situation like that of the solar surface.

Consider a vector field $B(x,t)$ whose structure we want to look at. This may be a magnetic or vorticity field whose field structure may be too complicated to pull out of numerical solutions of the MHD equations (for example). Thus, this is an example of how the theoretical developments of chaos theory may help in astrophysics by adding to the ways we have of thinking about problems, even when the data may not be good enough to confirm or deny the presence of chaos.

Let X be a function of an independent variable s such that

$$\frac{d\mathbf{X}}{ds} = \mathbf{B}(\mathbf{X}(s),t) \tag{1}$$

for fixed t. If $\mathbf{B}$ should happen to be a velocity field, we would identify s and t and integrate equation 1 to get the particle paths, as has been done for fluid flows in two dimensions[4,5]. However, if $\mathbf{B}$ is some other field, we can look at a snapshot of it by regarding t as a parameter that we hold fixed during a run in which we study equation 1 as a dynamical system with s as the "time." The trajectory in $\mathbf{X}$–space will give us a picture of the field. We can even go further and cut the $\mathbf{X}$–space with a plane and simply plot the points where the trajectory pierces it. By studying typical maps of the plane into itself, we can get an idea of the possibilities that lie in store with real fields, $\mathbf{B}$.

Perhaps the most typical, typical map is the standard map [6]:

$$x_{i+1} = x_i + k \sin 2\pi y_{i+1} \quad ; \quad y_{i+1} = x_i + y_i \tag{2}$$

This is an area-preserving map that seems a qualitativley appropriate choice when (the solenoidal) B does not vary much in the direction normal to the surface section. For given k (not too large) and for suitable initial coordinates, this map gives rise to regular behavior in the form of periodic orbits lying on tori. The cross sections of these tori in the surface of section form island chains that are like the cat's–eyes of the fluid dynamicist. Between the islands are saddle points, in the neighborhood of which there are smaller islands. And so on.

A trajectory that gets in amongst the small islands will go for many twists before reemerging into the chaotic sea. This sojourn is responsible for long-range correlations of the successive points on the orbits of equation 2[7,8]. Meiss and Ott[9] have modeled the tendency of an orbit to linger in the reefs, while McKay, Meiss, and Percival[10], among others, have studied the mechanism of escape from them.

Our own naive point of view about the long times spent by particles in the reefs of the map is to liken these regions to the attractors of dissipative theory. One of the simplest examples of a dynamical system with an attractor is the Landau equation for $A(t)$:

$$\frac{dA}{dt} = A - A^3 \, . \tag{3}$$

This system has attractors at $A = \pm 1$ and a repeller at $A = 0$. If we differentiate this system once and substitute, we get

$$\frac{d^2A}{dt^2} = -\frac{\partial V}{\partial A} \, , \tag{4}$$

where

$$V = -\frac{1}{2}A^2(A^2-1)^2 \,. \tag{5}$$

The original system (equation 3) is contained in equations 4 and 5 if we impose suitable initial conditions.

Where the original Landau equation had either attractors or repellers, the new system (which is Hamiltonian) has saddle points. In the neighborhood of these points, the motion is very slow. We call sets of these points accumulators because a representative point moving in this system will tend to spend more time in the neighborhood of these points. Hence, the points in an orbit will tend to accumulate there. In systems with stochasticity and island chains, we can have quite a complex of such points; together, these make an accumulator with very fine texture. The presence of such complicated accumulators, we suggest, gives rise to strong inhomogeneities in field structures.

In the left panels of the accompanying figure (FIGURE 1), we show the result of a long numerical integration based on the map of equation 2. The calculation was done on a finite ($2^{20} \times 2^{20}$) mesh that preserves the 1-1 character of the map of equation 2, as in the work of Rannou[11] (see Miller and Prendergast[12] for use of "noise-free" methods in dynamical astronomy). The result of this method (with a large, but finite number of grid points) is that every orbit calcualated is periodic. Indeed, any deterministic simulation on a digital computer tends, in finite time, to a perodic orbit. If we are using the result to visualize field lines, this means that we are computing only closed field lines. In this case with an explicit grid, phase volumes are exactly conserved.

Figure 1 shows coarse-grained histograms of the number of visits to each grid square obtained in two different simulations. The panels on the left show histograms from a periodic 2,764,949-iteration orbit for the numerically one-to-one standard map with $k = 1.25$, the lower panel being a blow-up on a finer grid. The panels on the right similarly illustrate a double-precision calculation for the Hénon area-preserving, quadratic map (the field is chosen after figure 14 of Hénon[13]). In the Hénon case we have followed the mapping for 2^{27} iterations. The calculations for the Hénon case, unlike those for the standard map, are not one-to-one numerically, hence the structure shown in the right panels may be transient. The range in density shown is a factor of several hundred. Already, from these first results, we can see why the discussants at the solar physics meeting were in some doubt about what to call a flux tube in the solar surface. The notion of flux tube will often be useful only locally, but then the tube may splay out into the surrounding stochastic regions.

The defficiency in this type of study is that it is a little too generic. We want to be able to derive actual maps for real situations. This can be done when the vector field being studied is a real velocity field. Indeed, Chaikin *et al.*[5] have set up real flows corresponding closely to their maps and have found excellent agreeement for the motion of advected particles. The flow in that case involved time-dependent open stremlines. We may also get open streamlines by studying the motion of particles drifting through a convecting fluid[14,15]. These studies suggest formation of strong inhomogeneities in the particle densities, but the results are, as yet, still limited.

In summation, we can say that this note is a conference publication *par excellence*. We

are suggesting a way for modeling processes that seem too complex for detailed simulation without yet offering any quantitative predictions for astrophysics. Nevertheless, our qualitative results from the numerical experiments on long–period orbits seem to have surprised many of those who have seen them. Thus, it seems worth pointing out our conclusion that complicated accumulators are at the origin of strongly inhomogeneous concentrations of advected fields in flows. These fields need not be passive. Though the fields are dynamic and feed back on the flow, we may still expect the structures to be given by maps, even if we do not know them explicitly. This is ultimately a useful way to think about inhomogeneous fields.

ACKNOWLEDGEMENTS

We are very greatful to B. Bayly, J. Meiss, R. Mackay, and K. Prendergast for illuminating discussions. We look forward to further illumination as we continue to pursue particles around the plane.

REFERENCES

1. RHINES, P. B., & W. R. YOUNG. 1983. J. Fluid Mech. **133**: 133-145.

2. PARKER, E. N. 1979. Cosmical Magnetic Fields. Chap. 16. Oxford Univ. Press (Clarendon). London/New York.

3. SCHMIDT, H. U., Ed. 1987. Theoretical problems in high resolution solar physics. Max-Planck-Inst. Phys. Astrophys. report no. MPA 212.

4. AREF, H. 1984. J. Fluid Mech. **143**: 1-21.

5. CHAIKEN, J., R. CHEVRAY, M. TABOR & Q. M. TAN. 1986. Proc. R. Soc. London **A405**: 165-174.

6. LICHTENBERG, A. J. & M. A. LIEBERMAN. 1983. Regular and Stochastic Motion, p.218. Springer-Verlag. New York/Berlin

7. KARNEY, C. F. F. 1983. Physica **8D**: 360-380.

8. CHIRIKOV,B. V. & D. L. SHEPELYANSKY. 1984. Physica **13D**: 55-81.

9. MEIS, J. D. & E. Ott. 1985. Phys. Rev. Lett. **55**: 2741-2744.

10. MACKAY, R. S. , J. D. MEISS & I. C. PERCIVAL. 1984. Physica **13D**: 55-81.

11. RANNOU, F. 1974. Astron. Astrophys. **31** 289-301.

12. MILLER, R. H.& K. H. PRENDERGAST. 1968. Astrophys. J. **151**: 699.

13. HÉNON, M. 1969. Quarterly of Applied Mathematics **27** No. 3: 91-312.

14. SMITH, L. A. & E. A. SPIEGEL. 1985. *In* Macroscopic Modelling of Turbulant Flows. U. Frisch, J.B. Keller, G. Papanicolaou & O. Pironneau, Eds.: 306-319. Lecture Notes in Physics **230**. Springer-Verlag. New York/Berlin.

15. PASMANTER, R. A. *In* Proc. Int. Symp. Phys. Proc. Estuaries. W. van Leussen, Ed. Springer-Verlag. New York/Berlin. In press. (Date not Available)

CAPTION

The panels on the left show the visitation histogram for the numerically one–to–one standard map ($k = 1.25$). The lower panel is a blow-up. On the right, simulations with the Hénon[13] conservative map ($\cos\alpha = 0.240$) are shown. The number of visitations, as indicated by each color, varies slightly from panel to panel for photographic reasons. In the upper left panel, black means no visitation, brown is 1 to 4, blue is 5 to 9, red is 10 to 19, green is 20 to 29, yellow is 30 to 50. White partitions were visited between 51 and 316 times. All histograms are calculated on a 2^9 by 2^9 grid.

REFERENCES

Abraham N.B., A.M. Albano, B. Das, G. De Guzman, S. Yong, R.S. Gioggia, G.P. Puccioni, and J.R. Tredicce (1986). Calculating the dimension of attractors from small data sets, *Phys. Lett.*, **114 A**, 217-221.

Abramowitz, M. and L. Stegun (1984). *Handbook of Mathematical Functions*, U.S. Government Printing Office, Washington, D.C.

Anselmet, F., Y. Gagne, E. Hopfinger and R. Antonia (1984). High-order velocity structure functions in turbulent shear flows, *J. Fluid Mech.* **140**, 63-89.

Albano, A. M., J. Abounadi, T.H. Chyba, C.E. Searle, S. Yong, R.S. Gioggia, and N.B. Abraham (1985). Low-dimensional chaotic attractors for an unstable, inhomogeneously broadened, single-mode laser, *J. Opt. Soc. Am.* **B 2**, 47.

Aref, H. (1983). Integrable, Chaotic, and Turbulent Vortex Motion in Two-Dimensional Flows, *Ann. Rev. Fluid Mech.* **15**, 345-89.

Aref, H. (1984). Stirring by chaotic advection, *J. Fluid Mech.* **143**, 1-21.

Arneodo, A. and P. Sornette (1984 preprint). Monte-Carlo Random Walk Experiments as a test of Chaotic Orbits of Maps of the Interval.

Arneodo, A., P. Coullet and E.A. Spiegel (1982). Chaos in a finite macroscopic system, *Phys. Lett.* **92A**, 369.

Arneodo, A., P. Coullet, and C. Tresser (1981). A possible new mechanism for the onset of turbulence, *Phys. Lett.* **81A**, 197.

Arneodo, A., P. Coullet, E.A. Spiegel, and C. Tresser (1985). Asymptotic Chaos, *Physica* **14D**, 327-347.

Arnold, V.I. (1978). *Mathematical methods of classical mechanics* (Springer, New York).

Arnold, V.I. and A. Avez (1968). *Ergodic Problems of Classical Mechanics* (Addison-Wesley, Reading, Mass.).

Arter, W. (1983). Ergodic stream-lines in steady convection, *Phys. Lett.* **97A**, 171-174.

Badii, R. and A. Politi (1984). Intrinsic Oscillations in Measuring the Fractal Dimension, *Phys. Lett.* **104A** #6,7, 303-305.

Badii, R. and A. Politi (1984). Hausdorff Dimension and Uniformity Factor of Strange Attractors, *Phys. Lett.* **52** #19, 1661-1664.

Badii and Politi (1985). Statistical descriptions of chaotic attractors: The dimension function, *J. Stat. Phys.* **40**, # 516, 725.

Baker, N.H., D.W. Moore, and E.A. Spiegel (1966). Nonlinear Oscillations in the One-Zone Model for Stellar Pulsation, *Astron. J.* **9**, 844.

Baker, N.H., D.W. Moore, and E.A. Spiegel (1971). Aperiodic Behavior of a Nonlinear Oscillator. *Quart. J. of Mech. and App. Math.* **24**, 391-422.

Balatoni, J., and A. Renyi (1956). On the notion of entropy, *Pub. Math. Inst. of the Hungarian Acad. Sci.* **1**, 9.

Barnsley, M.F. (1986). In: *Dynamics Days Meeting*, La Jolla, Ca., Jan. 7-11.

Barneley, M.F. and A.N. Harrington (1985). A mandelbrot set for pairs of linear maps, *Physica* **15 D**, 421-432.

Batchelor, G.K. (1953). *The Theory of Homogeneous Turbulence*, (Cambridge: Cambridge Univ. Press), 197 pp.

Batchelor, G.K. (1959). Small-scale variation of convected quantities like temperature in turbulent fluid, *J. Fluid Mech.* 5, 113.

Batchelor, G.K. and A.A. Townsend (1947). Decay of isotropic turbulence in the initial period, *Proc. Roy. Soc. (Lond.) A* **190**, 534-558.

Bennett, R. S. (1969). The Intrinsic Dimensionality of Signal Collections, *IEEE* **IT-15**, No 5.

Benzi, R. G. Paladin, G. Parisi and A. Vulpiani (1984). On the multifractal nature of fully developed turbulence and chaotic systems, *J. Phys. A: Math Gen.* **17**, 3521-3531.

Beran, M.J. (1968). *Statistical continuum theories* (Interscience Publishers, New York). pg 344.

Berry, M.V. (1978). Regular and irregular motion, in: *Topics in Nonlinear Dynamics*, ed. S. Jorna (AIP Conf. Proc. 46, New York).

Bertero, M. and E.R. Pike (1982). Resolution in diffraction-limited imaging, a singular value analysis, I: The case of coherent illumination, *Opt. Acta.*, **29**, 727-746.

Besicovitch, A.S. (1934). On rational approximations to real numbers, *J. London Math. Soc.* **9**, 126-131.

Besicovitch, A.S. (1935). On the sum of digits of real numbers represented in the dyadic system (Onsets of fractional dimension II), *Mathematische Annalen* **110**, 321-330.

Besicovitch, A.S., and H.O. Ursell (1937). Sets of fractional dimemsion (V), *J. London Math. Soc.* **12**, 18-25.

Besicovitch, A.S. and S.J. Taylor (1953). On the complementary intervals of a linear closed set of Lebesgue measure, *J. London Math. Soc.* **29**, 449-459.

Bessis, D., J.S. Geronimo and P. Moussa (1983). *J. Phys. (Paris) Lett.* **44**, L977.

Brandstater, A., J. Swift, H.L. Swinney, A. Wolf, J.D. Farmer, E. Jen, and P.J. Crutchfield (1983). *Phys. Rev. Lett.* **51**, 1442.

Broomhead, D.S. and G.P. King (1986). Extracting Qualitative Dynamics from Experimental Data, *Physica* **20D**, 217-238.

Brouwer, (1913). Über den natürlichen Dimensionbegriff, *Journ. f. Math.* **142**, 146-52.

Carnahan, B., H. A. Luther and J.O. Wilkes (1969). *Applied Numerical Methods* (John Wiley, New York).

Chaiken, J., R. Chevray, M. Tabor, and Q. M. Tan (1986). Experimental Study of Lagrangian Turbulence in a Stokes Flow, *Proc. Royal Soc.* **408 A**, 165-174.

Chaiken, J., C.K. Chu, M. Tabor, and Q.M. Tan (1987). Lagrangian Turbulence and Spatial Complexity in Stokes Flow, *Phys. of Fluids*, **30**, 687-694.

Chandraseker, S. (1961). *Hydrodynamic and Hydromagnetic Stability*, (Oxford University Press, London).

Cocke, W.J. (1969). Turbulent hydrodynamic line stretching: Consequences of isotropy, *Phys. Fluids* **12**, 2488-2492.

Collet, P. and J.-P. Eckman (1980). *Iterated maps on the unit interval as dynamical systems* (Birkhäuser, Boston).

Corrsin, S. (1950). Turbulent Flow, *American Scientist*, **38**, 300-325.

Corrsin, S. (1959). Outline of some topics in homogeneous turbulent flow, *J. Geophys. Res.* **64**, 2134-2150.

Corrsin, S. (1963). Estimates of the relations between Eulerian and Lagrangian scales in large Reynolds number turbulence, *J. Atmos. Sci.* **20**, 115-119.

Corrsin, S. and M. Karweit (1969). Fluid line growth in grid-generated isotropic turbulence, *J. Fluid Mech.* **39**, 87-96.

Crutchfield, J.P.,(1983) *Noisy Chaos*, Ph.D. dissertation, Univ. of California, Santa Cruz.

Crutchfield, J.P., J.D. Farmer, N.H. Packard, R. Shaw, G. Jones and R. Donnely (1980). Power spectral analysis of a dynamical system, *Phys. Lett.* **76A**, 1.

Crutchfield, J.P., J.D. Farmer, N.H. Packard, and R.S. Shaw (1986). Chaos, *Scientific American* **255** #6, 46-57.

Cvitanović, P. (1984). *Universality in Chaos.* (Adam Hilger Ltd., Bristol).

De Bruijn, N.G. (1948). On Mahler's partition problem *Proc. Kon. Ned. Akad. van Wettenschappen*, **51**, 659-669.

DEC (1982). *Digital Microcomputers and Memories*, Digital Equitment Corp. (Marlboro, MA).

Derrida, B., A. Gervois and Y. Pomeau (1979). Universal metric properties of bifurcations of endomorphisms, *J. Phys. A.* **12**, 269.

de Vaucoulers, G. (1970). The case for a hierarchical cosmology, *Science* **67** #3922, 1203-1213.

de Vaucouleurs, G. (1971). The large scale distribution of galaxies and clusters of galaxies, *Publications of the Astronomical Society of the Pacific* **83**, 492, 113-143

Farmer, J.D. (1982a). Chaotic attractors of an infinite dimensional system, *Physica* **4D**, 366.

Farmer, J.D. (1982b). Information dimension and the probabilistic structure of chaos, *Z. Naturforsch* **37a**, 1304.

Farmer, J.D. (1982c). Dimension, fractal measures and chaotic dynamics, in: *Order and Chaos*, H. Hoken, ed. (Springer-Verlag, New York).

Farmer, J.D., E. Ott and J.A. Yorke (1983). The dimension of chaotic attractors, *Physica* **7D**, 153.

Farmer, J.D., J.P. Crutchfield, H. Froehling, N.H. Packard, and R.S. Shaw (1980). Power spectra and mixing properties of strange attractors, *Annals N.Y. Acad. Sci.* **357**, 453.

Feigenbaum, M. (1978). Qualitative universality for a class of nonlinear transformations, *J. Stat. Phys.* **19**, 25.

Feigenbaum, M. (1979). The universal metric properties of nonlinear transformations, *J. Stat. Phys.* **21**, 669.

Feigenbaum, M.J. (1980). Universal behaviour in nonlinear systems, *Los Alamos Science* **1**, 4.

Franceschini, V. and L. Russo (1981). Stable and unstable manifolds of the Hénon mapping, *J. Stat. Phys.* 25 #4, 757-769.

Fraser, A.M. and H.L. Swinney (1986). Independent coordinates for strange attractors from mutual information, *Phys. Rev. A* **33**, 2, 1134-1140.

Frisch, U. and Morf (1981). Intermittency in nonlinear dynamics and singularities at complex times, *Phys. Rev A*, **23**, 2673.

Frisch, U. (1983). Fully developed turbulence and Intermittency, in *Turbulence and Predictability of Geophysical Flows and Climate Dynamics, Varenna Summer School* LXXXVII.

Frisch, U. and G. Parisi (1983). On the singularity structure of fully developed turbulence, in *Turbulence and Predictability of Geophysical Flows and Climate Dynamics, Varenna Summer School* LXXXVII.

Frisch, U., P.-L. Sulem and M. Nelkin (1978). A simple dynamical model of intermittent fully developed turbulence, *J. Fluid Mech.* **87**, 719.

Funkunage, K. and D. R. Olsen (1976). An algoritmn for finding Intrisic Dimensionality of Data, *IEEE Transactions*, **20**, 176-183.

Fry, J.N. (1983). Correlation functions in a filamentary clustering prescription, *Astrophys. J.* **270**, L31-L33.

Giglio, M., S. Musazzi, and U. Perini (1984). Low-Dimensionality Turbulent Convection, *Phys. Rev. Lett.* 53, 2402-2404.

Giorgillo A., D. Casati, L. Sironi, and L. Galgani (1986). An efficient procedure to compute fractal dimensions by box counting, *Phys. Lett.*, **115 A**, 202-206.

Glazier, J.A., M.H. Jensen, A. Libchaber, and J. Stavans (1986). Structure of Arnold tongues and the f(α) Spectrum for period doubling: Experimental results, *Phys. Rev. A*, **34**, 1621-1624.

Gollub, J.P. and T.H. Solomon (1987 preprint). Complex particle trajectories and transport in stationary and periodic convective flows, in: *Chaos and Related Nonlinear Phenomena: Where do we go from Here?*, (Proc. Fritz Haber Int. Symp., Rehovot Israel, Dec. 13-19, 1986), ed. I. Procaccia (Plenum, New York).

Grassberger, P. (1981). On the Hausdorff dimension of fractal attractors, *J. Stat. Phys.* **26**, 1, 173-179.

Grassberger, P. (1983). On the fractal dimension of the Hénon attractor, *Phys. Lett.* **97A**, 224.

Grassberger, P. and I. Procaccia (1983a). Characterization of strange attractors, *Phys. Rev. Lett.* **50**, 346-349.

Grassberger, P. and I. Procaccia (1983b). Measuring the strangeness of strange attractors, *Physica* **9D**, 189-208.

Grebogi, C., S.W. McDonald, E. Ott, and J. Yorke (1984). Fractal basin boundaries in nonlinear dynamical systems, in: *Statistical Physics and Chaos in Fusion Plasma*, ed. C.W. Hopton, Jr. and L.E. Reichl (John Wiley & Sons, New York).

Grebogi, C., S.W. McDonald, E. Ott, and J. Yorke (1985). Exterior dimension of fat fractals, *Phys. Lett.* **110A** #1:1-4.

Greenside, H.S., A. Wolf, J. Swift and T. Pignataro, (1982). Impracticality of a box counting algorithm for calculating the dimension of strange attractors, *Phys. Rev.* **A25**, 3453.

Groth, E.J. and P.J.E. Peebles (1986). The Shane-Wirtanen Counts: Plate Correction Factors and Correlation Functions, *Ap. J.* **310**, 499-507.

Guckenheimer, J. (1984). Dimension estimates for attractors, *Contemp. Math.* **28**, 357.

Haken, H., ed. (1981). Chaos and order in nature, *Proc. of Int. Symposium on Synergetics at Schloss Elmau, Bavaria* (Springer, New York).

Halsey, T.H., M.H. Jensen, L. P. Kadanoff, I. Procaccia and B.I. Shraiman (1986). Fractal measures and their singularities: The characterization of strange sets, *Phys.Rev A* **33**, 1141.

Hansen, J., G. Russel, D. Rind, P. Stone, A. Lacis, S. Lebedeff, R. Ruedy and L. Travis (1983). Efficient three-dimensional global models for climate studies: Models I and II, *Mon. Wea. Rev.* **III**, 4.

Hausdorf (1919). *Math. Ann.*, **79**, 157.

Helleman, R.H.G., ed. (1980). Nonlinear dynamics, *Ann. N.Y. Acad. Sci.* **357**, 1.

Hénon, M. (1969). Numerical Study of Quadratic Area Preserving Mappings, *Quart. Appl. Math.* **27**, 291-312.

Hénon, M. (1976). A two-dimensional mapping with a strange attractor, *Commun. Math. Phys.* **50**, 69-77.

Hénon (1983). Numerical exploration of Hamiltonian systems in *Chaotic Behaviour of Deterministic Systems* , Les Houches Session XXXVI. ed. G Iooss, R.H.G. Helleman, and R. Stora (North-Holland, New York).

Hénon, M. and C. Heiles (1964). The applicability of the third integral of the motion, some numerical experiments, *Astron. J.* **69**, 73.

Hénon, M., and Y. Pomeau (1977). "Two strange attractors with a simple structure," in: *Turbulence and the Navier-Stokes Equations*, ed. R. Teman, *Lect. Notes in Math.* **565** (Springer-Verlag, New York), p. 29.

Hentschel, H.G.E. and I. Procaccia (1983). The infinite number of generalized dimensions of fractal and strange attractors, *Physica* **8D**, 435-444.

Hoyle, F. (1953). On the fragmentation of gas clouds into galaxies and stars,. *Astrophys. J.* **118**, 513-528.

Huberman, B.A. and A.B. Zisook (1981). Power spectra of strange attractors, *Phys. Rev. Lett.* **46**, 626.

Hudson, J.L. and J.C. Mankin (1981). Chaos in the Belousov-Zhabotinsky reaction, *J. Chem. Phys.* **74**, 6171.

Huppert, H.E. (1984). Lectures on geological fluid dynamics, Woods Hole Oceanographic Institution Tech. Rept. WHOI-84-44.

Hurewicz, W. and H. Wallman (1941). *Dimension Theory* (Princeton University Press, Princeton, NJ)

Iansiti, M., Hu. Qing, R.M. Westervelt, and M. Tinkham (1985). Noise and Chaos in a Fractal Basin Boundary Regime of a Josephson Junction, *Phys Rev. Lett.* **55**, 746.

IBM (1984). *Technical Reference, Personal Computer XT 6322508 S229-9611-00*. (IBM Corporation, Boca Raton, FL).

IMSL (1978), *The IMSL Library*, Library Contents Document IMSL LCD-0007 (IMSL, Inc. 7500 Bellaire Blvd., Houston, TX).

Julia, G. (1918). Mémoire sur l'itération des fonctions rationelles, *J. Math. Pures et Appl.* **4**, 47.

Kadanoff, L.P. (1986). Fractal singularities in a measure and how to measure singularities on a fractal, *Prog. of Theor. Phys.* Supp. **86**, 383-386.

Kaplan, J. and J. Yorke (1979). In: Functional differential equations and approximations of fixed points, H.O. Peitgen and H.O. Walther, eds., *Springer Lecture Notes in Math. (Berlin)* **730**, 204.

Kolmogorov, A. (1941a). *C.R. Acad. Sci. USSR* **13**, 82.

Kolmogorov, A. (1941b). The local structure of turbulence in incompressible viscous fluid for very large Reynolds numbers, *C.R. (Doklady) Acad. Sci., USSR* **30**, 301-305.

Kolmogorov, A. (1962). A refinement of previous hypotheses concerning the local structure of turbulence in a viscous incompreeible fluis at high Reynolds number, *J. Fluid Mech.* **13**, 82-85.

Kuo, A. Y-S., and S. Corrsin (1971). Experiments on internal intermittency and fine-structure distribution functions in fully turbulent fluid, *J. Fluid Mech.* **50**, 2, 285-319.

Landau, L.D. (1944). On the problem of turbulence, *Acad. Nauk.* **44**, 311-339. English translation in *Collected Papers of L.D. Landau*, p. 387, D. der Haar, ed. (Gordon and Breach, 1965).

Landau, L.D. and E.M. Liftshitz (1979). *Fluid Mechanics*, (Pergamon Press, New York).

Langmuir, I. (1938). Surface motion of water induced by wind, *Science* **87**, No. 2250, 119.

Lapparent, V., M.J. Geller and J.P. Huchra (1986). A slice of the universe, *Ap. J.* **302**, 21-25.

Libchaber, A. (1982). Convection and turbulence in liquid helium I, *Physica* **109B**, **110B**, 1583.

Libchaber, A., C. Laroche and S. Fauve (1982). Period doubling in mercury, a quantitative measurement, *J. de Phys. Lett.* **43**, L211.

Libchaber, A., and J. Maurer (1982). A Rayleigh Bénard Experiment: Helium in a small box, in: *Nonlinear phenomena at phase transitions and instabilities*, ed. T. Riste (Plenum, New York), 259.

Lichtenberg, A.J. and M.A. Lieberman (1983). *Regular and "Stochastic" Motion* (Springer-Verlag, Berlin, New York).

Lorenz, E.A. (1963). Deterministic nonperiodic flow, *J. Atmos. Sci.*, **20**, 130.

Lorenz, E.A. (1982). *Atmospheric Models as Dynamical Systems* in Perspectives in Nonlinear Dynamics, ed. M.F. Schlesinger, R. Conley, A.N. Sûenz and W. Zachary (World Scientific, Singapore).

Mandelbrot, B.B. (1974). Intermittent turbulence in self-similar cascades: divergence of high moments and dimension of the carrier, *J. Fluid Mech.* **62**, 2, 331-358.

Mandelbrot, B.B. (1975). *Les objects fractals: forme, hasard et dimension* (Flammarion, Paris).

Mandelbrot, B.B. (1977). *Fractals: Form, Chance and Dimension* (Freeman, San Francisco).

Mandelbrot, B.B. (1982). *The Fractal Geometry of Nature* (Freeman, San Francisco).

Mandelbrot, B.B., Libchaber, A., C. Laroche and S. Fauve (1982). Period doubling cascade in mercury, a quantitative measurement. *Le Journal de Physique - Lettres* **43**, L-211-L-216.

Mandelbrot, B.B., D.F. Passoja and A.J. Paullay (1984). Fractal character of fracture surfaces of metals. *Nature* **308**, 721-722.

Martien, P., S.C. Pope, P.L. Scott and R.S. Shaw (1985). The Chaotic Behavior of the Leaky Faucet. *Phys. Lett.* **110A**, 399-404.

Marzec, C.J. and E.A. Spiegel (1980). Oddinary dufferential equations with strange attractors, *J. App. Math.* **38**, 403-421.

Maxey M.R. and S. Corrsin (1985). Gravitational Settling of Aerosol Particles in Randomly Oreinted Cellular Flow Fields, *J. Atmos. Sci.* **43**, 1112-1134.

May, R.M. (1976). Simple mathematical models with very complicated dynamics, *Nature* **261**, 261-459.

Mayor, A. H. (1985). *Hokusai*, (Metropolitan Museum of Art, New York).

Moore, D.W. and E.A. Spiegel (1966). A thermally excited non-linear oscillator, *Astrophys. J.* **143**, 871-887.

Moser, J. (1968). Lectures on Hamiltonian systems, *Memoirs Am. Math. Soc.* **81**, 1.

Moser, J. (1973). Stable and Random Motions in Dynamical Systems, *Annals of Math. Studies* 77 (Princeton Univ. Press, Princeton, N.J.).

Neuringer, J.L. (1968). Green's function for an instantaneous line particle source diffusing in a gravitational field and under the influence of a linear shear wind, *Siam J. Appl. Math.* **16**, 834-841.

Novikov, E.A. and R.W. Stewart (1964). Intermittency of turbulence

and the spectrum of fluctuations of energy dissipation, *Isv. Akad. Nauk. SSSR, Seria Geofiz.* **3**, 408.

Novikov, E.A. (1966) Mathematical Model for the Intermittence of Turbulent Flow, *Soviet Physics-Doklady*, **11**, No. 6, 497-499.

Novikov, E.A. (1986). Intermittency, Lacunarity and Logarithmically-periodic Modulation of Spectra, in *Scaling, Fractals and Nonlinear Variability in Geophysics*, NVAG Abstracts (McGill University).

Ott, E. (1981). Strange attactors and chaotic motions of dynamical systems, *Rev. Mod. Phys.* **53**, 655.

Ott, E., W.D. Withers, and J.A. Yorke (1984). Is the dimension of chaotic attractors invariant under coordinate changes? *J. Stat. Phys.* **36**, 516, 687-697.

Packard, N.H., J.P. Crutchfield, J.D. Farmer and R.S. Shaw (1980). Geometry from a time series, *Phys. Rev. Lett.* **45**, 712.

Pawelzik, K. and H.G. Schuster (1987). Generalized dimensions and entropies from a measured time series, *Phys. Rev. A* **35** #1, 481-484.

Peebles, P.J.E. (1973). Statistical Analysis fo catalogs of extraga;actic objects. I. Theory, *Ap. J.* **185**, 413-440.

Pérez, J. and C. Jeffries (1982). Direct observations of a tangent bifurcation in a nonlinear oscillator, *Phys. Lett.* **92A**, 82.

Pettis K.W., T.A. Bailey, A.K. Jain, and R.C. Dubes (1979). An Intrinsic Dimensionality Estimator from Near-Neighbor Information, *IEEE PAMI-1*, **1**, 25-37.

Pike, E.R., J.G. McWhirter, M. bertero, and C. de Mol (1984). Generalised information theory for inverse problems in signal processing, *IEE Proceedings*, **131**, Part F, # 6, 660-667.

Poincaré H. (1892). *Les methodes nouvelles de la méchanique céleste* (Gauthier-Villars, Paris).

Poincaré H. (1963). *New Methods of Celestial Mechanics*, NASA Technical Translation, code NASA TT F-450. (Clearinghouse for Federal Scientific and Technical Information, Springfield, Virginia).

Poincaré H. (1982). *The Foundations of Science* (Unversity Press of America, New York).

Quinn, P.J. (1984). On the formation dynamics of shells around elliptical galaxies, *Astrophys. J.* **279**, 596-609.

Rannou, F. (1974). Numerical study of discrete plane area-preserving mappings, *Astron. & Astrophys* **31**, 289-301.

Renyi (1970). *Probability Theory* (North Holland).

Richardson, L.F. (1961). The problem of contiguity: an appendix of statistics of deadly quarrels, *General Systems Yearbook* 6, 139-187.

Richardson, L.F. and H. Stommel (1948). Note on eddy diffusion in the sea, *J. Meteor.* 5, 238-240.

Roberts, P.H. and R.J. Donnelly (1974). Superfluid Mechanics. *Ann. Rev. Fluid Mech.* **6**,179-225.

Rogers, R.R. (1976). *A Short Course in Cloud Physics* (Pergamon Press, Elmstaid, New York).

Ruelle, D. (1980). Strange attractors, *Math Intelligencer* **2**, 126 (In French: [1980] La Récherche II, 132-144).

Ruelle, D. and F. Takens (1971). On the nature of turbulence, *Commun. Math. Phys.* **20**, 167.

Russel D.A., J.D. Hanson and E. Ott (1980). Dimension of Strange Attractors, *Phys. Rev. Lett.*, 45, 1175-1178.

Schuster, G.S. (1984). *Deterministic Chaos* (Physik-Verlag, Weihheim), p. 50.

Shanon and Weaver (1964). *The Mathematical Theory of Communication* (University of Illinois Press, Urbana, Ill.).

Shaw, R.S. (1981). Strange attractors, chaotic behavior and information flow, *Z. Naturforsch* **36**a, 80.

Shepard, R.N. (1962a). The Analysis of Proximities: Multidimensional Scaling With An Unknown Distance Function I, *Psychometrica*, 27, 125-140.

Shepard, R.N. (1962b). The Analysis of Proximities: Multidimensional Scaling With An Unknown Distance Function II, *Psychometrica*, 27, 219-246.

Shepard, R.N. and Carrol (1966). Parametric Representations of Nonlinear Data Structures, in *Proc. Int. Symp. on Multivariant Analysis*, P.R. Krishnaiah, Ed. (Academic Press,New York).

Smith, L.A. (1984). Particulate dispersal in a time-dependent flow, Fellow's lecture in Woods Hole Oceanographic Institution Tech. Rept. WHOI-84-44.

Smith, L.A., Fournier J.-D. and E. A. Spiegel (1986). Lacunarity and intermittency in fluid turbulence, *Phys. Lett.* **114A** #8,9, 465-468.

Smith, L.A. and E. A. Spiegel (1987). Strange accumulators, in *Chaotic Phenomena in Astrophysics*, Ann. N.Y. Acad. Sci. **497**.

Soneira, R.M. and P.J.E. Peebles (1978). A computer model universe: Simulation of the nature of the galaxy distribution the Lick Catalog, *Astron. J.* **83**, 7, 845-861.

Sparrow, C. (1982). *The Lorenz Equations: Bifurcations, Chaos, and Strange Attractors* (Springer-Verlag, New York).

Spiegel, E.A. (1957). The smoothing of temperature fluctuations by radiative transfer, *Ap. J.*,**126**, 202.

Spiegel, E.A. (1986). Cosimic Arrithmias in *Chaotic Behavior in Astrophysics*, ed R. Buchler, J. Perdang, and E.A. Spiegel. (Reidel, Dordrecht) pg 91.

Sreenivasan, K.R. and C. Meneveau (1986 preprint). The fractal facets of turbulence.

Stommel, H. (1949). Trajectories of small bodies sinking slowly through convection cells, *J. Mar. Res.* **8**, 24-29.

Struble, G.W. (1975). *Assembly Language Programming: The IBM System /360 and 370*, (2nd Edition, Addison-Wesley, Reading, MA).

Swinney, H.L. and J.P. Gollub (1979). The transition to turbulence, *Physics Today*.

Swinney, H.L. and J.P. Gollub, eds. (1981). *Hydrodynamic instabilities and the transition to turbulence* (Springer, New York).

Tabor, M. (1984). Modern dynamics and clasical analysis, *Nature*, **310**, 277-282.

Takens, F. (1981)."Detecting Strange Attractors in Turbulence", in: *Lecture Notes in Mathematics*, ed. by D.A. Rand and L.-S. Young, p. 366 (Springer, New York).

Taylor, G.I. (1921). Diffusion by continuous movements, *Proc. London Math. Soc.* **A, 20**, 195-211.

Tenekes H. and J.L. Lumley (1972). *A First Course in turbulence*, (MIT Press, Cambridge).

Termonia, Y. and Z. Alexandrowicz (1983). Fractal dimension of strange attractors from radius versus size of arbitrary clusters, *Phys. Rev. Lett.* **51**, 4, 1265-1268.

Termonia, Y. (1984). Kolmogorov entropy from a time series, *Phys. Rev. A*, **29**, 1612-1614.

Theiler, J. (1986). Spurious dimension from correlation algorithms applied to limited time-series data, *Phys. Rev. A*, **34**, 2427-2432.

Tooby, P.F., G.L. Wick, and J.D. Isaacs (1977). The motion of a small sphere in a rotating velocity field: A possible mechanism for suspending particles in turbulence, *J. Geophys. Res.* **82**, 2096-2100.

Townsend, A.A. (1951). The diffusion of heat spots in isotropic turbulence, *Proc. Roy. Soc.* **A 224**, 487.

Ulam, S. M. and J. von Neumann, (1947). On combinations of stochastic and deterministic process, *Bull. Am. Math. Soc.* 53, 1120.

Umberger, D.K. and J.D. Farmer (1985). Fat Fractals on the Energy Surface. Phys. Rev. Lett. 55, 661-664.

Walker, G.H. and J. Ford (1969). Amplitude instability and ergodic behavior for conservative nonlinear oscillator systems, *Phys. Rev.* **188**, 416.

van de Water, W. and H.M. Bessem (1987 preprint). Chaos and coherent structures in turbulent shear flow.

Witten, T.A. and L.M. Sander (1981). Diffusion-limited Aggregation, a Kinetic Critical Phenomenon, *Phys. Rev. Lett.* **47**, 1400.

Witten, T.A. and L.M. Sander (1983). Diffusion-limited Aggregation, *Phys. Rev. B.* **23**, 5686.

Wolfram, S. (1985). Twenty Problems in the Theory of Cellular Automata, *Physica Scripta* **T9**, 170-183.

Zaiken, A.N., and A.M. Zhabotinsky (1970). Concentration Wave Propagation in Two-dimensional Liquid-phase Self-oscillating System, *Nature* **225**, 535.

Zaslavski, G.M. (1978). The simplest case of a strange attractor. *Phys. Lett.* **69A**, 145.